Composite materials on the basis of a shape memory alloy & a pyro/piezoelectric material for thermal energy harvesting

Dmitry Zakharov

UNIVERSITÉ DE GRENOBLE

THÈSE

Pour obtenir le grade de

DOCTEUR DE L'UNIVERSITÉ DE GRENOBLE

Spécialité : **Génie Electrique**

Arrêté ministériel : 7 août 2006

Présentée par

Dmitry ZAKHAROV

Thèse dirigée par **Orphée CUGAT** et
codirigée par **Bernard VIALA** et **Leticia GIMENO**
co-encadrée par **Jérôme DELAMARE** et **Nora DEMPSEY**

préparée au sein du **Laboratoire de Génie Electrique de Grenoble**
dans **l'École Doctorale Electronique Electrotechnique Automatique Traitement du Signal (EEATS)**

Matériaux composites à base d'alliage à mémoire de forme et pyro-/piézoélectrique pour la récupération d'énergie thermique

Thèse soutenue publiquement le **20.02.2014**,
devant le jury composé de :

Prof. Christian LEXCELLENT
Professeur Emérite, FEMTO-ST, Rapporteur, Président de jury
Dr. Alain BOSSEBOEUF
DR CNRS, IEF, Université Paris-Sud, Rapporteur
Dr. Alain HAUTCOEUR
Directeur Technique, NIMESIS Metz, Membre
Dr. Orphée CUGAT
DR CNRS, G2Elab, Membre
Dr. Bernard VIALA
Ingénieur de Recherche, HDR, CEA LETI, Membre
Dr. Leticia GIMENO
Maitre de Conférence, UJF, Membre

Acknowledgements

This work was carried out in the framework of the collaboration between 3 scientific teams in Grenoble:

- *Magnetic μSystems team (Mag-MEMS) at Grenoble Electrical Engineering Laboratory (G2Elab);*
- *Laboratoire d'électronique des technologies de l'information (LETI) at Commissariat à l'Energie Atomique et aux Energies Alternatives (CEA);*
- *Micro- and Nano-Magnetism team at Institut Néel.*

First of all I would like to thank all my supervisors for their incessant scientific and moral support: Orphée CUGAT, Bernard VIALA, Nora DEMPSEY, Jérôme DELAMARE, Leticia GIMENO. It was a great luck to be supervised by such interesting, efficient, honest and responsible persons.

Thank you, Orphée, for your open and curious mind always full of ideas, for your unforgettable courses I had a chance to attend, for the various help you gave me during my settling down, and of course for your valuable "pinaillages". Thank you, Bernard, for your firm belief, unquenchable optimism and your high-end scientific expertise. Thank you, Jérôme, for your cheerful humour, your delicate openness, your striking physical intuition and, of course, for proving that one man can build an airplane and fly on it! Thank you, Nora, for letting me be a part of your team, for your sincerity, honesty and fairness, energy and enthusiasm, and for teaching me the secrets of thin film fabrication. Thank you, Leticia, for your cheerfulness, readiness to help, valuable advices and corrections. I thank all of you once again for that comfortable ambience you created for pleasant and fruitful work!

I am very pleased to mention here my very old friend and colleague Dr. Gor LEBEDEV, whose ideas and inspiration and also a helping hand were of key importance for this project to appear as well as to advance. Thank you for having invited me to do science together on that day many years ago.

I would like to thank the members of the jury for their goodwill, starting by the reporters, Prof. Christian LEXCELLENT and Dr. Alain BOSSEBOEUF, who have promptly but very attentively read this manuscript and made a detailed feedback. I am grateful to Dr. Alain HAUTCOEUR for his valuable judgement from the industry side. I thank you all for your remarks and comments which have allowed improving significantly this manuscript.

I also thank James ROUDET, the director of G2Elab, and Hervé COURTOIS, the director of Nanosciences Department of Institut Néel, for their welcome and organisation of all the necessary conditions for productive and pleasant work. I address my merci to Elise RIADO, Charlotte BEAUSSIER, Sabine GADAL, and Véronique FAUVEL for their charm and kind assistance with numerous administrative questions and "paperasse". I am thankful to the employees of Nanosciences Foundation for always nice communication: Stéphanie MONFRONT, Marie-Anne CARRE, Alain FONTAINE.

I would like to express my thanks to all those who were teaching and helping me these three years. I am grateful to Victor GAUDE who assured my first steps in clean room and to Marie-Thérèse DELAYE and Julien VIDAL for helping with process-flows. I thank Thibault RICART and once again Leticia for fabrication of shape memory membranes; Daniel BOURGAULT, Laurent RANNO and Denis BLACHIER for first electrical transport measurements and useful advices; Sébastien PAIRIS for teaching me SEM and EDX; Eric MOSSANG and Olivier LEYNAUD for their kind help with XRD; Alain SYLVESTRE for help with first measurements with electrostatic voltmeter. My special thanks to Patrice GERGAUD for high-quality XRD measurements and help with interpretation; to Eugénie MARTINEZ for AES measurements and data treatment and to Francois PIERRE for help with RBS interpretation. I appreciate a lot the help and assistance of Frédéric GAY with both elevated and low temperature electric transport measurements. Many thanks to Aleksandr SHELYAKOV for providing Ti-Ni-Cu ribbons, to Nikolay ANDREEV for TEM analysis and his sincere attention to this work, and to Boris GUSAROV for his important help with pyroelectric effect measurements. I would like to address my grand merci to Richard HAETTEL: I cannot imagine to succeed without your help, your fine engineering flair, your useful advices, and without your high-end vacuum furnace!

I will never forget my dear friends and colleagues Luiz, Geta, Yuepeng, Fréderic, Dominique, Ozan & Nilay, Damien, André, Filippo, Heidi, Tim, Shakti, Svetlana, Thomas, Guillaume, Anja, Yannick, and Oksana. Thank you for having shared with me all the ups and downs of this interesting time, I miss you all. I appreciate a lot the support, understanding and outstanding culinary talents of my dear flatmates: Olivier, Bertrand, and Giovanni. I've learnt a lot from you! Thank you, Boris & Lena, for your friendship and productive team work, I wish you good luck and success on your scientific pathway! Thank you, Viktoriya, for your significant contribution to this victory.

It is my honour to sincerely thank here Dr. Victor KOLEDOV, who supervised me in Russia during many years and who formed the bases of my scientific thinking. I appreciate very much that enormous time and energy you devoted to me and other students as well as scientific knowledge and everyday wisdom you generously shared with us. The experience of studying shape memory composites I acquired with you is one of the building blocks of this work.

I would like also to think of my University professors, notably Boris BOKSHTEIN and Aleksandr RUSAKOV, teachers with a capital "T" which catalysed my interest in science.

Finally, I deeply thank my dear parents, grandparents and my sister without whom nothing would have been possible for me.

And to finish, I thank you, dear reader, for your attention to this work and I hope very much it will bring you some useful answers and inspiring questions.

This work was supported by the Nanosciences Foundation of Grenoble under RTRA program and by the French National Research Agency (ANR) under the Carnot Institute Program. The research leading to these

results has received funding from the European Community's Seventh Framework Programme (FP7/2007-2013) under grant agreement NANOFUNCTION n°257375.

Contents

Part III: Towards thin film harvester fabrication

1 Introduction

1.1 Context of energy harvesting

The increasing demand in alternative energy sources for low-power electronics and autonomous wireless sensors has given rise to substantial research activities in the field of energy harvesting. Among the different energy sources, thermal sources are widely available. Usually, thermal energy can be directly converted into electricity by means of thermoelectric [**1**] (Seebeck effect) or pyroelectric [**2**] materials. Thermoelectric power generators have already been demonstrated. However, such devices require large spatial temperature gradients with cold source management in order to be efficient. Another scheme is to indirectly convert heat into electricity through mechanical transformations [**3**]. This concept requires two materials being mechanically coupled. The first material (i.e. sensor) must exhibit a large thermally induced strain. The second material (i.e. convertor) must exhibit a large stress-induced electric field. In this way, the thermally induced strain is converted into voltage. This work investigates the coupling between a shape memory alloy (SMA) and a piezoelectric material. It concerns any pyroelectric material as well, since all pyroelectrics are piezoelectrics. In the vicinity of thermoelastic martensitic phase transition temperatures SMAs exhibit the largest thermally induced strains (up to 10 % [**4**]) compared to any other inorganic material [**5**]. Together with a large force generated at the phase transformation, it results in the largest actuation energy density for SMAs (up to 100 J/cm^3) compared to any other known material [**5**]. The best candidates for SMA are Ti-Ni and Ti-Ni-Cu alloys which are already used for industrial applications. Regarding polycrystalline piezoelectric materials, PZT has the highest piezoelectric constants. Thus, by coupling Ti-Ni-Cu or Ti-Ni with PZT, one may expect efficient indirect thermal-to-electrical energy conversion and harvesting of temporal thermal variations. Additionally, no radiator would be required in order to force a reference “cold state”. We believe it is a significant advantage for applications whose growing trend is going thinner, flexible and ultra-compact.

The early concept of the SMA/piezo harvester was proposed in 2005 [**6**], but no experimental studies have been realized to our knowledge. We first reported experimental results on harvesting low-frequency thermal variations in 2011 [**7**]. Very recently, both analytical model and experimental characterization of a SMA/piezo structure clamped in a rigid frame was given in [**8**]. The authors have reported generated power at various heating frequencies for temperature amplitude of ~100 °C. In this thesis, two different original bending-type harvesters are considered and the results for lower temperature variations (~10-60 °C) are presented. The experimental value of energy generated per thermal cycle (heating and subsequent cooling through the temperature range of phase transition) lies within the same order of magnitude (~ 100 μJ). However, since no information on the harvester dimensions was provided, accurate comparisons cannot be made.

It is also worth reminding that, since most of the published works on energy harvesting using piezoelectrics concerns the vibration energy, mechanical harvesting systems are usually described in terms of frequency and power. Even though thermal hysteresis of SMA can be decreased by the adjustment of composition [**9**] (with inevitable decrease of its mechanical work output), a variation of at least several degrees is required for producing useful work. Such thermal fluctuations can hardly be rapid in natural systems. For this reason, here the term of energy per cycle is used instead of power, and frequency-dependence is not of interest since thermal energy is harvested in the quasi-static regime. In contrast, in the case where the heat is presented or somehow converted in form of temperature gradient, frequency-dependence for an SMA/piezoelectric harvester would indeed be an important characteristic [**6**].

1.2 Feasibility: thermal-to-electrical energy conversion using combined shape memory and piezoelectric effects

This section aims at giving basic idea about the efficiency of thermal energy conversion into electricity using SMA/piezo harvester, exploiting commercially available TiNi-based SMAs and PZT piezoceramics.

Firstly, the phenomenon of shape memory effect (SME) will be shortly introduced. During cooling, SMA undergoes martensitic transformation which is a diffusionless first order phase transition. As a result, the crystal lattice of SMA deforms by a shear-like mechanism. The product of this transformation (cold) is called martensite and the parent phase (hot) is austenite. Not all the alloys undergoing martensite transformation exhibit shape memory (e.g. martensitic steels), but only those where this transformation is thermoelastic, i.e. the coherence between two phases is conserved. This coherence conservation allows reverse martensite transformation. Both direct and reverse transformations occur within some temperature interval and are characterized by start and finish temperatures. In addition, thermodynamically conditioned thermal hysteresis prevents these temperature intervals from coinciding. Large stress and strain can be developed by an SMA at heating (up to 600 MPa and 10 % for NiTi). Generally, the larger the strain and stress the larger the temperature intervals and hysteresis. This imposes restrictions on the energy that can be harvested from a given system. Moreover, all these characteristics are significantly dependent on the SMA composition. That means that the choice of an optimal alloy and the adjustment of its composition for specific energy harvesting applications are required.

Thorough calculation of the efficiency of heat conversion into mechanical energy by SMA will not be provided here since so-called “martensitic engines” have been already intensively studied [**10**,**11**,**12**]. The input thermal energy required by the SMA body to perform mechanical work consists

of the heat for increasing its temperature (by typically 20 °C [**13**]) and of the latent heat of transformation (~20 J/g for NiTi [**12**]). The typical value of input energy is about 30 J/g.

Specific mechanical work that can be produced by SMA can be calculated as a product of the mechanical stress generated (~500 MPa) and its relative deformation (~ 3 %). In this way the extractable work can be estimated as 15 J/cm^3 or 2.3 J/g (taking the density of NiTi as 6.5 g/cm^3 [**14**]). The efficiency, which is the ratio of work to input heat, can then be estimated at 8 %. While the published values vary within ~3-30 % [**12**], in the majority of theoretical and experimental publications the reported efficiency is ~10 %.

Then the mechanical energy can be converted into electricity by PZT ceramics with the efficiency characterized by the coupling coefficient k^2. For a given material, k^2 depends on the reciprocal orientation of the applied mechanical stress and the induced electrical field. When the force is applied in the same direction as the poling direction, the efficiency can be as high as 50 % in the case of PZT [**15**].

Thereby, total efficiency of the SMA/piezoelectric harvester can be estimated at about 4 % which is higher than typical pyroelectric and thermoelectric conversion efficiencies (~1 %) [**2**,**16**]. The reasoning given above is illustrated by an explanatory scheme in the Fig. 1.1 on the example of 1 gram of NiTi.

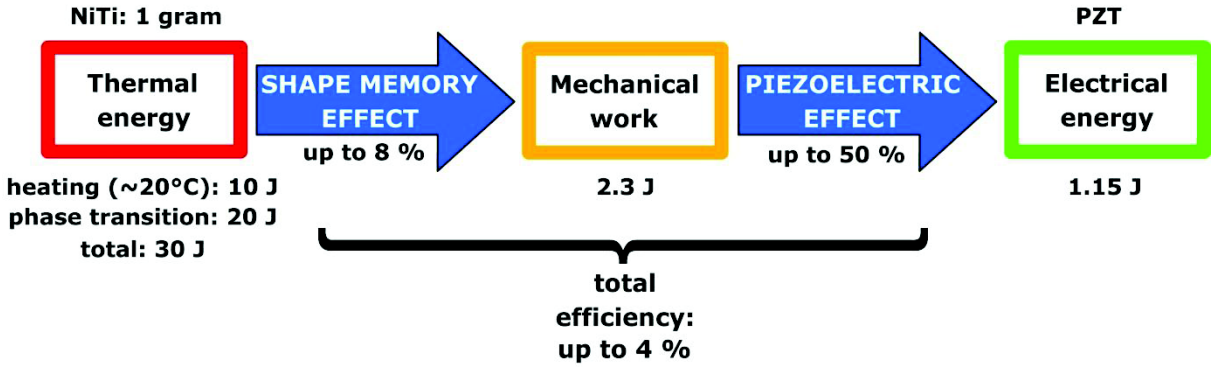

Fig. 1.1. Explanatory scheme of thermal-to-electrical energy conversion using shape memory and piezoelectric effects.

It is worth noting that SMA can only produce work during heating, and some mechanical bias element (spring etc.) is needed to return it to its cold state shape. This means that part of the work is diverted into elastic energy within the bias element. To minimize losses, the harvester should be designed in such a way that the piezoelectric element would act as a bias element for SMA. In the case of a laminated composite, an effective pre-strained configuration [**17**] is proposed here.

Since both shape memory and piezoelectric effects do not deteriorate on micro-scale, the proposed harvesting systems can be miniaturized. With the modern protocols of wireless data

transmission (~pJ/bit [**18**]), microsystems would potentially generate sufficient energy for simple data transmission

1.3 Aims of this work

The aims of this work were:

1. **to experimentally demonstrate and evaluate the interest of coupling piezoelectric and shape memory effects (and additionally pyroelectric) for thermal energy harvesting applications;**
2. **to propose and investigate technological building blocks towards future MEMS harvester integration on silicon.**

1.4 Organizational context

This work was carried out in the framework of the long-standing and fruitful collaboration between 3 scientific teams in Grenoble:

• *Magnetic µSystems* team (Mag-MEMS) at *Grenoble Electrical Engineering Laboratory* (G2Elab);

• *Laboratoire d'électronique des technologies de l'information* (LETI) at *Commissariat à l'Energie Atomique et aux Energies Alternatives* (CEA);

• *Micro- and Nano-Magnetism* team at *Institut Néel*.

The fabrication of mezzo-scale prototypes of energy harvesters and their characterization was done in the CIME-NANOTEC at MINATEC. Shape memory films were fabricated in Institut Néel, while their characterization and patterning was done using numerous facilities of both Institut Néel and CEA. In consideration to our close collaboration, in this manuscript these three teams are often referred to as "our group".

Two researchers from "our group", notably Gor Lebedev and myself, were previously studying shape memory composites under the guidance of Dr. Victor Koledov in Magnetic Phenomena Lab at Kotelnikov Institute of Radioengineering and Electronics (Moscow, Russia). Pre-strained shape memory composite configuration proposed there is used in this work thereby resulting in an informal collaboration with our Russian colleagues. In corresponding cases they are naturally included in the term "our group".

Part I: State of the art

2 Thermal energy harvesting and functional materials

2.1 Energy harvesting

2.1.1 Terminology

Energy harvesting, by general definition, is the conversion of freely available energy existing in various forms in the surrounding environment, into a useful electrical energy. It has also other names: energy scavenging, power harvesting. While, in principle, this term can be also applied to large energy volumes, e.g. power plants, in practice it is habitually used in relation with small scale energy existing within limited volumes and being used for specific applications such as wireless ultra-low power devices as an alternative to batteries.

Although most researchers use the terms "energy scavenging" and "energy harvesting" as synonyms, another opinion can be found in the literature. Citing D. Steingart, "*energy scavenging refers to environments where the ambient sources are unknown or highly irregular, whereas energy harvesting refers to situations where the ambient energy sources are well characterized and regular*" [**19**]. This semantic nuance is not generally recognized, but it underlines an important issue with energy harvesting: a deep understanding of the available energy sources is required in order to be able to exploit them for a useful application.

2.1.2 History

We are curious to learn who was the first to propose the term "energy harvesting", but up to our knowledge and quick literature scan, it likely appeared naturally within the last few decades. The earliest paper where we could find this term was "*Molecular topography of solar energy harvesting pigments in marine algae*" published in 1978 by Pill-Soon Song from Texas Tech University [**20**]. Then, in the late 80's other works related to photo-electric materials were published: "*Picosecond spectroscopy of photoreceptor molecules*" by Aussenegg et al. from Austria [**21**] and "*Very efficient visible light energy harvesting and conversion by spectral sensitization of high surface area polycrystalline titanium dioxide films*" by Vlachopoulos et al. from Switzerland [**22**]. This latter work, by the way, gave birth to the famous Grätzel cell (dye-sensitized solar cell). We can now see that

initially the term referred to solar energy, which is quite natural since it is the most widely available outdoor energy.

Energy harvesting as it is known today, notably as an alternative to batteries, likely appeared in the late 90's. In 1996, T. Starner, a PhD student from MIT, published a paper "*Human-powered wearable computing*", where the idea was proposed that "*power generation by body heat, breath, or motion can potentially power a computer*" [**23**]. He did not use the words "harvesting" or "scavenging", but a year later "*Parasitic power harvesting in shoes*" was reported by a group from the same MIT Media Laboratory [**24**]. They built a PVDF-based piezoelectric power generator and a shoe-mounted rotary magnetic generator to potentially "*replace batteries in certain wearable subsystems*".

The next jump in energy harvesting concept is related with the development of an ultra-low power wireless networking proposed in 2000 by Rabaey et al. from the Berkeley Wireless Research Center [**25**]. The authors showed how to decrease the overall energy consumption by a factor of 50, and proposed an idea for their network nodes "*to be self-contained and self-powered using energy extracted from the environment (energy-scavenging)*". They also demonstrated that for indoor applications solar energy does not supply enough power, and proposed to harvest energy from vibrations using chip-scale MEMS generators.

It may be that this work of Rabaey et al. cited several hundred times was the one which triggered the avalanche of subsequent researches on vibrational energy harvesting during the next decade [**26**,**27**,**28**]. In fact, the development of the energy harvesting concept was, in many respects, a response to the development of new wireless data transmission technologies and low-power devices. For example, in 2001 EnOcean GmbH, a spin-off company of Siemens AG, was founded, offering self-powered solutions for building automation based on their original low-power wireless protocol [**29**]. Since then, many other energy harvesting technologies have been commercialized, e.g. ALGRA AG [**30**], Micropelt [**31**], Pertuum Ltd [**32**], etc.

2.1.3 Thermal energy harvesting

Thermal energy is present in most environments: either as a temperature gradient or as a temporal temperature variation. In the first case, thermoelectric materials (Seebeck effect) can be used to harvest this energy, and pyroelectric materials in the second case. Also, it is possible to transform a temperature gradient into a temporal temperature variation using a caloric fluid pumping between hot and cold sources [**33**] for example, or using a mechanical system with a temperature-sensitive (e.g. pyroelectric) element oscillating between hot and cold sources [**34**,**35**]. Conversely, by maintaining a constant temperature at one end of the thermoelectric generator (TEG) (usually the cold side, with a

radiator), it is possible to harvest temperature variations at the other end. The latter approach recently commercialized by EnOcean® and Micropelt® already exists on the market.

As shown, whatever the initial form of thermal energy, both Seebeck and pyroelectric effects can be exploited for harvesting. Therefore the question arises: what method is the most efficient under given conditions ? Sebald et al. [**33**] have made such comparison and they found that, choosing a proper thermodynamic cycle, the pyroelectric efficiency may largely exceed that of thermoelectricity by a factor of ~30.

Within the next subsections we will give a brief overview of the state of the art for thermal energy harvesting materials: thermoelectrics, pyroelectrics and functional composites.

2.2 Thermoelectrics

Thermoelectric generators (TEGs) produce electrical power from a temperature gradient [**36**]. As illustrated in Fig. 2.1, a heat flow associated with this temperature gradient induces a flow of free charge carriers (Seebeck effect). By connecting n-type and p-type materials in series, a net voltage V is produced. It is proportional to the temperature difference ΔT via the Seebeck coefficient α ($V = \alpha \Delta T$). A good thermoelectric material exhibits $\alpha = \sim 10^{-4}$ V/K. Thus, in order to obtain a voltage which can be realistically exploited, many thermoelectric couples must be connected in series.

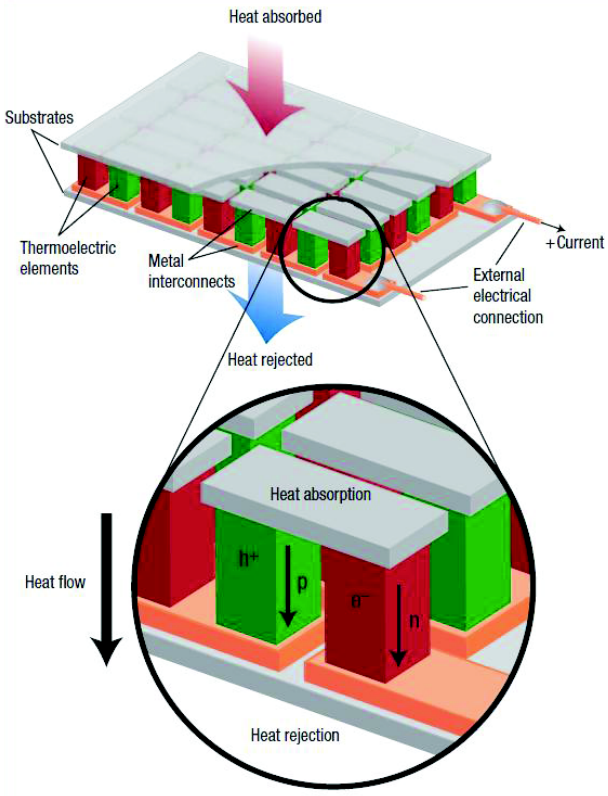

Fig. 2.1. Schematic of a thermoelectric module (G. Snyder [**37**]). h^+ (holes) and e^- (electrons) are negative and positive charge carriers for p-type and n-type material respectively. Both types of charges move with the heat flow, from hot to cold.

The power generation efficiency of a thermoelectric material is characterized by its figure of merit *zT*. Besides the Seebeck coefficient and the temperature, it also depends on the electrical resistivity ρ and thermal conductivity κ [**37**]:

$$zT = \frac{\alpha^2 T}{\rho\kappa}, \tag{2.1}$$

As seen from the formula, a large *zT* requires the optimization of various conflicting properties: high Seebeck coefficient, high electrical conductivity and low thermal conductivity are needed simultaneously. The best state-of-the-art materials have $zT \approx 1$ near room temperature. The material's figure of merit *zT* should be distinguished from the device's figure of merit *ZT* (with a capital *Z*), which is basically an average of the component materials' *zT* values [**38**].

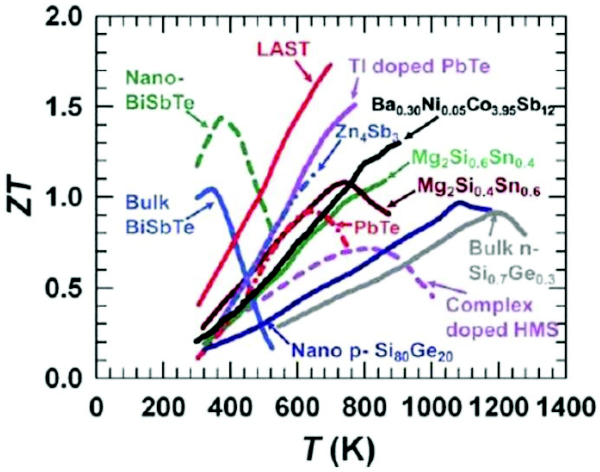

Fig. 2.2. State-of-the-art (2011) comparison of ZT from various materials [**39**]. Originally courtesy of Shi: 2011 (University of Texas, Austin).

When the temperature difference across the thermoelectric is Th–Tc=ΔT, the power generation efficiency can be expressed as [**38**]:

$$\eta = \frac{\Delta T}{T_h} \cdot \frac{\sqrt{1+ZT}-1}{\sqrt{1+ZT}+T_c/T_h}. \tag{2.2}$$

In fact, the efficiency increases almost linearly with the temperature difference. The ideal material efficiency of bismuth telluride-based thermoelectrics (BiTe, one of the best at room temperature) with no losses is ~0.04% for each 1 K of *ΔT* (Fig. 2.3). The device efficiency will be the same at best…

The advantages of TEGs comprise an absence of moving parts, silent operation, reliability and scalability. On the other hand, their efficiency is low, the price is quite high and a massive cold reservoir is indispensible. Despite these problems, TEGs have traditionally been considered the main candidates for thermal energy harvesting, including in microsystems [**40**]. Several TEG energy harvesting solutions were commercialized. Several TEG energy harvesting solutions were commercialized. The first product appeared in 1998: Seiko Thermic, world's first watch driven by body heat [**41**].

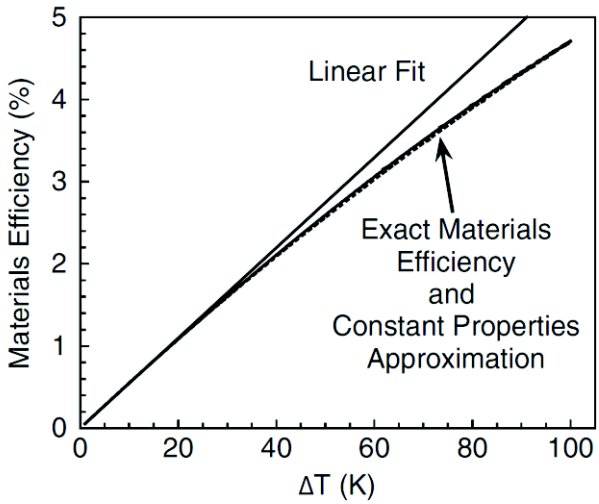

Fig. 2.3. Ideal material efficiency of a BiTe-based thermoelectric (Tc = 300 K) [**38**].

2.3 Pyroelectrics

A solid explanation of pyroelectricity given by Cady can be found in [**42**]. Pyroelectricity can be defined as "*the change with temperature of positive and negative polarization charges on certain portions of crystals belonging to certain classes*". Pyroelectric crystals are polar and have a spontaneous polarization $\mathbf{P}_s$ (average electric dipole moment per unit volume, [C·m^{-2}], vector) in the absence of an applied electric field. In compliance with the orientation of $\mathbf{P}_s$, bound charges form on the surface of the pyroelectric and free charges (ions or electrons) are thus attracted to the charged surfaces to form a screening layer of unbound charge (Fig. 2.4, top). The pyroelectric effect arises from the polarization dependence on temperature. If electrodes are connected to a pyroelectric and short-circuited, no charges flow at constant temperature (Fig. 2.4, middle). A temperature increase ($dT/dt > 0$) results in the average decrease of the dipole moments, leading to the polarization decrease. To compensate the corresponding change of bound charges, the free charges flow from one electrode to another, generating a current (Fig. 2.4, bottom). On cooling ($dT/dt < 0$), an inverse process takes place resulting in a reverse current flow. If the pyroelectric was open-circuited during the temperature change, the unbound charges would stay on the electrodes "against their will", thus accumulating (assuming no leakage) an associated electric energy which can then be harvested.

The observed phenomenon is called primary pyroelectricity. However, due to their polar crystal structure, all pyroelectrics are also piezoelectric (although the converse is not true). This means that the thermal expansion will change the polarization of the pyroelectric due to the piezoelectric effect. This phenomenon is called the secondary pyroelectric effect. Moreover, if heating is not uniform and a temperature gradient appears, the tertiary effect will contribute.

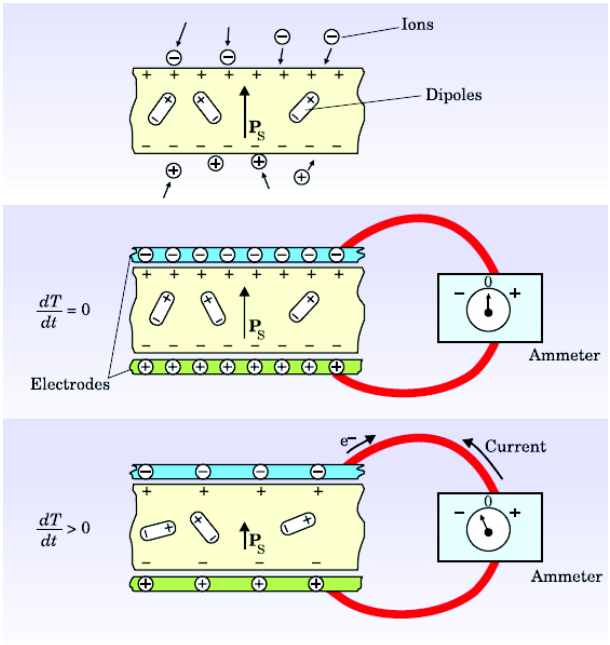

Fig. 2.4. Top: pyroelectric crystal with polarization $\mathbf{P}_S$ in open circuit.

Middle: Pyroelectric with the electrodes in short circuit. Steady state: dT/dt=0.

Bottom: When temperature rises (dT/dt>0), dipole moments, on average, diminish in magnitude (on the image the dipoles become tilted), resulting in the decrease of $\mathbf{P}_S$. The compensating current flow can be detected by an amperemeter.

S. Lang [**43**].

Assuming homogeneous heating, the total pyroelectric coefficient for the crystallographic direction m of the pyroelectric, $p_m \equiv \Delta P_m/\Delta T$, can be written as

$$p_m = p_m^I + \sum_{i=1}^{6} e_{mi}\alpha_i \equiv p_m^I + p_m^{II}, \qquad (2.3)$$

where e_{mi} are anisotropic piezoelectric constants (charge density/strain, $C\cdot m^{-2}$), α_i are anisotropic thermal expansion coefficients (K^{-1}), and p_m^I & p_m^{II} are primary and secondary pyroelectric coefficients.

These pyroelectric coefficients are also called pyroelectric charge coefficients ($C\cdot m^{-2}K^{-1}$), in contrast to pyroelectric voltage coefficients (VK^{-1} or $Vm^{-1}K^{-1}$).

Interestingly, most of the recent reviews on energy harvesting technologies did not mention the pyroelectric effect [**39**,**44**,**45**,**46**]. It is likely related to the low efficiency, and to the fact that natural time-dependent temperature variations are usually slow and not omnipresent, whereas usual wasted heat more likely creates spatial gradients. The attitude of the energy harvesting community towards pyroelectricity started to change around 2008, after Sebald et al. reported on optimization principles of pyroelectric energy conversion [**2**]. In particular, they showed that while the conversion ratio (defined as the ratio of net harvested energy divided by the heat taken from the hot reservoir) of thermoelectrics is highly limited by the materials properties, the conversion ratio for pyroelectrics could theoretically reach the conversion ratio of the Carnot cycle.

Since then, a few dozen publications on pyroelectric energy harvesting appeared. In 2008 Xie et al. studied thermal energy harvesting by PZT pyroelectric material both theoretically and experimentally, and reported that output power is highly dependent upon the surface area and the pyroelectric coefficient [**47**]. In 2011 the same group demonstrated thermal energy harvesting using a PZT, a pre-stressed PZT composite, and a single-crystal PMN-30PT, subjected to periodic temperature

changes [**48**]. The PZT composite was a unimorph with an adaptive PZT layer and two inactive metal layers forming a sandwich, showed twice higher pyroelectric coefficient compared to simple PZT ceramics. However, the reasons of this enhancement were not explained in the paper.

In 2010 Cuadras et al. demonstrated thermal energy harvesting by PZT (ceramic) and PVDF (polymer) pyroelectric materials both theoretically and experimentally, and showed that the generated charge depends on the difference of temperatures between two instant times but not on the temporal evolution of the temperature [**49**]. This means that pyroelectricity could be potentially suitable even for slow temperature variations.

Also in 2010, Fang et al. reported an interesting concept of nanoscale thermal radiation harvesting [**16**]. They used a pyroelectric plate oscillating in a gap between hot and cold plates without touching them (Fig. 2.5). The interesting effect is that "*energy transfer by thermal radiation between two semi-infinite solids is nearly instantaneous and can be enhanced by several orders of magnitude from the conventional Stefan-Boltzmann law as the gap separating them becomes smaller than Wien's displacement wavelength*". The authors conclude that *"(1) parallelism is not essential to the device operation and (2) a gap smaller than 100 nm, if it can be achieved in practice, would result in larger temperature oscillations or operating frequencies for a given temperature swing. In turn, the power density and efficiency of the device would increase. Touching, however, would not be beneficial since heat transfer would then be by conduction, which is slow and limited by the thermal contact resistance between the pyroelectric plate and the cold or hot plates*".

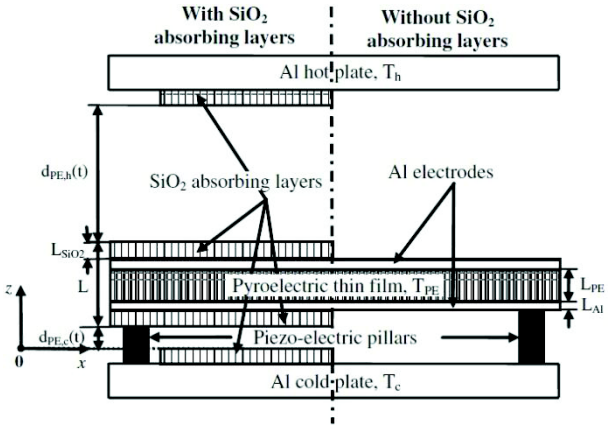

Fig. 2.5. Schematic of a pyroelectric plate oscillating between the hot and cold plates proposed by Fang et al. [**16**].

In 2011 Hunter et al. studied another approach, where a MEMS pyroelectric cantilever touches cold and hot surfaces while oscillating [**35**] (Fig. 2.6). (A similar concept was proposed in 2012 by Ravindran et al. [**34**]; a similar idea could be found already in 2005 in the patent of Nersessian et al. [**6**]). Large arrays of devices could be used to increase power, and this approach allows the device to potentially operate at frequencies up to 20 Hz or higher. In 2012 the same team published the first (to our knowledge) review devoted to pyroelectric energy harvesting, reporting that "*this field has been relatively unexplored until recently due primarily to the disappointing energy conversion efficiencies*

obtained from early modelling and experimental studies". The authors conclude that more recent studies have shown pyroelectric device efficiencies comparable to those obtained using thermoelectric techniques, and even higher efficiencies were theoretically predicted.

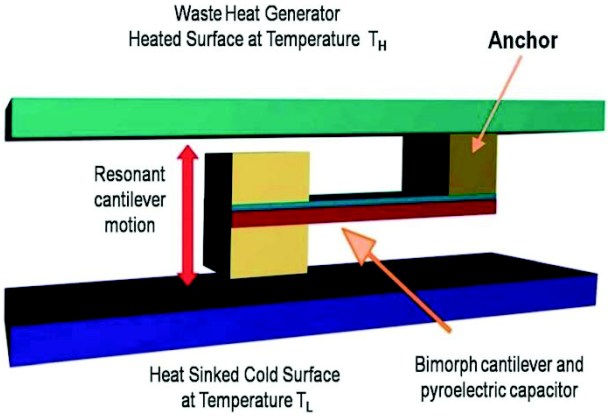

Fig. 2.6. Schematic of a pyroelectric energy harvester, consisting of a bi-material cantilever, which oscillates between cold and hot surfaces, proposed by Hunter et al. [**35**].

For more thorough information about pyroelectric energy harvesting we address the reader to a very recent review by Bowen et al. [**50**].

2.4 Pyroelectric bimorphs

As mentioned, secondary pyroelectricity originating from the piezoelectric properties of a pyroelectric material can contribute to the total pyroelectric effect. Naturally, the idea thus appeared to enhance pyroelectric generation by coupling a pyroelectric material with an additional elastic material. Being heated or cooled, the difference in thermal expansion coefficients between the two layers will generate the strain in the pyro/piezoelectric layer.

Piezoelectric-pyroelectric composites seem to have been first considered in 1978 by Newnham et al., with regard to piezoelectrics optimization for hydrostatic sensors [**51**]. Micromechanics of coupled electroelastic composites was then studied analytically in 1993 by Dunn, confirming the result of Newnham that "*pyroelectric composite materials can be obtained from the combination of two non-pyroelectric constituents*", meaning the contribution of the secondary pyroelectricity [**52**].

In 1994 Nan showed analytically that when designing piezoelectric composites one can use thermal expansion either to eliminate the pyroelectric effect or to increase it, depending on the purpose [**53**]. Then, in 1995 and 2000, the equivalent pyroelectric coefficient of a pyroelectric bimorph structure was analytically deduced by Pintilie et al. [**54**,**55**]. They reported that "*the bimorph structure can be designed in order to obtain high values of the pyroelectric coefficients*".

In 2008 Chang and Huang showed by mathematical modelling more than 100% enhancement in pyroelectric coefficient in laminated Steel/PZT/Steel structures [**56**]. In the same work they reported a good agreement with their experimental results, and concluded that strain transfer loss towards a

pyroelectric layer is an important issue. In their next publications they demonstrated by mathematical and numerical simulations the importance of the measurement method (pyroelectric in open or in short circuit) for pyroelectric coefficient determination [**57**,**58**,**59**]. In 2010 they proposed a pyroelectric energy harvesting device based on laminated pyroelectric structures, and experimentally showed 88 % enhancement in pyroelectric coefficient [**60**].

To our knowledge, Chang and Huang were the first to demonstrate experimentally an enhancement of pyroelectric coefficient in laminated composites. However, from our impression, the details of their experimental procedure for pyroelectric coefficient measurements seem unclear. We can conclude that today there is a lack of experimental studies on this subject.

2.5 Hybrid systems for thermal energy harvesting

By hybrid systems we understand here those which exploit a combination of different physical effects for conversion of thermal energy into electrical energy.

For example, in 2008 Carlioz et al. proposed an interesting hybrid thermal energy harvesting system compatible with slow and small temperature variations [**61**,**62**]. The prototype was composed of three elements: a PZT/brass bimorph cut from a piezo buzzer converts mechanical deformation into electricity (Fig. 2.7). This bimorph is deformed by the magnetic attraction force between a permanent magnet (Nd-Fe-B) stuck to the centre of the piezo beam and a soft ferromagnetic material (Fe-Ni) attached to the housing of the system. The Fe-Ni sample has a Curie temperature T_C below which the beam is attracted to the Fe-Ni, when the temperature reaches T_C the beam is released (upon release, it can oscillate for some time). The system is reversible with temperature: the beam is clamped again to the Fe-Ni once this cools down. Due to the non-linearity of the magnetic force vs. distance, when the threshold balance between the forces is crossed, the beam "jumps" from one position to the other, generating charges faster than the piezo can dissipate them through internal leakage.

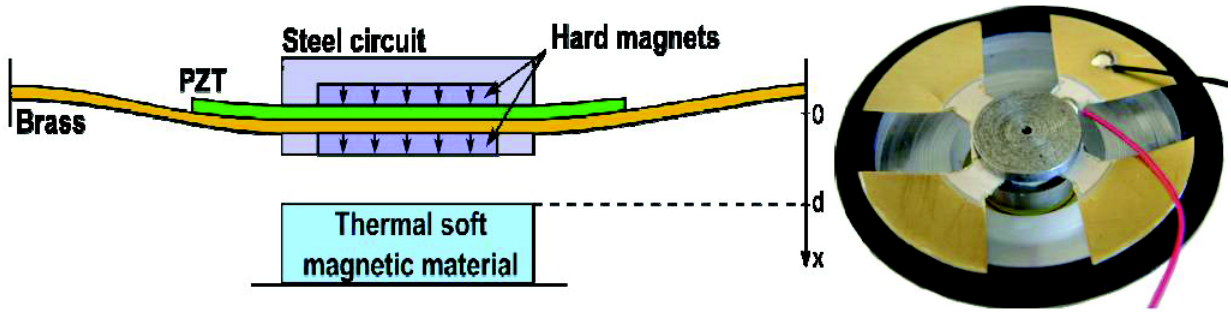

Fig. 2.7. Thermo-magnetically triggered piezo generator by Carlioz et al. Left: Schematic cross-section. Right: 60 mm prototype [**63**].

In 2011 Srivastava et al. proposed to use a thermally-induced ferromagnetic-nonferromagnetic phase transformation in Ni-Co-Mn-Sn SMA placed inside coil to produce electrical energy [**64**]. The authors call their method "*direct conversion of heat to electricity*", which seems surprising given that the conversion exploits an indirect combination of the complex magnetostructural phase transformation and the Faraday's law of induction ; nevertheless the method is interesting and it was the first proposition to use magnetic SMA for thermal energy harvesting. (Use of stress-induced magnetic martensite twins reorientation for mechanical energy harvesting was proposed earlier by other researchers [**65**,**66**,**67**].)

2.6 Hybrid shape memory alloy (SMA)/piezoelectric structures

SMAs were introduced in Introduction. In 1992 Chen et al. from Pennsylvania State University proposed for the first time the hybridization of an SMA and a piezoelectric and were the first to fabricate a thin laminated composite and to demonstrate its shape memory and ferroelectric properties [**68**]. It was the same laboratory which was first to study piezoelectric-pyroelectric composites in 1978 [**51**]. We would like to provide a citation from their paper: "By combining shape memory alloys with piezoelectric ceramics we intend to fabricate a family of smart materials which retain the best characteristics of both types of actuators. We call these composites "SMARTIES", an acronym for "Shape Memory Actuators and Regulating Transducers for Intelligent Electronic Systems." There are a number of ways in which the alloys and ceramics can be assembled in different connectivity patterns to optimize the actuating and sensing functions." The authors fabricated a simple 2-2 composite (2 layers) in which sol-gel films of PZT or PLZT are laid down on commercial 100 μm thick ribbons of Ni-Ti shape memory alloy. To measure ferroelectric properties of PZLT, the Ni-Ti layer was used as one of the electrodes, while the second one was sputter-deposited. The composite showed two-way shape memory effect of 0.4 % (transition temperature ~82 °C) without any electrical of mechanical degradation of PZLT. However, a 0.5 % strain resulted in the PLZT layer crack. Piezoelectric property measurements were reported to be in progress.

Unfortunately, after this pioneer and very interesting work, no more publications about SMARTIES appeared. Since then, there were few analytical studies of SMA/piezo heterostructures for sensing and actuating applications [**69**,**70**,**71**,**72**,**73**]. In [**71**], Jiang & Batra analytically studied a 3-phase composite consisting of a polymer matrix, with SMA and piezoceramic (PZT) inclusions. The authors reported that "*the hybrid composite exhibits pyroelectric effect even if none of its constituents is pyroelectric*", confirming the general-case results of Newnham & Dunn. This is likely the first mention of SMA/piezo composite thermally-induced electricity (2001).

Alam et al. were likely the first to study the problem of thin film integration of SMA and piezoelectric on a Si wafer substrate [**74**,**75**]. In 1997 they reported that the $BaTiO_3$ and PZT buffer

layers improved the crystallinity of Ti-Ni films deposited at high temperatures and the films were obtained smooth. Kim & Lee studied the fabrication of Ti-Ni films onto PZT/Pt/Ti/SiO2/Si and Pt/PZT/Pt/Ti/SiO2/Si and reported successfully obtaining the intended phases. A similar study was published by Zhu et al., but in their work PZT was deposited onto Ti-Ni/SiO_2/Si [**76**].

Although ferroelectric properties of the PZT films were demonstrated, neither shape memory nor piezoelectric properties were studied in any of these works. As far as we know, only Sato succeeded to experimentally demonstrate these properties for his SMA/piezo composite wire for self-sensing actuator application [**77**].

We would like also to mention the works of Zeng et al. on coupling magnetic SMA Ni-Mn-Ga with PMN-PT [**78**] and PVDF [**79**,**80**] piezoelectrics, in which the magnetoelectric effect was studied. Potentially, the same systems could be tested for thermal energy harvesting.

For the first time, SMA/piezo composite for fluctuating temperature harvesting was experimentally demonstrated in 2011 by our group (Lebedev et al.) [**7**] and independently by Namli & Taya [**8**]. The latter group previously (2007) published an analytical model of thermal-to-electrical energy conversion by SMA/piezo system [**81**]. While our group proposed a freely deforming bimorph laminated energy harvester (Ti-Ni-Cu/MFC, Fig. 2.8), Namli's harvester had the two materials rigidly clamped (Ti-Ni/PZT, Fig. 2.9). Since the dimensions of their harvester were not reported, correct comparison of the devices' performances seems not possible.

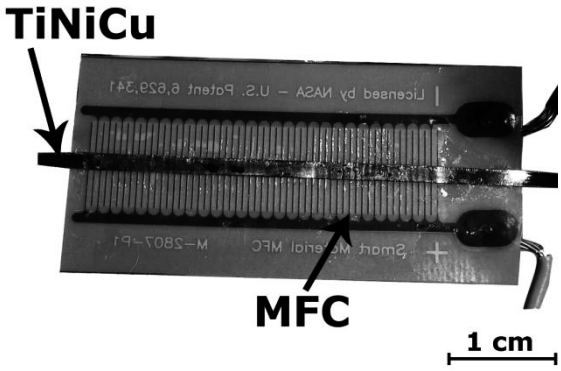

Fig. 2.8. First SMA/piezo energy harvester proposed by our group, 2011 [**7**].

In 2012, our group has already reported an original Ti-Ni/PZT "machine" harvester [**82**], which will be described in the next chapter of this report. A year later, a paper of Avirovik et al. appeared proposing a similar concept for remote harvesting of laser radiation Fig. 2.10 [**83**].

Finally, we note that no fabricated MEMS SMA/piezoelectric harvesters were reported so far. Neither were reported calculations of possible output energy and efficiency of such micro-sized systems.

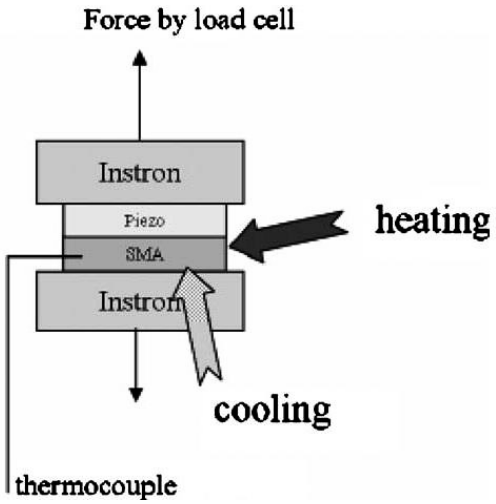

Fig. 2.9. SMA/piezo energy harvester proposed by Namli and Taya, 2011 [**8**].

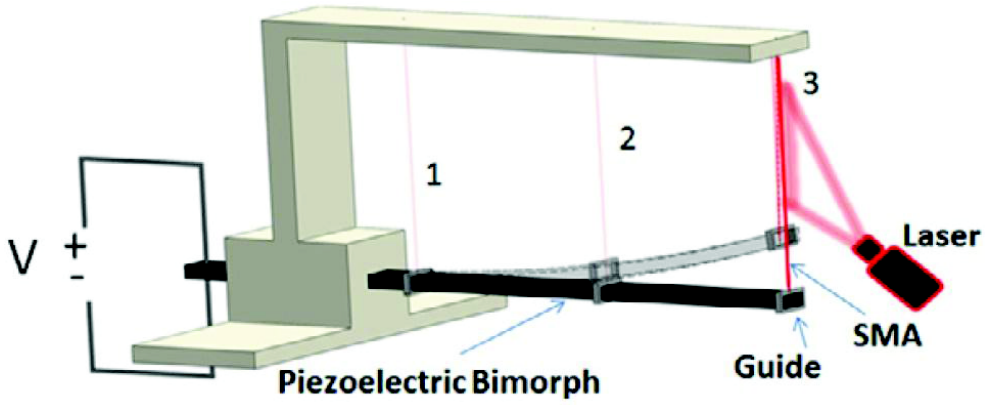

Fig. 2.10. Shape memory alloy-piezoelectric hybrid transducer proposed by Avirovik et al. [**83**].

2.7 Enhanced shape memory composite scheme

SMAs exhibit the highest actuation energy density among all known materials exhibiting solid-state transformation (up to 10 MJ/m^3) [**5**]. Thereby, for a given required amount of mechanical work to be done, an actuator made of SMA would have a minimal size. SMA layers of submicron thickness exhibit the shape memory effect (SME) and can be potentially applied for MEMS and NEMS energy harvesters [**84**]. However, SMAs have an inherent drawback, as the SME is a one-way effect. SMA memorizes only its "hot" shape and thereby needs a bias element to recover its initial "cold" shape There exists also the two-way SME associated with a special distribution of crystalline defects, but it is difficult to control and the corresponding actuation strain and stress are usually one order lower [**13**].

In our previous works, an enhanced scheme of shape memory composite was proposed and studied on mezzo- [**17**,**85**,**86**,**87**] and submicron-scales [**88**,**89**]. The composite exhibits "two-way" SME while keeping the actuation properties of SMA with one-way SME.

The scheme is shown in Fig. 2.11. The composite consists of an SMA layer rigidly connected to an elastic layer, e.g. of a usual metal.

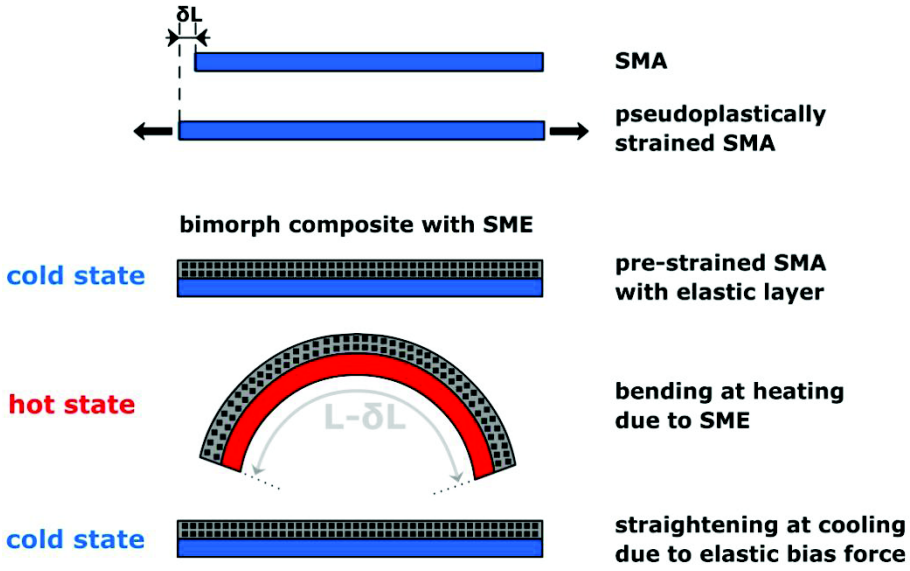

Fig. 2.11. Principle of the enhanced scheme of a bimorph composite with SME.

A novel feature of such bimorph composite is that the SMA element is subjected to a pseudoplastic tensile pre-straining prior to connecting with the elastic element. This scheme is quantitatively enhanced by providing higher reversible strain compared to previous solutions where the pseudoplastic straining of SMA was induced using thermal expansion difference of the layers *after* their connection [**90**]. Such composite is a thermally controlled actuator which bends on heating due to the SME and recovers its shape on cooling thanks to an elastic layer, which acts as a bias spring. It is worth noting that if the SMA is ferromagnetic, the actuator can be also controlled by a magnetic field [**89**,**91**].

Let us estimate the strain generated in the composite at heating. With the assumption of pure bending and equal mechanical constants and thicknesses of the two layers, according to the Euler-Bernoulli beam theory, the neutral fibre of deformation lies in the middle of the composite on the boundary between the two layers, and the maximal strain is at the composite's outer borders. This maximum value can be roughly estimated at the initially imposed pseudoplastic linear strain of the SMA.

In the case of Ti-Ni, the pseudoplastic strain is typically 1-10 %, meaning that a material with high elasticity limit is needed as the elastic layer. Typically, the elasticity limit of metallic materials is

below 1 %, and even lower for ceramics (~0.1 %). However, in practice, mezzoscale composites are fabricated by gluing, and a significant part of the strain may be lost in the glue layer, thus allowing using metals or even ceramics for this scheme. But this solution is not optimal, if the aim is to efficiently convert the thermal energy into the elastic layer mechanical energy. An alternative would be to use soft polymers for the elastic layer.

2.8 Shape memory composite scheme for pyroelectric enhancement

As explained in Section 2.4, the pyroelectric coefficient of a pyroelectric composite can be higher than that of a pyroelectric alone. Our group proposed for the first time to use the enhanced shape memory composite scheme for pyroelectric materials. Depending on its nature, an SMA can provide strains as high as 1-10 % even for small temperature variations, typically ~1-30 K, whatever the temperature variation rate. Previous researchers exploited a difference in thermal expansion coefficients of the two layers. Taking an extreme case, polypropylene has one of the highest thermal expansion coefficients: 150 ppm/K. Assuming non-expanding pyroelectric, for 30 K it would give just 0.45 % strain, which is still lower than the minimal SMA strain. Moreover, typical thermal expansion of solids is lower, ~1-30 ppm, which, taking into account the pyroelectric layer expansion, results in much lower pyroelectric coefficient compared to that provided by our composite scheme.

The principle is illustrated in Fig. 2.12. On image (a), a pyroelectric material alone is shown, which pyroelectric effect is characterized by the sum of primary and secondary pyroelectric coefficients. Considering the SMA/pyro-piezoelectric bimorph exploiting pre-strained composite scheme on image (b), its secondary coefficient is increased by the thermally-induced strain of the SMA.

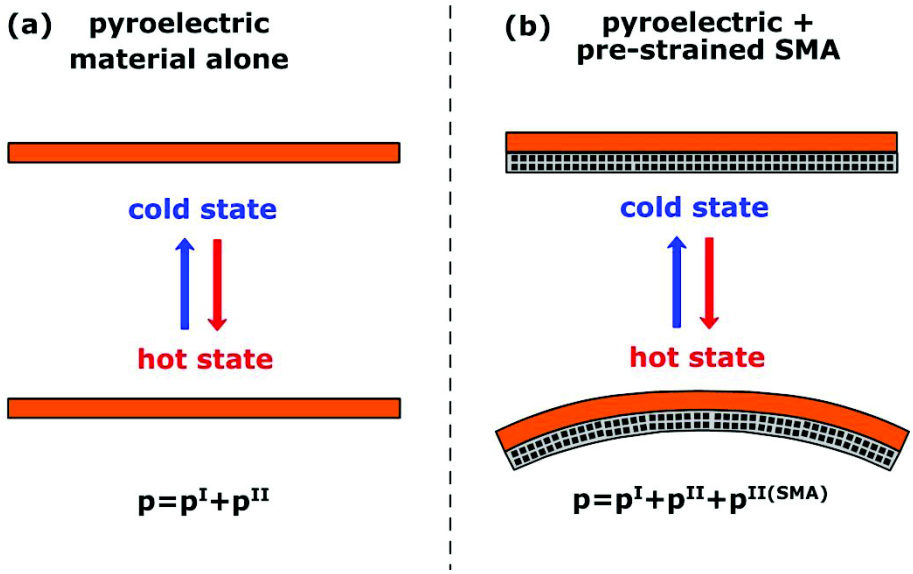

Fig. 2.12. Principle of pyroelectric coefficient enhancement by coupling a pyroelectric material with an SMA.

The scheme described could also be potentially used for piezoelectrics which are not pyroelectric, to create "artificial" pyroelectrics. The latter would be interesting only if there existed non-pyroelectric piezoelectrics with piezoelectric constants higher than those of pyroelectric ones. However, to the best of our knowledge, this was not observed.

2.9 Ti-Ni-Cu SMA films

2.9.1 Introduction

Ti-Ni-based SMA thin films have been the subject of extensive research since the early 1990's. This reflects first the technological interest for applications, due to the outstanding shape memory properties of these alloys that have rapidly invaded industry. This also indicates that physics, metallurgy and thermodynamics in such materials is remarkably rich and stimulate numerous researches in lab. During this project we became familiar with about a hundred papers on this topic. We do not aim here to give an overview of all these works.

A good overview of shape memory materials (alloys, ceramics, and polymers) and explanation of the mechanisms of shape memory effect and superelasticity can be found in the book edited by Otsuka & Wayman [**92**]. Thorough information about physical metallurgy of Ti-Ni-based SMAs can be found in an excellent paper by Otsuka & Ren [**93**]. For an overview of SMA thin films (deposition techniques, characterization, applications, MEMS design) we address to a very useful book edited by Miyazaki et al. [**13**]. Finally, information about development and characterization of thin film Ti-Ni-Cu SMAs was given in an impressive combinatorial study by Zarnetta [**94**].

2.9.2 Phase transformation in Ti-Ni-Cu SMAs

This section exposes some basic information on phase transformations in Ti-Ni-Cu SMAs. Since copper is usually a minor component in these alloys, we can consider the binary Ti-Ni diagram as the first approximation (shown in Fig. 2.13). The phase which undergoes the martensitic transformation is $Ti_{50-x}Ni_{50+x}$, with x within ±0.5 at.% below 600 °C [**94**]. As seen in the diagram, Ni-rich alloys contain at equilibrium the Ni_4Ti_3 phase, while Ti-rich alloys contain the Ti_2Ni.

During cooling, TiNi undergoes a direct martensitic transformation. The parent phase of all Ti Ni-based alloys has a cubic B2 (ordered b.c.c.) structure. Depending on composition and thermo-mechanical treatment, the B2 phase may take one of three transformation paths shown in Fig. 2.14: to monoclinic martensite (B19'), orthorhombic martensite (B19), or trigonal martensite (R-phase) [**93**]. For the latter two, an additional successive transformation step to monoclinic martensite can be observed, this resulting in a two-step transformation. Transformation paths for Ti-Ni-Cu alloys with

various compositions reported by Zarneta are shown in Fig. 2.15 [**94**]. The samples were thin films vacuum-annealed for 1 h at various temperatures: 500 °C; 600 °C; 700 °C. As seen, while Ni-rich compositions exhibit all 3 transformation paths, for the Ti-rich ones only B19 and B19' can be found.

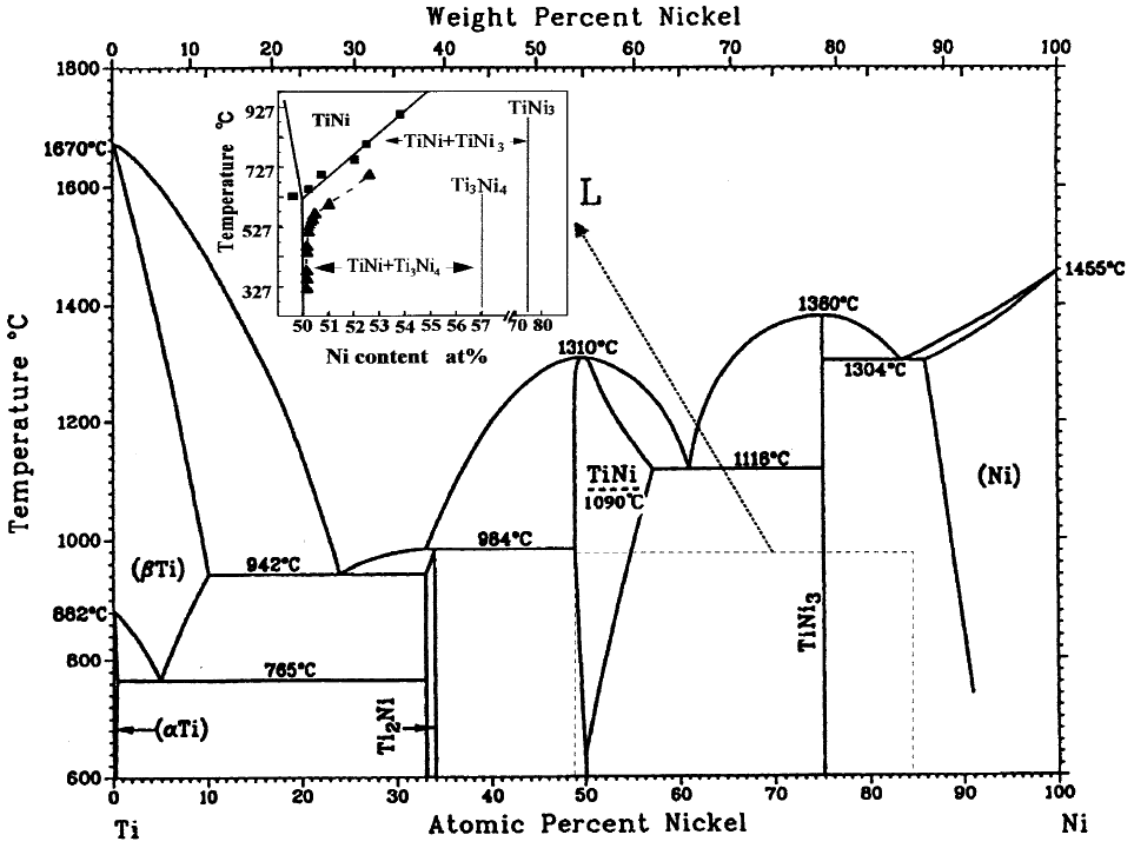

Fig. 2.13. Phase diagram of Ti-Ni system [**93**].

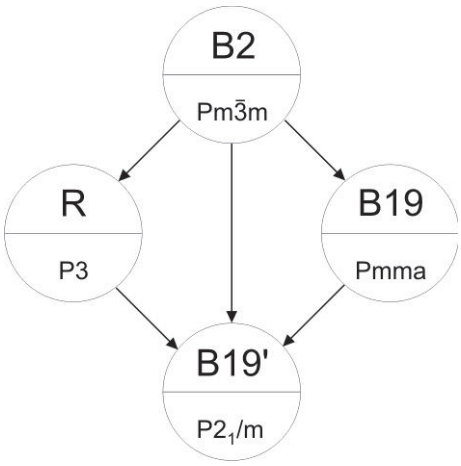

Fig. 2.14. Schematic of three possible transformation paths for Ti-Ni-based SMAs. Space groups are indicated for the phases [**93**].

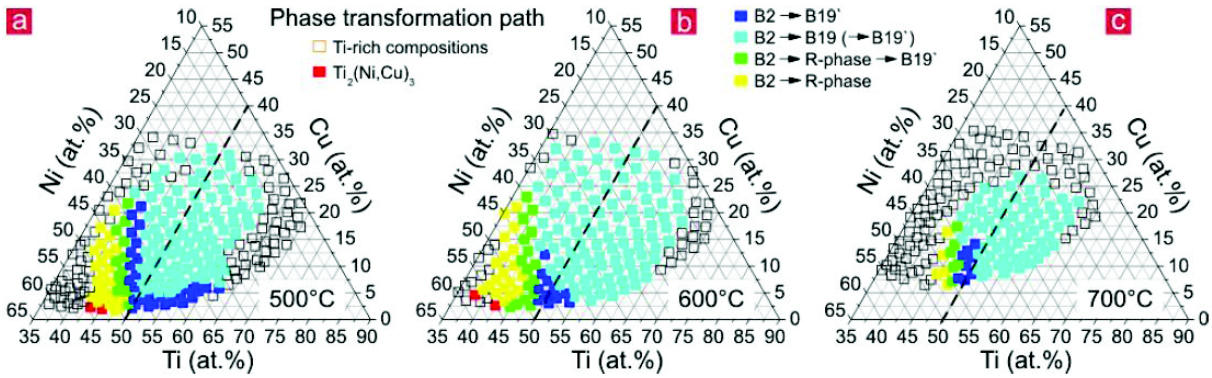

Fig. 2.15. Colour coded phase transformation paths for Ti-Ni-Cu thin films with various compositions. The films were vacuum-annealed for 1 h at: (a) 500 °C; (b) 600 °C; (c) 700 °C. Dashed lines indicate $Ti_{50}Ni_{50-x}Cu_x$ compositions. From Zarnetta [**94**].

As mentioned in Chapter 1, martensitic transformations occur within a certain thermodynamically-conditioned temperature interval, which is schematically shown in Fig. 2.16. During cooling, a direct transformation takes place within the temperature interval ΔT_M: starting at M_s and finishing at M_f. Similarly, during heating a reverse transformation happens within the temperature interval ΔT_A: starting at A_s and finishing at A_f. The two transformations are shifted by ΔT_{hys} corresponding to the supercooling/superheating required to overpass the interface energy. One can also remark a transformation interval $\Delta T_{transf} \equiv A_f - M_f$: the minimal amplitude of a thermal cycle required to complete both the direct and inverse transformations.

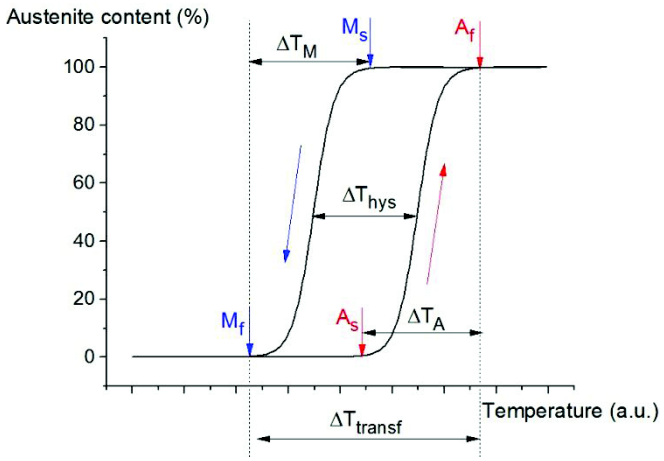

Fig. 2.16. Schematic of martensitic phase transformation in SMAs.

Fig. 2.17 shows martensite start (for various martensite types) and austenite finish temperatures and corresponding transformation hysteresis for Ti-Ni-Cu thin films annealed for 1 h at 600 °C [**94**]. The characteristic temperatures lie above room temperature within 26~86 °C, being maximal at ~50 at.% Ti. The ΔT_{hys} is at maximum near ~26 K, reducing to ~0 K for the R-phase (compare with Fig. 2.15). Unfortunately, since M_f and A_s were not reported by the author, ΔT_{transf} cannot be estimated

[**94**]. We would like to underline that the ΔT_{transf} is an important characteristic for practical applications.

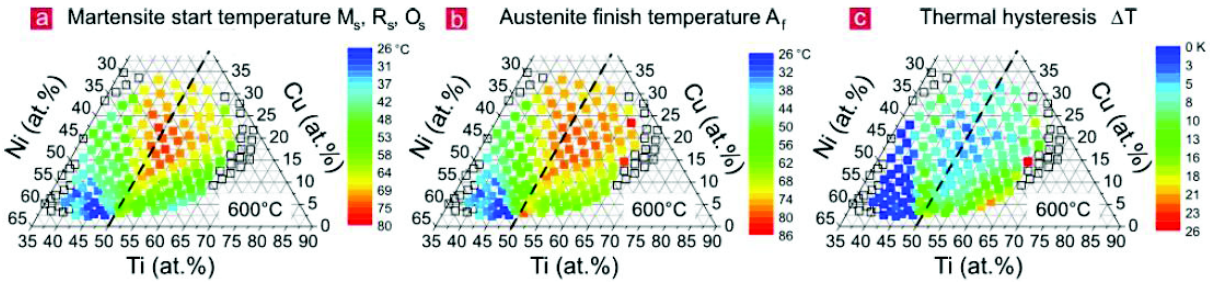

Fig. 2.17. Phase transformation characteristics for Ti-Ni-Cu thin films with various compositions annealed for 1 h at 600 °C. The M_s, R_s and O_s martensite start temperatures correspond to the B19, R and B19' martensite types. Dashed lines indicate $Ti_{50}Ni_{50-x}Cu_x$ compositions. From Zarnetta [**94**].

2.9.3 Thermally actuated membranes

We should consider here in more detail another work, which was for us an important guide for fabrication of shape memory membranes. Tomozawa et al. successfully fabricated SMA membranes on Si wafers, consisting in a 1.5 µm Ti-Ni-Cu layer on the top of a 1 µm SiO_2 layer (Fig. 2.18) [**95**,**96**].

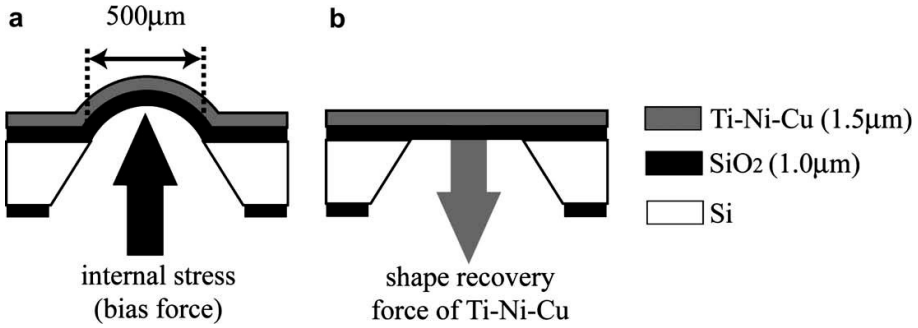

Fig. 2.18. Cross-sections of a microactuator utilizing a Ti-Ni-Cu thin film proposed by Tomozawa et al. at (a) room temperature and (b) high temperature [**95**].

The silicon was etched from the back side all the way up to the oxide layer to form a membrane. The authors demonstrated that it can be thermally actuated by passing an electrical current through the SMA layer. At room temperature the membrane bulges up due to the accommodation of thermal deformation accumulated during cooling down after annealing. This accommodation occurs in the martensitic transformation thanks to the martensite phase pseudoplasticity. When reverse martensite

transformation happens during heating, the membrane is straightened (shortened) due to the SME. When the current is switched off, thanks to its small mass the membrane quickly recovers its bulged shape. As seen from Fig. 2.19, the use of $Ti_{42.0}Ni_{38.0}Cu_{10.0}$ SMA allowed the complete shape change within ~20 K of temperature variation, with a transformation hysteresis of only ~6 K. The height change was quite high, at ~2 % of the membrane longitudinal size. As seen in Fig. 2.20, this amplitude remained for heating frequencies up to 50 Hz, then gradually decreasing, losing only ~25 % at 100 Hz.

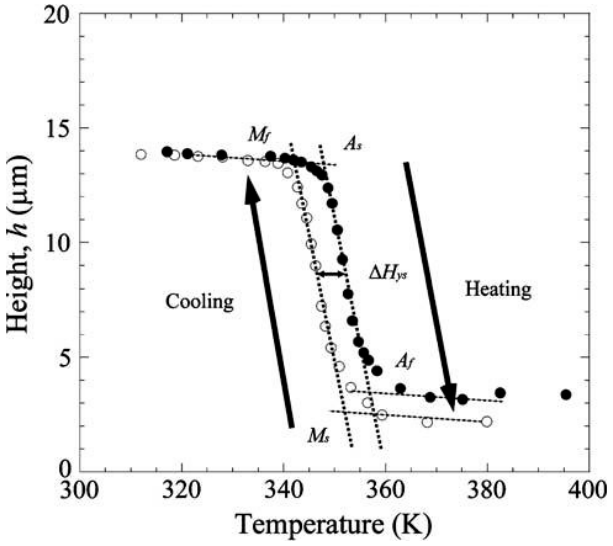

Fig. 2.19. Temperature dependence of the height of a bulging microactuator utilizing a $Ti_{38.0}Ni_{10.0}Cu$ thin film heat-treated at 700 °C for 10 min [**95**].

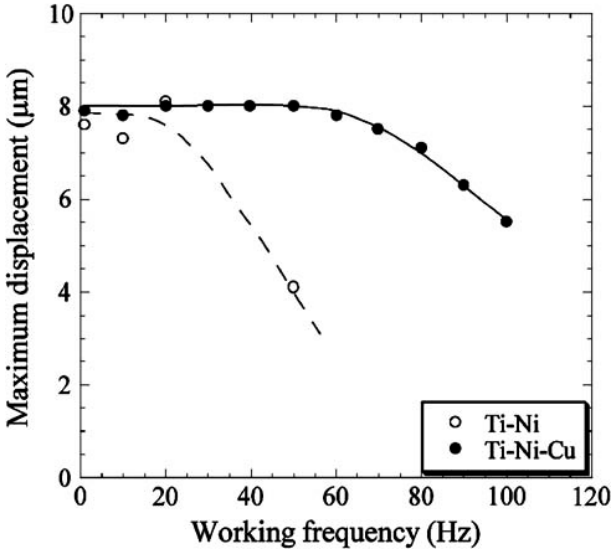

Fig. 2.20. Comparison of the maximum displacement vs. working frequency for two types of microactuators [**95**].

The Ti-Ni film based actuator previously fabricated by the authors had much higher hysteresis (27 K), and its displacement decreased quickly at higher frequencies (Fig. 2.20). Another alloy tested by this group, $Ti_{52.7}Ni_{47.3}$, exploited he R-phase martensite with hysteresis of only ~3 K [**97**]. Although it showed no decrease of actuation amplitude up to 125 Hz, its displacement was lower at ~4 μm. The authors conclude that Ti Ni-Cu is an optimal SMA for high-speed, large displacement microactuators.

In our work we intended to fabricate a similar system with an additional layer of piezoelectric material for thermal energy harvesting purpose. We paid so much attention here to the results of Tomozawa et al., since they experimentally proved the feasibility of a micro-scale SMA-based bimorph, showing a thermally controlled deformation with high speed and high strain.

Finally, we would like to mention that at the beginning of this work we were dreaming that the system described (SMA/piezo micro-composite) would allow a multi-mode energy harvesting: it is sensitive to vibrations due to piezoelectric effect; to thermal variations due to both "intrinsic" and "artificial" pyroelectric effects; in the case of magnetic SMA (e.g. Ni-Mn-Ga-based alloys), it would also be sensitive to magnetic fields. However, each mode would require quite different system optimization, and it would be hard to find a realistic compromise. Therefore our project was primarily focused on the thermal energy harvester development.

Part II: Proof of concept

3 Mezzo-scale demonstrators

3.1 SMA/piezoelectric hybrid machine

The first approach to couple shape memory and piezoelectric effects for thermal energy harvesting that we present in this report is a hybrid SMA/piezoelectric "machine" with a localized bonding between the two active materials, each taken as a separate element: a PZT plate working in flexion, and an SMA ribbon or wire working in contraction. The SMA wire is connected to the end of the PZT plate via an intermediate compliant body (Fig. 3.1). The thermally induced linear contraction of SMA (up to 5 %) bends the PZT cantilever-type plate by pulling on a specially designed, flexible mechanical structure (see video demonstration on http://youtu.be/uS0z4ZEBeYw). In contrast to the laminated structure, this configuration exploits the full mechanical work generated by the SMA: therefore it should have higher efficiency of energy harvesting.

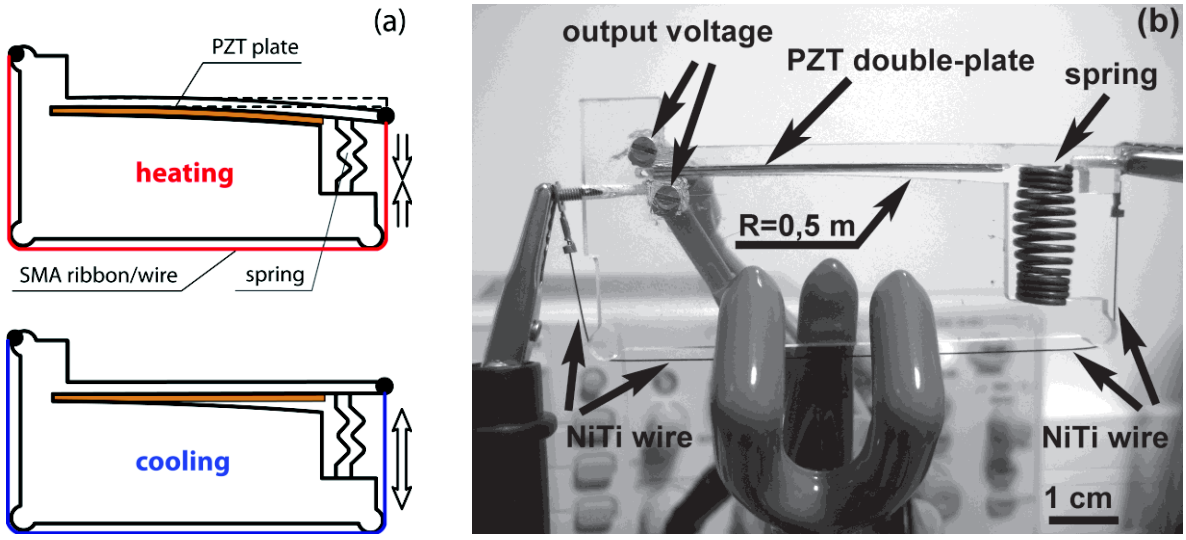

Fig. 3.1. Schematic views (a) and photo (b) of the SMA/piezoelectric machine. The NiTi wire is drawn around 3 sides of the plexiglass bending system (to save space). The PZT double-plate is inserted in the bending frame. Electrical contacts on the left and on the right are used for applying the heating current to the NiTi wire.

The curvature imposed by the compliant beam onto the PZT is controlled and limited by the curvature of the bulk frame, thus ensuring an optimal deformation of the PZT plate. The spring in this "machine" provides shape recovery of the SMA during cooling. We remind that usual SME is a one-

way effect since only the high-temperature shape is memorized and the work is produced by SMA only at heating. It should be noted that an optimized SMA/piezoelectric "machine" should not need any spring since the piezoelectric material would be thick and stiff enough to act as a spring itself. The optimized PZT thickness will thus allow (1) to use all the strain generated by SMA and (2) to be stiff enough to return the SMA to its initial shape upon cooling.

3.1.1 Materials and methods

The reported case is as follows.

1. SMA: NiTi wire, continuous SMA heating mode (no cycling);
2. piezoelectric: double plate consisting of two PZT ceramic plates with a serial electrical connection;
3. instant electrical PZT discharge using mechanical switch.

3.1.1.1 Materials

Commercial "PIC 255"-type PZT (lead zirconate titanate, $Pb[Zr_xTi_{1-x}]O_3$) plate from "PI Ceramic GmbH" was used [**15**]. It had electrodes coated on both sides. A 0.5 mm thick plate was cut into 50 mm × 6 mm pieces by a dicing saw. Two pieces were glued together using non-conductive commercial epoxy adhesive "3M Scotch-Weld DP460 Off-White" locally substituted with silver lacquer to provide electrical connection between the electrodes. The connection sides for each piece were chosen in such a way as to provide the charges of opposite signs on double-plate sides when bending. After application of the epoxy, the double-plate was slightly pressed with a vice at room temperature for 24 h.

For some samples, an elastic spacer was added between the PZT plates in order to shift the strain neutral fibre. It was a 0.25 thick stainless steel sheet shaped to have almost the same width and length as the PZT plates.

Commercial NiTi wire (product name: "Tensile actuator") from "Memry Corp." was 13 mm long with ⌀ 250 μm. The wire was heated up during about 3 s through the thermoelastic transformation using 1.7 W of Joule heating (2 V × 0.85 A, in agreement with the wire datasheet) thus provoking its shortening by ~5 mm, which corresponds to a strain of ~3.8 %. The start & finish temperatures of the inverse martensitic transformation (i.e. at heating) were estimated approximately with a thermal camera at 45 & 80 °C respectively. For the direct transformation they were 65 & 30 °C, giving the same transformation interval of 35 °C at both cooling and heating. Consequently, the transformation hysteresis was ~15 °C. Although the overall temperature interval experienced by the

wire was from room temperature up to ~90 °C, the strain was generated only during phase transformation. For this reason, we relate the voltage generated to the temperate change of 35 °C.

When the wire shortens, the PZT double-plate becomes constrained within the plexiglass bending frame which is shaped as an arc with a constant curvature radius of 0.5 m. Thereby the piezoelectric is subjected to a limited deformation which for a first approximation can be considered as a homogenous bending. With the assumption of pure bending, according to the Euler-Bernoulli beam theory, the maximal strain in the piezoelectric s_{max} is:

$$s_{max} = \frac{h}{R}, \tag{3.1}$$

where h is a single-plate thickness and R is the curvature radius.

In our case s_{max} = 0.1 %. This value is close to the elastic strain limit of PZT, ~0.1-0.2 % [**98**,**99**]. (However, some researchers report lower values ~0.03% [**100**,**101**].)

The overall volume of active materials (2 PZT plates and NiTi wire) was ~0.3 cm^3, calculated from the geometric parameters compiled in Table 3.1 (taking into account that 2 PZT plates are used).

Table 3.1. Geometric parameters of the materials used for preparation of the SMA/piezoelectric machine.

Size (mm)	PZT	NiTi
length	50	130
width	6	⌀ 0.25
thickness	0.5	

3.1.1.2 Output energy measurement

The evaluation of the charges generated by a piezoelectric may be done in various ways. As illustrated in Fig. 3.2, two electric configurations were tested, with the piezoelectric element: (a) in closed circuit and (b) in open circuit with a switch. When the piezoelectric is continuously connected to the oscilloscope input impedance, all the charges will continuously disappear immediately after generation with the characteristic time constant. When the piezoelectric is in open circuit during voltage generation, the charges will continuously accumulate, and then can be evaluated from the corresponding discharge curve after closing the circuit. In both cases, the electrical energy E dissipated in the load resistance R_L can be calculated from a corresponding change of the piezoelectric voltage V with time t as

$$E = \frac{1}{R_L}\int_t V^2(t)dt\,. \tag{3.2}$$

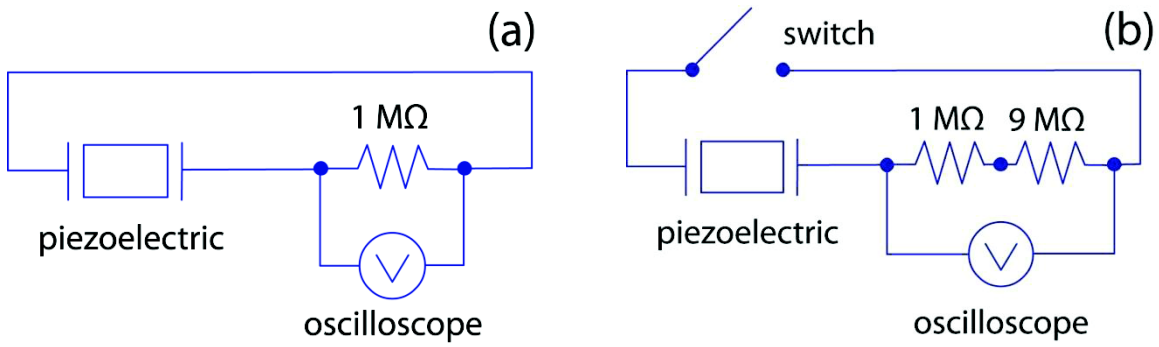

Fig. 3.2. (a) Closed circuit and (b) open circuit harvesting configurations for piezoelectric element.

3.1.2 Results and discussion

3.1.2.1 Energy harvested at heating and cooling

Fig. 3.3 shows the absolute electric response of the NiTi/PZT hybrid machine when heating and cooling the NiTi wire by 35 °C, through the thermoelastic transition.

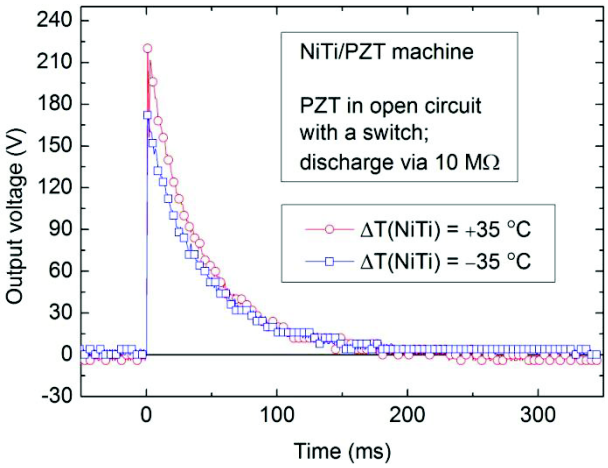

Fig. 3.3. Absolute output voltage, generated by the SMA/piezoelectric hybrid machine, harvested from a single temperature change of 35 °C of the NiTi wire through the thermoelastic transition. The voltage is discharged in the 10 MΩ oscilloscope input immediately after the temperature change (with a switch).

When heating, a positive voltage was generated by the PZT double-plate which was bent due to the NiTi wire shortening. During bending, the electrical circuit remained open (Fig. 3.2a). Just after the bending was complete, the electrical circuit was closed with the switch, and the voltage was discharged in the 10 MΩ oscilloscope input. As seen in the figure, the discharge time was ~200 ms. The harvested energy was ~60 μJ, calculated using formula (3.2). Then the electrical circuit was opened again, and only after that the heating was stopped, and the NiTi wire was naturally cooled down to room temperature. Finally, just after the PZT double-plate has completely recovered its straight shape, the electrical switch closed the circuit again. The harvested energy was similarly

calculated at ~90 µJ. We do not believe that this difference in energy for cooling and heating cases is reliable, more experimental data is needed to confirm this.

The present results were obtained for the PZT double-plate with the intermediate spacer. Several samples without spacer were also tested, but the results did not differ significantly. Within a series of different samples without spacer, the generated voltage value difference ranged from few µJ up to few tens of µJ. We ascribe it to the quality of preparation of the samples which could cause PZT damage or formation of parasitic electrical connections on the surface. Monitoring of samples' electrical resistance is needed to understand the data scattering.

As regards reproducibility of the results for a given sample, the measured values could differ by ~10-30% from one measurement to another or from one day to another. We believe it can be partly related to a phenomenon of charge leakage, which has been reported to depend on air humidity [**102**]. An evaluation of leakage for our samples is presented hereunder.

3.1.2.2 Charge leakage

When the electrical circuit is open it could be expected that the electrical charges will not dissipate at the PZT electrodes. However, it was found that the charges vanish rather quickly: typically 15 s was enough for complete vanishing. This may be due to some parasitic electrical connections between the PZT electrodes, either externally via conductive pollution, or within the PZT itself, but no clear evidence has been found by visual observation. It also means that some harvested energy was lost before closing the circuit, and that the values obtained were not maximal.

In order to determine the time constant of charge leakage for the PZT used, the electric response of the NiTi/PZT machine was measured using a contactless electrostatic voltmeter. The result is shown in Fig. 3.4. The charges vanished completely after ~3 min. This value is one order of magnitude slower than that observed in the experiments with the switch. This may be explained by possible electrical arcs in the switch air gap when closing the circuit. The maximal output voltage value of the

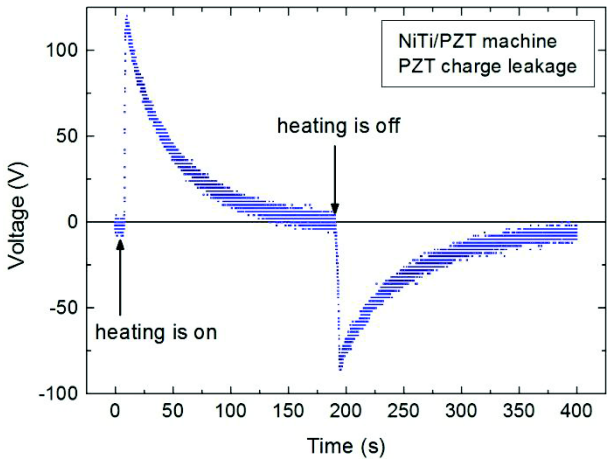

Fig. 3.4. Voltage generation by the hybrid NiTi/PZT machine and its dissipation due to intrinsic piezoelectric leakage. The measurement was made using a contactless voltmeter. The voltage was generated twice: during direct Joule current heating (0-200 s) of the NiTi wire, then during subsequent natural air cooling (200-400 s).

machine in this experiment was less than that in the previous ones (compare with Fig. 3.3). It could be due to possible degradation of the PZT ceramic plate.

3.1.3 Use of a toggle mechanism

When a piezoelectric element is deformed slowly, intrinsic leakage can cause significant decrease of harvester efficiency. For slow temperature variation, a possible solution is to use a toggle mechanism providing fast deformation of the piezoelectric even at slow deformation of an SMA element. Such alternative machine configuration was tested, based on a commercial piezoelectric generator from EnOcean Piezo Transmitter Module PTM 100. This generator is actually a linear motion converter which at some point has been used in autonomous wireless light switches: energy for wireless transmission is generated when pushing the button.

Its structure is shown in Fig. 3.5a. At initial position, the piezoelectric plate is bent by the rocker and abutted against the arc-shaped inside wall of the plastic housing. Independently of the speed of pressing the button, the rocker abruptly moves the piezoelectric plate to the opposite position. In the same way, realising the button abruptly sends the plate back to its initial position. The piezoelectric plate is a bimorph consisting of two PZT plates separated by a 0.2 mm thick metallic spacer. The size of one PZT plate is 33×7×0.25 mm^3, resulting in overall PZT volume of ~0.1cm^3. The PZT plates are connected electrically in parallel.

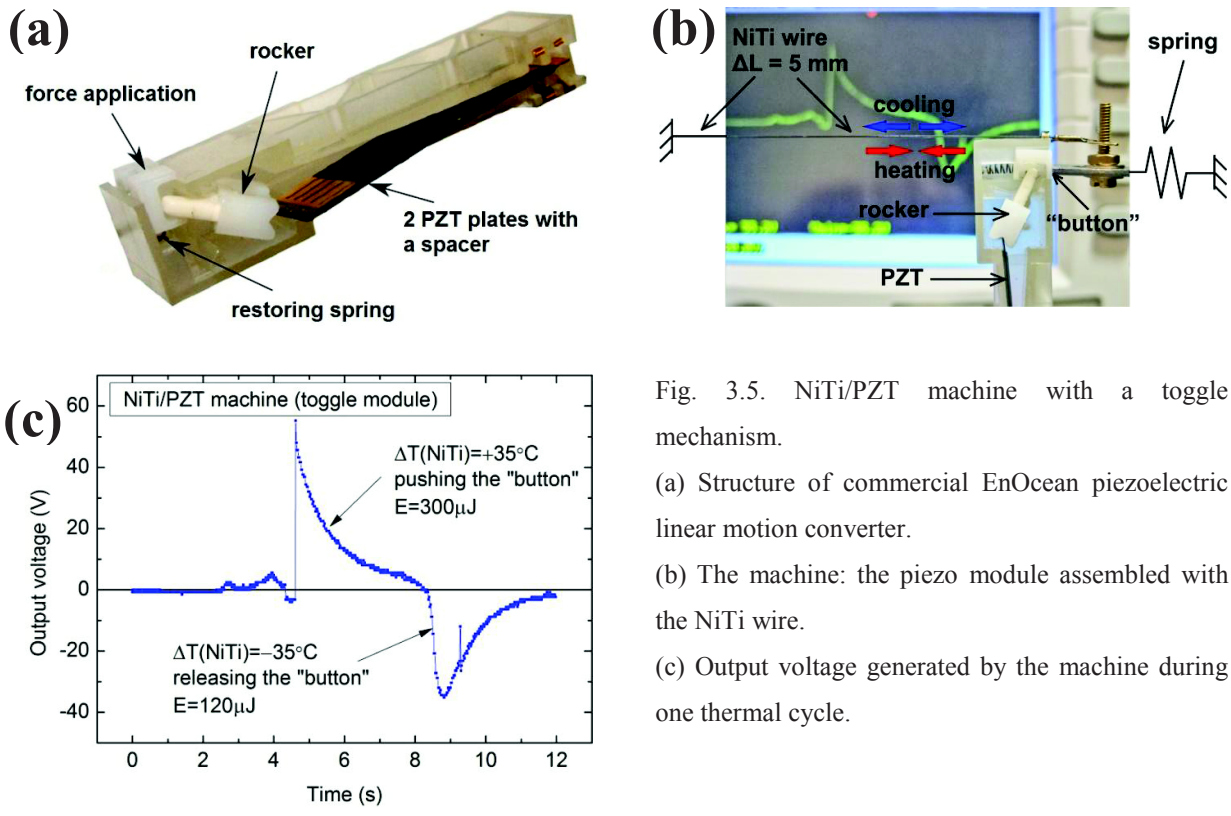

Fig. 3.5. NiTi/PZT machine with a toggle mechanism.

(a) Structure of commercial EnOcean piezoelectric linear motion converter.

(b) The machine: the piezo module assembled with the NiTi wire.

(c) Output voltage generated by the machine during one thermal cycle.

The alternative version of the NiTi/PZT machine consists of this piezo module and of the same NiTi wire as was used in the previous version. The module was assembled with the wire as shown in Fig. 3.5b: one of the wire's ends is rigid while the other is connected to a small metallic piece with a spring and thereby movable. One end of the metallic piece is abutted upon the module's "button" thereby playing the role of a finger while the NiTi wire is its thermally actuated muscle. Heating the wire here is equivalent to pushing the "button"; cooling back is equivalent to releasing the "button". See video demonstration at http://youtu.be/IXA3rC25zjA.

The output voltage generated during one thermal cycle is plotted in Fig. 3.5c. At heating, this machine generates 0.3 mJ of electrical energy, which is ~3 times more than it was generated with the previous, "toggle-less", machine. We remind that the latter was using the same NiTi wire whereas exploiting ~3 times more of PZT material. In addition, in contrast to the previous experiment, this time the electrical switch was not used and the piezoelectric was continuously connected to the load resistance. As it will be shown below for laminated composites, such electrical scheme can result in lower values of harvested energy. To sum up, the use of toggle mechanism together with higher-quality commercial piezoelectric plate provided ~10 times higher specific harvested energy even with unfavourable electrical scheme. This shows that the performance of our prototype machines is limited by imperfect piezoelectric element rather than by SMA element.

Finally, we should point out that toggle-type configuration creates an artificial threshold of thermal variations below which they cannot be harvested. This should be taken in consideration when choosing an optimal design for a specific application.

3.1.4 Intermediary summary and conclusions

1. The original hybrid SMA/piezoelectric machine was proposed and fabricated, and its ability to generate electrical energy during heating and cooling was experimentally demonstrated.
2. For a temperature variation of 35 °C, the machine harvested ~75 μJ (2.5 mJ/cm^3). Therefore, this rather compact but not yet optimized system meets the requirement for wireless data transmission and can be potentially used for such applications.
3. Intrinsic charge leakage was observed for some PZT ceramics. This problem is important for applications and should be studied comprehensively, particularly the materials science aspects.
4. Under conditions of non-negligible leakage, a toggle-type machine providing fast deformation of a piezoelectric would be advantageous. However, it creates an artificial threshold of thermal variations below which they cannot be harvested.
5. Use of higher-quality commercial piezoelectric plate together with advantageous toggle mechanism allowed increasing specific harvested energy by the factor of 10. This shows

that the performance of our prototype machines is limited by imperfect piezoelectric element rather than by SMA element.

3.2 SMA / (pyro-)piezoelectric hybrid laminated composite

As mentioned above, all pyroelectric materials are piezoelectric, and therefore their electric response can be enhanced by coupling with a shape memory material. For this case it seems logical to assemble both materials into a compact composite structure.

3.2.1 Materials and methods

3.2.1.1 Materials and fabrication

An original SMA/piezoelectric laminated composite was fabricated for energy harvesting of small quasi-static temperature variations. It was realized by assembling a Ti-Ni-Cu SMA ribbon and a Macro Fibre Composite (MFC) piezoelectric into a bilayered structure using cyanoacrylate glue (Fig. 3.6). Before assembling, the Ti-Ni-Cu ribbon was pseudo-plastically pre-strained in order to define a preferential strain direction during thermoelastic phase transformation (see Section 2.7 "Enhanced shape memory composite scheme"). The overall volume of active materials (MFC and Ti-Ni-Cu) was ~0.1 cm^3, calculated from the data compiled in Table 3.2.

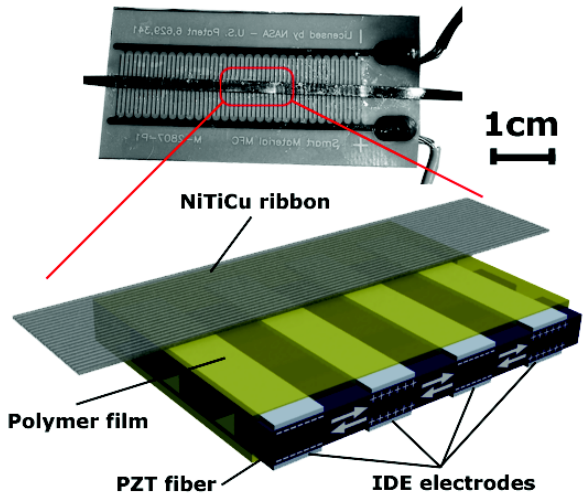

Fig. 3.6. Top: photo of the thermal energy composite harvester. The Ti-Ni-Cu ribbon is connected to the MFC with cyanoacrylate glue.

Bottom: schematic view of the MFC composite, with ribbon on top.

Table 3.2. Geometric parameters of the materials used for preparation of the laminated composite.

Size	MFC	Ti-Ni-Cu
length, mm	28	28
width, mm	12	2
thickness, μm	300	40

3.2.1.2 MFC piezoelectric

MFC is a composite piezoelectric material commercialized by "Smart Materials Inc." [**103**,**104**]. It consists of a sheet of rectangular ~100 μm thick PZT fibres aligned between top and bottom electrodes and embedded within polymer insulating Kapton films (Fig. 3.6 bottom). The MFC type used was M-2814-P1. P1-type exploits the superior g_{33} piezoelectric effect of PZT by using inter-digitated electrodes. When being elongated or shortened, the PZT fibres generate electrical charges which can be collected at the bonding pads. The capacitance value reported in the datasheet is 0.61 nF.

3.2.1.3 Ti-Ni-Cu SMA

The SMA layer was a 40 μm thick ribbon of $Ti_{50}Ni_{25}Cu_{25}$ (the numbers in lowercase correspond to the content in at.%), kindly provided by Dr. A. Shelyakov (NRNU "MEPhI", Moscow). It was prepared by melt spinning technique as described in [**105**]. The ribbon was vacuum annealed for 5 min at 500 °C to obtain a suitable microcrystalline structure. Such thermal treatment was already used in the previous study of a bimorph laminated composite comprising a steel ribbon and a Ti-Ni-Cu ribbon [**17**]. There, flexural thermally-induced deformation of the composite reaching 0.6 % was observed in the region 51-66 °C (Fig. 3.7). The start and finish temperatures of the direct and inverse transformations almost coincided and the hysteresis was rather small and did not exceed 2 °C. In the current work, similar thermoelastic behaviour was assumed for the SMA/piezoelectric composite.

It is worth noting that the maximal operational strain for the MFC reported in the datasheet is ~0.5 %, which is lower than the maximal strain expected in the composite. However, practice showed that the imperfection of the cyanoacrylate glue contact can considerably decrease the strain transmitted to the second (non-SMA) layer. In the present case, this allowed us not to destroy the piezoelectric layer during operation; on the other hand, part of the mechanical work generated by the SMA is lost, and the efficiency of the energy harvesting is thus decreased. Using soft (pyro-)piezo-polymers would be advantageous for our composites. For instance, (pyro-)piezoelectric polyvinylidene difluoride (PVDF) is currently under investigation by our group. First results have shown its promising properties [**106**].

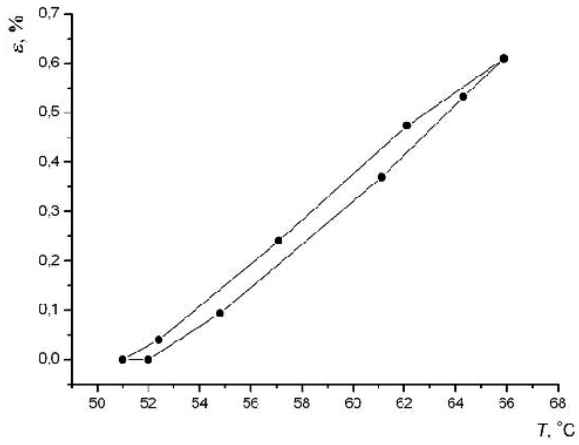

Fig. 3.7. Temperature dependence of the flexural strain of a previous laminated composite Ti-Ni-Cu/steel [**17**].

3.2.1.4 Heating through Joule effect

To induce the deformation of the Ti-Ni-Cu/MFC composite, the ribbon was heated by applying a direct electrical current. The resistance of the ribbon was 1.6 Ω, and Joule power of 2 W (2 V × 1 A) was used to heat it from room temperature up to ~80 °C in ~1 min. This temperature was assumed to be high enough to finish the phase transformation of the Ti-Ni-Cu (finish temperature ~70 °C with the composition used), and low enough to prevent the MFC from degradation (the maximum operating temperature of the MFC reported in the datasheet is 140 °C). Then the ribbon was naturally cooled down in air. As the ribbon was glued onto the MFC, the MFC participated in the thermal exchange.

The temperature was measured using a commercial thermal camera SC500 (FLIR Systems) with 0.1 °C thermal resolution. An additional magnifying lens allowed a spatial resolution of ~0.1 mm. The start moment of the temperature measurement was manually synchronized with the start of heating. The experimental error of time determination can be estimated at 0.5 s. The composite's surface was covered with a temperature-resistant black paint (Crown® 7221) from the side of the ribbon in order to provide homogeneous thermal emissivity.

Different from many other works on thermal energy harvesting, we do not consider frequency dependencies, since a quasi-static regime is of interest here. Single heating-cooling cycles were studied.

3.2.1.5 Heating in water thermostat

Passing a current through the ribbon results in strongly inhomogeneous heating of the entire composite, and a water thermostat was eventually used to properly compare the electric response of the MFC alone with that of the composite. Basically, it was a glass (250 cl) of hot water (~70 °C) which was naturally let to cool down to room temperature. This cooling was slow, and together with rapid thermal stabilization of our rather thin composite, it allowed us to assume the temperature being

unchanged during one given measurement. The temperature was monitored by a thermocouple connected to a multimeter. This simple system allowed for very quick experiments.

The MFC was in open circuit during the measurements. Voltage generation and subsequent intrinsic charge leakage were monitored with a non-contact electrostatic voltmeter. By observing the voltage evolution, we could also estimate the finish moment of the composite thermal stabilization.

3.2.2 Results and discussion

3.2.2.1 Theoretical estimation of MFC pyroelectric properties

Pyroelectric effect is usually neglected for MFC [**107**], but as far as we know, no measurements have been reported before our work [**106**]. However, MFC consists of PZT which is a pyroelectric material [**108**,**49**]. One can estimate the pyroelectric voltage V obtained for a temperature change ΔT knowing the pyroelectric charge coefficient ρ_Q, relative dielectric permittivity ε_r and thickness h using the following expression [**109**]:

$$V = h\frac{\rho_Q}{\varepsilon_r \cdot \varepsilon_0}\Delta T, \tag{3.3}$$

where ε_0 is the vacuum permittivity ($8.85 \cdot 10^{-12}$ Fm^{-1}).

Using the values indicated in Table 3.3, one obtains ~1.9 V/K, which represents the pyroelectric voltage coefficient ρ_V [**110**]. This is not negligible and the pyroelectric effect in MFC needs to be studied individually.

In addition, since MFC is a composite material, a thermal strain may also be induced therein by the difference in dilatation coefficients of PZT fibres, Cu electrodes, epoxy matrix and Kapton package. For example, Kapton is a polymer, which thermal expansion is about one order of magnitude higher than that of ceramics [**107**]. This may cause thermally-induced mechanical tension of PZT fibres and contribute to voltage generation.

Table 3.3. Properties of PZT5A (fibres used in MFC).

Property	Value
pyroelectric charge coefficient ρ_Q	$2.38 \cdot 10^{-4}$ $Cm^{-2}K^{-1}$ [**111**]
relative dielectric constant κ_r	~1800 at room temperature [**112**]
thickness h	127 μm [**107**]

3.2.2.2 Piezoelectric in closed circuit (continuous discharge), Joule heating

In the case of short-circuited piezoelectric (Fig. 3.2a), the MFC electrodes are continuously connected to the moderate oscilloscope input impedance (1 MΩ). Fig. 3.8 shows the thermally-induced voltage generated by the composite during a single heating/cooling cycle. The measured

ribbon temperature is also reported in the graph (20-80 °C). Fig. 3.9 plots the voltage versus temperature extracted from Fig. 3.8.

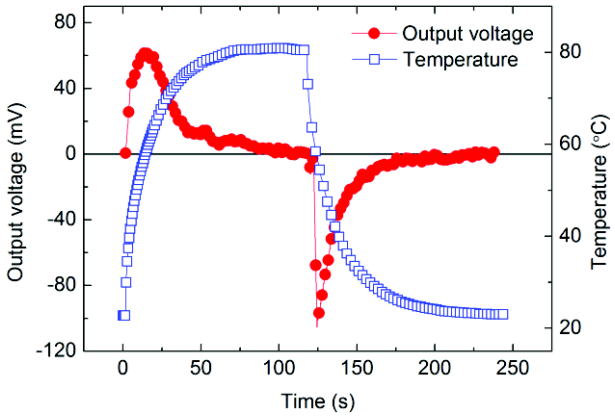

Fig. 3.8. Output voltage generated by the Ti-Ni-Cu/MFC composite and Ti-Ni-Cu temperature, during a single heating/cooling cycle, with direct Joule current heating (0-120 s) and subsequent natural air cooling (120-240 s), as a function of time.

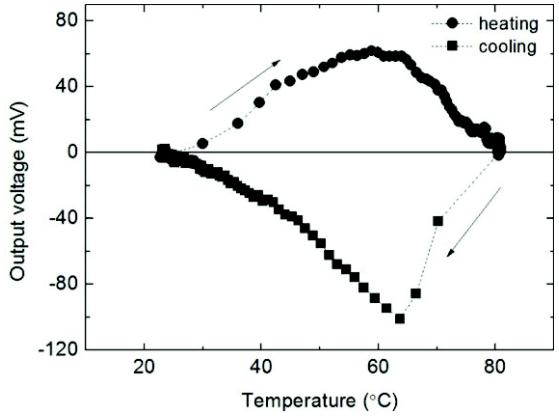

Fig. 3.9. Output voltage generated by the Ti-Ni-Cu/MFC composite during a single heating/cooling cycle, as a function of the Ti-Ni-Cu temperature. (Extracted from Fig. 3.8.)

A positive voltage generation (up to +60 mV) is observed at heating, and a negative voltage (up to –100 mV) at cooling. Both positive and negative voltage peaks can be interpreted as the result of the superposition of two competing processes: (1) continuous electrical charging of the piezoelectric and (2) continuous discharging of the piezoelectric in the oscilloscope input impedance. The charging rate increases with the heating/cooling speed. This seems logical since both "intrinsically" pyroelectric charges and the charges induced by SME-driven piezoelectric effect increase with temperature. The discharging rate depends on the capacitance of MFC, which might also depend on temperature. Another phenomenon involved is a piezoelectric leakage which will be shown below to be significant, especially at high temperatures.

An average harvested energy of ~0.1 μJ was found representative for both heating and cooling processes (formula (3.2)). As shown in our previous work, an MFC / magnetostrictive composite controlled by a magnetic field, generates an output voltage of a few hundred volts with the corresponding energy of few hundred μJ [**113**]. It means that in the current experiment a very low output was obtained. We believe the difference is related to the glue used (cyanoacrylate instead of

epoxy) and also with the measurement method (closed circuit instead of open). In the next section we show much higher values obtained with open circuit measurements.

3.2.2.3 Piezoelectric in open circuit (instant discharge), Joule heating

The second configuration was the instant discharge mode with the piezoelectric being in open circuit during the deformation (Fig. 3.2b). The MFC electrodes were connected to the oscilloscope input with an electrical switch via an additional 9 MΩ probe. The probe was added to increase the measurement limit of the oscilloscope, since the voltage peak was much higher in this configuration.

This experiment was basically the same as the previous one (with closed circuit), but while the latter was done only for one temperature interval (~23→ 80→ ~23 °C), this time different intervals were tested (~23→ T→ ~23 °C), but still below 80°C. Fig. 3.10 explains the measurement procedure. The composite was heated for different times with constant power and subsequently naturally cooled. The temperature profile *T(t)* for the maximal temperature (80 °C) is the same as in Fig. 3.8. At each heating/cooling, the switch was turned on for a short period (~1 s) twice and the corresponding output voltage was measured: (1) just after heating; (2) after cooling back down to ~23 °C. The discharge time was ~100 ms, thus the switching on period (~1 s) was enough to collect all the charges.

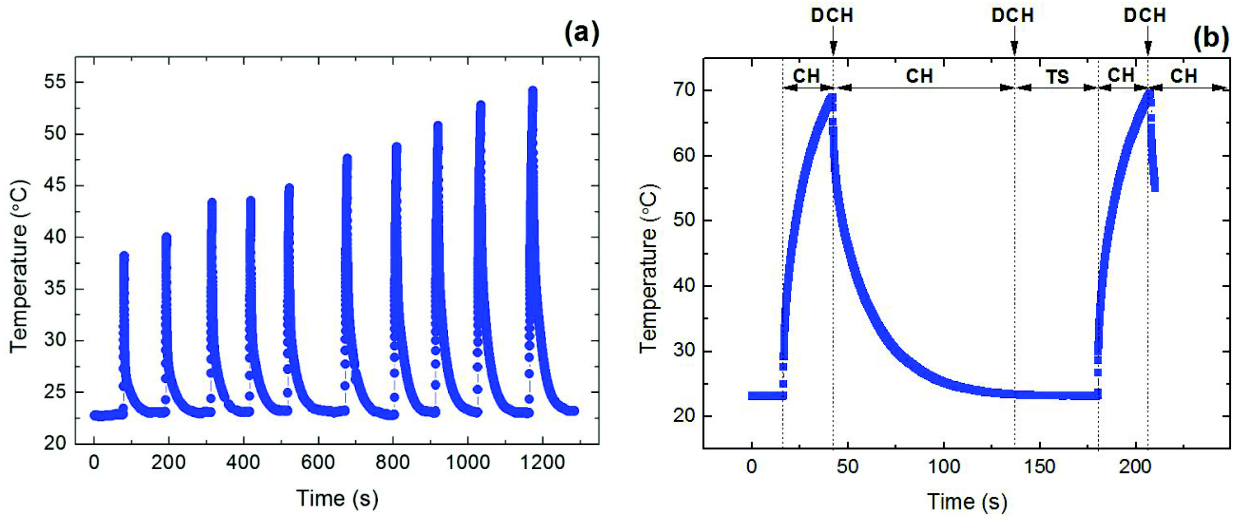

CH: charging of MFC; DCH: discharging of MFC (switch is on for ~1 s); TS: thermal stabilization

Fig. 3.10. The experiment procedure for instant discharge mode (with a switch). (a) An example of temperature profiles; (b) an explanation of generated charge evaluation. The charges were generated both at heating and cooling. Discharging was realized by closing the circuit using a switch for ~1 s twice for each thermal cycle: (1) immediately after heating up to a given temperature and (2) immediately after cooling back down to room temperature.

Fig. 3.11 shows absolute values of the peak output voltage generated by the composite at various heatings/coolings (as in previous configuration, the voltage was positive at heating and negative at cooling). We can make the following observations.

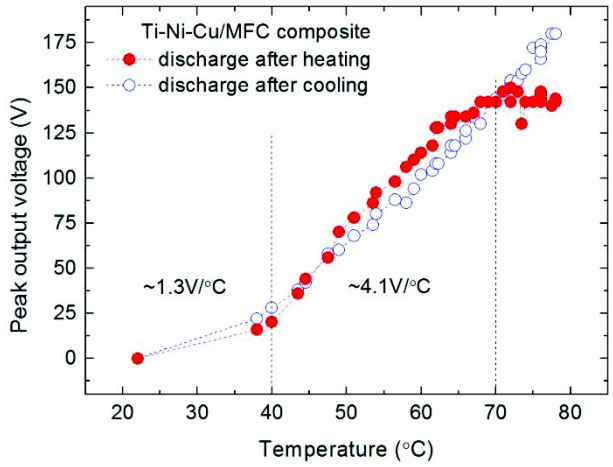

Fig. 3.11. Output voltage generated by the Ti-Ni-Cu/MFC composite, in instant discharge mode, as a function of heating time by Joule effect (filled red circles) and subsequent natural air cooling to room temperature (empty blue circles).

1. Heating and cooling curves differ above ~70 °C: "heating" generation starts to saturate and even decrease, while "cooling" generation keeps increasing with the same rate. Taking into consideration our temperature profile, we ascribe this to the fact that charge leakage is higher at high temperatures. Thus, during a heating cycle the voltage generated is highest when leakage is maximal, whereas in contrast, during cooling, the leakage is minimal when the voltage is maximal, thus reducing overall losses. This fact is compounded by the additional problem that close to the final plateau the temperature changes are slow, and so does the corresponding charge generation.

2. Below ~70 °C both curves behave similarly, and one can discriminate two likely linear regions: ~20°-40°C and ~40°-70°C. Within the low region, voltage increases with temperature as ~1.3 V/°C, while for the middle region it is ~4.1 V/°C. We will name this value the composite pyroelectric voltage coefficient ρ_V^{comp}. We have expected ρ_V^{comp} to increase in the region of Ti-Ni-Cu phase transformation, i.e. 50-70 °C. But, in the experiment the increase starts earlier, at ~40 °C (both curves), and did not finish at 70 °C (cooling case). In fact, in the current test it is difficult to interpret such thermal shifts, since there was no thermal stabilization and the synchronization of voltage and temperature measurements was manual. Moreover, the MFC and the ribbon were not at the same temperatures (see Fig. 3.12), therefore the determination of ρ_V^{comp} can only be approximated. Nevertheless, the obtained values are quite close to the theoretically estimated 1.9 V/°C.
3. Maximal voltage of 198 V was generated by the composite at cooling from 80 °C to 20°C.

4. Compared with the previous experiment (continuous discharge mode), the output energy for the same temperature change (20-80 °C) is about 3 orders higher in this one (with a switch). The deformation of a short-circuited piezoelectric does not allow an accumulation of the electrical energy: the deformation is stored mainly as mechanical energy. That means that the continuous discharge is not an appropriate way of energy harvesting.

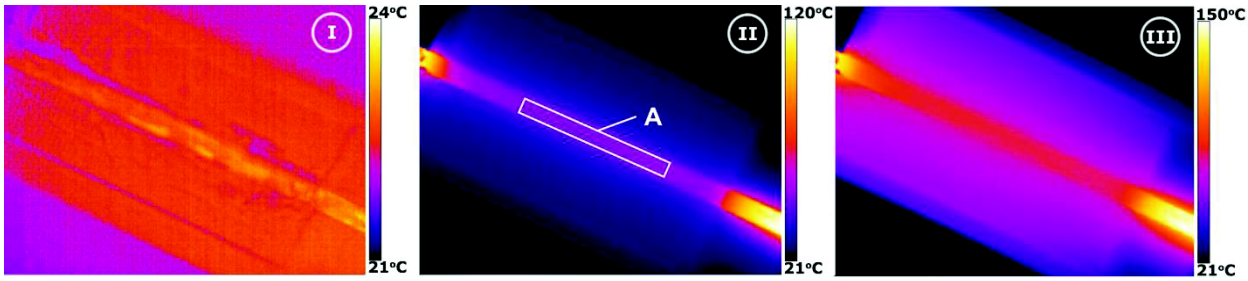

Fig. 3.12. Thermal contrast images of the Ti-Ni-Cu/MFC composite at different heating moments. Average temperature in the region "A" was taken as a value of the ribbon temperature. The ends of the ribbon are hotter with Joule heating because they are not glued to the MFC: there the ribbon and MFC had different temperatures.

Let us now calculate the corresponding harvested energy. The discharge curves were not acquired in the current experimental procedure (since it was not convenient), and we cannot determine the energy as an integral (3.2). Another method is considering the MFC as a capacitor with capacitance C and energy $E = ½ CV^2$. The use of this formula could be criticized since the permittivity of a ferroelectric depends on applied electrical field [**114**,**115**] and temperature [**112**]. However, these parameters do not vary much in our experiments, and as can be seen in the works cited above, within 0-15 kV/cm and 20-80 °C the permittivity is quite stable. Indeed, taking a +144 V discharge of the MFC through 10 MΩ load resistance as an example (Fig. 3.13), we found that both the integral (3.2) and the $½ CV^2$ give the same energy of ~35 μJ. Capacitance C = 3.5 nF was determined from the time constant. The same value was obtained using another curve for -200 V discharge, confirming its constancy. Taking this capacitance value, we obtain ~70 μJ for 198 V, which gives the maximal harvested energy density of 0.7 mJ/cm^3 for ΔT ~60 °C.

Specific harvested energy as a function of temperature is an important characteristic of a harvester allowing comparison with other systems. As seen for our harvester in Fig. 3.14, the energy increases nonlinearly with ΔT, reflecting two facts: (1) two different linear regions of generated voltage increase with temperature (Fig. 3.11) and (2) square-law energy increase versus voltage. It shows, in fact, that in order to harvest small ΔT, it is critical to increase the electric response within this small ΔT, and therefore a use of an SMA with sharp phase transition is required. However, it is

worth noting that generally the sharper the transition the less the mechanical work produced by SMA, and a compromise should be found depending on application.

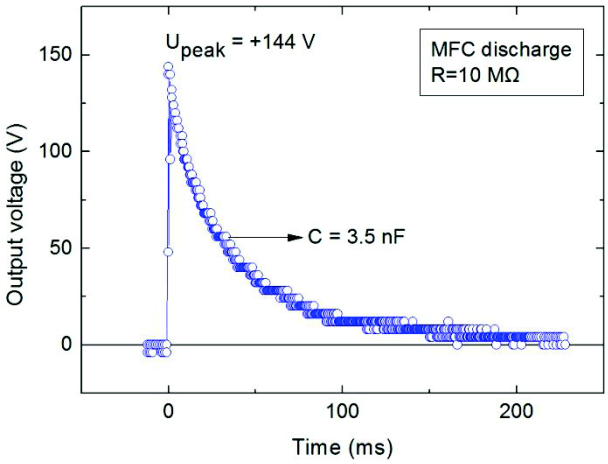

Fig. 3.13. An example of discharge curve for MFC. The voltage was generated in open circuit during heating of the composite, and then dissipated through a load resistance. The capacitance was calculated from the time constant.

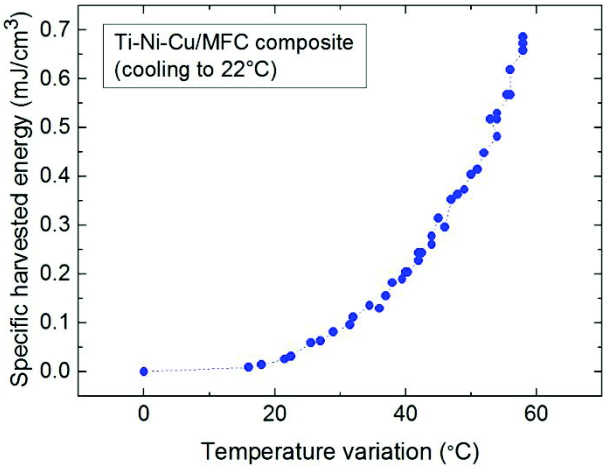

Fig. 3.14. Specific energy harvested at cooling of the Ti-Ni-Cu/MFC composite as a function of corresponding temperature change. The values were determined from the experiment with Joule heating and open-circuited piezoelectric.

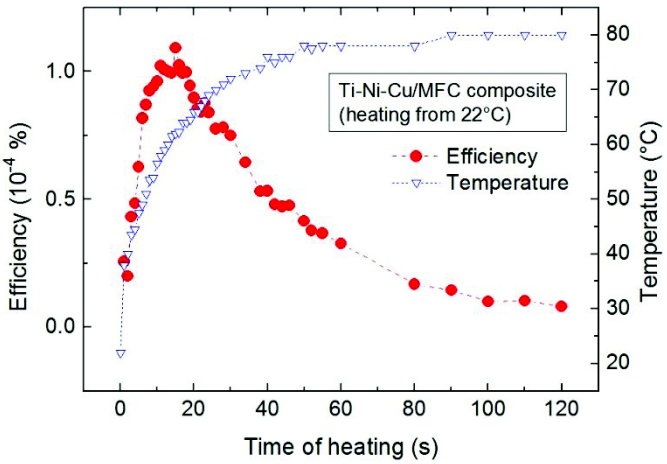

Fig. 3.15. Temperature (full circles) and conversion efficiency (empty triangles) vs. heating time.

Conversion efficiency is calculated as the output electrical energy produced by the Ti-Ni-Cu/MFC composite, divided by the input electrical energy used for Joule heating.

Knowing that the ribbon was heated with 2 W of electrical power, for each experimental point the input electrical energy can be calculated. The calculated efficiency of its conversion into the output electrical energy by the composite at heating is very low ~10^{-6}! (Fig. 3.15). We see two possible

reasons for this value. Firstly, the glue connection was probably not good enough to transfer all the mechanical work generated by the SMA to the piezoelectric layer. Secondly, we believe a part of charges to be lost due to leakage in MFC, which is considerable at elevated temperatures. This explains the existence of a maximum on the curve.

3.2.2.4 Pyroelectric effect in MFC alone, heating in thermostat, electrostatic measurement

Fig. 3.16 shows absolute values of the voltage generated by the MFC alone when dipping in hot and cold water, measured by an electrostatic non-contact voltmeter. The use of an electrostatic voltmeter allows observing time-dependent direct voltage generation with no losses [**106**]. In this experiment, the MFC was firstly moved from the air (room temperature) into the hot water for ~1 min (curve 1). After registering the curve but before taking the sample out, the generated voltage was discharged into a resistor, thereby bringing the MFC back to its uncharged state. Then it was quickly taken out from the hot water and put into the cold water (curve 2, the first slope between 0 and ~2 s corresponds to the travel in air before immersion in cold water). For both cases the voltage firstly increased due to pyroelectricity and then decreased due to intrinsic charge leakage. The leakage at heating was significantly higher (the discharge time $t_{1/2}$ from maximum to half– was 3 s at heating versus 30 s at cooling).

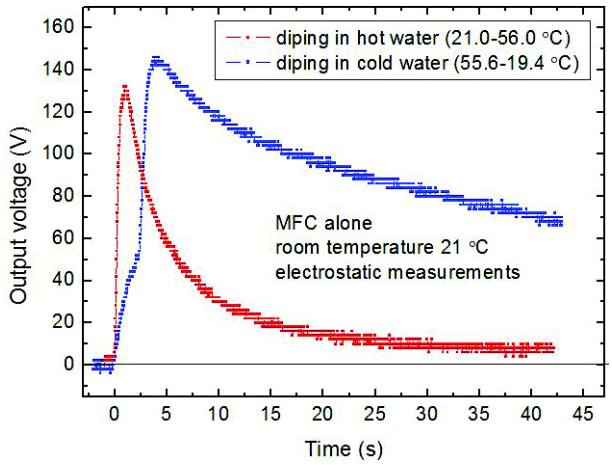

Fig. 3.16. Absolute electric response of the MFC alone when heated (1) and cooled (2) by dipping in hot and cold water (opposite voltage signs). Voltage firstly increases due to pyroelectricity, and then decreases due to intrinsic charge leakage. The leakage is faster at high temperatures, explaining the much faster decline of the hot curve.

The peak voltage generated by the MFC alone was measured at various temperatures. This dependence was linear and characterized by a pyroelectric voltage coefficient ρ_V ~4 V/°C (Fig. 3.17, red filled squares). In fact, up to now MFC has been used mainly as an actuator and its pyroelectric properties were not studied before. Our current work shows evidence of significant pyroelectric effect for MFC in the working conditions described above. The measured value is close to the theoretical one (~2 V/°C).

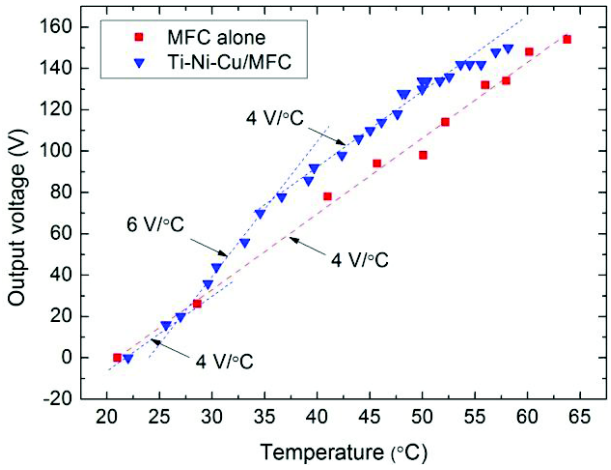

Fig. 3.17. Peak voltage generated by the MFC alone and by the Ti-Ni-Cu/MFC composite, when heated to various temperatures. In the region ~30-40 °C the composite shows an increase of "pyro"-electric voltage coefficient due to thermoelastic straining of the Ti-Ni-Cu SMA, and then resumes the "pyro" slope.

Our results about the leakage are in agreement with the literature. Indeed, a leakage phenomenon is known to occur for MFC as well as for bulk PZT piezoelectrics [**102**,**113**]. This means that even when the piezoelectric is in open circuit during the charge generation, the charges do not stay forever on the electrodes. In fact, the voltage can drop rather quickly. As observed by our group [**113**], at room temperature the voltage on the MFC electrodes measured by a non-contact method decreased by 25-30 % in first 3 seconds from 300-400 V (3-4 kV/mm), but then it stayed rather stable at ~200 V (2 kV/mm). Lipscomb et al. [**102**] observed that the leakage current increases when increasing temperature, humidity and also electric field. In particular, at 85 % humidity and 1.6 kV/mm electric field, the PZT resistance decreased by 1 order when increasing the temperature from 45 to 85 °C. Therefore, based on these data, one may expect having much higher voltage losses at high temperatures due to a higher leakage current.

3.2.2.5 Ti-Ni-Cu/MFC vs. MFC alone, heating in thermostat, electrostatic measurement

After having measured the pyroelectric effect of an MFC alone, the same MFC was glued onto the Ti-Ni-Cu ribbon and tested using thermostat heating. Therefore, it was not the same sample which was tested using Joule heating. The electric response of the new Ti-Ni-Cu/MFC composite is compared with that of the MFC alone in Fig. 3.17 (filled blue triangles). The pyroelectric voltage coefficient ρ_V is the same as for the MFC alone below ~30 °C. But in the region ~30-40 °C it increases by ~50% (up to 6 V/°C) due to the thermoelastic straining of the Ti-Ni-Cu. Thereby, above ~40 °C, after the SMA transformation is completed, the output voltage of the composite stays higher than that of the MFC alone, since the piezoelectric voltage contributes in addition to the pyroelectric one.

In fact, this increase was expected to be much higher since the SMA was pre-strained to ~1-3 %. Part of the strain is believed to be lost at the interface (glue), which is critical for the performance of such functional composites. Also, the sizes of the SMA ribbon and the MFC used in

this work were not adapted: the SMA covered only 15% of the MFC. As a consequence, some parts of the PZT fibres were probably not experiencing the deformation.

A comparison of corresponding specific energies is given in Fig. 3.18. The composite harvests ~50 μJ/cm^3 more than the MFC alone for ΔT above ~15 °C (i.e. above the finish of the phase transformation).

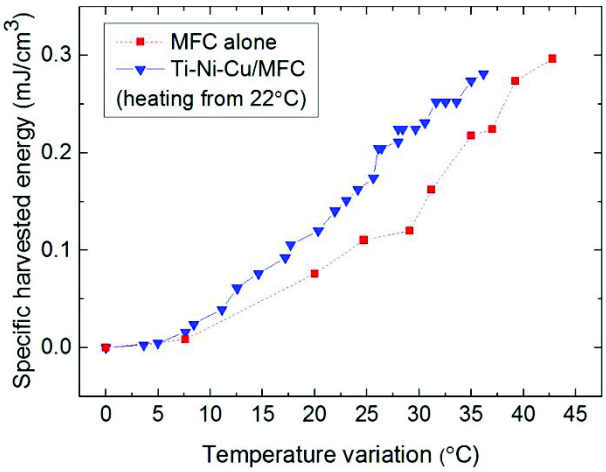

Fig. 3.18. Specific energy harvested at heating of the Ti-Ni-Cu/MFC composite (triangles) as a function of corresponding temperature change, compared to the MFC alone (squares). The values were determined in the experiment with thermostat heating and electrostatic voltmeter.

Both the ρ_V value and the phase transformation temperatures determined in this experiment are close to those obtained previously (with Joule heating), however some difference can be observed. We trust more the latest results, since quasi-instant and homogeneous heating in thermostat and non-contact electrostatic measurements allow more accurate evaluation of the composite harvester. However, more samples should be fabricated and tested in order to obtain reliable values of the ρ_V and the phase transformation temperatures of the composite.

It is worth noting that the thermoelastic strain was expected to take place in the region of ~50-70 °C, but it was different in the experiments. This supposition was based on the behaviour of a similar composite [**17**], but the actual strain of Ti-Ni-Cu/MFC composite was not measured. Of course, the piezoelectric layer is a natural strain sensor itself, but this method is indirect. Arrangements should be made to observe directly the composite deformation in order to confirm that the strain of the Ti-Ni-Cu is well transferred to the piezoelectric layer through the glue connection.

3.2.2.6 Sign of the effects

The composite must be designed in such as way as to provide pyroelectric and piezoelectric effects of the same sign. Therefore, the sign of the SMA layer strain (tension or contraction) must be chosen in respect to the sign of the piezoelectric constants exploited.

In our Ti-Ni-Cu/MFC harvester the effects are of the same sign, resulting in increased generated energy. Since this bilayered composite was assumed to bend during heating, it was difficult to

determine the neutral strain fibre position and the corresponding PZT fibres strain sign. Therefore we tested another configuration with the Ti-Ni-Cu ribbon glued on both sides of the MFC, providing explicit shortening of the MFC (not shown here). This symmetrical composite behaves similarly to the bilayer composite and gives even higher voltage. The negative strain during heating for the PZT fibres in our composites is thus proven. Therefore, in our experiments, the pyroelectric effect at heating had the same sign as the piezoelectric effect at longitudinal contraction.

To conclude, for such type of composites mechanical engineering (planar or flexural deformation) must be considered with respect to the sign of piezo- and pyro-coefficients.

NB: As received from the manufacturer, the MFCs have two electrode pads marked "+" and "–". In our experiments, the "+" electrode was always connected to the "+" of the voltmeter, while both "–" were grounded. Connected in this way, when the MFC was subjected to heating, we observed positive voltage, indicating a positive pyroelectric coefficient. However, as far as we have understood, the correct sign is negative due to the fact that for most ferroelectric crystals the spontaneous polarization decreases with increasing temperature [**116**]. *This discrepancy makes us question the manufacturer's choice of positive and negative electrode pads. (The choice of the pyroelectric effect sign must be understood deeper, and the corresponding standards should be found, since the contradictory data reported in literature are confusing: some researchers report negative coefficients* [**117**,**59**]*, others positive* [**33**,**111**]*.)*

The same discrepancy was observed for the sign of the PZT piezoelectric effect. This is determined by the piezoelectric voltage coefficient d_{33}, which is positive [**112**]. *Therefore the generated voltage should be positive for tensile strain. However, in our experiments (not shown here) we observed the opposite, i.e. negative generated voltage for tensile strain. The choice of the signs of piezoelectric constants and electrodes should be clarified and uniformized.*

3.2.2.7 Optimization

These first experiments were aimed at proving the proposed concept of enhanced thermal energy harvester, and the system was not optimized. Optimization of the composite can be realized by taking an SMA element of the same area as the MFC in order to provide homogeneous deformation of all the PZT fibres. The thickness of the SMA element and its preset strain should be optimized in order to apply an adequate strain and stress to the MFC. The optimized glue connection should allow transferring the mechanical work of the SMA with minimal losses. All these arrangements should allow us to obtain thermally-induced stain in MFC layer close to 0.1% and corresponding contribution of piezoelectric effect of more than 300 V [**113**] in a narrow temperature range (ΔT ~10-20 °C for Ti-Ni-Cu SMA) resulting in significant enhancement of the electric response.

3.2.3 Intermediary summary and conclusions

1. An original hybrid laminated composite consisting of a Ti-Ni-Cu SMA and an MFC pyro-/piezoelectric material was fabricated: its ability to generate electrical energy from temperature variations was experimentally proved.
2. The pyroelectric effect of the MFC was studied (to our knowledge for the first time), and a significant pyroelectric voltage coefficient of ~4 V/°C was reported: this value is in agreement with the calculated value for PZT fibres.
3. Hybridization of an SMA and a pyro-/piezo-material is effective: non-optimized coupling of MFC with Ti-Ni-Cu SMA increased ρ_V by ~50%. The gain was accumulated in the narrow temperature region ~30-40 °C and maintained.
4. A piezoelectric should be open-circuited during deformation for effective energy harvesting: the charges generated must accumulate to their maximum before connecting the piezoelectric.
5. Charge leakage is considerable at high temperatures: this should be studied comprehensively.
6. Sharp SMA phase transition is needed for effective harvesting of small temperature variations.
7. The proposed concept is proved, but the reliability of the values obtained must be checked by testing more samples.

3.3 Conclusions and perspectives

1. One example of original hybrid NiTi/PZT concept coupling SME and piezoelectric effects for thermal energy harvesting was validated. Following our presentations at "Transducers'11" (Beijing) and "PowerMEMS'11" (Seoul) and the publication of the corresponding papers [**7**,**82**], this concept was proposed in 2013 by Avirovik et al. for laser radiation harvesting [**83**].
2. One example of the original hybrid Ti-Ni-Cu/MFC laminated composite concept coupling shape memory and pyro-/piezoelectric materials for thermal energy harvesting was validated. Harvested energy increase compared to a pyroelectric material alone was proved experimentally.
3. The advantage of the machine is that the mechanical design can always be made in such a way as to adapt high strain of an SMA with low ultimate strain of a piezoceramic. On the other hand, the laminated composite system exploits the additional pyroelectric effect and therefore should in principle produce more energy. Moreover, it is more compact, and its fabrication is convenient technologically. However, with the latter system, the high strain of SMA cannot be transferred completely to the piezoceramic material. Using soft pyro/piezo-polymer would be advantageous.
4. The proposed harvesting systems were not optimized and their efficiencies were low: optimization directions were proposed.
5. Since the effects used do not deteriorate on microscale, the proposed harvesting systems can be miniaturized. With the modern protocols of wireless data transmission, even nanosystems would potentially generate sufficient energy for simple data transmission.

Part III: Towards thin film harvester fabrication

4 Preparation of functional Ti-Ni-Cu thin films

4.1 Preparation method

In order to fabricate micro-scale energy harvesters, the first step is to fabricate micro- and nano-layers of SMA with the martensitic phase transformation taking place in the convenient temperature range. Ti-Ni-Cu was chosen as the SMA since it is known to have good mechanical properties, relatively narrow temperature hysteresis of transformation and relatively low sensitivity of transformation temperatures to the composition [**94**].

Ti-Ni-Cu thin films were deposited using a triode sputtering system at Institut Néel. The typical film thickness was about 1 μm. This is a convenient value both for studying the obtained layers and for subsequent harvester microfabrication. In thinner films the transformation can be hindered due to fundamental and/or technological reasons. As for microfabrication, thinner membranes and cantilevers may not be rigid enough.

The substrates used were standard ⌀ 100 mm single-crystal (100) Si wafers. Non-oxidized Si wafers were tried first, but Si was found to react with the film layer upon annealing, resulting in film cracking and delamination. Thermally oxidized wafers were then used to avoid this.

4.1.1 Sputter deposition

4.1.1.1 Triode sputtering method

SMA thin films were prepared using a high-yield triode sputter deposition system designed for the deposition of metallic thick films. The schematic view of the system is shown in Fig. 4.1. The apparatus consists of an anode (1), a cathode (filament) (2), permanent magnets (3), a substrate holder (4) and a target holder (5) allowing the positioning of 4 targets (6) surrounded by target shields (7). The set-up also comprises a computer control, a power supply, water cooling circuits, vacuum pumps, Ar and N_2 gas introduction systems, etc.

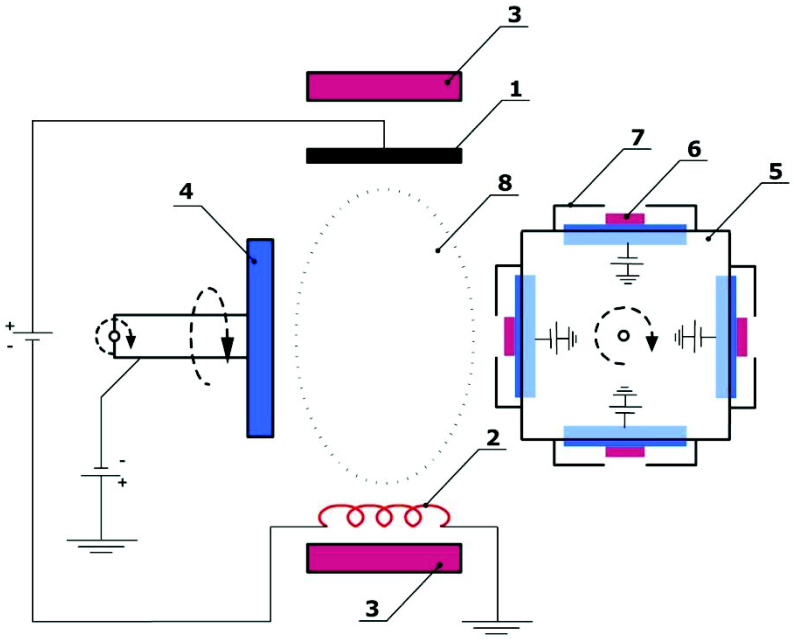

Fig. 4.1. Schematic of triode sputtering system. 1 – anode; 2 – filament (cathode) protected by filament box; 3 – permanent magnets; 4 – substrate holder; 5 – target holder; 6 – 4 targets; 7 – target shields; 8 – plasma region.

After loading the suitable target/s and substrate to the chamber, the process starts by pumping the chamber (primary rotary pump and secondary turbomolecular pump) in order to obtain a base vacuum of ~$5 \cdot 10^{-6}$ Torr in typically 2 hours. Then Ar gas is introduced and the flow rate controlled to achieve an Ar pressure of about 1 mTorr. Once the chamber is in these conditions, a current is applied to the filament (cathode), a commercial tungsten rod. With this current, the filament heats up to thermionic emission temperature (~2000 °C). Subsequent application of a positive electrical potential to the anode creates an electrical field. As a result, thermionic electrons are attracted towards the anode and collide with Ar atoms, thus creating a plasma in the region (8) between the target and the substrate. To enhance the confinement of the plasma, 2 permanent magnets are attached both to anode and cathode.

Once the plasma is created, a negative potential is applied to the target, and ionized Ar ions bombard the target surface thus causing target sputtering. The target holder can hold up to 4 targets and is cooled through a water circuit. The targets can be sputtered one at a time, and target choice is done by rotation of the holder. This feature provides an option for multilayer fabrication without need of chamber venting for target change, which is particularly useful for bottom and capping layer deposition. This option was not used for Ti-Ni-Cu film preparation (but is worth trying in the future work), but allowed deposition of Al/Cr lift-off bilayers (see Chapter 5).

The substrate holder was designed for 100 mm wafers and can be rotated around the axis perpendicular to the substrate in order to homogenize the composition and the thickness

circumferentially. In our case the rotation was not used in order to increase compositional gradients for a combinatorial approach. The substrate holder has two positions: one facing to the target, used for deposition, and another facing to the chamber's top, used during target pre-sputtering. The substrate holder temperature can be cooled by using an "active" water cooling circuit.

4.1.1.2 Substrate temperature

MEMS fabrication requires SMA film patterning. With conventional photolithography, a common option is film deposition on a substrate previously patterned with a polymer photoresist. With our sputtering system, we observed photoresist degradation when depositing a film on a patterned substrate. This was attributed to inefficient substrate cooling, and a subsequent study of substrate temperature during the deposition process was made. The aim of this study was to reveal the actual substrate surface temperature and to find out what process steps are critical. In particular, we had the question of whether the fractioning of deposition time ("making stops" during sputtering) would help to avoid the polymer overheating (maximal allowed temperature for conventional photoresists is ~150 °C).

A thermocouple was introduced through a vacuum port and its junction was attached using kapton tape onto Si wafer "free" surface. The signal was recorded through a pre-installed data acquisition system. The result is shown in the Fig. 4.2.

Firstly, the filament current is "on", and wafer temperature reaches 120 °C in 9 min and then progressively rises up to 134 °C in 23 min. After this, once the anode current is "on" and the plasma is generated, the temperature rises up to 230 °C in 4 min and continues rising up to 275 °C in 16 min. This considerable heating was due to poor thermal contact with the water-cooled substrate holder and explains photoresist degradation. This temperature becomes a critical step and imposed restrictions for using resist-coated substrates. Additionally, since the temperature rises too quickly when plasma is "on", making stops while sputtering is not a solution.

This temperature study helped identify a limitation of the apparatus and a solution has been found since. The substrate holder was modified to allow a several-millimeter-thick copper plate to be screwed on it. A substrate can now be glued on this plate with silver paste to enhance thermal transfer and ensure efficient cooling. Unfortunately, there was not enough of time to try it for Ti-Ni-Cu film patterning.

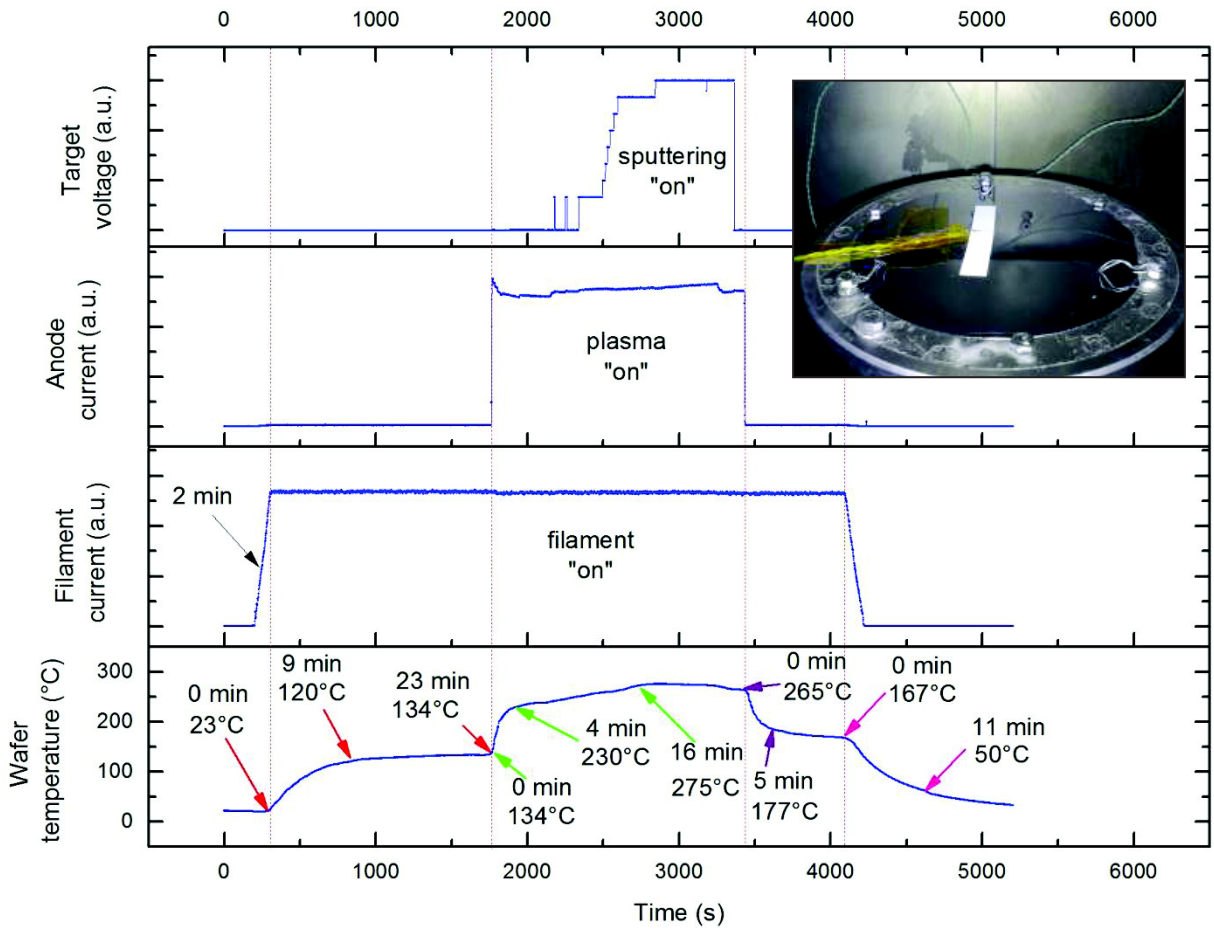

Fig. 4.2. Study of substrate (Si wafer) temperature during sputtering process. Inset: Setup for in-situ temperature measures: thermocouple attached to the Si wafer surface placed in the chamber of the sputtering machine.

4.1.1.3 Target fabrication

The alloy target was fabricated in the laboratory by induction melting of the mixture of the initial elements taken in such a proportion as to obtain the composition $Ti_{49.5}Ni_{45.3}Cu_{5.2}$. This Ti-rich composition was chosen from [**118**] as a composition of the film having a martensitic transition at room temperature (Fig. 4.3). The masses of Ti, Ni and Cu raw materials (purity 99.9%) taken for the mixture were 22.16, 24.85 and 3.11 g, respectively. This mixture was charged into a cold crucible induction furnace, where it was melted several times, turning over the ingot after each solidification to ensure its homogeneity.

Together with the ingot (Fig. 4.4), some alloy flakes were accidentally obtained (as observed on the image). Deformed at room temperature, these flakes showed shape recovery when put in hot water. That means that the obtained bulk alloy exhibited a martensitic transition in the range between room temperature and 100 °C.

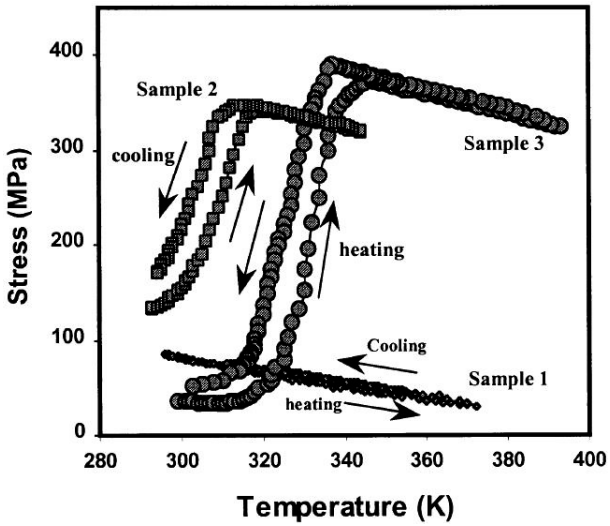

Fig. 4.3. Residual stress evolution with the change of temperature for three types of Ti-Ni-Cu films RF-sputtered onto Si (100) wafers [**118**]. Sample 3 ($Ti_{49.5}Ni_{45.3}Cu_{5.2}$) showed the martensitic transformation just above room temperature after vacuum-annealing (1 h at 923 K).

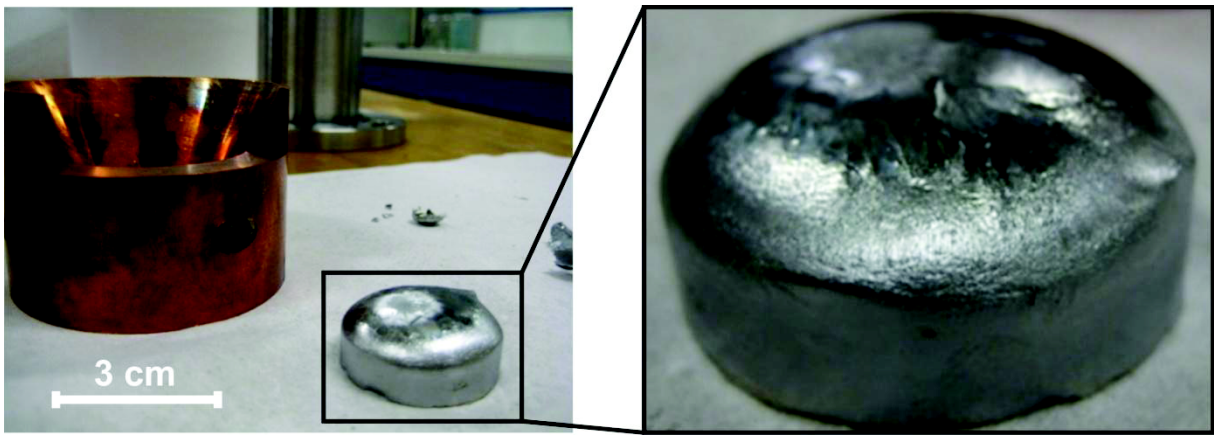

Fig. 4.4. Ti-Ni-Cu ingot obtained by induction melting for target fabrication.

The ingot was cut by electroerosion to a cylinder shape (⌀ 29.3 mm, height ~5 mm). The obtained target was polished using diamond paper and then sand blasted. Its composition was checked using EDX at different points of the surface. The target was found to be rather homogeneous with an average composition $Ti_{46.1}Ni_{44.8}Cu_{9.1}$ (expected $Ti_{49.5}Ni_{45.3}Cu_{5.2}$.). This composition is still Ti-rich (Ti/Ni = 1.09), but the Cu content is higher than expected. That could be due to the loss of the initial material in the furnace.

4.1.1.4 Target mounting

After preparation and analysis, the target was glued with a conductive silver epoxy onto the Cu backing plate (Fig. 4.5), which was subsequently mounted onto the target holder. A shield of non-magnetic stainless steel was used to protect the Cu backing plate from being sputtered (Fig. 4.1, pointer 7). Although the shield opening was slightly wider than the target (⌀ 32.5 mm), small Cu

contamination is usually negligible when sputtering a material and anyway the uncovered Cu from the backing plate around the target is covered in time thanks to re-sputtering of the target material. However, as it will be discussed in the following paragraph, in our case, the fact that some Cu was sputtered affects the Ti-Ni-Cu alloy composition (Fig. 4.5), and it is suspected to be one of the reasons of Cu content irreproducibility from one deposition to another. As seen in Fig. 4.5, the Cu backing plate still visible was indeed progressively, but not fully, covered with a Ti-Ni-Cu layer during sputtering. In future work, a target shield with the tailored dimensions should be prepared to minimize this problem (target dimensions are limited by induction furnace moulds).

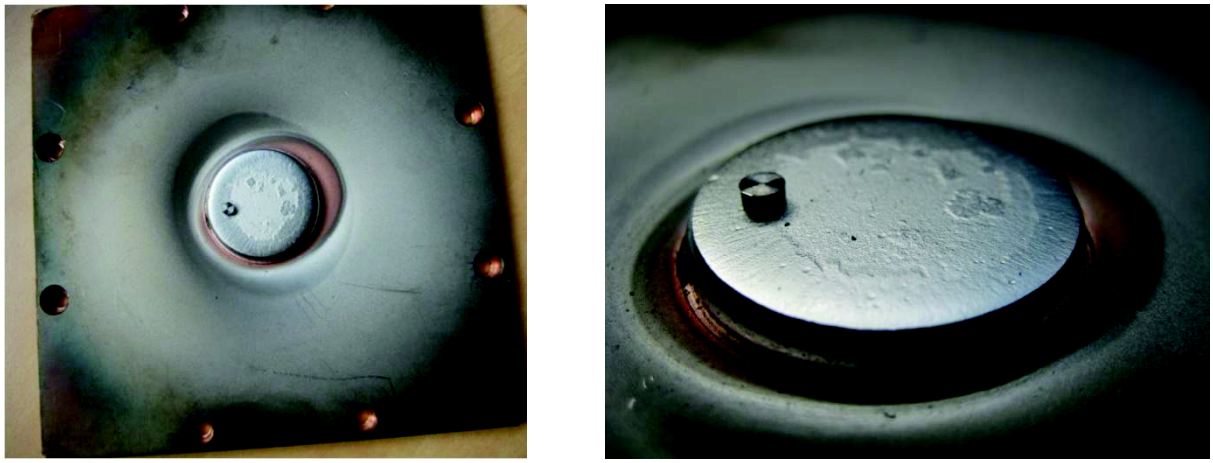

Fig. 4.5. View of the Ti-Ni-Cu target (⌀ 29.3 mm) glued onto the Cu backing plate. The target was modified by inserting a piece of pure Ti into it. Surface state of the target was due to inhomogeneous sputtering.

4.1.1.5 Contamination

In order to trace possible reasons for the irreproducibility of Cu content in film composition other than the target backing plate, the following experiment was made. A substrate and the target were loaded in the chamber and the procedure used was exactly the same as for film deposition, described at the beginning of this section, but no potential was applied to the targets. Thus nothing should have been deposited on the substrate. In reality, a thin reddish layer was clearly observed on the substrate after this procedure. EDX analysis was performed, and it showed that the layer consisted mainly of Cu (Fig. 4.6), with some Fe also present.

The observed gradient of Cu signal reveals that the deposition of this layer is more significant for the bottom (“South”) part of substrate. This parasitic copper deposition could be explained by considering that sputtering of the filament box, made of Cu, occurs. When inspected, the gap between the tungsten filament and its box was found to be rather small, and it is possible that due to thermal deformation they come in touch during the deposition randomly. And since the filament potential is – 80 V, it led to the box sputtering.

It should be noted that usually the machine is used for rapid deposition of relatively thick layers using larger targets. In such cases, target material covers rather quickly all the interior of the sputtering system, and this problem is not observable. In future work, a larger Ti-Ni-Cu target should be used to minimize as much as possible the problem of contamination.

4.1.1.6 Target modification

As it will be shown further, there were significant losses of Ti during deposition, so the target needed to be modified. It was realized by making a small hole in the target and then introducing a pure Ti nail-shaped piece therein (Fig. 4.5). Ti "nails" with different head surfaces were fabricated to adjust

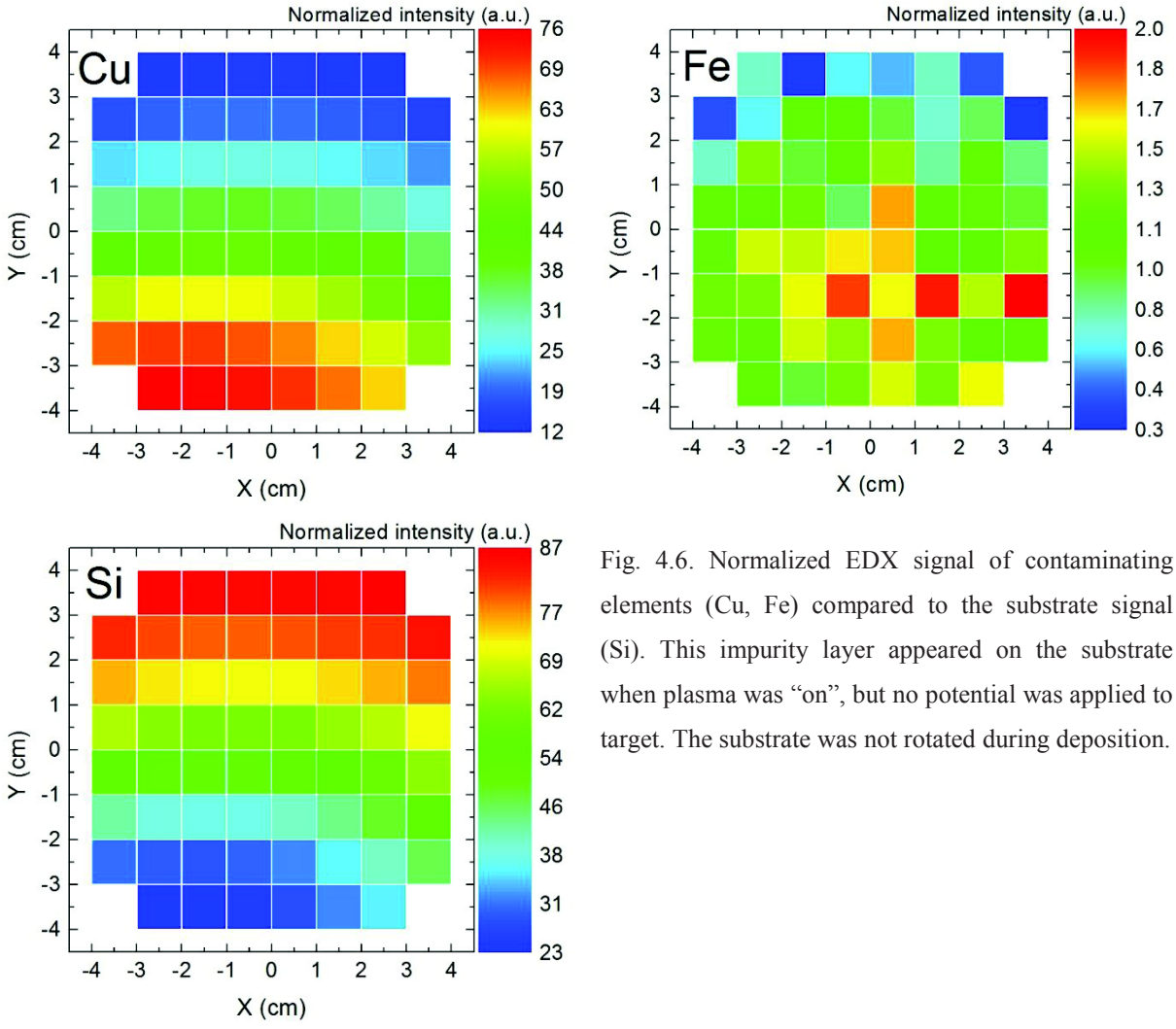

Fig. 4.6. Normalized EDX signal of contaminating elements (Cu, Fe) compared to the substrate signal (Si). This impurity layer appeared on the substrate when plasma was "on", but no potential was applied to target. The substrate was not rotated during deposition.

the composition. Several Ti pieces were eventually used at the same time. The size of the first piece was chosen almost intuitively, since it is complicated to calculate a sputtering yield of pure Ti compared to the remaining surface of the target and also the relative losses of Ti. A piece of ⌀ 3 mm was used for the first modification of the target, ⌀ 6 mm for the second one, both of them for the third

one. Finally, 2 pieces of ⌀ 6 mm and one piece of ⌀ 5 mm were inserted at the same time (Table 4.1). For each case, the target name is a letter "T" followed by a number indicating the surface part occupied by pure Ti. The size of the pieces (both thickness and diameter) was observed to noticeably decrease with depositions, due to their sputtering. In the final case (3 pieces), it was noticed that Ti was re-depositing in the area between the pieces.

Table 4.1. List of the target ($Ti_{46.1}Ni_{44.8}Cu_{9.1}$) modifications.

Target notation	Modification	Ti surface/target surface, %
T0	Unmodified	0
T1.1	Ti piece ⌀ 3 mm	1.1
T4.6	Ti piece ⌀ 6 mm	4.6
T5.7	2 pieces (⌀: 3;6 mm)	5.7
T12.4	3 pieces (⌀: 5;6;6 mm)	12.4

4.1.2 Annealing

As-deposited Ti-Ni-Cu films were amorphous (confirmed by electron diffraction). The martensitic transformation and shape memory effect require a minimum grain size, which is typically about several tens of nanometres [**93**]. To obtain this crystal structure, films were annealed.

Three different furnaces were used in this work. Two of them were horizontal resistive furnaces providing conventional thermal annealing (CTA). They had almost the same dimensions, heating rate and thermal inertia, but the level of vacuum was different. The other furnace used infrared lamps for rapid thermal annealing (RTA). The information on vacuum level, furnace notation and maximal sample size is shown in Table 4.2.

Table 4.2. Furnace list.

Furnace	Notation	Vacuum, Torr	Max. sample size
1	CTA1	$\sim 10^{-7}$	½ 100 mm wafer
2	RTA	$\sim 10^{-5}$	100 mm wafer
3	CTA2	$\sim 10^{-8}$	½ 100 mm wafer

CTA and RTA are very different in terms of heating and cooling rates. The typical temperature profiles used for film annealing are shown in Fig. 4.7. In case of CTA, the heating rate used was 500 °C/h, being close to its upper limit. The cooling was realized by turning off the power. Due to significant thermal inertia, the cooling rate is rather slow (~30 °C/h), needing ~24 h to reach room temperature. In contrast, in the case of RTA, the heating rate was 6900 °C/h, being close to its lower limit. Cooling and heating rates were the same.

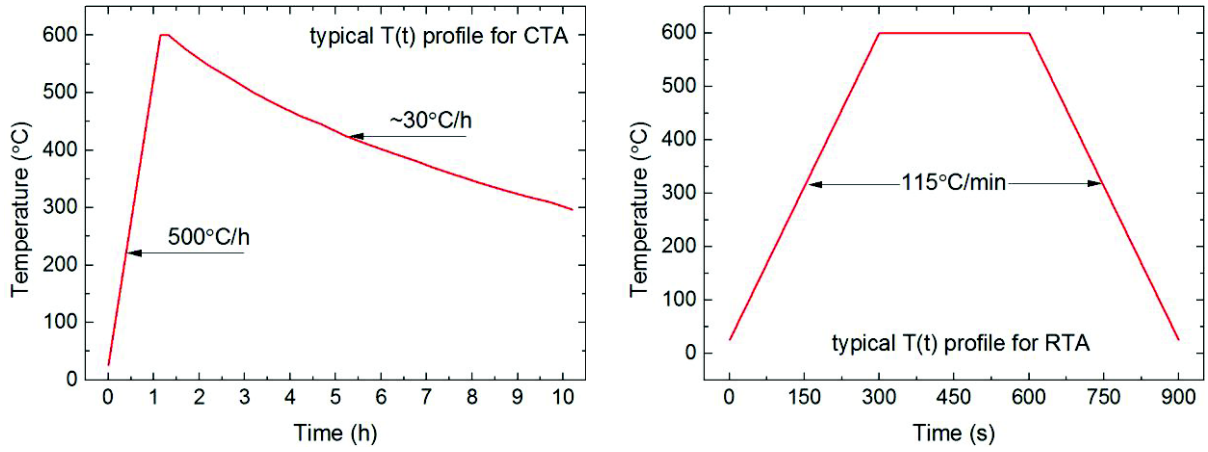

Fig. 4.7. Typical temperature profiles for CTA (left) and RTA (right) furnaces. In both cases, the sample spent 10 min at 600 °C.

It is worth noting that CTA and RTA are very different in terms of rate of supplying thermal energy to a sample. This difference will be discussed in detail when analyzing annealing results.

The temperature measurement was different for the two types of annealing as well. In the case of CTA, the thermocouple was installed in the sample holder. Since heating and cooling rates were not high, the temperatures of the sample and the holder can be assumed very close. In contrast, in the case of RTA, the sample holder was Si wafer, supported by three quartz feet. The thermocouple was touching the wafer from the back side, while the infrared lamps were from the front side. Moreover, the samples were just put on the wafer without adding any thermal contact layer. Considering the very high heating rate, it could possibly result in underestimation of the real sample temperature.

4.2 Characterization techniques

Facing the difficulty of complex material, different and complementary techniques have been used at Institut Néel, CEA-LETI and CEA-PFNC (PlateForme de NanoCaractérisation). Specific characterization works have been contracted out and discussed with specialists while scanning electron microscope observations, composition mapping, and four-probe resistance measurements for phase transition analysis have been entirely performed by me.

4.2.1 Energy dispersive X-ray analysis (EDX)

As we used a gradient deposition method, mapping film composition at wafer scale is a key issue. This was done using EDX analysis and scanning the wafer manually. The system used was a Bruker AXS Microanalysis combined with Zeiss Ultra Plus Scanning Electron Microscope (SEM). 60 areas of 1×1 cm^2 were marked on film surface (⌀ 100 mm wafer). It was done by drawing a network of

lines by a felt pen (Fig. 4.8). The whole wafer was put in the SEM chamber, and the lines and numbers simplified navigation.

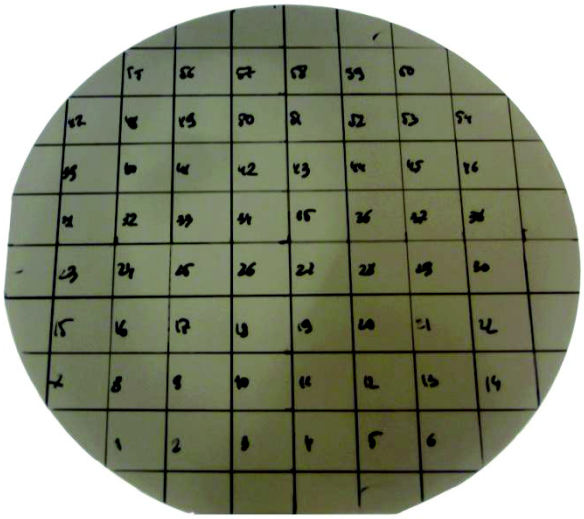

Fig. 4.8. Photo of Ti-Ni-Cu film deposited on oxidized Si (100) wafer with areas marked for EDX analysis.

EDX analysis was performed approximately in the centre of each area, and the surface analyzed was approximately 3×3 mm^2 (magnification ×50 was always used). Electron beam acceleration voltage and working distance were always set at 20 kV and 8 mm, respectively. For spectrum acquisition, 60 μm aperture was used to increase the signal up to 15-40 kilocounts per second (dead time ~6%). 500 kilocounts were collected for each acquisition, taking ~15-30 s per spectrum.

For analysis, the standard Bruker "Esprit" software was used with "Physical" mode for background and standard-less "PhiRhoZ" model for quantification. The "PhiRhoZ" (or "Phi-Rho-Z") model is based on a φ(ρZ) depth-distribution function, that is defined as the X-ray intensity generated by a thin layer at depth Z relative to an isolated layer of the same thickness [**119**]. Although Si and O peaks were clearly observed, they were ignored during analysis (peaks of C and, if observed, Fe were ignored as well). In order to check analysis repeatability, it was performed twice for the same sample with a lag of several weeks. The concentration values were found to be the same to within 0.1 at.%.

The composition was found to be rather homogeneous within 1 cm^2 area. So, in this work, a value measured in the sample centre (3 mm^2 area) was considered as an average value for this sample.

It is worth noting that quantification was precise to within ~5% for our samples for 3 following reasons.

1. It was based on the assumptions of sample homogeneity and infinite film thickness. Since the film thickness was less than the electron beam penetration depth (substrate was clearly observed), the studied case did not fit the assumptions used for the quantification.
2. Ni and Cu peaks were very close and needed to be deconvolved, increasing an error for Ni/Cu ratio.

3. Ti and O peaks needed to be deconvolved as well, increasing an error for Ti content.

Nevertheless, this method gave good indications on metal contents and was suitable to observe film composition variations throughout the wafer. However, for correct comparison with other works and for better understanding of our results, the composition of some samples was measured using Rutherford Backscattering Spectrometry (RBS).

4.2.2 Rutherford Backscattering (RBS)

The principle of RBS is based on the elastic interaction of the nuclei of incident high energy ions with solid-state target atoms. This technique is considered as one of the most precise for quantitative elemental analysis of "massive" layers.

For this purpose 1 cm^2 samples were taken from the wafer and put for analysis in a vacuum chamber ($2 \cdot 10^{-6}$ Torr) with the surface facing to incident particle beam. The latter was a $^4He^+$ ion flux with energy of 2.9 MeV. It resulted in a target current of 3 nA for an analyzed surface of several mm^2. Incident particles backscattered upon the target atom nuclei were detected at 160° from the initial direction and were treated afterwards by an acquisition circuit to form spectra.

The X-axis of obtained spectrum represents the energies of the detected particles after backscattering converted in channel numbers of acquisition circuit. The Y-axis represents the quantity of the detected particles, which represents a concentration of the detected element over a given depth. Thereby, the response of the principal components of a sample appears on the spectrum as a plateau for a "massive" material or a peak for a thin layer.

Unfortunately, RBS doesn't allow Ni and Cu discrimination since they are neighbours in the periodic table. To solve this task, another technique was used – Particle Induced X-Ray Emission (PIXE).

4.2.3 Particle Induced X-Ray Emission (PIXE)

This technique was used to determine the Ni/Cu ratio in our Ti-Ni-Cu films. The measured value was used to correct the RBS results.

The principle of PIXE analysis is a detection of X-ray radiation emitted at the interaction of an incident particle beam with target atoms of the studied material. A flux of H^+ ions is used, creating vacancies in deep electronic levels of the target atom. When the latter comes back to its fundamental state, an exterior level electron completes this vacancy with simultaneous emission of X-rays with the energy equal to the energy difference between the two levels.

A beam of protons with energy of 2.83 MeV was used. It had a size of ⌀ 3 mm and formed an incident current of 4 nA. A 315 μm thick carbon absorbent was inserted between the sample and the

detector in order to block a majority of backscattered ions which may damage the detector crystal and to absorb the low energy signals which saturate it.

Counting the number of X-ray photons and their energy allows identification and quantification of present elements.

4.2.4 Auger electron spectroscopy (AES)

This technique provides elemental analysis of a sample surface layer (several nm). It is sensitive to both light and heavy elements and can have a spatial resolution of up to 10-20 nm. To obtain composition depth profiles, it is usually accompanied with surface sputtering. However, this option is limited to sample thicknesses of maximum ~200 nm. For thicker samples, a cross section of the sample must be prepared. Preparation should be done carefully, since the AES signal is sensitive to topography.

Four different samples of Ti-Ni-Cu film were analyzed. They were cleaved just before putting inside the measurement system. So the cross-sections were exposed to air for less than 15 min.

The measurement system was a PHI 700Xi Scanning Auger Nanoprobe. The accelerating electron beam voltage, surface current, working distance, vacuum level and beam width were 20 kV, 1 nA, ~15 mm, $2 \cdot 10^{-9}$ Torr and 10 nm, respectively. The spatial resolution of secondary electron imaging for our sample was not high enough to clearly see the topography. This means that possible "artefact -like" concentration variations could not be directly associated with the surface quality. Therefore, sometimes several profiles were made to reveal if such features were representative or not. The samples were tilted by ~3° to provide perpendicularity to the beam. Prior to acquisition, the surface was subjected to an abrasion with Ar^+ ions for 6 min at 500 eV to remove the adsorbed carbon. A line-scan of 1 μm consisted of 128 points analyzed during 50 acquisition cycles. To avoid sample drift during acquisition, a feedback correction system was used.

4.2.5 Scanning electron microscopy (SEM)

A Zeiss Ultra Plus SEM was used to observe thin film cross-sections and to estimate their thickness. The cross-sections were obtained by cleaving the sample at room temperature. The images were typically taken with a magnification ×65000 using the InLens detector. The accelerating voltage and working distance were typically 3 kV and 3 mm. A special sample holder was used to put the samples vertically in order to have the film's cross-section perpendicular to the electron beam. In case of need, sample orientation was adjusted by tilting the sample holder inside the SEM chamber.

4.2.6 Transmission electron microscopy (TEM)

TEM was used at the end to observe Ti-Ni-Cu film cross-section microstructures. For TEM sample preparation and study, the samples were sent to Common-Use Scientific Centre "Material Science and Metallurgy" at NUST "MISiS" (Moscow, Russia).

Lamella-like cross-sections were prepared by lift-out technique using a FEI 201 Focused Ion Beam (FIB) device. This method requires deposition of ~1 μm Pt layer in order to protect the samples from ion beam induced damage. The microscope was a Jeol JEM-2100 with accelerating voltage of 200 kV.

4.2.7 Structural analysis – X-ray diffraction method (XRD)

In order to determine phases and their crystal structures, a Panalytical X'Pert MRD diffractometer was used with Cu radiation ($\lambda_{K\alpha1}$ = 1.5405980 Å, $\lambda_{K\alpha2}$ = 1.5444260 Å, $\lambda_{K\beta}$ = 1.3922500 Å) at 1.8 kW power (45 kV and 40 mA). Three following modes were used.

1. The θ/2θ mode for high-throughput routine measurements of reflections parallel to the film's surface. An offset of 2° was applied to remove single-crystalline Si (100) substrate peaks and to reduce the associated background level. Usually a series of 1 cm^2 samples was glued with silver paste onto a Si wafer piece. Sample holder allowed automatic scanning through the wafer to successively acquire spectra for all samples of a series.
2. The θ/2θ mode at different tilt angles ψ with $\sin^2\psi$ varying from 0 to 0.8 with a 0.1 step in order to indentify the occurrence of fibre texture. This technique also allows to determine stress value for a present phase if its Young modulus is known (so-called "$\sin^2\psi$ method"). An offset of 2° was applied as for previous mode.
3. Grazing incidence XRD to increase the signal of film's possible top layer.

4.2.8 Four-probe resistance measurement under controlled heating and cooling

Electrical transport measurements are commonly used technique to determine transition temperatures for SMAs. It is highly sensitive to any structural changes and rather simple to perform and can be performed in automatic mode.

4.2.8.1 Elevated temperatures

Elevated temperature DC electrical resistance of the samples was measured by a standard four-probe technique in the temperature range from room temperature up to ~120 °C using metallic probes. The latter were elastic metal wires installed in such a way as to provide slight mechanical pressure to the sample at the contact points to ensure good electrical connection. The experimental set-up is schematically shown in Fig. 4.9. It consisted of a vacuum chamber with a silica window (1) and two ellipsoidal lamps (3). Inside this chamber, a measurement unit (2) with a sample holder (4) was introduced. A sample of 1 cm^2 fitted well the sample holder. With inter-probe distance of 1 mm, the measurement is relatively close to the sample's edges.

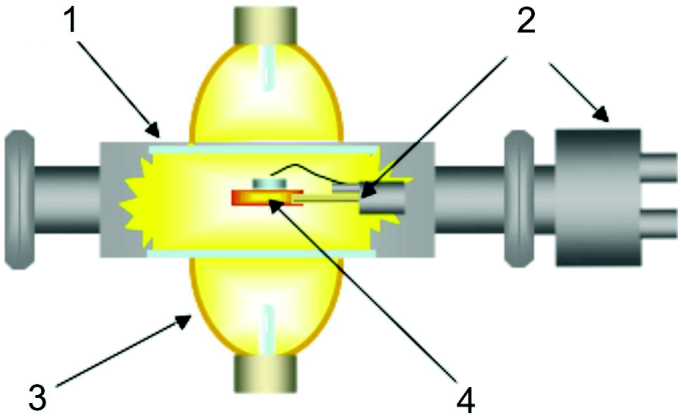

Fig. 4.9. Scheme of the set-up for electrical resistance measurements at elevated temperatures (from room temperature up to 1000 °C). 1 – silica window; 2 – measurement unit; 3 – ellipsoidal heating lamp; 4 – sample holder.

The following procedure was repeated several times after inserting the measurement unit: helium gas was purged into the chamber and then it was pumped out using a primary pump. So at the end the vacuum was not high, but the chamber was cleaned from other gases, protecting the sample from oxidation. Two ellipsoidal lamps (3) were simultaneously used for heating above and below the sample to provide homogeneous heating. A thermocouple was installed inside the sample holder. To ensure cooling down to room temperature, the chamber was cooled with a fan.

The measurements were performed in automated mode using direct current, typically 20 mA. This value was found to be optimal to have the signal high enough and not to provoke any significant heating by the measurement unit. The typical voltage applied to the sample at this current was ~7 μV.

Typical heating and cooling rates were ~400-600 °C/h for draft measurements and ~200-300 °C/h for final measurements.

4.2.8.2 Low temperatures

For low temperature measurements, another set-up was used with a different sample holder. After having been measured at elevated temperatures, the sample was cut down to 3×5 mm^2 size. It was then glued with a water-based glue onto a mica support of the sample holder. The measurement unit electrical circuit was connected to the sample surface by ⌀ 10 μm Pt wires using silver paste, which was dried under a hot halogen lamp for ~15 min. The distance between two neighbour contact points was ~1 mm. The resulting contact resistance was typically ~20-200 Ω, depending on the sample, probably due to surface oxidation. The measurement unit with the sample was then connected to the automatic control and acquisition system and immersed into a liquid He cryostat. By controlling both He flow and resistive heater power, the temperature could be varied in the range ~4-320 K. The typical rate was 1 K/min for the temperature range were the phase transition was observed and 5 K/min when beyond it. A current of 1 mA was usually used for measurements, providing high measurement signal. No current-induced heating of sample was observed down to ~20 K.

4.3 Results and discussion

4.3.1 Introductory remarks

4.3.1.1 Sample nomenclature

The sample names used thorough this section represent a serial number of the deposition. It is done on purpose, in order to give an indication of how many depositions were made in between two deposits reported here. It must be said that the triode sputtering machine is a shared facility, systematically used to prepare films of other materials too. Therefore, this number may help to have an idea about the probability of having pollution or other changes in the sputtering system from one deposition to another depending on what's been done before.

When different areas of a sample were analysed, an area number is put after a deposition number (see area numeration on Fig. 4.8). For example, a sample N1042P1 means the deposition 1042, area 1 ("P" for "point").

4.3.1.2 Choice of substrate

The first test film was deposited on a Si(100) wafer. After annealing for 10 min at 600 °C in a conventional vacuum furnace, it was found to peel off. Observation by optical microscope revealed that peeled-off pieces of the film showed changes at the interface, indicating probable diffusion

problems with silicon. For this reason, it was decided to use thermally oxidized substrates (Si/SiO_2) as a diffusion barrier. Depending on stock, substrates with 2 µm, 1 µm and 100 nm wet thermal oxide were used. With these substrates, most of the deposited films adhered well after annealing, but some of them nevertheless peeled off, depending on annealing parameters.

4.3.2 Film thickness

The thickness of Ti-Ni-Cu films varied depending on the position within the wafer, which was to be expected based on the size difference between the target (⌀ ~30 mm) and the substrate (⌀ 100 mm). Relying on numerous SEM observations of cross-sections, thickness was maximal in the wafer central part (~1000 nm) and minimal at the borders (~600 nm). When no rotation, this distribution was not concentric, since the magnetic field maxima was not concentric.

For a quick test, one of the films was cleaved in two halves, and the thickness was measured by SEM (Fig. 4.10). Indeed, the thickness maximum was shifted off the centre by ~1 cm to the wafer's "South".

More precise information on thickness variation could be obtained, for example, by preparing lithographically patterned steps and measuring their heights by atomic force microscopy or profilometer. Apriori, such a thickness decrease at the edges was not problematic for film characterization, since it was still above the threshold of SME deterioration (~100 nm). Moreover, it could potentially allow us testing an additional geometrical parameter when fabricating membranes in a single run. On the other hand, it could complicate the analysis of relationships "structure-composition-properties".

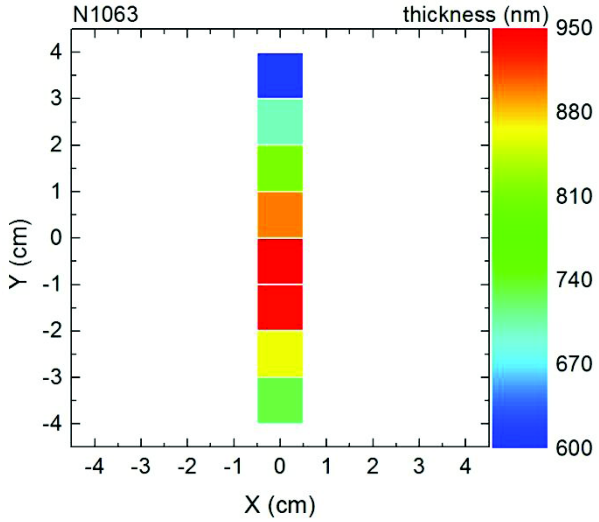

Fig. 4.10. Film thickness versus position on wafer. It was measured by SEM when observing cross-sections on the "South-North" line of the wafer, passing through its centre.

4.3.3 Compositional analysis – EDX and RBS

4.3.3.1 Desired composition

As it has been mentioned above, the $Ti_{49.5}Ni_{45.3}Cu_{5.2}$ composition was chosen as a starting point. In fact, as we have learned from the literature on the Ti-Ni-Cu system, one of the main parameters influencing the transformation temperature and transformation path is the Ti/Ni ratio (at.%/at.%). At Cu concentrations above ~10 at.%, when Ti/Ni changes from 0.7 to 3.0, the transformation temperature mainly increases [**94**]. At lower Cu concentrations, the temperature is maximal near 50 at.% Ti. On the other hand, not only the transformation temperature is important, but also the transformation path. When Ti/Ni is below ~1, a B2→R transformation takes place, characterized by a low lattice distortion. Tomozawa et al. reported that a diaphragm-type microactuator exploiting this transition shows high actuating speed [**120**]. However, actuation strain was found to be 20 % of that obtained with the B2→B19/B19' transformation. In principle, we were interested in trying both options, but we preferred the high-strain phase transformation (B2→B19/B19') to begin with. The latter takes place when Ti/Ni is above ~1.08, and that was our aim for the ratio value.

Thereby, our method implicated an adjustment of the Ti/Ni ratio as a first step by adjusting the Ti concentration. In future work, if needed, an adjustment of the Cu concentration can be similarly realized.

4.3.3.2 Combinatorial approach

As mentioned, we did not rotate the substrate holder in order to have continuous compositional spreads on wafer and to exploit the so-called "combinatorial approach". This approach, in principle, aims at obtaining a material "library" including all possible compositions on a single substrate and subsequent use of "high-throughput" characterization techniques [**121**]. Although our sputtering system was not designed for this purpose, we decided to use the intrinsic inhomogeneity of deposition as an advantage. Therefore, in our case the composition range was imposed by the system and was not known precisely prior to the study. A first combinatorial analysis of the Ti-Ni-Cu ternary system has been already reported [**94**] and served as a useful guideline.

4.3.3.3 EDX: first film composition and compositional variation map

Typical average compositions of films obtained with the unmodified target was $Ti_{43.1}Ni_{50.8}Cu_{7.9}$ (film N1042). Compared to the target composition ($Ti_{46.1}Ni_{44.8}Cu_{9.1}$), it was Ti-poor, and Cu content also decreased. The loss of Ti was ascribed to oxidation, since Ti is known for its high affinity for

oxygen. Apparently, the base vacuum of the sputtering system (~$5 \cdot 10^{-6}$ Torr) was not high enough to avoid Ti oxidation.

A typical element concentration map throughout the wafer is shown in Fig. 4.11 (film N1042). The Ti, Ni and Cu contents were maximal on the "East", "North-West" and "South-West" side of the wafer, respectively. The variation of each element concentration was of the order of several at.%. As observed, the obtained compositions did not contain the intended Ti/Ni ratio and the films were Ti-poor.

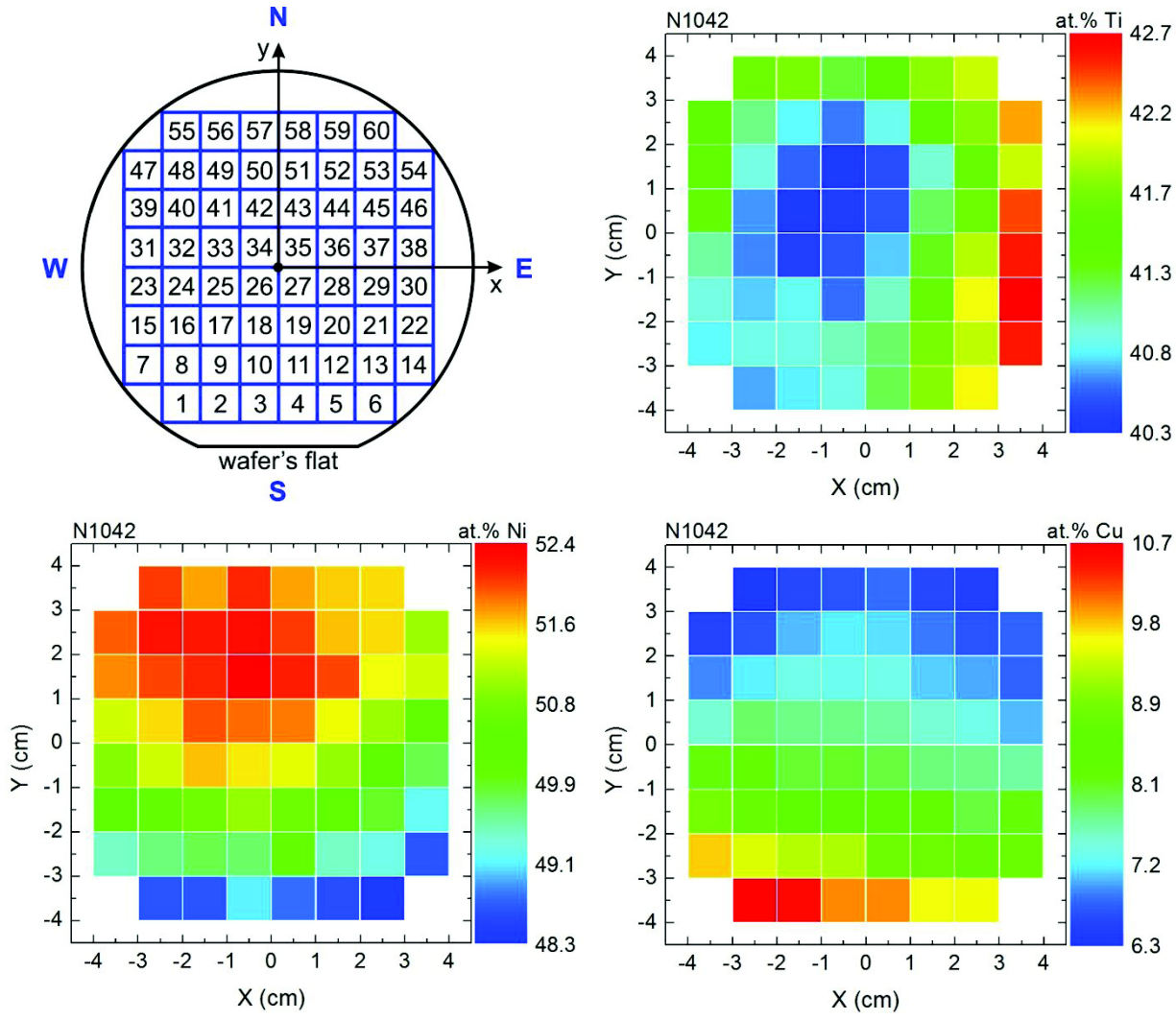

Fig. 4.11. Measurement map and results of EDX analysis of Ti-Ni-Cu continuous thin film composition spread.

4.3.3.4 EDX: adjustment of Ti content

As described previously, the target was modified by inserting Ti pieces of different size to increase the Ti content. In this way, films with 4 different composition spreads were fabricated. Their average compositions are shown in Table 4.3 (Target names noted on Table 4.1). The whole range of compositions produced is shown on a ternary diagram in Fig. 4.12. The desired composition is

marked by a star. On this graph, there is also a dotted line representing alloys with the Ti/Ni = 1.09 desired ratio.

Table 4.3. Average composition values for Ti-Ni-Cu films obtained from different targets.

Deposition	Target	at.% Ti	at.% Ni	at.% Cu
N1042	T0.0	41.3	50.8	7.9
N1062	T1.1 (orient. 1)	42.1	51.1	6.8
N1063	T1.1 (orient. 2)	42.1	50.9	7.0
N1071	T4.6	44.2	47.9	7.9
N1078	T5.7	44.6	47.0	8.4
N1312	T12.4	46.3	42.2	11.5

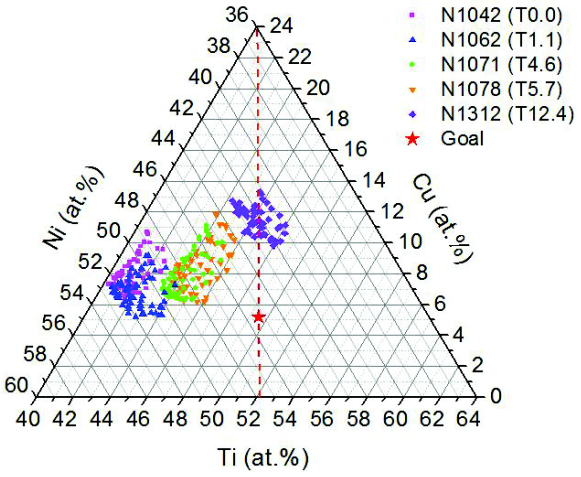

Fig. 4.12. Results of EDX analysis of Ti-Ni-Cu continuous thin film composition spreads obtained from different targets. The desired composition is denoted by a star. The dotted line corresponds to the intended atomic ratio Ti/Ni = 1.09.

The size of the Ti pieces was increased step by step up to 5.7 % of the target's surface. The sizes were chosen intuitively. As one can see, the film obtained with the target T5.7 did not yet contain enough Ti. Then a linear dependency of Ti/Ni versus relative size of Ti piece was assumed, and the next size was chosen using the plot in Fig. 4.13. The point for N1312 was put there *a posteriori*, and as seen, it fits well the plotted line.

It also follows from Fig 4.12 that increasing Ti content entails a tendency to increase Cu content as well. This can be explained by a sum of two facts: (1) we have an additional Cu source polluting the depositions (Fig. 4.6) and (2) the more Ti-rich is the target, the lower the sputtering rate is. In order to show it explicitly, we have compiled the corresponding sputtering yields in Table 4.4. The yield represents the number of target atoms sputtered per argon ion striking the target with a kinetic energy of 600 eV, which is typical for an argon plasma. Other process parameters will affect these data, of course, but they remain useful for comparison purposes. As seen, the sputtering yields of our target elements are related as follows: Cu > Ni > Ti.

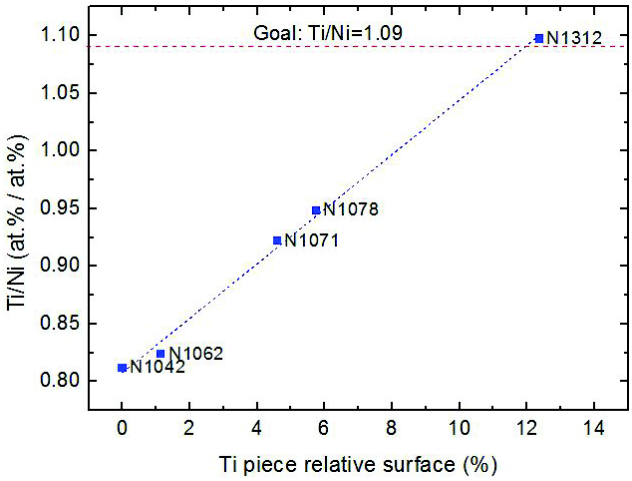

Fig. 4.13. Dependence of an atomic ratio of Ti to Ni content in Ti-Ni-Cu films versus the part of the target surface covered by pure Ti. Blue squares are the experimental points; the blue dotted line is the linear approximation of the dependence. The dotted red line indicates the intended Ti/Ni=1.09 ratio.

Table 4.4. Sputtering yield of various materials [**122**].

Target material	Ti	Ni	Cu
Sputtering yield at 600 eV	0.6	1.5	2.3

4.3.3.5 EDX: compositional spread versus target orientation

The Ti piece was attached onto the target off-centre with the purpose of increasing the gradient of Ti content in the film. Two different orientations were tested in order to check the influence on the compositional spreads (Fig. 4.14). The average composition of the film did not show any significant dependence (Table 4.3), while the distribution of element contents slightly differs for two orientations (Fig. 4.14a). We ascribe this difference to the irreproducibility of Cu contents due to contamination from the sputtering machine.

4.3.3.6 EDX: composition reproducibility

As it has been mentioned above, composition reproducibility was problematic for our Ti-Ni-Cu films. Fig. 4.15 can give an idea of the compositional dispersion for different depositions produced with the same target. In three of five cases (N1312, N1344, N1446), the composition spreads were very similar, while in the other two there was enhanced Cu contamination. Taking into account this problem, for each film compositional spread was determined separately.

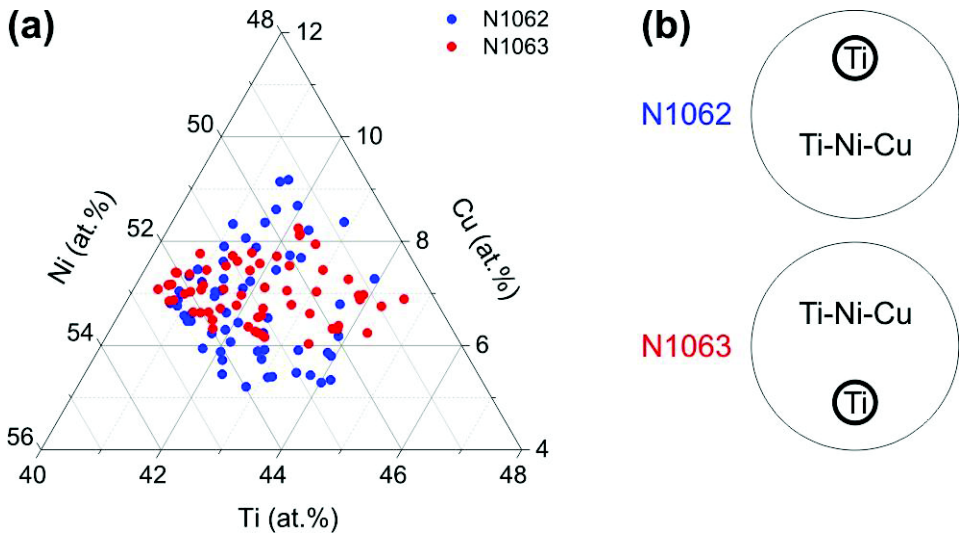

Fig. 4.14. Results of experiment on target orientation influence on film composition spread: (a) ternary diagram showing the obtained compositions; (b) schematic of target orientation – Ti piece on the "North" (for N1062) and on the "South" (N1063) of the target.

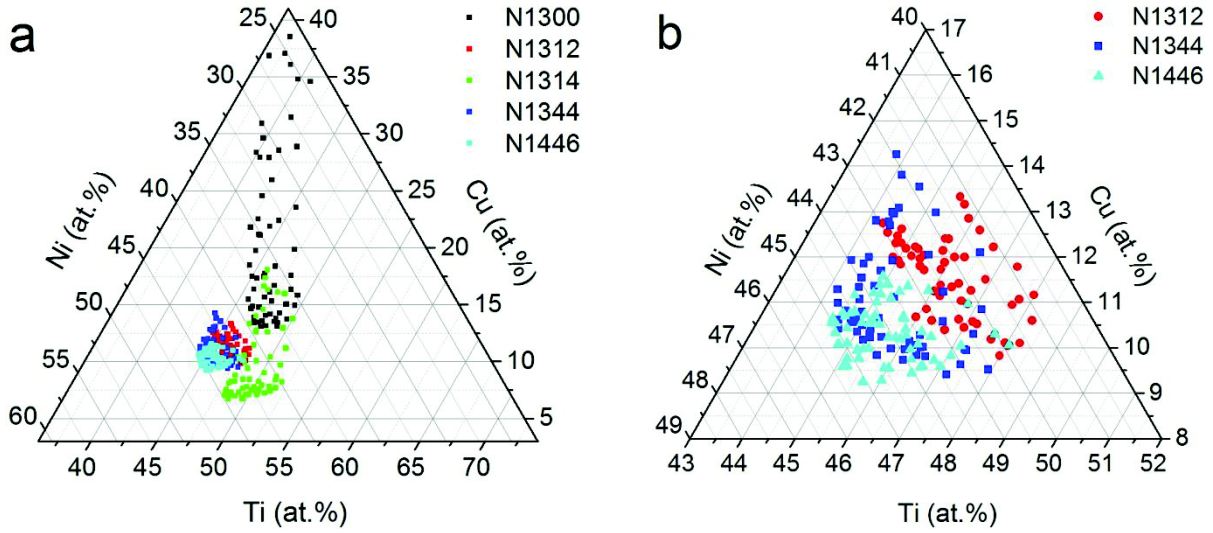

Fig. 4.15. Composition reproducibility on an example of films produced with the same target T12.4: (a) ternary diagram showing the obtained compositions; (b) zoom in for the films having representative composition.

4.3.3.7 RBS and PIXE

In order to determine correction factors for EDX composition values, four samples from the film N1446 were chosen for RBS. Simulated and theoretical RBS spectra are shown in Fig. 4.16. Briefly, the quantification procedure was as following.

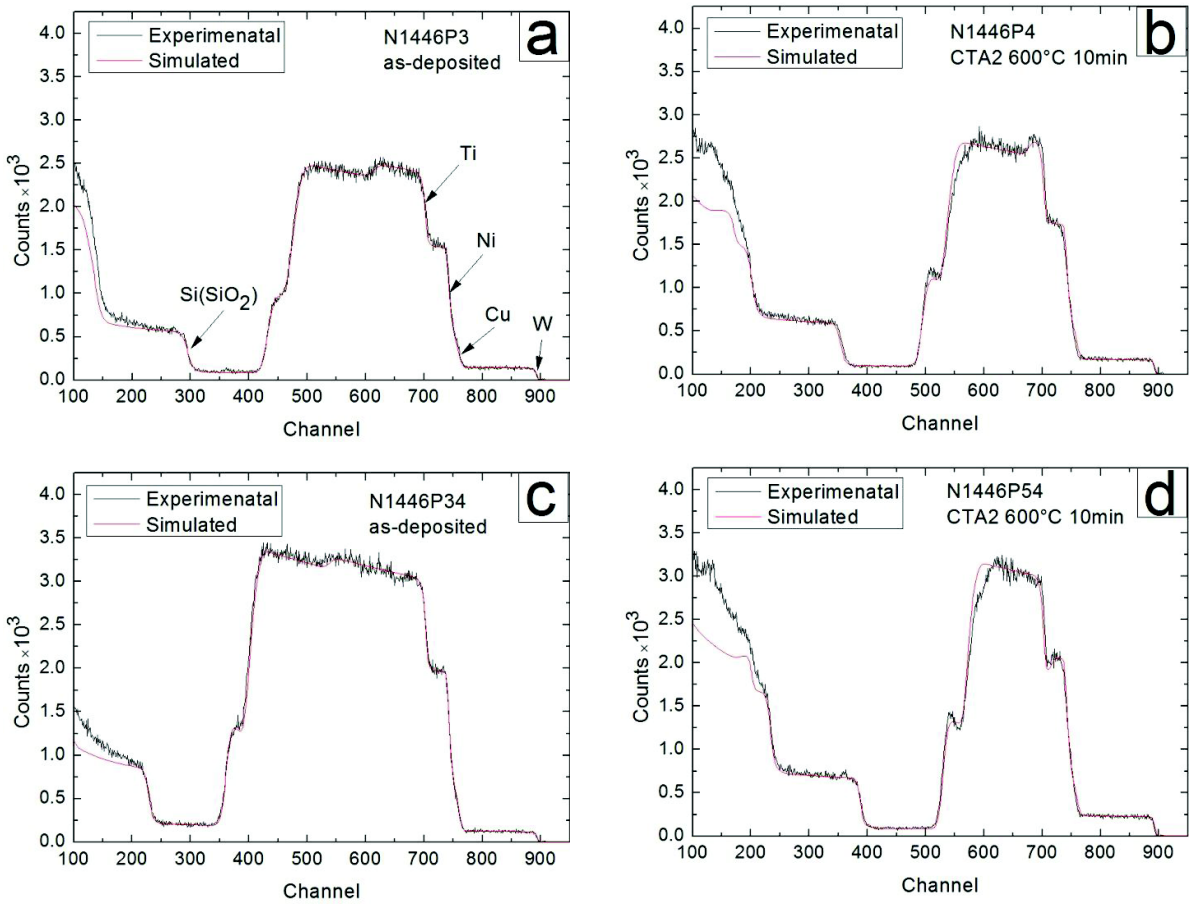

Fig. 4.16. Experimental RBS spectra and corresponding simulated fit curves.

1. Simulation of theoretical spectra.
2. Calculation of peak surfaces for Ti, Ni and Cu. The ratio Cu/Ni was obtained by PIXE (Fig. 4.17).
3. Comparison of calculated and theoretical spectra.

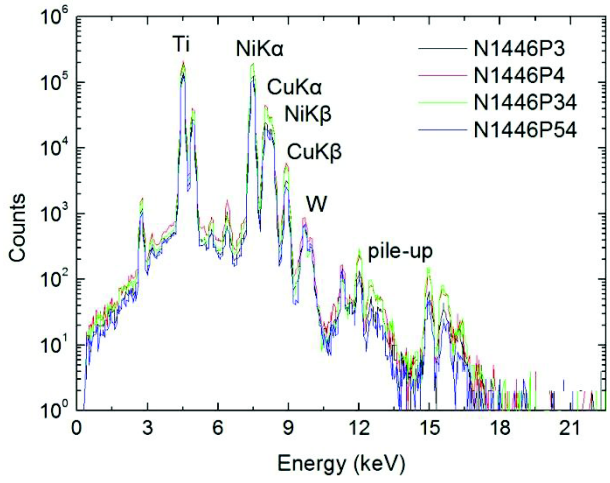

Fig. 4.17. PIXE spectra for determination of Cu/Ni ratio.

As it can be seen from the RBS spectra, for annealed samples the simulated curve did not fit the experimental one, notably in proximity of the interface with the SiO_2 layer. In fact, the Ti concentration increased at the interface (and the Ni(Cu) concentration decreased correspondingly). Ti migration towards SiO_2 and its subsequent oxidation can be supposed here. This hypothesis will be confirmed below with AES results.

The determined composition values are shown in Table 4.5. The film was found to contain ~0.8 at.% tungsten. As it has been explained above, contamination with W is attributed to filament. It could not be determined by EDX since the peak of W superposes with that of Si in the substrate with that technique.

To determine the correction factors, relative contents of Ti, Ni and Cu were calculated and compared with those obtained by EDX. The resulting factors are shown in Table 4.6. As seen, EDX analysis underestimated the Ti content. To recalculate more exact composition, a factor of 1.1 for Ti and 0.9 for Ni should be taken into account.

Table 4.5. Elemental composition in at.% determined by RBS. The ratio Cu/Ni was determined by PIXE.

Sample	Ti (±1)	Ni (±1)	Cu (±0.7)	W (±0.1)	Cu/Ni (±0.01)
N1446P3	49.6	40.0	9.6	0.75	0.24
N1446P4	49.2	40.0	10.0	0.80	0.25
N1446P34	47.9	41.0	10.6	0.50	0.26
N1446P54	50.7	40.0	8.4	0.90	0.21

Table 4.6. Correction factors obtained by RBS for concentrations (at.%) quantified by EDX.

Sample	Ti	Ni	Cu
N1446P3	1.11	0.93	0.85
N1446P4	1.09	0.93	0.89
N1446P34	1.09	0.91	1.01
N1446P54	1.09	0.93	0.88

EDX calculation results should depend on SiO_2 layer thickness, since it contributes to the EDX signal. The correction factors were obtained for the film N1446, having a 1 μm thick SiO_2 layer. Other samples had 2 μm and 100 nm oxide layers, and the target did not have any SiO_2 layer. Therefore, it is possible that the correction factors for the other samples (besides N1446) and especially for the target are not exactly the same. The value of this difference should be checked separately. That is why below we will still use the uncorrected EDX values. However, we assume that the difference in correction factors, if it exists, is not big.

4.3.3.8 Compositional analysis: summary and conclusions

1. Intrinsic inhomogeneity of the sputtering system allowed obtaining a variation of each element concentration of the order of several at.%. Such modest variation does not allow a real combinatorial approach. However, taking into account the high sensitivity of Ti-Ni-Cu alloy

transformation temperatures to its composition, it can be helpful to find the intended composition for a film fabricated this way.

2. Relying on EDX analysis, the obtained films where poorer in Ti than the target. That is probably due to Ti loss due to oxidation in the sputtering chamber. To increase the Ti/Ni ratio, the target was modified by adding pure Ti pieces. The dependence of Ti/Ni in the films versus the target's surface part occupied by pure Ti was found to be linear within the studied range. The intended ratio Ti/Ni=1.09 was successfully obtained. The linear dependence allows the adjustment of the composition rather easily.
3. Even though the Ti piece was attached away from the target's centre, a change of target orientation around its axis did not change the film's average composition. This means that a position of the Ti piece on the target's surface has little importance, which is convenient from a technological point of view.
4. Contamination in Cu, probably coming from the filament box, had different random intensities from one deposition to another, causing problems with the composition reproducibility. Composition control after each deposition was indispensable. Additionally, contamination in W (filament material) of ~1 at.% was revealed by RBS.
5. Correction factors for EDX quantification obtained by RBS for the sample N1446 were 1.1 for Ti and 0.9 for Ni. These factors can be different for samples with different SiO_2 layer thickness, but the difference is assumed to be small.
6. Relying on the analysis of RBS spectra, Ti diffusion from the film's volume towards the interface with SiO_2 is suspected for the annealed samples.

4.3.4 Evolution of microstructure and composition upon annealing – AES, SEM, TEM

As mentioned, as-deposited films were amorphous, and crystal structure is indispensible for SME. Therefore, post-annealing is mandatory for crystallization and crystal growth, but they are not the only processes taking place when annealing. The other phenomena may include: formation of more thermodynamically stable phases (including precipitates), evolution of internal stresses and microstructure, chemical reactions with a substrate and residual oxygen in furnace vacuum chamber, interdiffusion of constituent layers, etc. All these phenomena may strongly affect the SME down to cancelling the effect. To study film evolution upon annealing, AES, SEM and TEM methods were used.

4.3.4.1 AES: compositional profiles for cross-sections

Information about four samples studied by AES is shown in Table 4.7. As seen, all the four had different composition and also a different heat treatment: one sample was as-deposited, while three others were annealed at different furnaces (conventional resistive furnace for CTA and rapid infrared lamp furnace for RTA) but with the same nominal parameters (maximal temperature and time spent at that temperature). Thus, one sample served as a reference for as-deposited state allowing a comparison of annealings obtained by different furnaces. We should note that two of the samples had 100 nm of SiO_2 layer, while two others had 2 μm.

Table 4.7. Samples studied by AES.

Sample	EDX	SiO_2	Annealing
N1043P30	$Ti_{42.6}Ni_{49.8}Cu_{7.6}$	2 μm	as-deposited
N1042P55	$Ti_{41.7}Ni_{52.0}Cu_{6.3}$	2 μm	CTA1 600°C 10 min
N1312P38	$Ti_{48.0}Ni_{41.9}Cu_{10.1}$	100 nm	CTA2 600°C 10 min
N1312P2	$Ti_{45.5}Ni_{41.2}Cu_{13.3}$	100 nm	RTA 600°C 10 min

The resulting AES profiles together with SEM images of corresponding cross-sections are shown in Fig. 4.18. Here we should make two notes. Firstly, SEM images are given for the samples which were not exactly the same as those used for AES. That was due to insufficient resolution of the SEM of the AES set-up. They had the same heat treatment and SiO_2 thickness, and differed only in composition, which means that their cross-section images can be considered as representative. Secondly, we do not show here quantitative results (in at.%) for AES since they would be imprecise, so we only give a characteristic signal profile (intensity, in a.u.).

The following observations can be made from SEM micro-images.

1. The as-deposited sample does not exhibit any clear features of crystal structure. It appears like there is some top layer, but it was not confirmed by other methods (TEM, AES), so it is probably just an artefact from fracture. All the annealed samples, in contrast, have clearly observed grain-like features with the sizes well below 100 nm. As it will be shown below, it is in agreement with XRD data confirming film crystallization upon annealing.
2. Cross-sections of CTA-annealed samples in images (d) and (f) in Fig. 4.18 show similar microstructures (with a slightly different fracture character). This suggests that the vacuum level in the conventional furnace (10^{-7} Torr for CTA1 and 10^{-8} Tor for CTA2) and SiO_2 thickness (100 nm and 2 μm) did not cause any significant difference in microstructure. For both samples, ~30 nm thick top and bottom layers were formed.

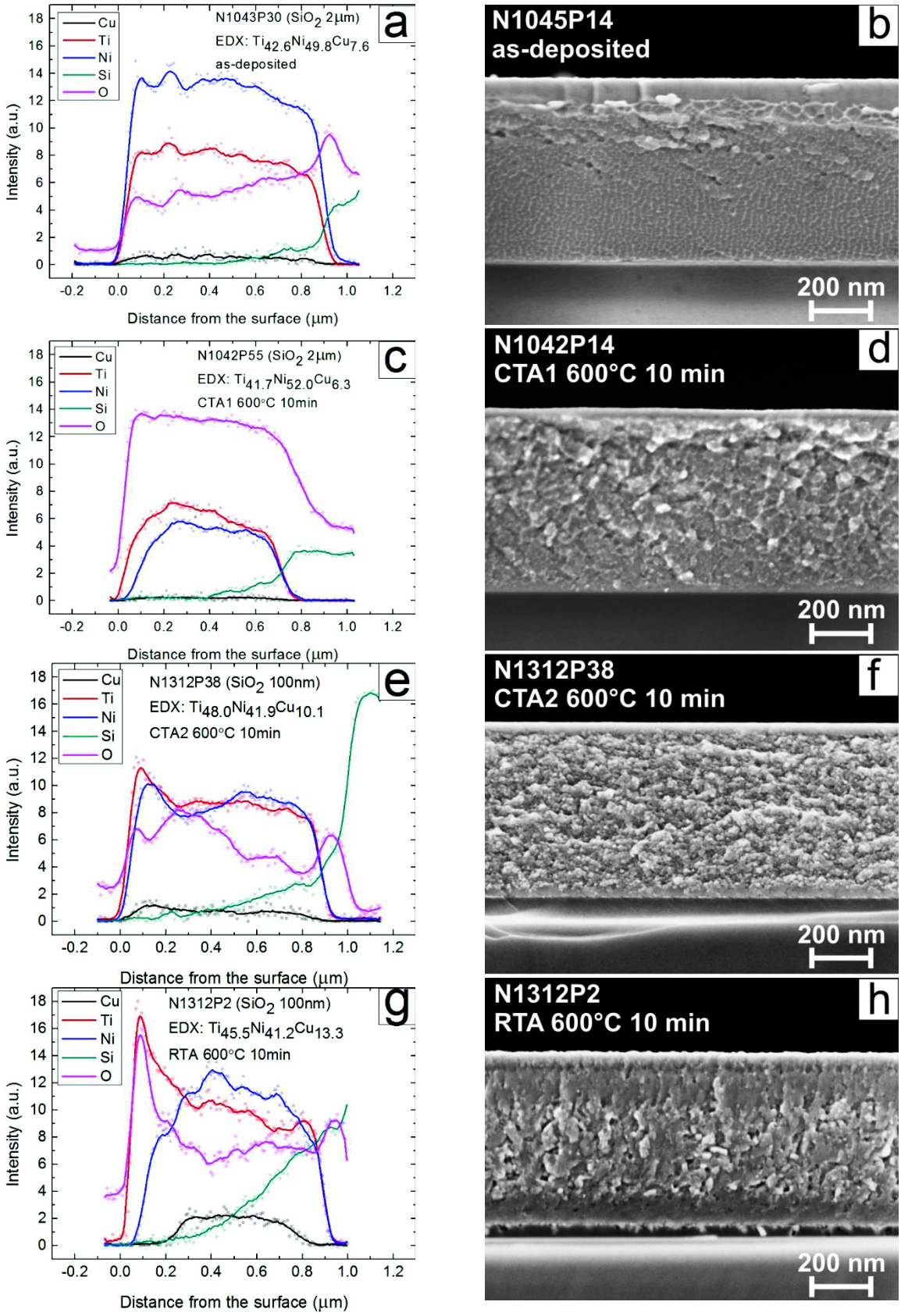

Fig. 4.18. (a,c,e,g) AES elemental profiles for cross-section line-scans and (b,d,f,h) typical micro-images of corresponding cross-sections. Raw data is shown by semi-transparent points; smoothed data – by lines.

3. As for the sample annealed with RTA (Fig. 4.18h), its microstructure is clearly different from that produced with CTA. Top and bottom layers for this case are about ~190 and ~90 nm respectively. As it can be noticed, the top layer itself likely consists of 2 layers.

Now let us have a look at AES line-scans in Fig. 4.18. It is worth recalling here two points. Firstly, the Auger signal is also sensitive to topography and that should be kept in mind when interpreting Auger curve shapes. Secondly, Auger signal characterizes the first few nanometres of the analyzed surface, and the latter in our case has a tendency to oxidize rather quickly. Therefore, we expect oxygen signal to be higher and, as a consequence, other signals to be lower, compared to "intrinsic" film signal. (Argon for etching was used to remove the adsorbed carbon, but it was applied for a rather short time since it deteriorates the sample's surface.)

The following observations can be made from AES line-scans.

1. While the distribution of Ti, Ni and Cu elements is rather homogeneous in the film's volume (moving from one film's edge to another) for the as-deposited sample, compositional gradients appear clearly for annealed samples.
2. The intensity of the oxygen signal (magenta curve), as mentioned, is difficult to interpret, since the method is sensitive only to few first nanometres of the surface, which oxidizes quickly. On the other hand, considering that all the samples were fractured just before the analysis and we can assume the fractures were oxidized similarly. However, the intensity of the oxygen signal is maximal for the sample N1042P55 and equals ~13 a.u., while it is ~6 a.u. for all the other samples. The possible reason may be sample aging with time (15 months separate the series N1042 & N1312). Taking into account that the as-deposited sample did not show such high oxygen intensity, it can be supposed that long-term air exposure leads to film oxidation through grain boundary diffusion. Long-term chemical stability in air (and possible the need of a protective layer) is an important issue to study in further. However, once again, more data is needed to evaluate the validity of this observation. For instance, depth-profile AES and/or secondary ion/neutron mass spectroscopy would help to understand whether the oxygen comes from the surface when exposed to air or already from vacuum chamber during deposition.
3. Let us compare the signals for Ti and Ni. As observed for the as-deposited sample, both for air/film and film/SiO_2 interfaces, the two signals decay almost simultaneously. In contrast, for the annealed samples, at the interface with air, the Ti signal is observed to decay "later" than that of Ni. This is the most pronounced for the case of RTA (vacuum of 10^{-5} Torr). For the later, there is also a clear peak of O accompanying that of Ti. The shift between Ni and Ti "steps" is below 50 nm. This may indicate the formation of a thin surface Ti oxide and as a consequence depletion of the films in Ti.
4. The signal corresponding to Si does not disappear abruptly on the film/SiO_2 interface. In fact, even for the as-deposited film, Si seems to persist by ~200 nm into the film's volume

(we recall that the spatial resolution was 20 nm). This effect is the most pronounced in the case of RTA, where Si diffusion depth reached 600 nm. While for the samples with only 100 nm thick SiO_2 layer, Si diffusion from the substrate through the oxide can be suspected, it would be hardly possible with 2 μm thick SiO_2, especially for an as-deposited sample. Thereby, we ascribe this phenomenon rather to a chemical reaction between the Ti-Ni-Cu film and the SiO_2. The details will be provided when describing XRD results.

5. The signal for Cu is too low for an interpretation, but it seems like both film's interfaces are impoverished in Cu.

4.3.4.2 TEM: cross-section microstructure

Information about four samples chosen for TEM is shown in Table 4.8. They differed in composition, heat treatment and SiO_2 thickness.

Table 4.8. Samples for TEM.

Sample	**EDX**	**SiO_2**	**Annealing**
N1045P14	$Ti_{42.6}Ni_{48.9}Cu_{8.5}$	2 μm	as-deposited
N1042P14	$Ti_{42.6}Ni_{48.6}Cu_{8.8}$	2 μm	CTA1 600°C 10 min
N1312P53	$Ti_{47.7}Ni_{42.1}Cu_{10.2}$	100 nm	RTA 600°C 10 min
N1071P1	$Ti_{43.7}Ni_{45.2}Cu_{11.1}$	100 nm	RTA 600°C 10 min

We recall here that the lamella samples were prepared by lift-out technique using FIB. This required covering the film's surface with a Pt protective layer. When fabricating this layer by FIB-assisted deposition, ~10-30 nm of the film's surface can be damaged by the ion beam [**89**]. In addition, at TEM analysis, perpendicularity of the electron beam with respect to cross-section plane was not perfectly adjusted. This means that parasitic contrast change at the film's edges may be observed due to possible sample tilt (for both edges) or from ion-beam damage (surface side).

The obtained TEM bright-field micro-images are shown in Fig. 4.19 to Fig. 4.21.The following observations can be made on the micro-images.

1. The as-deposited sample (Fig. 4.19) has a feature-less contrast in the Ti-Ni-Cu layer. Selected area electron diffraction (SAED) proved an amorphous state of this layer (not shown here). No sign of interaction of the Ti-Ni-Cu layer with SiO_2 at bottom interface or air at top interface is observed.
2. The micro-image of the CTA-annealed sample (Fig. 4.19) demonstrates crystals without clear faceting. No sign of interaction of the Ti-Ni-Cu layer with SiO_2 or air is observed.

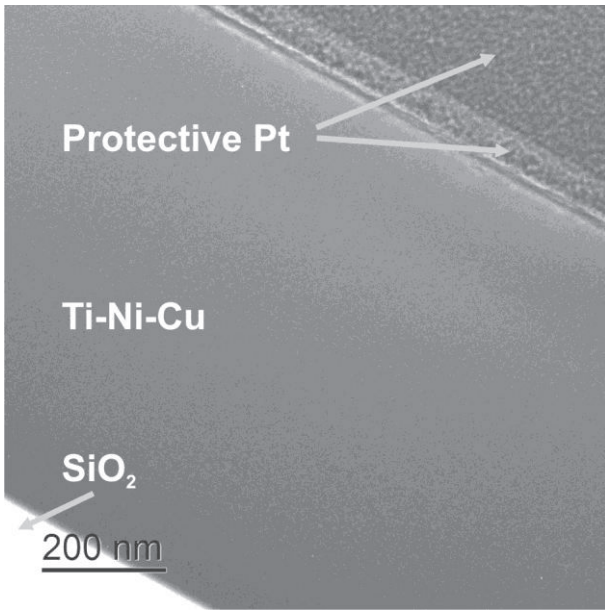

Fig. 4.19. Bright-field TEM micro-image of as-deposited sample N1045P14.

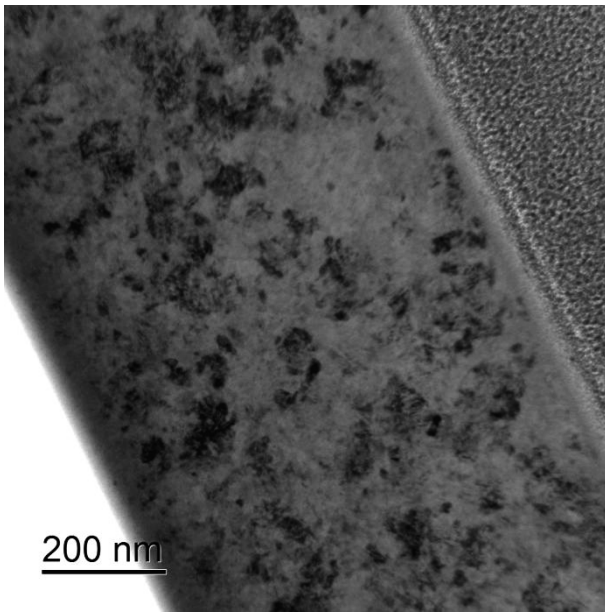

Fig. 4.20. Bright-field TEM micro-image of CTA1-annealed sample N1042P14.

3. The microstructure of RTA-annealed samples N1312P53 and N1071P1 was found to be very similar, so only that of N1312P53 is shown (Fig. 4.21). As can be seen, it is rather different from the microstructure produced with CTA. A multitude of equiaxial well-faceted grains is observed, indicating higher thermal energy supplied to the sample in the case of RTA. Observing the contrast, one can distinguish 4 layers within the Ti-Ni-Cu film. Firstly a ~80 nm thick layer (layer 4), which formed at the interface with SiO_2, with some crystals growing into the latter (Fig. 4.19c). At the air interface of the film, 2 layers are clearly observed (Fig. 4.19d): ~70 nm (layer 1) with a brighter contrast and ~170 nm (layer 2) with a microstructure similar to that of layer 4. The formation of these interface layers can be ascribed to chemical reactions of Ti-Ni-Cu with SiO_2 and atmosphere. The remaining layer (layer 3) is of ~530 nm out of 850 nm of the overall film thickness. Obviously, the composition of this layer should be different from the average one measured by EDX (or RBS), because of the reactions which took place.

4.3.5 Structural analysis – XRD

In order to fabricate films with SME, we aimed at obtaining an alloy which contains, first of all, the TiNi phase which shows a phase transformation. Depending on whether the alloy is Ti- or Ni-rich, a small amount of secondary phases may be present. Before presenting the results, we will discuss in detail the possible phases we could have obtained in our films.

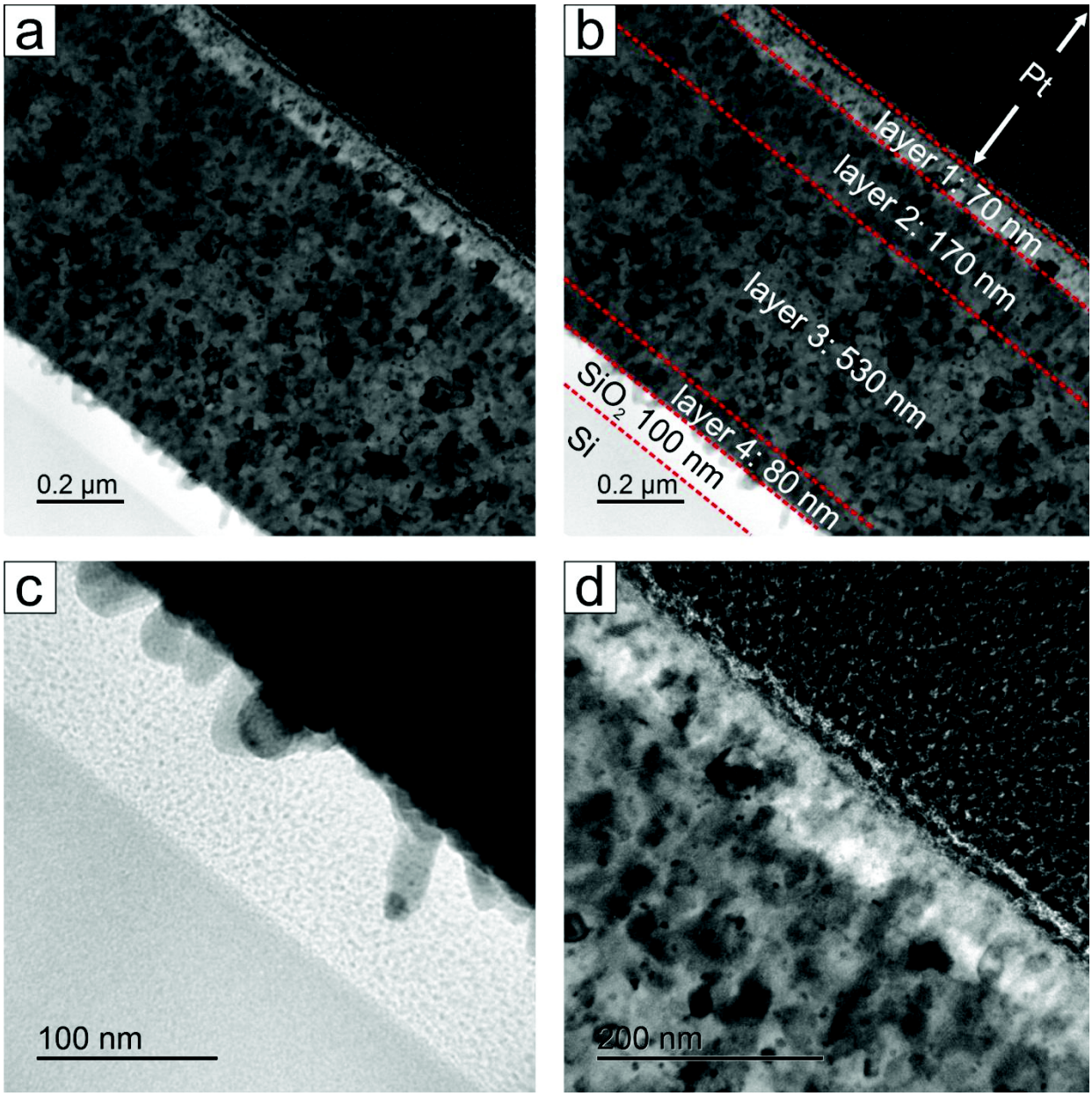

Fig. 4.21. Bright-field TEM micro-image of RTA-annealed sample N1312P53. (a) General view; (b) distinguished layers; (c) zoom for Ti-Ni-Cu/SiO_2 interface; (d) zoom for Ti-Ni-Cu/"air" interface (covered with Pt).

4.3.5.1 Expected phases: Ti-Ni-Cu system

Let us discuss what phases could be expected in our system considering the equilibrium phase diagram (Fig. 4.22) and literature data. It should be recalled here that Cu within the quantities used in our alloys is known to form a substitution type solid solution in binary Ti-Ni phases. This allows us to consider the binary structures of Ti-Ni system for the Ti-Ni-Cu system analysis at the concentrations of interest. Concerning Cu site occupancy, it is still not very clear for the Ti-Ni system. Under certain conditions, it likely does not have preference between Ti and Ni sites [**93**].

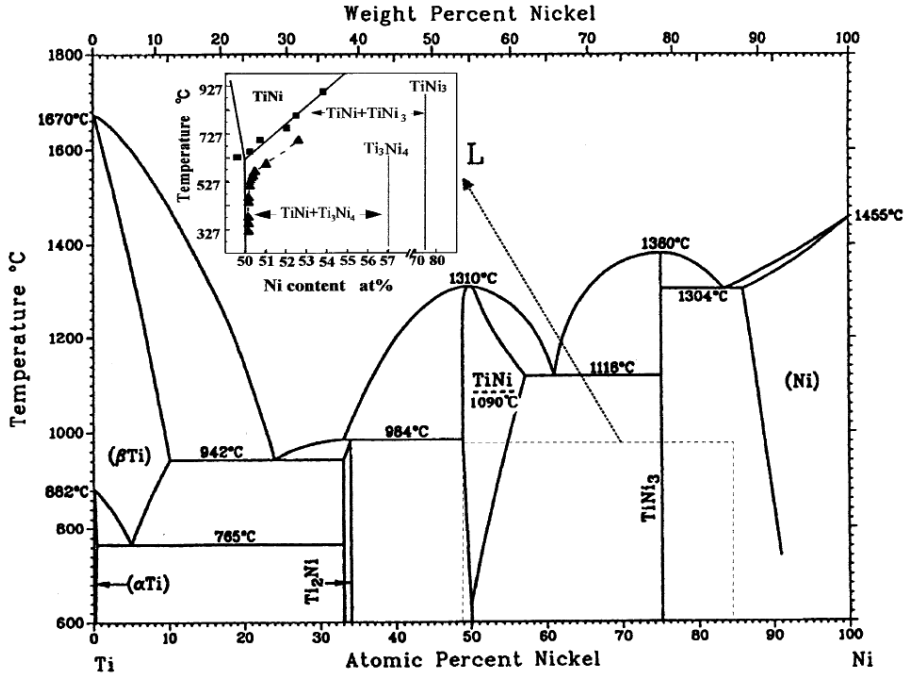

Fig. 4.22. Phase diagram of Ni-Ti system [**93**].

As seen in the diagram, 2 equilibrium phases can be found for Ni-rich Ti-Ni alloy: TiNi based phases (which can be either austenite or one of 3 different types of martensite) and Ni_3Ti. On the other hand, it has been reported that before the Ni_3Ti stable phase appears, several metastable phases form as follows: $Ni_4Ti_3 \rightarrow Ni_3Ti_2 \rightarrow Ni_3Ti$ [**123**]. Since our films were not annealed for a long time and temperatures were not too high, one would expect having Ni4Ti3 or Ni_3Ti_2 phases rather than Ni_3Ti. As regards the phase Ni_3Ti_2, interestingly it is known to undergo a martensitic transformation (similar to the TiNi phase). It has high-temperature tetragonal and low-temperature orthorhombic structures. However, the direct transformation (i.e. when cooling) may be hindered by stress [**93**].

Ti_2Ni is a stable phase for Ti-rich alloys. However, together with the Ti_4Ni_2O phase, it is also often found in Ni-rich alloys. In fact, these two phases have the same crystal structure and therefore their XRD patterns are indistinguishable [**123**,**124**]. Moreover, oxygen reacts easily with Ti_2Ni to form Ti_4Ni_2O [**124**]. 20-50 nm of Ti_2Ni boundary layer have been reported to form close to the SiO_2/Si(100) substrate in Ni-rich Ti-Ni-Cu films [**94**], stabilized by oxygen from the SiO_2. Ti_4Ni_2O is known to be a main oxide in Ti-Ni-Cu system [**93**].

Another phase that can be present in Ni-rich alloys is $TiNi_2$ (or $Ti(Ni,Cu)_2$ for Ti-Ni-Cu alloys). It is a kind of precipitate which is known to appear with aging of Ti-poor alloys at 600 °C [**93**,**125**]. However, taking into account the short annealing time used, this phase is not expected.

To summarize, considering solid state phase transformations, 10 different phases of the Ti-Ni-Cu system may occur (of course, not all simultaneously) in the samples. Corresponding crystallographic data are shown in Table 4.9.

Table 4.9. Phases reported for Ti-Ni(-Cu) alloys and their crystal structures.

Phase	Crystal system	Lattice system	Struktur-bericht symbol	Space group	Ref.
TiNi austenite, B2	Cubic	Cubic	B2	Pm-3m (221)	[**126**]
TiNi martensite, R-phase	Trigonal	Rhombohedral	-	P-3 (147)	[**93**]
TiNi martensite, B19'	Monoclinic	Monoclinic	B19'	$P2_1/m$ (11)	[**126**]
TiNi martensite, B19	Orthorhombic	Orthorhombic	B19	Pmmb	[**126**]
Ti_3Ni_4	Trigonal	Rhombohedral	-	R-3 (148)	[**126**]
$TiNi_2$	Tetragonal	Tetragonal	$C11_b$	I4/mmm (139)	[**93**]
$TiNi_3$	Hexagonal	Hexagonal	$D0_{24}$	$P6_3/mmc$ (194)	[**126**]
Ti_2Ni	Cubic	Cubic	-	Fd-3m (227)	[**126**]
Ti_2Ni_3	Tetragonal	Tetragonal	-	I4/mmm (139)	[**93**]
Ti_2Ni_3	Orthorhombic	Orthorhombic	-	Bbmm (63)	[**93**]

In order to index an experimental spectrum, one needs to know standard patterns (positions and intensities of reference phase reflections), which are determined by atom positions and crystal lattice parameters. The PDF-4 database was used for standard patterns (Table 4.10). Some phases were not found in the database and their patterns were calculated using "PowderCell" free software (version 2.4 for WinOS). The calculations were based on crystal structure, cell parameters and Wyckoff positions taken from the literature with an assumption of texture absence (powder diffraction). It will be confirmed below that the samples were indeed not textured.

Table 4.10. Cell parameters of possible phases in Ti-Ni(-Cu) alloys and corresponding PDF patterns used for indexing of the XRD spectra. When the PDF files were not available, the patterns were calculated using PowderCell software.

Chemical formula (phase name)	Lattice parameters						PDF number	Pattern quality	Ref.
	a (Å)	b (Å)	c (Å)	α (°)	β (°)	γ (°)			
TiNi (B2)	2.998	2.998	2.998	90	90	90	03-065-5537	Calculated	[**127**]
TiNi (R-phase)	7.354	7.354	5.283	90	90	120	04-011-1996	Calculated	[**128**]
TiNi (B19')	2.884	4.110	4.665	90	98.10	90	03-065-0365	Calculated	[**129**]
TiNi (B19)	2.919	4.288	4.5	90	90	90	04-015-7392	Indexed	[**130**]
Ti_3Ni_4	11.24	11.24	5.077	90	90	120	03-065-3957	Calculated	[**131**]
$TiNi_2$	3.11	3.11	7.98	90	90	90	PowderCell	Calculated	[**125**]
$TiNi_3$	5.092	5.092	8.298	90	90	120	00-051-1169	High	[**132**]
Ti_2Ni	11.32	11.32	11.32	90	90	90	01-072-0442	Calculated	[**133**]
Ti_2Ni_3 tetragonal	3.095	3.095	13.59	90	90	90	PowderCell	Calculated	[**134**]
Ti_2Ni_3 orthorhombic	4.398	4.370	13.54	90	90	90	PowderCell	Calculated	[**134**]

4.3.5.2 Expected phases: Ti-Ni-Si system

As it was revealed by AES, considerable Si diffusion into the Ti-Ni-Cu layer took place. Therefore we should also consider the possible formation of corresponding phases. Stemmer et al. studied the interaction between TiNi films and Si substrates and reported the formation of hexagonal Ti_2Ni_3Si phase [**135**], while Hung et al. reported orthorhombic TiNiSi phase [**136**]. In another study, dealing with Ni/Ti/Si nanolayers, Sieber et al. found Ni_2Si, V-phase $Ti_4Ni_4Si_7$ and a small amount of TiSi [**137**]. Finally, in the work of Tomozawa et al. on Ti-Ni-Cu on SiO_2/Si, which is the most similar to ours, it is reported that a reaction layer of the film and the substrate possibly contains $Ni_{16}Ti_6Si_7$ (cF116, a = 1.12 nm) [**120**].

Therefore, 6 possible silicides may form in our films. Corresponding crystallographic data are shown in Table 4.11 and Table 4.12.

Table 4.11. Phases of Ti-Ni-Si system reported for Ti-Ni(-Cu) alloys on Si and SiO_2 substrates and their crystal structures.

Phase	**Crystal system**	**Lattice system**	**Struktur-bericht symbol**	**Space group**	**Ref.**
δ-Ni_2Si	Orthorhombic	Orthorhombic	C23	Pnma (62)	[**138**]
TiSi	Orthorhombic	Orthorhombic	B27	Pnma (62)	[**139**]
Ti_2Ni_3Si λ-phase	Hexagonal	Hexagonal	C14	$P6_3/mmc$ (194)	[**140**]
TiNiSi E-phase	Orthorhombic	Orthorhombic	-	Pnma (62)	[**140**]
$Ti_4Ni_4Si_7$ ($TiNiSi_2$) V-phase	Tetragonal	Tetragonal	-	I4/mmm (139)	[**140**]
$Ni_{16}Ti_6Si_7$ G-phase	Cubic	Cubic	-	Fm-3m (225)	[**141**]

Table 4.12. Cell parameters of possible phases of Ti-Ni-Si system and corresponding PDF patterns used for indexing the XRD spectra.

Chemical formula (phase name)	**Lattice parameters**						**PDF number**	**Pattern quality**	**Ref.**
	a (Å)	**b (Å)**	**c (Å)**	**α (°)**	**β (°)**	**γ (°)**			
δ-Ni_2Si	5.009	7.066	3.732	90	90	90	00-048-1339	High	[**142**]
TiNiSi	6.148	7.017	3.630	90	90	90	04-008-7170	Indexed	[**143**]
TiSi	4.970	6.479	3.618	90	90	90	04-002-5542	High	[**144**]
Ti_2Ni_3Si	4.788	4.788	7.681	90	90	120	04-014-4152	High	[**145**]
$Ti_4Ni_4Si_7$	12.569	12.569	4.939	90	90	90	00-042-1122	Indexed	[**146**]
$Ni_{16.7}Ti_6Si_7$	11.259	11.259	11.259	90	90	90	04-014-7187	High	[**141**]

4.3.5.3 θ/2θ XRD of the film N1042 (unmodified target): as-deposited structure and effect of RTA

We start with the film N1042, which was fabricated with the unmodified target. Extreme compositions of the spread were chosen to study the structure after annealing (Table 4.13). The sample P1 of this film was chosen to study the as-deposited structure. An as-deposited film was expected to be amorphous or nanocrystalline, as generally occurs for deposition of intermetallic films onto unheated substrates. This state was also assumed to be essentially independent of the position on the wafer, since the composition variation was not so high. For the same reason, it was assumed to stay unchanged with all the targets.

Table 4.13. EDX-determined composition and Ti/Ni atomic ratio for the samples chosen for structural analysis of the film N1042.

Sample	Ti, at.%	Ni, at.%	Cu, at.%	Ti/Ni
N1042 P33	40.4	51.9	7.7	0.78
N1042 P48	41.1	52.2	6.7	0.79
N1042 P53	41.8	51.5	6.7	0.81
N1042 P8	40.9	49.7	9.5	0.82
N1042 P22	42.7	49.2	8.1	0.87
N1042 P1	40.7	48.6	10.7	0.84

The samples were annealed all together at 600 °C for 10 min in a vacuum furnace (CTA1, 10^{-6} Torr). The obtained spectra are shown in Fig. 4.23. The peak around 69° corresponds to Si(400) reflection (the samples were tilted by 2° to remove this peak, but it was still observed because of the high relative volume of the substrate). All the other peaks come from the film. The amorphous state of the as-deposited film is evident from the corresponding fuzzy spectrum. In contrast, we can notice at least 11 peaks (marked with vertical dotted lines) for the annealed samples. This shows that the annealing resulted in crystallization.

On the bottom of Fig. 4.23, the best fitting standard patterns are shown: B2, Ti_3Ni_4, Ti_4Ni_2O and Ni_3Ti_2Si phases. They were chosen among all the possible candidates given in Table 4.9 and Table 4.11 and also among all the other compounds containing Ti, Ni, Cu, Si and/or O existing in PDF library. Comparison was made using either “manually” made plots, or “EVA” (Bruker®) or “Highscore” (PANalytical®) software.

As seen from the figure, the phases B2 (austenite) and Ti_3Ni_4 fit very well the spectra. It agrees with our expectations based on the equilibrium diagram of Ni-rich alloy. In contrast, the peak (422) of Ti_4Ni_2O is not observed, while it should have the same intensity as (440). In addition, the intensity ratio of the peaks (511) and (440) is different from the standard. Possibly, (440) of Ti_4Ni_2O sums up with (201) and (112) of Ni_3Ti_2Si. However, (002) of Ni_3Ti_2Si is not observed.

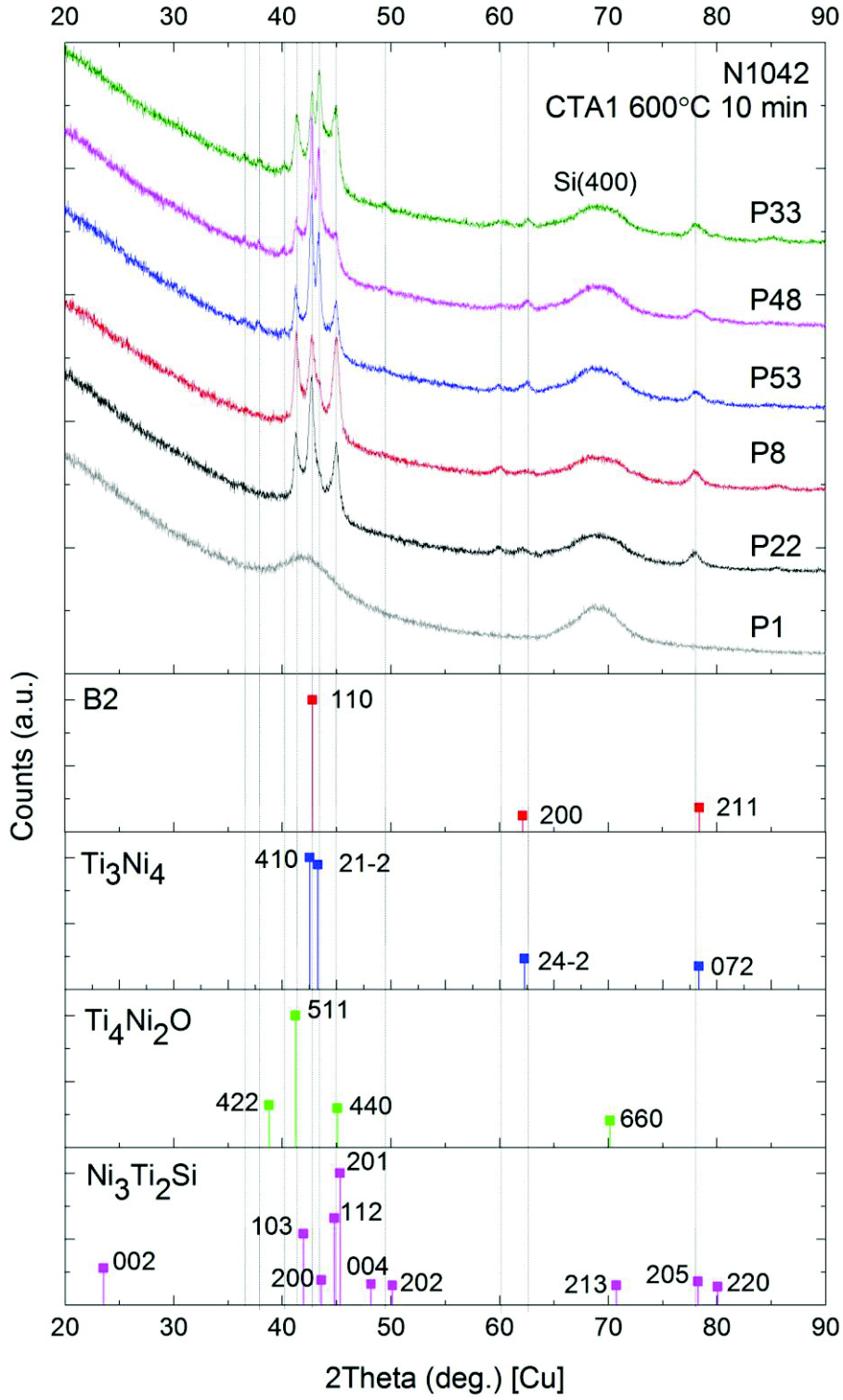

Fig. 4.23. XRD spectra obtained at room temperature with Cu radiation for different positions, P, of the film N1042 detailed in Table 4.13. The offset of 2° was applied in order to remove the reflections of the single-crystal Si (100) substrate. The bottom spectrum corresponds to the as-deposited sample (P1). On the bottom of the figure, the best fitting normalized standard patterns of possible phases taken from PDF library are given (only the peaks with intensity higher than 10 % of maximal peak are shown). Dotted vertical lines are included to facilitate the comparison.

As it can be also noticed, some small peaks (e.g. at ~40.2° and ~60.0°) do not fit any of the proposed patterns. It will be shown below that the films were not textured, so the discrepancies are to be clarified in further studies (e.g. using SAED).

It is worth noting that some of the experimental peaks are likely a combination of several peaks of different phases. Assuming this, it is possible that a small amount of $Ni_{16}Ti_6Si_7$ is also present (its standard pattern is not shown here). However, its Ni content is considered as too high for formation of this compound with our film compositions.

4.3.5.4 θ/2θ XRD(T) of the film N1042 (unmodified target): search for martensite

In order to check if there were any martensite phases (notably, B19, B19', R-phase and/or orthorhombic $Ti_2(Ni,Cu)_3$), an XRD analysis at different temperatures (XRD(T)) was performed for all the samples in the same 2θ range as for the room temperature measurements. The samples were heated from room temperature to different temperatures up to 182 °C, which is higher than the maximal observed transformation temperature for the Ti-Ni-Cu system (90 °C [**94**]). As seen from Fig. 4.24, none of the principal peaks changed their intensities, confirming an absence of martensite (other peaks stayed unchanged as well, we show only the 40-47° range on this figure for easier perception), which means that there is no phase transformation within this temperature range. The shift of the spectrum at high temperature towards small angles is due to thermal dilatation of the sample.

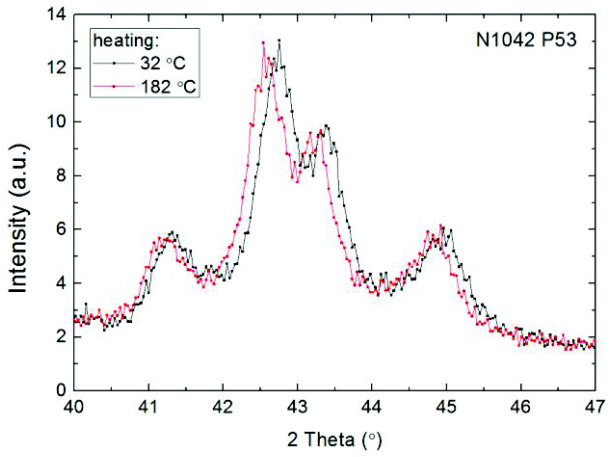

Fig. 4.24. Characteristic region of XRD spectra obtained with Cu radiation at two different temperatures for the sample N1042 P53.

4.3.5.5 θ/2θ XRD of the film N1312 (target T12.4): effect of time and temperature of RTA

After having described the results for the film N1042 obtained with the unmodified target, we present next the film N1312 obtained with the target T12.4 (the richest in Ti). The films obtained with "intermediate" targets were not characterized (except of composition measurements, of course).

A series of samples from this film N1312 were annealed in RTA furnace with different parameters given in Table 4.14. RTA is less time-consuming compared to CTA and its heating and especially cooling rates are better controlled. Another important feature is a possibility to anneal an entire 4 inch wafer without cutting, which was not possible with our CTA furnaces. The latter option is essential for microfabrication technology.

Table 4.14. EDX-determined composition and RTA parameters for the samples chosen for structural analysis of the film N1312.

Sample	Ti, at.%	Ni, at.%	Cu, at.%	RTA
N1312P13	47.8	41.2	11.0	500 °C, 1 min
N1312P14	48.0	40.8	11.2	600 °C, 10 s
N1312P15	46.3	42.4	11.3	600 °C, 1 min
N1312P2	45.5	41.2	13.3	600 °C, 10 min

The obtained spectra are shown in Fig. 4.25. Let us consider first the sample N1312P13, annealed at the lowest temperature. As seen, RTA for 1 min at 500 °C was enough to crystallize the sample. B2 austenite and Ti_4Ni_2O were found to best fit this spectrum. The quantity of the oxide seems to be comparable with that of the austenite, indicating significant oxidation of the sample. Comparing this sample with the others (see all the other spectra), it is evident that the higher the temperature of RTA and the longer the annealing time, the less of the austenite and the more of the oxide is present in the samples.

It is worth recalling here that Ti_2Ni, which is an equilibrium phase for Ti-rich alloys, has the same XRD pattern as Ti_4Ni_2O. However, as shown in [**94**], within our Cu content, the former phase becomes considerable at Ti concentrations above 55 at.%, which is not our case. In addition, the presence of these peaks in Ni-rich film (N1042) also speaks in favour of Ti_4Ni_2O phase.

To explain the origin of such significant oxidation, we need to recall that the level of vacuum in the RTA furnace was relatively low (~10^{-5} Torr). As has been seen from SEM and TEM cross-sectional observations, the formation of a top oxide layer was much more pronounced for the case of RTA compared to the higher-vacuum CTA. It is also worth noting here that the RTA provoked a yellowish colour on the samples' surface. This was not observed with the CTA. The higher the temperature and time of RTA, the more intense was this yellowish colour. We ascribe it to the formation of an amorphous Ti oxide, which was observed as the layer 1 on the cross-sectional TEM image in Fig. 4.21b (however, the layer 1 contained some crystalline inclusions which were probably a different phase). We believe it to be amorphous or poorly crystalline since no XRD peaks of any crystalline Ti oxide were found.

With the increase of heat energy supplied to the samples, several new peaks appeared. Most of them can be explained by the formation of the Ni_3Ti_2Si phase, but the one at 60.0° does not fit the pattern. Also, for all the annealings, a small peak at 39.1° is left unexplained.

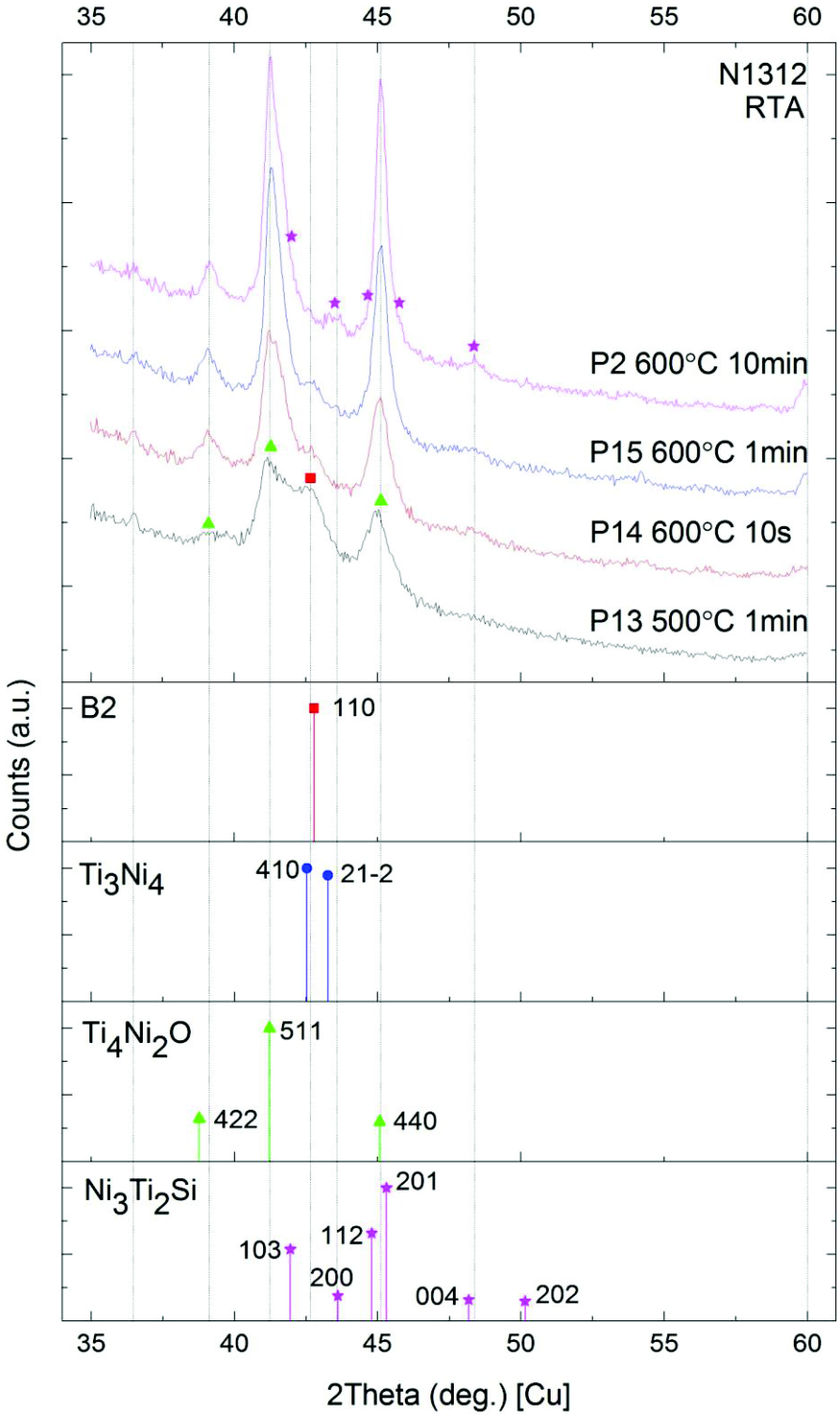

Fig. 4.25. XRD spectra of the film N1312 for the points with different annealing conditions in the RTA furnace. On the bottom of the figure, the best fitting normalized standard patterns of possible phases taken from PDF library are given (only the peaks with intensity higher than 10 % of maximal peak are shown). Dotted vertical lines are added to facilitate comparison.

Finally, we would like to mention that despite the fact of taking samples with different compositions for comparing the annealing effect, the comparison is assumed to be correct. Fig. 4.26 gives evidence that for given annealing parameters (600 °C, 10 min) all the spectra are basically the same for various compositions of the film N1312.

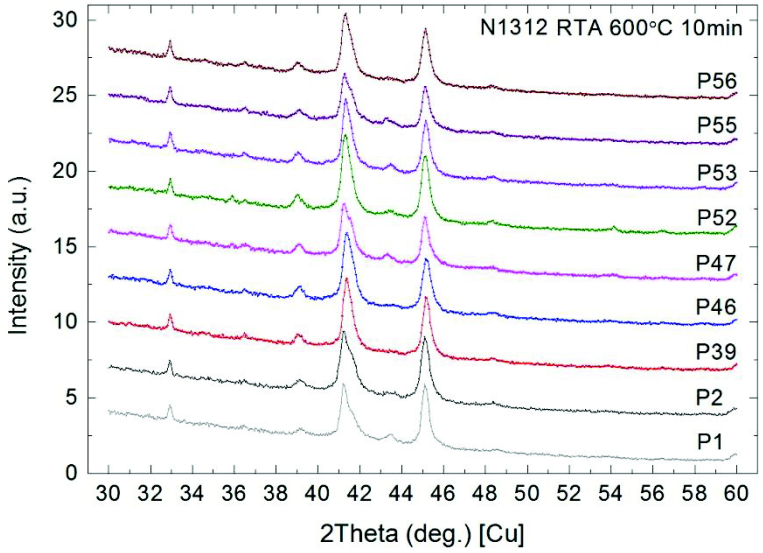

Fig. 4.26. XRD spectra of the film N1312 for the points with different compositions annealed for 10 min at 600 °C in the RTA furnace.

4.3.5.6 GIXRD of the film N1312 (target T12.4): search for a top layer

As it has been just explained in the previous part, the formation of an amorphous top oxide layer was suspected. However, it could be possible that due to its small thickness it was not observed by a regular θ/2θ XRD. In order to check this point, GIXRD was performed for the sample N1312P55 annealed in the RTA furnace at 600 °C for 10 min (the one assumed to have the thickest top layer). This method is the most sensitive to superficial layers of a material. The obtained spectrum is shown in Fig. 4.27. If we compare it with θ/2θ XRD in the Fig. 4.26 (or Fig. 4.25), no additional peaks are observed, except for a small peak at 53.6°. Peaks at ~57° are (311) reflections of Si appeared at the grazing incidence angle used. One can also notice that an unexplained peak at ~33° observed with θ/2θ XRD is not present in the GIXRD spectrum. This indicates that it could originate from the boundary layer or from the substrate.

Since no reflections of any oxide of any of Ti, Ni, Cu, Si were observed with GIXRD, we conclude that the top layer formed was amorphous. This is probably a Ti oxide since an increased AES signal on the film's surface was demonstrated for Ti.

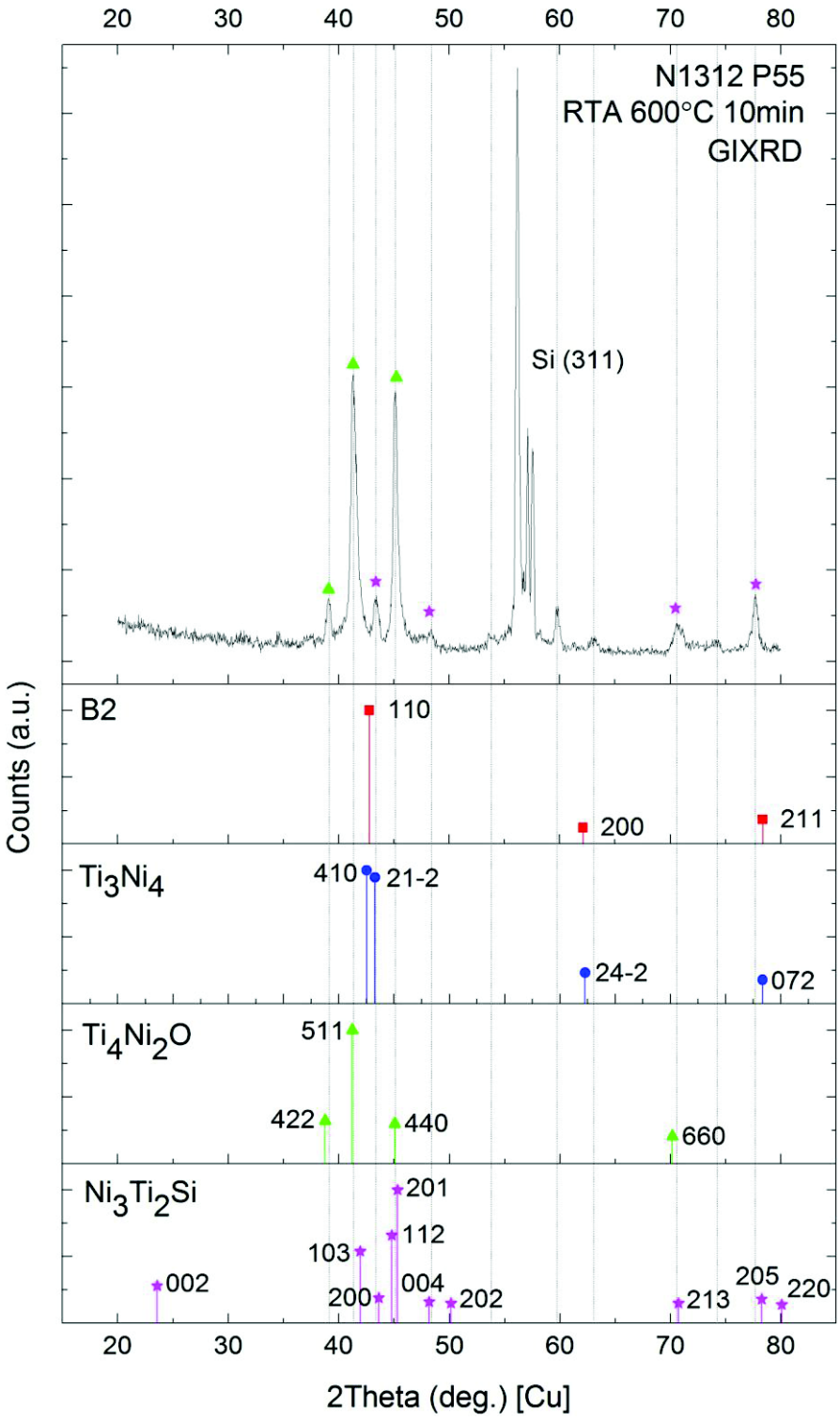

Fig. 4.27. GIXRD spectra of the film N1312 for the point P55 annealed in the RTA furnace at 600 °C for 10 min. On the bottom of the figure, the best fitting, normalized standard patterns of possible phases taken from PDF library are given (only the peaks with intensity higher than 10 % of maximal peak are shown). Dotted vertical lines are added to facilitate comparison.

4.3.5.7 θ/2θ mode at different tilt angles ψ for the film N1312 (target T12.4): search for a fibre texture and estimation of residual stress

Here we will demonstrate an absence of a fibre texture in our films. A fibre texture in a thin film is the preferential orientation of a certain lattice planes parallel to the substrate plane. This is important information for an XRD spectrum interpretation.

The tilt angle ψ varied in the range 0-63° with a 0.1 step for $\sin^2\psi$. As observed from Fig. 4.28, the spectra are basically identical for all the tilt angles, indicating the absence of fibre texture. (400) Si reflections are observed when not tilted.

Additional information that can be extracted from this measurement is a value of stresses in the sample [**147**]. As can be noticed from the figure, all the peaks shift to smaller angles when increasing $\sin^2\psi$, indicating positive film stress, i.e. tension. This result is logical since the Si substrate has a lower coefficient of thermal expansion than a metallic film, resulting in stronger shrinking of the latter at cooling after annealing.

Using Bragg's law, crystal lattice spacings d_ψ can be determined for each angle ψ for any (hkl) reflection knowing the position of the corresponding peak. It is related to the biaxial stress σ experienced by a corresponding phase in the following way [**147**]:

$$\frac{d_\psi - d_0}{d_0} = \frac{1+\nu}{E}\sigma\sin^2\psi - 2\frac{\nu}{E}\sigma, \tag{4.1}$$

where d_0 is an unstrained lattice spacing, ν is Poisson's ratio and E is Young's modulus.

Using this equation one can determine a stress value σ for a given phase, if its elastic constants are known, by plotting dψ versus sin2ψ. For example, the plot for a peak at ~78° is given in Fig. 4.29. It is easy to show that σ can be expressed through the slope α and the intercept dψo of this plot as following:

$$\sigma = \frac{E}{\nu}\cdot\frac{\alpha}{2\alpha + d_{\psi 0}\dfrac{1+\nu}{\nu}},$$

Taking the calculated slope and intercept values (given in the figure) and $\nu \sim 0.3$ and assuming $E \sim 100$ GPa, we can estimate the stress at ~700 MPa. This value is rather high and close to yield strength for most metals. We expect Young's modulus to be at least 70 GPa for our possible phases, that would give ~500 MPa of stress. This value is still rather high and in case of austenite can provoke a plastic deformation. The latter, in turn, can suppress martensitic transformation. At the same time, the value of 600 MPa was reported for a 1.7 μm thick $Ti_{51.7}Ni_{39.7}Cu_{8.6}$ film on Si/SiO_2 substrate, and this film exhibited a phase transformation near room temperature (see the literature review in [**94**]).

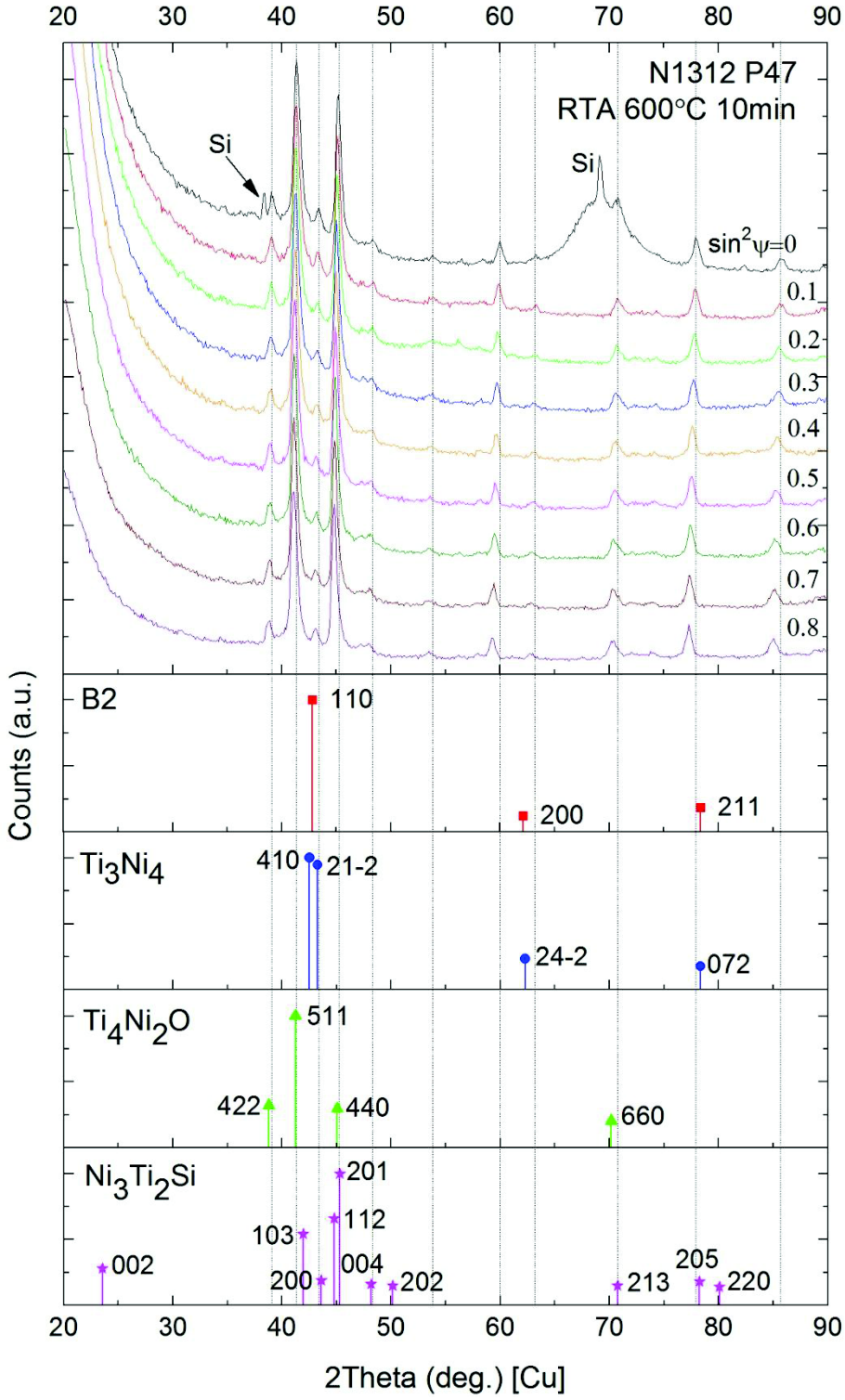

Fig. 4.28. θ/2θ XRD spectra at different tilt angles ψ for the film N1312 annealed in the RTA furnace at 600 °C for 10 min. On the bottom of the figure, the best fitting, normalized standard patterns of possible phases taken from PDF library are given (only the peaks with intensity higher than 10 % of maximal peak are shown). Dotted vertical lines are added to facilitate comparison.

Unfortunately, it was not possible to identify unambiguously the phases in our films, and we cannot know what elastic constants to take, but once the peaks are indexed, one will be able to recalculate the corresponding film stress.

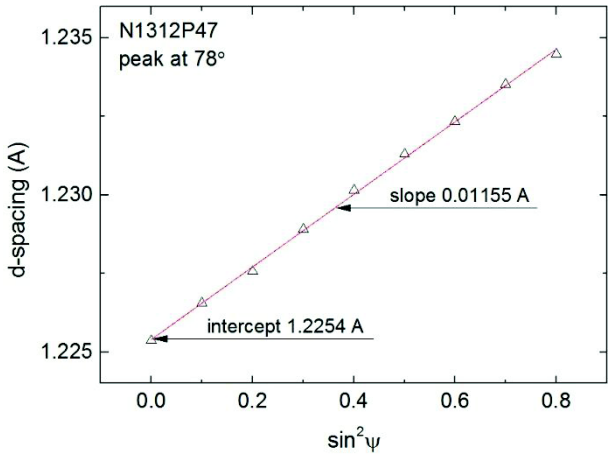

Fig. 4.29. Crystal lattice spacings as a function of $\sin^2\psi$ for the sample N1312P47. Empty triangles correspond to the values determined from the XRD measurement, the red line is a corresponding linear fit.

4.3.5.8 θ/2θ mode for the film N1446 (target T12.4): structure after high-vacuum annealing

The film N1446 was deposited with the same target as N1312, but it had thicker SiO_2 layer (1 μm vs 100 nm) to prevent possible Si diffusion when annealing. For this film, the annealing was made with another furnace, CTA2, which allowed higher vacuum (10^{-8} Torr). This furnace was believed to cause less oxidation. The XRD spectrum for the sample N1446P35 (EDX-determined composition $Ti_{44.6}Ni_{44.3}Cu_{11.1}$) is shown in Fig. 4.30. Indeed, the peaks that are believed to come from Ti_4Ni_2O are much less pronounced when compared to the case of RTA (see Fig. 4.25). On the other hand, they seem not to be very different from the case of CTA1 with the vacuum of 10^{-7} Torr (compare with Fig. 4.23).

Another observation that can be made is that the peaks that could be explained by a silicide Ni_3Ti_2Si are not observed for this sample, indicating less chemical interaction of the film with the substrate.

Two unexplained peaks at ~37.9° and ~60.0° are present on the spectrum. The former one was observed for the first time for our films.

To summarize, we cannot attribute the lower oxidation level obtained with CTA2 compared to RTA only to the level of vacuum, because other peaks also differ, including those which could be explained by a silicide. We point out two main differences for CTA and RTA furnaces used: (1) the RTA furnace has a lower vacuum causing the formation of an amorphous oxide (yellowish colour appeared); (2) higher energy supply rate with RTA causing more reaction with the substrate (SiO_2). We also remind that the real temperature of the sample annealed with RTA could be higher than the nominal one due to the temperature measurement system. Furnaces CTA1 and CTA2 do not seem to have different impact on our films.

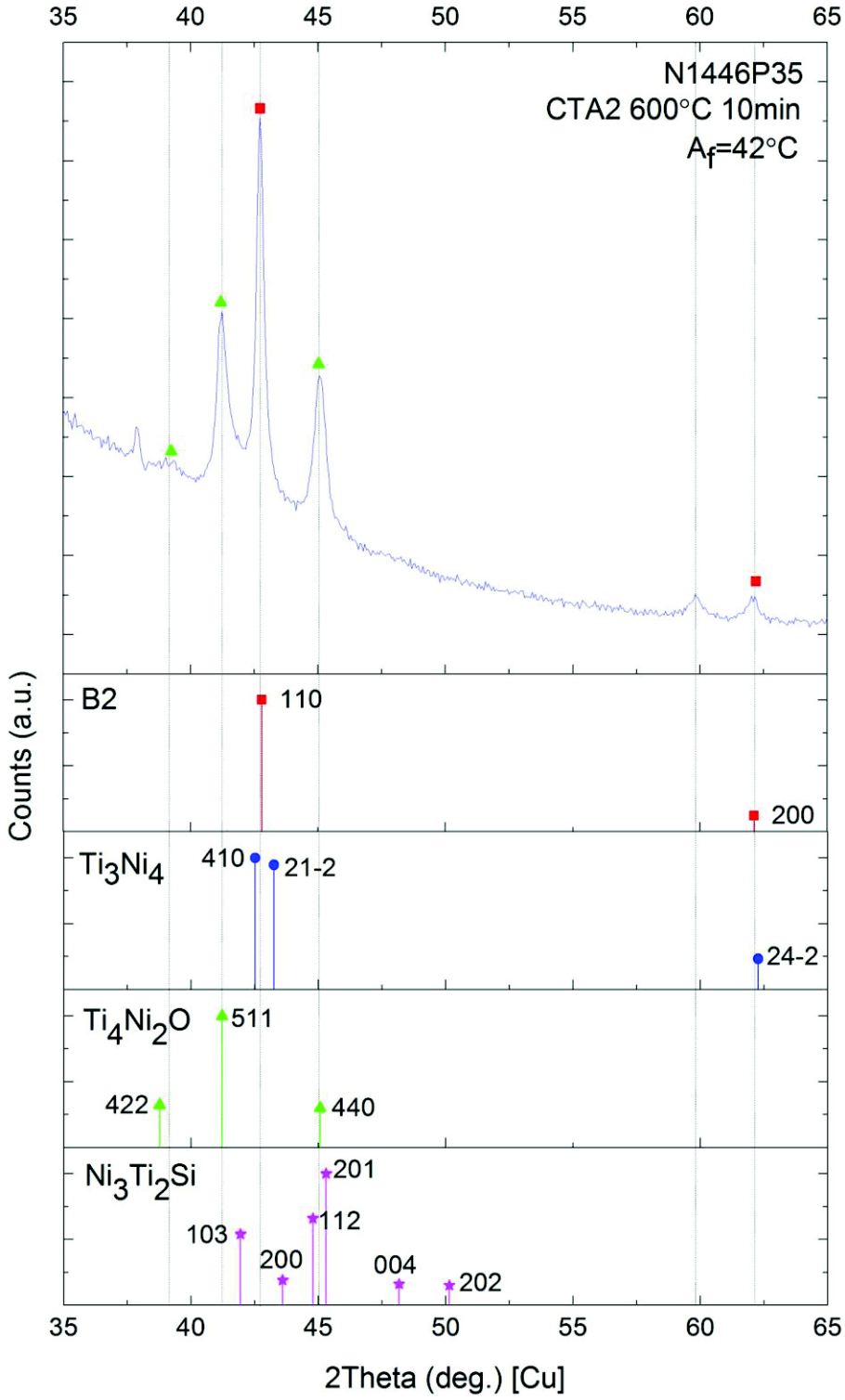

Fig. 4.30. XRD spectrum of the sample N1446P35 annealed in CTA2 furnace (~10^{-8} Torr) at 600 °C for 10 min compared with the standard patterns of possible phases. A_f is the austenite finish temperature determined by R(T) measurements.

4.3.5.9 XRD: summary and conclusions

1. XRD measurements were performed for as-deposited and annealed samples of Ti-Ni-Cu films with different compositions. The obtained experimental spectra were compared with standard patterns of expected phases. The work [**93**] was used as a comprehensive overview of Ti-Ni(-Cu) system possible phases. Phase identification was realized firstly in "semi-manual" mode using "HighScore" software (PANalytical) and PDF-4 database for all possible compounds of Ti, Ni, Cu, Si and O. For those phases which were reported in literature "manual" comparison was done also. If a standard pattern did not exist in PDF-4, it was calculated using "PowderCell" software and literature data.
2. Experimental spectra were complex and not trivial to analyse. Complicating features included superposition of peaks and the presence of a substrate signal. The studied system was complex intrinsically due to numerous components and to a multitude of possible reactions with the substrate and the air.
3. As-deposited films were amorphous. Annealings for 10 min at 600 °C in CTA furnace and above 1 min at 500 °C in RTA furnace led to film crystallization.
4. XRD spectra of a given annealed film did not vary significantly within the compositional spread of that film.
5. The most probable indentified phases in annealed films included: B2 austenite, Ti_3Ni_4 Ni-rich compound for Ni-rich films, Ti_4Ni_2O Ti-rich oxide (having an identical pattern to Ti_2Ni). Ni_3Ti_2Si Ni-rich ternary silicide fitted the spectra satisfactory. However, for all the spectra some minor peaks were left unexplained.
6. The quantity of Ti_4Ni_2O in the films seems to be too high to be explained just by residual oxygen in the furnace. It could happen that as-deposited films were already oxidized during sputtering. Depth chemical analysis sensitive to oxygen would examine this hypothesis.
7. XRD(T) showed the absence of martensite phases at room temperature in the film N1042. However, other researchers [**94**] observed a phase transformation above room temperature at these same compositions. We ascribe it to a high quantity of secondary phases formed due to a reaction with the substrate, which could shift the transition to lower temperatures. Low temperature measurements (XRD/electrical resistance/DSC/etc) are needed to examine the existence of the transition in the alloys below room temperature.
8. XRD with a varying tilt angle showed the absence of texture in the films. The misfit of experimental and standard intensities is believed to be due mainly to a superposition of coincident peaks.
9. The method of $\sin^2\psi$ showed that the film N1312 is stressed positively (tension). It is quite expected considering the difference of thermal expansion coefficients. For one of the reflections, the value of the stress was estimated at ~500-700 MPa if Young's modulus is

~70-100 GPa. This stress value is consistent with others work and was demonstrated for "working" shape memory Ti-Ni-Cu films. Nevertheless, we consider it as rather high and close to the austenite yield point. Possible plastic deformation can hinder or even suppress martensitic transformation.

10. GIXRD did not show the formation of any top layer in the film annealed with the RTA. On the other hand, a thin top layer was observed in TEM and the surface turned yellowish after annealing. A supposition can be made that this top layer is an amorphous Ti oxide (with the inclusions of another phase), which is in accordance with the literature [**94**].
11. XRD for the samples with different parameters of RTA showed that the higher the temperature of RTA and the longer the annealing time, the less of the austenite and the more of the oxide is present in the samples. For the same nominal annealing time and temperature, oxidation was more pronounced for RTA compared to CTA. This is ascribed to the following reasons: (1) lower vacuum at RTA; (2) more intensive reaction with the substrate due to higher heat energy supply with RTA; (3) possible underestimation of the sample's actual temperature in the RTA furnace.
12. A confirmation of XRD phase identification should be made by Selective Area Electron Diffraction, which should allow obtaining an independent pattern for each phase.

4.3.6 Phase transformation properties – temperature-dependent electrical resistance measurements (R(T))

While XRD(T) allows the detection of structure change and the determination the crystal structures, it is not convenient for measurement of transition temperatures. For the latter task, electrical transport measurement is a more convenient technique. It is highly sensitive to any structural changes, rather simple to perform and can be realized in automatic mode.

4.3.6.1 Film N1042 (unmodified target): searching for a phase transformation above room temperature

In the previous subsection, XRD(T) showed an absence of phase transformation above room temperature in the film N1042. The sample N1042P22 was selected for R(T) since it had the highest Ti/Ni ratio and therefore was expected to have the highest probability to undergo the martensitic transformation. The result of the measurement is shown in the Fig. 4.31. As seen, the R(T) dependence is nearly linear, indicating no structural phase transition in the studied temperature range, which confirms the results of XRD(T) analysis. The slight shift of the heating and cooling curves is due to a thermal inertia of the system since the rate of temperature change was rather high. One can observe

that at the beginning the heating the curve is deviated more towards low temperatures because the heating power of the set-up is not well adjusted at the beginning.

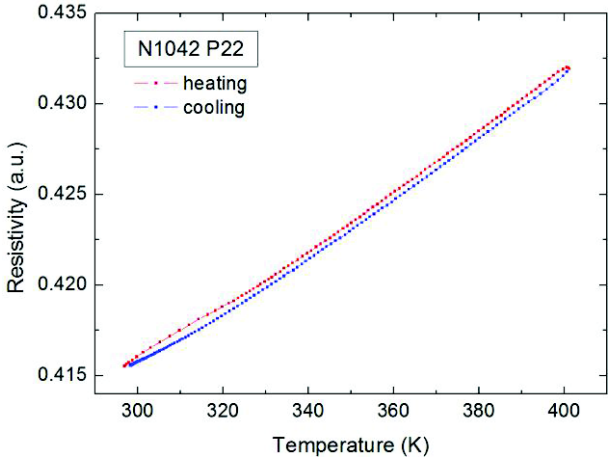

Fig. 4.31. Temperature dependence of electrical resistivity of the sample N1042P22.

4.3.6.2 Film N1446 (Ti-richest target): phase transformation near room temperature

A series of 13 samples selected from the right half of the film N1446 and annealed in the high-vacuum CTA2 furnace was studied by R(T) measurements above room temperature (18-21 °C). Some of the samples were also studied using a cryogenic set-up allowing measurements from ~4 K up to 50 °C. Typical R(T) curves obtained with both set-ups are shown in Fig. 4.32, on the example of the sample N1446P35, which was measured to have the highest transformation temperatures. As can be observed, starting from a certain low temperature the resistance begins to decrease at heating and then at another point the R(T) function comes back to its normal almost-linear increasing behaviour. The first temperature is called austenite start temperature A_s and the second is austenite finish A_f. As can be noticed, heating and cooling curves almost coincide, indicating the R-phase martensite as a low temperature phase, which is usually observed for Ni-rich films [**94**]. Transformation to R-phase is characterized by low lattice distortion and as a consequence small hysteresis.

We should explain here the convention we used for the characteristic temperature determination. Usually, the so-called tangent method is used, consisting in plotting tangent lines: one for the part of the curve corresponding to the monophase region and another for the transition part of the curve. The temperature at which the intersection of the two tangents takes place is taken as the characteristic temperature. However, as can be seen from Fig. 4.32, it is not clear at which point one should take the tangents. It will depend on how large is the range of measurement temperatures, since "linear" monophase regions are not perfectly linear. In order to have an objective method, it was decided to take the minimum and maximum of the curve as the characteristic points. Austenite finish temperature A_f determined in such a way with both set-ups was found to be the same to within 2 °C, as

seen on the figure. The transformation interval for all the samples was quite large, ~70 °C, which may be related to a possible chemical inhomogeneity of the sample.

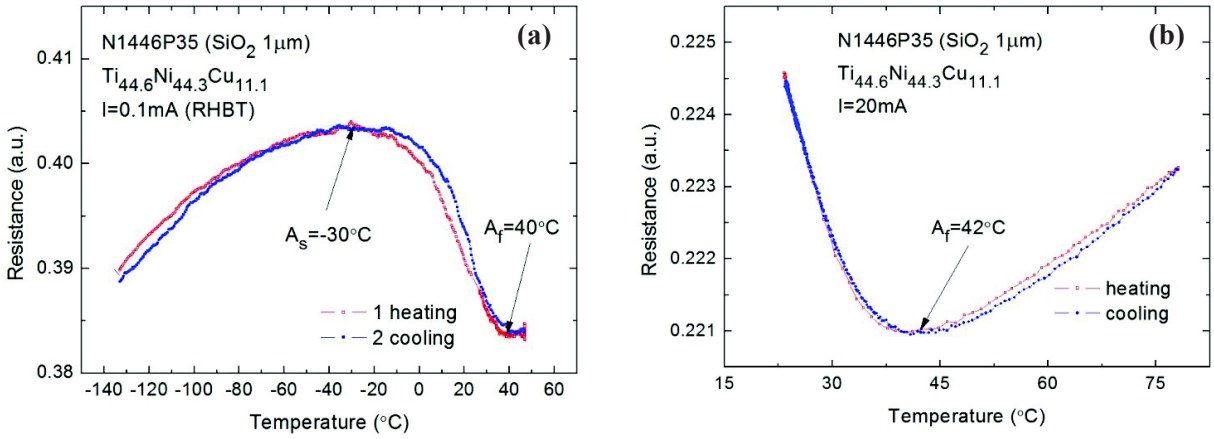

Fig. 4.32. Typical R(T) curves obtained with (a) cryogenic set-up and (b) elevated temperature set-up.

Measured A_f values were put on the ternary plot in Fig. 4.33 as a function of composition. As seen on the figure (a), the observed values vary from 27 to 42 °C, which is in a good agreement with

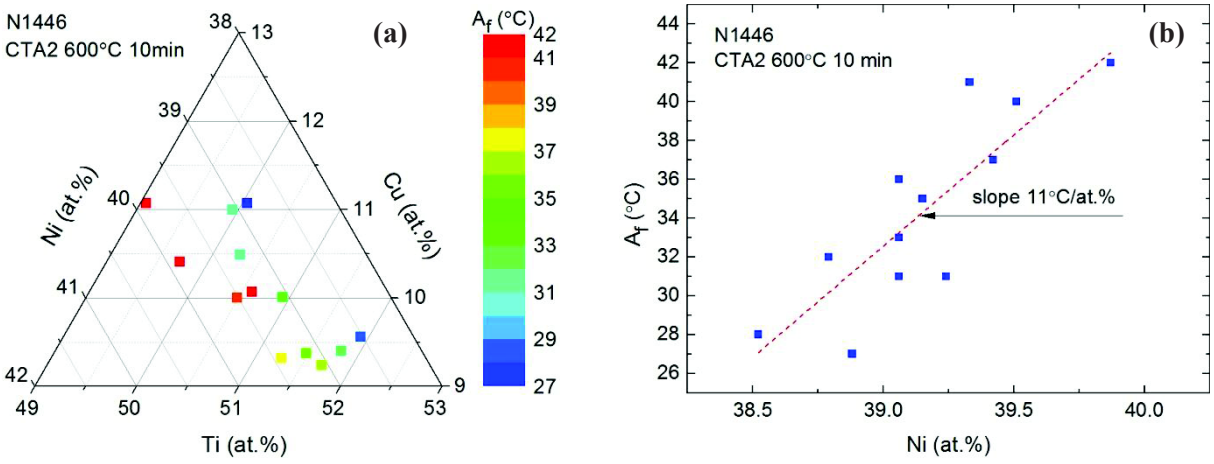

Fig. 4.33. Austenite finish temperature of the film N1446 as a function of composition: (a) put on a ternary plot; (b) plotted versus Ni content. The composition given was measured by EDX and corrected using RBS data.

the work [**94**] for the R-phase region. On the other hand, in that work: (1) such a large variation of A_f was observed for a larger variation of composition; (2) at the same compositions, the type of martensite was not R-phase, but B19 or B19'. Unfortunately, we do not know the actual composition of the transforming phase neither in our case nor for the work [**94**], so a correct comparison becomes problematic. Another possible reason of different transformation path may concern grain size. It was shown in [**148**] that transformation to B19' is suppressed when the grain size is below 60-150 nm, and

R-phase appears instead. As can be estimated from TEM images in Fig. 4.20, the grain size in our samples was ~100 nm, so the suppression of B19' could possibly take place.

Among all the parameters, such as Ti, Ni and Cu contents, Ti/Ni ratio and film thickness, the A_f value was found to correlate only with the Ni atomic concentration. The corresponding plot is shown in figure (b) and it is seen that the A_f increases linearly with increasing the Ni content with a rate of ~11 °C/at.%. This is an interesting result since the general trend is opposite [**94**]. However, the general trend characterizes a large compositional area, and we believe it might happen that within a small part of this area the dependence can be different. More measurements should be made in order to have more experimental points to confirm this result.

4.3.6.3 R(T): summary and conclusions

1. The measurement of electric resistance of samples as a function of temperature was performed using 2 set-ups: the high-temperature one operated above room temperature and the cryogenic one operated below. The latter had a possibility to heat up to ~50 °C and allowed determining of both transformation start and finish temperatures, but measurement preparation was more complicated and the measurement was more time-consuming. For most of the samples, only A_f was determined.
2. The absence of the transformation above room temperature was confirmed for the film N1042.
3. The film N1446 showed R(T) curves typical for phase transformation.
4. This transformation did not exhibit any hysteresis and was therefore ascribed to the R-phase path. However, a direct technique is needed to confirm this (e.g. low temperature XRD). Other researchers reported different transformation path for these compositions, but the path can depend also on the grain size.
5. A_f varied from 27 to 42 °C. These values are consistent with other works on the R-phase, but in our case the variation takes place within a narrower compositional region. However, a correct comparison is difficult since the transformation temperatures depend not only on the film composition itself but also on the microstructure and on the nature of other phases present.
6. A_f was found to increase linearly with Ni atomic concentration with a rate of ~11°C/at.%. This is opposite to the generally observed dependence, but it was obtained for a rather narrow region of Ni concentrations. More experimental points for a wider region are needed to confirm this result.

4.4 Summary and conclusions

1. Ti-Ni-Cu thin films were fabricated by triode sputtering from a single alloy target. Intrinsic inhomogeneity of the sputtering system was taken as an advantage to produce compositional spreads and to implement a "quasi-combinatorial" approach. This approach allowed us to obtain a variation of few at.% for the component elements. This, in turn, allowed the measurement of the dependence of the transformation temperatures versus the composition on a single wafer. A possible disadvantage of our "quasi-combinatorial" approach is a variation of the film's thickness, which may influence the film's properties and thereby complicate the analysis.
2. Ti concentration in the film was be adjusted by adding pieces of pure Ti to the target. Within the studied range, the Ti concentration was found to depend linearly on the part of the target's surface covered with Ti. This is convenient from a technological point of view.
3. A problem of composition irreproducibility due to "parasitic" sputtering was experienced. It is believed it can be minimized by taking a larger target, which would have a higher sputtering rate.
4. The evolution of the films' composition and microstructure upon annealing was studied by AES, SEM and TEM. A drastic difference between RTA and CTA was revealed and ascribed to: (1) different kinetics of the heat energy supplied to a sample; (2) different base pressure; (3) possible underestimation of the sample's temperature in the RTA furnace. The relatively low vacuum of the RTA furnace makes its use for our films delicate.
5. Relying on AES, SEM and TEM results and on visual observations, we believe that 30-70 nm of Ti oxide are formed as a top layer at annealing. Relying on literature data and on our XRD measurements, we believe this oxide to be amorphous.
6. Formation of ~70 nm bottom layer and ~170 nm top layer (below amorphous Ti oxide) was observed by TEM for the case of RTA, but not for higher-vacuum CTA. Relying on our XRD results and the literature data, we believe it to be Ti_4Ni_2O oxide formed due to a reaction with residual oxygen in the furnace (top layer) and with SiO_2 layer (bottom layer) for both cases of RTA and CTA.
7. XRD-based phase identification was made, but SAED is needed to confirm the results. Analysis of XRD patterns was complicated by superposition of peaks and a multitude of possible phases. Some minor peaks were not identified.
8. One of the films with the highest Ti concentration was analysed by temperature-dependent resistance measurements and it was shown to exhibit a phase transformation. Since this transformation did not have hysteresis, relying on literature data, the martensite is believed to be R-phase, but a more direct technique is needed to confirm this.

9. Within the studied range of compositions, the austenite finish temperature A_f was found to increase linearly with Ni atomic concentration, which contradicts the general trend reported in literature. However, since it was reported for a large compositional region, we believe it possible that for the narrow range we studied here the dependence can be different. More measurements should be made to confirm this result.
10. Fabrication of shape memory thin films was successful. Unfortunately, no time was left to examine their actuation properties, which is indispensable to demonstrate their usefulness for energy harvesting applications.

5 Fabrication of Ti-Ni-Cu-based micro-structures

5.1 Introduction

One of the objectives of this work is to develop a fabrication method for a Ti-Ni-Cu micro-actuator which would be able to apply a mechanical stress to other functional layers, more specifically piezoelectric in our global energy harvesting context. In order to achieve this, it is logic to start with a simple bimorph actuator comprised of a Ti-Ni-Cu layer coupled to any convenient elastic material, prior to the next step, which would be the addition of another functional layer (PZT).

A functional harvester will require the patterning of the Ti-Ni-Cu layer into a suitable configuration, such as membranes, bridges and cantilevers, which imply through holes in the wafer. However, a patterning of this alloy is not simple: (1) the layer was deposited at elevated temperatures, thus making delicate the use of lift-off method (deposition on patterned polymers); (2) wet-etching requires the use of HF which is restricted at our facility. These issues will be discussed in detail in corresponding sections.

Prior to dealing with the patterning of Ti-Ni-Cu films, we present first a simple membrane structure that will help monitor how film properties evolve with microfabrication. In [**120**], a bimorph membrane Ti-Ni-Cu/SiO_2 was fabricated using thin film deposition and micro-patterning technologies, and it was experimentally proved to show a repeatable thermally controlled actuation. Inspired by this work, the fabrication of such a structure was realized in our clean room.

5.1.1 Cleanroom equipment

Fabrication of Ti-Ni-Cu-based micro-structures has been developed at PTA (CEA Grenoble), which is a clean room equipped for using of up to 100 mm wafers. The following equipment was used there:

1. chemical benches for spinning, drying, development and stripping of photoresists, etching of metals, cleaning and drying of chromium masks;
2. SUSS MicroTec MJB4 UV365 manual aligner photolithography system for ultra-violet (UV) exposure and mask alignment;
3. Veeco Dektak 150 profilometer;
4. Leica optical digital microscope with a magnification of up to ×100;
5. Plassys MEB400S electron beam evaporator for deposition of Al, Cr and Ni;
6. Tegal 915 reactive ion etcher with high pressure O_2 plasma for elimination of residual polymers.

Ti-Ni-Cu layer was deposited by triode sputtering at Institut Néel (Grenoble).

5.2 Fabricated test membranes

5.2.1 Procedure, results and discussion

As a proof of concept, large bimorph membranes were fabricated (Fig. 5.1). This was a simple process since only one lithography step was needed to pattern the Si wafer. Openings with vertical walls were etched from the back side by deep reactive ion etching (deep RIE), using the SiO_2 layer as etch stop layer. The pattern was an array of 5 x 5 mm squares, with 5 mm gaps in between. The main steps of the procedure were as follows.

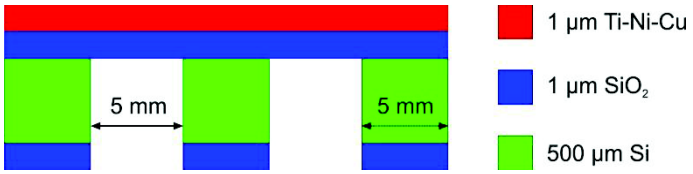

Fig. 5.1. Scheme of bimorph membranes fabricated in this work.

1. Sputter-deposition of ~1 µm Ti-Ni-Cu layer (triode system) onto a SiO_2/Si (1 µm / 500 µm) wafer and its posterior vacuum annealing.
2. Back side sputter-deposition of ~200-300 nm Al mask layer ("Nordico" system).
3. Photolithography of AZ1512 resist.
4. Al etching and resist stripping.
5. Cleaving the wafer in 4 parts and mounting a sample onto the deep RIE system wafer sample holder with vacuum water-solvent grease.
6. Back-side SiO_2 layer plasma etching and deep RIE Si etching using standard parameters (etching 8 s / passivation 3 s): ~50 min for 500 µm of Si.
7. Detaching the sample in a hot plate (~60 °C) and front side cleaning (gentle wiping with moist cleanroom paper).

Fig. 5.2 shows an SEM image of one of the fabricated membranes. The internal wall is not perfectly vertical, which is normal for fast Deep RIE processes. Also, for this membrane the SiO_2 layer was not reached during etching (residual Si thickness ~30 µm).Each membrane was observed to be quite homogeneous in thickness. However, depending on the position on the sample, membrane thickness was variable. The etching depth was maximal close to the sample holder's centre, and minimal at the borders. For example, the membrane shown was ~30 µm thick, but for those at the centre, SiO_2 layer could be clearly observed through the openings. Since deep RIE is known to be non-uniform at a wafer scale [**149**,**150**], this was to be expected. Dummy structures can be added to the final process mask to minimize these effects [**151**]. It is worth noting that none of the membranes broke at the fabrication.

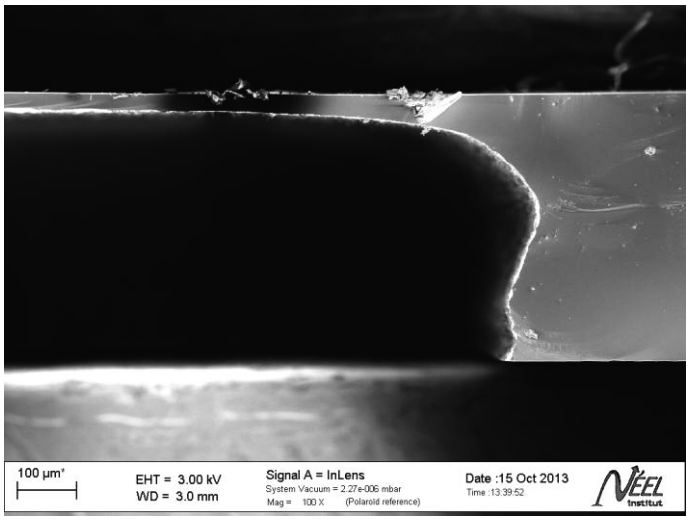

Fig. 5.2. SEM image of one of the fabricated membranes.

To test possible changes in functional properties of the Ti-Ni-Cu layer after DRIE, temperature-dependent resistance measurements were made both for the membranes and corresponding unpatterned samples with a close composition of the Ti-Ni-Cu layer. The wafer was cleaved with a manual micro-cleaving machine so as to separate each membrane. Most membranes (roughly 95 %) remained unbroken after this procedure and four of them were chosen for measurements.

A typical result is shown in Fig. 5.3. The film on the membrane still exhibited a phase transformation, and the A_f temperature did not change significantly. Thereby, the functional properties were mostly unchanged after the patterning procedure, which is an important result from a technological point of view. The observed difference in resistance and current values is conditioned by set-up modifications made between the two measurements.

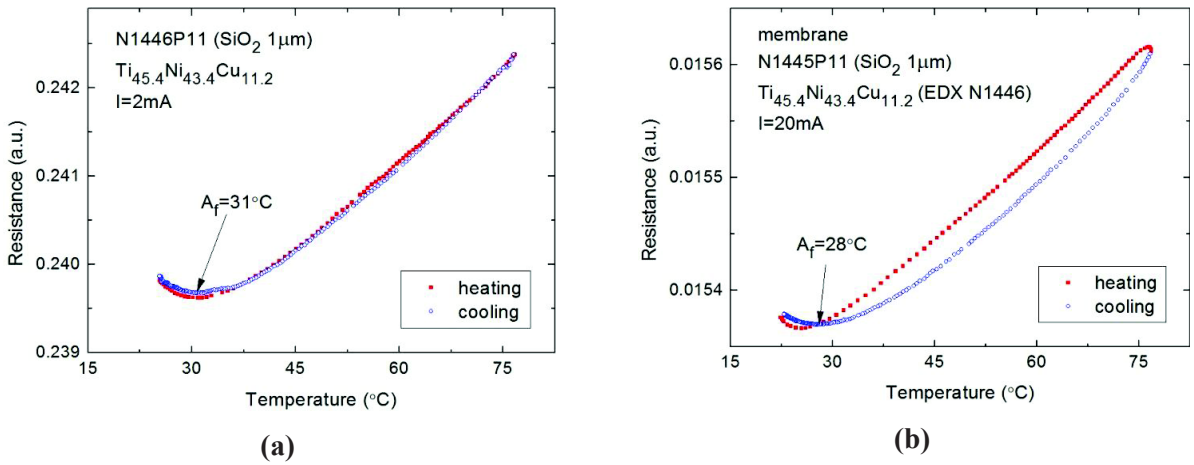

Fig. 5.3. Temperature-dependent resistance measurements of (a) a Ti-Ni-Cu film on unpatterned substrate vs. (b) a corresponding membrane (with the Ti-Ni-Cu layer of close composition).

However, the measurements on the same membranes with a cryostat system did not work properly, probably because some non-conductive superficial layer remained after fabrication. This was either a residue of the vacuum grease used for mounting the sample or a superficial layer formed during fabrication. This was not a problem for high temperature measurements because the sharp probes of the set-up are pressed mechanically and are able reach beyond a superficial layer (however, the probes did not break the membranes), while for the cryostat systems the contacts are simply glued to the surface with a silver paste. The surface resistance was simply measured with a multimeter at ~MΩ scale, while the unpatterned samples have typically shown ~Ω values. We tried various cleaning methods to get rid of this superficial residual layer. Simple exposure to hot water (60 °C), acetone, ethanol, 3-Cl-ethylene, 2-Cl-methane and RBS® T305 detergent for up to 24 h was not effective. Neither was wiping anew with cleanroom paper in 60 °C water. Finally, a 10 second exposure firstly to 3-Cl-ethylene and then to RBS with simultaneous ultrasound agitation (45 kHz, 40 % power, normal sweep mode) led to a decrease of the samples' resistance down to ~2 Ω. However, many of the membranes (especially the thinnest ones) broke because of the ultrasounds. Manual wiping with cotton buds was also effective for cleaning, but it was not better in terms of membrane damage. Surprisingly, even the cleaned samples turned to be non-conductive again on the next day, preventing the cryostat measurements. We conclude that there is an issue with non-intrusive electrical contacts most probably due to a non-conductive superficial layer present over the Ti-Ni-Cu deposit after DRIE etching. This non-conductive layer could be either a residue of the vacuum grease used for DRIE sample holding or a surface oxidation of the Ti-Ni-Cu. It is proposed for future tests to avoid this problem by adding contact pads to the process and consider a protective layer for the front side prior to DRIE.

5.2.2 Summary and conclusions

1. A simple method of Ti-Ni-Cu/SiO_2 membrane fabrication on Si wafer was tested. The membranes were successfully fabricated and were quite robust mechanically.
2. The fabrication process did not cause remarkable changes in Ti-Ni-Cu functional properties.
3. There is an issue probably due to a non-conductive superficial layer present over the Ti-Ni-Cu deposit after DRIE etching. To avoid future problems with non-intrusive electrical contacts it is proposed to add contact pads to the process and consider a protective layer for the front side prior to DRIE.

5.3 Patterning Ti-Ni-Cu thin films

5.3.1 Introduction

As one can learn from the literature, various techniques have been used to pattern Ti-Ni-based alloy layers: wet etching [**152**,**153**,**154**,**155**,**156**,**157**,**158**,**159**], ion-milling [**154**], lift-off [**160**,**161**,**162**] and laser ablation [**163**]. Ion-milling and laser ablation are not suitable methods for 1 μm thick Ti-Ni-Cu films because the etching rate is too low. Wet etching is more suitable, but this method is known to cause a significant undercut on the patterns [**154**]. Moreover, it would require the use of HF which is restricted in our clean rooms. On the other hand, lift-off method is advantageous since it normally requires only conventional photoresists and can be applied to any other SMA once the procedure is developed. Both wet etch and lift-off methods were tested in this work.

5.3.2 Lift-off patterning

5.3.2.1 Choice of the procedure

A lift-off patterning method consists in creating an inverse pattern with one or more easy-to-pattern and easy-to-strip sacrificial materials, prior to the deposition of the goal material. Afterwards, the goal material is deposited and the sacrificial material is stripped. As a result, the goal material is "lift-off" together with the sacrificial material where this last is present on the substrate, and the desired pattern for the goal material is thus obtained. As a sacrificial material, various photoresists are usually used.

The advantage of this method is that it is almost independent on what goal material is deposited and therefore can be used for any new material without consuming time for development of a new specific physical or chemical patterning method. Moreover, it does not cause any undercut in the goal material film. However, this method is sensitive to temperature and conformity of the deposition (the edges of the sacrificial resist should not be metalized). The best results are usually obtained for room temperature non-conformal (highly directional) deposition techniques, e.g. evaporation, ion beam sputtering, etc.

When the goal material is relatively thick and/or the deposition technique is not unidirectional, a bilayer sacrificial structure is used to improve lift-off (Fig. 5.4). In this case there is an undercut, the bottom layer opening being wider than the upper layer. This allows forming a cap profile which will prevent the vertical walls of the bottom layer to be covered with the goal material and thus will allow the solvent to remove the sacrificial layer and to execute the lift-off.

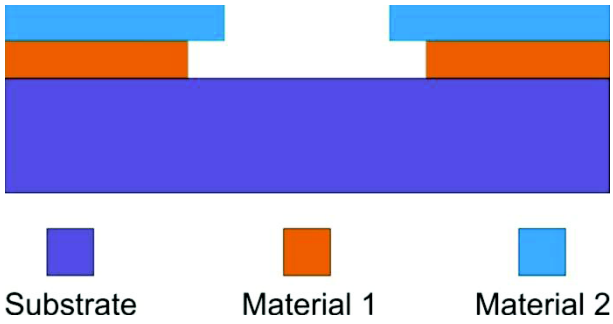

Fig. 5.4. Schematic of bilayer lift-off structure.

Several lift-off procedures for pattering NiTi SMA were found in literature. As can be seen from Table 5.1, a lift-off was used for relatively thick films, because otherwise wet etching would produce a significant undercut. Since sputter deposition led to significant heating of the substrate, the researchers used relatively thermostable materials for the bottom layer of the cap profile, such as polyimide or PMGI. PMGI is a product name and an abbreviation for polydimethylglutarimide. This product is actually a denser modification of LOR, which is also a product name and an abbreviation for "lift-off resist" [**164**,**165**]. While polyimide is more thermostable than PMGI (maximal temperature is 300 °C compared to 200 °C), its deposition is more complicated and its removing requires a process which may be not available at each clean room (hot KOH). In contrast, PMGI and LOR resists need only standard processes and standard solvents.

Table 5.1. Literature data on lift-off patterning of SMA films.

Lift-off materials (bottom/top), thickness in brackets (µm)	**Remover**	**SMA deposition**	**SMA thickness**	**Reference**
polyimide(11)/Cr(0.15)	hot KOH	DC sputtering	10 µm	[**160**]
SF11-PMGI(9.6)/SRJ5138(1.4)	not reported	DC sputtering	6-7 µm	[**161**]
SF11-PMGI(10)/Cr(0.15)	not reported	DC sputtering	8 µm	[**162**]

In this work, our own lift-off procedure has been developed. To start with, a standard lift-off procedure developed by Marie-Thérèse Delaye from CEA LETI (Grenoble) was used. The lift-off structure consisted of LOR10A as a bottom layer and AZ1512HS photoresist as a top layer. However, a strong deformation of this structure was observed after the deposition of Ti-Ni-Cu film using the triode sputtering system. It is important to note that on standard lift-off procedures, the photoresists used for the top layer are particularly sensible to temperature. As was mentioned in Chapter 4, this deformation was due to an overheating of the sample's surface because of the inefficient substrate cooling.

Before a solution of enhancing substrate cooling was found (very recently), we have been trying to increase the thermal stability of the polymers (preliminary heat treatment) and substituting of the top layer polymer for denser polymers and metals. Unfortunately, no satisfactory results were

obtained. At the same time, wafer-to-target distance and target voltage did not have significant influence on the temperature. The use of thermal conducting grease to improve the wafer cooling was impossible due to the risk of system pollution and vacuum stability.

Finally, a structure of Al (bottom layer) and Ni (top layer) was found to have sufficient thermal stability. However, the complexity related to its fabrication and especially the removing of the sacrificial layers (lateral etching of Al is rather low with any etchant) became close to that of the SMA wet etching procedure, performed with a mixture of HF and HNO_3. With the recent changes made to the sputtering machine to avoid excessive substrate heating, easier bilayer photoresist cap profiles should be reconsidered for future work.

The detailed description of the procedures and the results of the tests are given below.

5.3.2.2 Procedure LO1: LOR10A/AZ1512HS

The procedure LO1 consisted of the following steps.

1. Cleaning of 100 mm Si wafer surface with acetone, ethanol, IPA.
2. Dehydration: drying for 20 min at 200 °C.
3. Spinning LOR10A at 4000 rpm, 60 s, 2000 rpm/s. Drying at 200 °C for 5 min.
4. Spinning AZ1512HS at 4000 rpm, 60 s, 2000 rpm/s. Drying at 100 °C for 1 min 30 s.
5. UV mask-exposure for 25 s. A chromium mask was used for photolithography. The pattern was an array of circles and squares with the sizes of 50-200 μm.
6. Development of both photoresist and LOR with AZ MIF326 for 1 min 30 s.
7. Washing with DI water, drying with compressed air.
8. Sputter deposition of 500 nm layer of Ti-Ni-Cu.
9. Lift-off using PG remover at 60 °C and simultaneous ultrasound agitation during 2 h.
10. Washing with DI water, drying with compressed air.

Observation with optical microscope did not reveal any defect after the photolithography (**Ошибка! Источник ссылки не найден.**). The measured size of the cap was ~1 μm. Strong deformation of the surface was observed after Ti-Ni-Cu deposition (**Ошибка! Источник ссылки не найден.**). This was due to a thermal deformation of the photoresist during the deposition.

Before the lift-off, the sample was cleaved in 4 parts for different solvent tests. The first test was made with acetone. The result of this test was negative (LOR is not compatible with acetone [**164**]). The second test was made using PG remover at 60 °C and ultrasound agitation during 2 h. The result of this test is presented in Fig. 5.7. Lift-off was successful on most parts of the sample, but some residual material was present together with the desired pattern. The edges of the pattern objects were jagged.

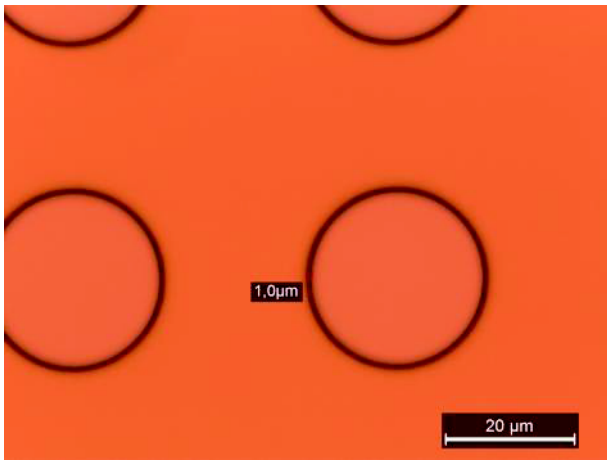

Fig. 5.5. Optical image after photolithography stage for the procedure LO1.

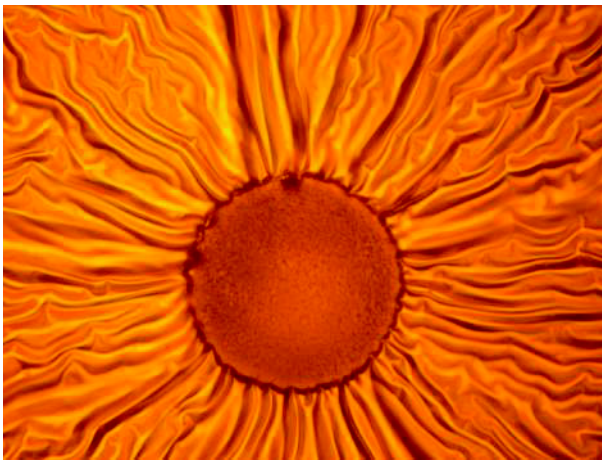

Fig. 5.6. Optical image after Ti-Ni-Cu deposition for the procedure LO1. Strong deformation of the surface is observed.

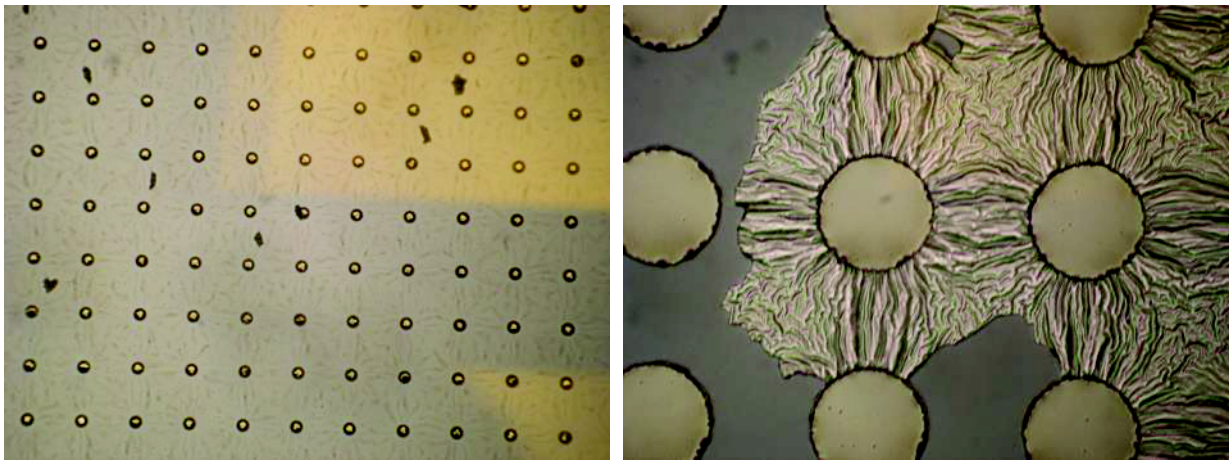

Fig. 5.7. Optical images after realizing the lift-off for the procedure LO1. Together with the pattern objects, residual material is observed on the surface.

It can be concluded for the procedure LO1 that the lift-off quality was not sufficient and the probable reason for this is an overheating of the sample during Ti-Ni-Cu deposition.

5.3.2.3 Procedure LO2: 2×LOR10A/AZ1512HS

The next idea was: (1) to add a polymerization (hard bake) step at the end of photolithography to harden the resist AZ1512HS and (2) to double the thickness of LOR by two successive spinnings. The spin rate for LOR was decreased to increase its thickness. The hard bake of AZ1512 should

increase its thermal stability and to hinder its bending down and touching the Ti-Ni-Cu layer at deposition. The procedure LO2 consisted of the following steps.

1. Cleaning of 100 mm Si wafer surface with acetone, ethanol, IPA.
2. Dehydration: drying for 5 min at 150 °C.
3. Spinning of the first layer of LOR10A at 2500 rpm, 60 s, 1000 rpm/s. Drying at 200 °C for 5 min.
4. Spinning of the second layer of LOR10A at 2500 rpm, 60 s, 1000 rpm/s. Drying at 200 °C for 5 min.
5. Spinning of AZ1512HS at 4000 rpm, 60 s, 1000 rpm/s. Drying at 100 °C for 1 min 30 s.
6. UV mask-exposure for 25 s.
7. Development of AZ1512HS with AZ developer during 1 min.
8. Development of LOR10A with AZ MIF326 during 4 min.
9. Washing with DI water, drying with compressed air.
10. Hard bake at 200 °C for 5 min.
11. Sputter deposition of 500 nm Ti-Ni-Cu layer.
12. Lift-off using AR-300-70 remover at 50 °C and simultaneous ultrasound agitation during 30 min.
13. Washing with DI water, drying with compressed air.

Observation with an optical microscope and an SEM did not reveal major defects after the photolithography (Fig. 5.8), although the top layer appears to deform slightly at the edges. The measured thickness of the bottom layer was ~2.5 µm and the cap undercut was ~3µm.

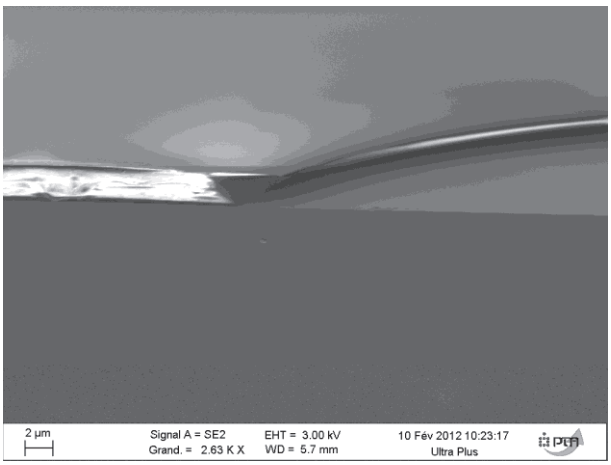

Fig. 5.8. SEM secondary electron image after the photolithography stage of the procedure LO2.

Strong deformation of the surface was observed after the Ti-Ni-Cu deposition (Fig. 5.9). First and foremost the AZ1512HS bent and touched the pattern motifs, thus removing the interest of a cap

profile. This is most likely due to the undercut size (~3 µm), obtained after a 4min development of LOR, which may be too much for our thickness. Also, the AZ1512HS photoresist was found to thin on the openings' edges probably due to an attack of the AZ MIF326. Finally, the LOR was found to become inhomogeneous in thickness: the part close to the opening swelled up. That means that apart from wrinkling of the surface, deformation happens in the whole volume of the lift-off bi-layer. This is likely due to a thermal creep of the photoresist during the sputter deposition.

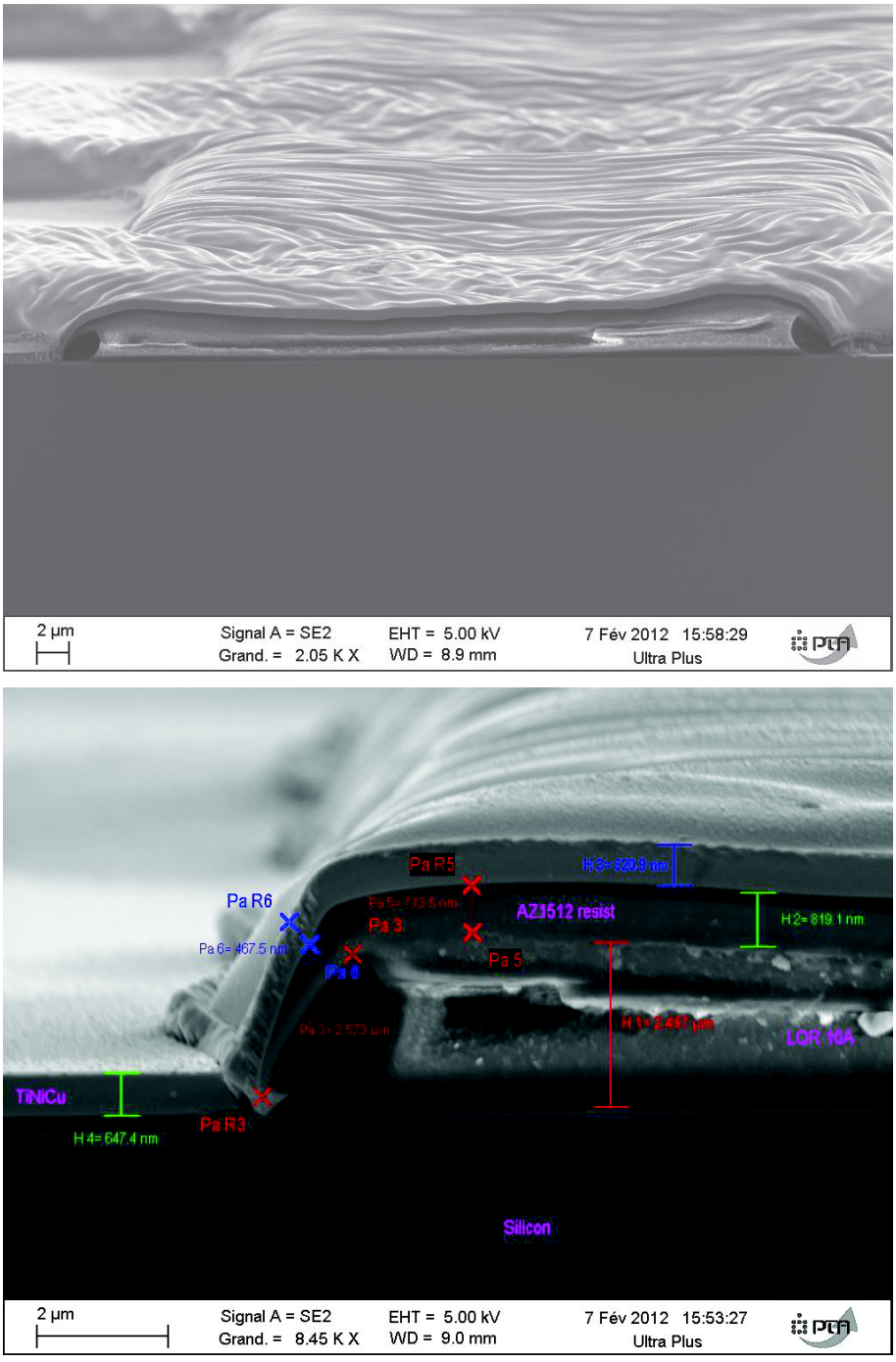

Fig. 5.9. SEM secondary electron images after the Ti-Ni-Cu deposition for the procedure LO2. Strong deformation of the surface is observed.

A test of lift-off was made on a quarter of sample using AR-300-70 remover at 50 °C with simultaneous ultrasound agitation during 30 min. As it can be seen from the optical images (Fig. 5.10), in spite of the deformation, the lift-off worked on most of the sample. However, some residual material and poor quality of the pattern edges due to the AZ1512HS folding were revealed.

It can be concluded for the procedure LO2 that the lift-off quality was not sufficient and once again the probable reason for that is an overheating of the sample during SMA deposition.

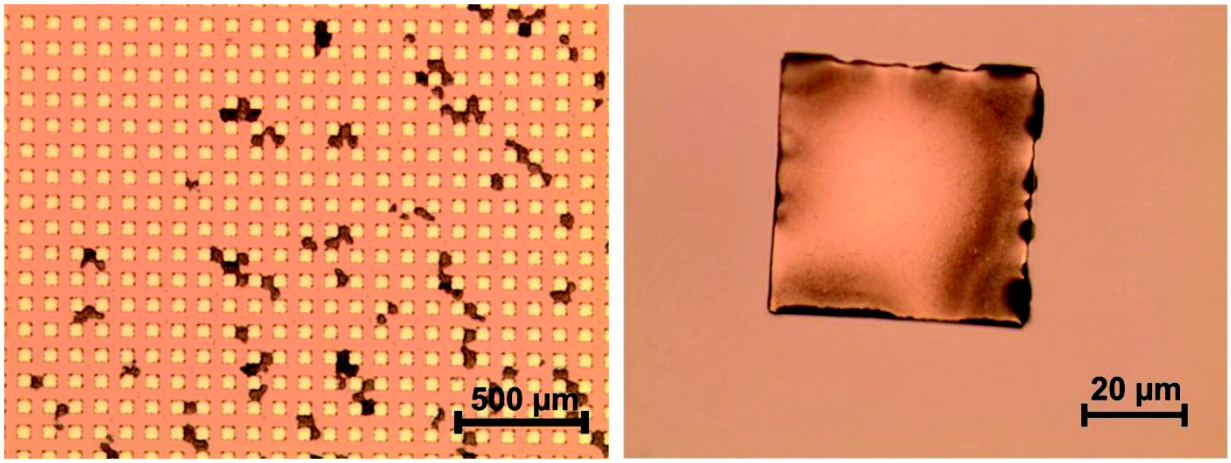

Fig. 5.10. Optical images of the pattern after lift-off stage for the procedure LO2. Some residual material and poor quality of the objects' edges can be observed.

5.3.2.4 Procedure LO3: LOR10A/AZ4562

The next idea was to use a thicker photoresist for the top layer to avoid the problem of thinning at the opening edge. To avoid excessive cap profile undercut, it was decided to leave only one layer of LOR. Also, the time of LOR development with AZ MIF was reduced down to 3 min. The procedure LO3 consisted of the following steps.

1. Cleaning of 100 mm Si wafer surface with acetone, ethanol, IPA.
2. Dehydration: drying for 5 min at 150 °C.
3. Spinning of LOR10A at 1000 rpm, 30 s, 200 rpm/s. Drying at 200 °C for 5 min.
4. Spinning of AZ4562 at 4000 rpm, 30 s, 2000 rpm/s. Drying at 100 °C for 2 min (with the progressive heating from 90 to 100 °C).
5. UV mask-exposure for 120 s.
6. Development of AZ4562 with AZ developer during 3 min. Drying 2 min at 110 °C.
7. Development of LOR10A with AZ MIF326 during 3 min.
8. Washing with DI water, drying with compressed air.
9. Hard bake: 1 min at 90 °C, 1 min at 110 °C, 1 min at 130 °C, 5 min at 150 °C.

10. Sputter deposition of 500 nm layer of Ti-Ni-Cu.
11. Lift-off using AR-300-70 remover at 50 °C and simultaneous ultrasound agitation during 30 min.
12. Washing with DI water, drying with compressed air.

Observations with an optical microscope and an SEM did not reveal any defect after the photolithography (Fig. 5.11 and Fig. 5.12). However, the strong thinning of the photoresist was observed near the openings. This was probably due to the hard bake.

Once again, a strong surface deformation was observed after the Ti-Ni-Cu deposition (Fig. 5.13). It can be observed that the cap profile was no longer observed and the Ti-Ni-Cu layer formed a continuous layer on the entire substrate surface. The reasons for this are twofold: first of all, an excessive undercut combined to the top photoresist thinning led once more to the cap folding. Also, the LOR layer, about twice as thick as the Ti-Ni-Cu deposit, may have not been thick enough for the excessive undercut obtained. This led to unsatisfactory lift-off results (Fig. 5.14). It was observed that the pattern objects were partly gone from the substrate and their edges were of poor quality.

It can be concluded for the procedure LO3 that the lift-off quality was not sufficient and the probable reason for that is an excessive undercut for the used LOR thickness, which combined with the overheating of the sample during SMA deposition led to a complete folding of the cap profile.

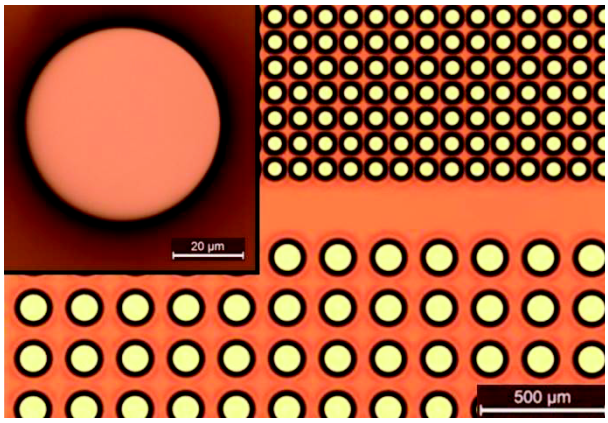

Fig. 5.11. Optical images after the photolithography step of the procedure LO3.

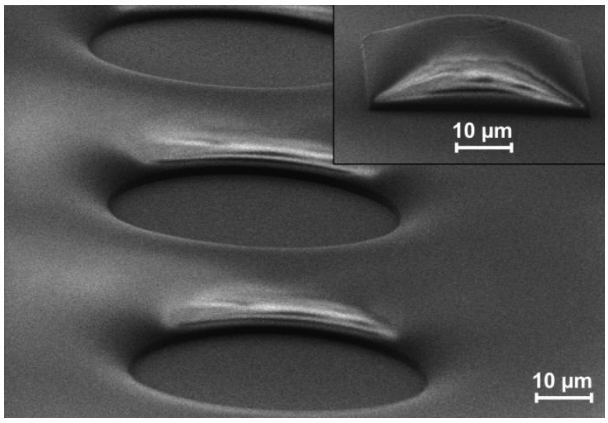

Fig. 5.12. SEM secondary electron images after the photolithography step of the procedure LO3.

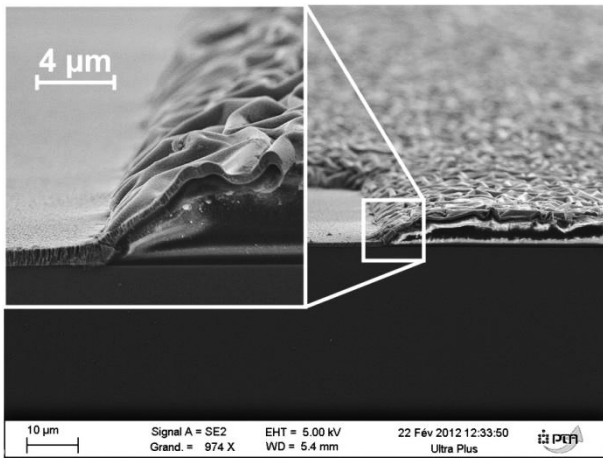

Fig. 5.13. SEM secondary electron images after the Ti-Ni-Cu layer deposition for the procedure LO3.

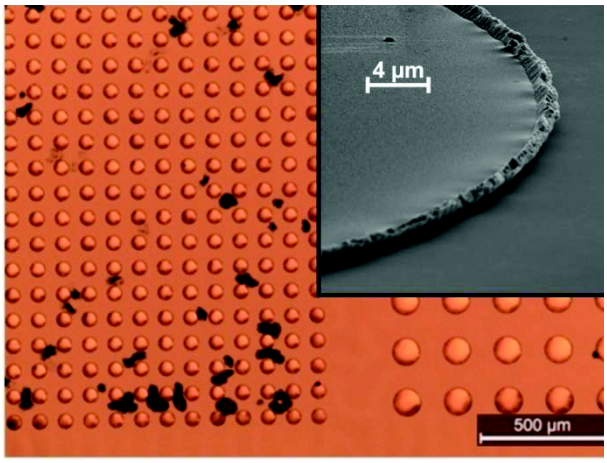

Fig. 5.14. Optical image after the lift-off step of the procedure LO3. Inset: SEM secondary electron image of the same sample showing the edge of the final pattern.

5.3.2.5 Procedure LO4: 2×LOR10A/AZ4562

Since for the previous procedure LOR seemed to be not thick enough given the obtained undercut, for the current procedure it was decided to double the thickness. In addition, the deposition of the Ti-Ni-Cu layer was done on the entire wafer and not on the quarter of the sample, as it was done in all the previous cases. This may reduce thermal problems, because when the deposition is done on a piece of a wafer, an intermediate wafer is placed between the sample's part and the substrate holder (to protect the latter). An intermediate wafer could result in a deterioration of the thermal conductance, leading to additional increasing of the sample surface temperature. The lift-off was performed also for the entire sample. This could slow the process compared to the previous cases, since in a cleaved sample the remover has additional access to the resist through the sample side. The procedure LO4 consisted of the following steps.

1. Cleaning of 100 mm Si wafer surface with acetone, ethanol, IPA.
2. Dehydration: drying for 5 min at 150 °C.
3. Spinning of the first layer of LOR10A at 2500 rpm, 60 s, 1000 rpm/s. Drying at 200 °C for 5 min.
4. Spinning of the second layer of LOR10A at 2500 rpm, 60 s, 1000 rpm/s. Drying at 200 °C for 5 min.
5. Spinning of AZ4562 at 4000 rpm, 30 s, 2000 rpm/s. Drying at 100 °C for 2 min (with progressive heating from 90 to 100 °C).
6. UV mask-exposure for 120 s.

7. Development of AZ4562 with AZ developer during 3 min. Drying for 2 min at 110 °C. The step value measured by a profilometer after this stage was 6.1 µm, which is a proper value.
8. Development of LOR10A with AZ MIF326 during 2 min 45 s. The step value measured by profilometer after this stage was 8.3 µm. It gives a value of LOR double layer of 2.2 µm, which was the desired thickness.
9. Washing with DI water, drying with compressed air.
10. Hard bake: 5 min at 200 °C (with a progressive heating during ~5 min from 136 °C). The step value measured by profilometer after this stage was 7.7 µm. That means this operation led to the shrink of the polymers by ~0.6 µm.
11. Sputter deposition of the 500 nm Ti-Ni-Cu layer.
12. Lift-off using AR-300-70 remover at 50 °C during 30 min and then at 20 °C during 10 min with ultrasound agitation.
13. Washing with DI water, drying with compressed air.

Observations with an optical microscope did not reveal any defect after the photolithography (Fig. 5.15). Since in our clean room there was no tank for a 100 mm sample allowing to heat and to apply an ultrasound simultaneously, those two steps were performed one after the other. So, firstly the sample was immerged into the hot remover without any agitation for ~30 min. Almost no sign of lift-off was observed visually after this procedure. Then the sample was held in the ultrasound tank for ~10 min. No significant improvement was observed after this step. Optical microscopy (Fig. 5.16) showed that the Ti-Ni-Cu was partly removed at some regions, but even there some residual layer of the polymer remained (a dark region on the image). These difficulties point once more to a folded cap. Clearly, the top photoresists of the AZ series used for the bilayer do not withstand the deposit temperatures of the triode and the cap profile systematically folds compromising the lift-off procedure despite several tests.

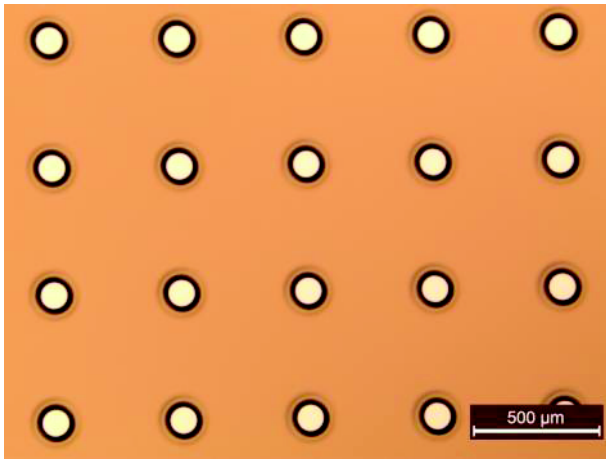

Fig. 5.15. Optical images after the photolithography step of the procedure LO4.

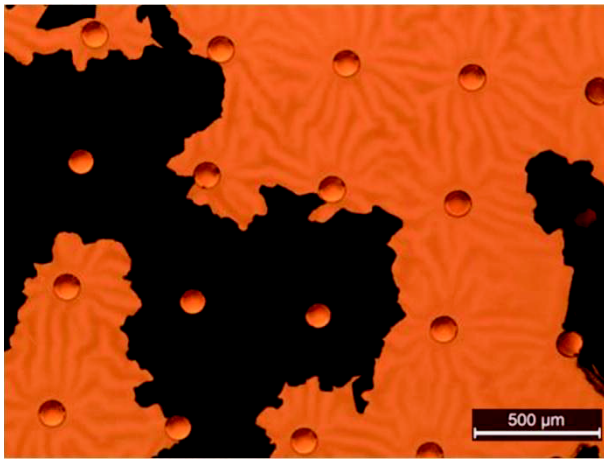

Fig. 5.16. Optical image after the lift-off step of the procedure LO4.

It can be concluded here, that using an ordinary polymer for the top layer was not compatible with our deposition parameters (significant heating of the substrate) and therefore some other materials, which would be more thermally stable, such as metals, should be tried.

5.3.2.6 Procedure LO5: 2×LOR10A/Cr

Inspired by the work [**162**], it was decided to try Cr as a top layer of the bi-layer lift-off structure. The procedure LO5 consisted of the following steps.

1. Cleaning of a 100 mm Si wafer surface with acetone, ethanol, IPA.
2. Dehydration: drying for 5 min at 150 °C.
3. Spinning of the first layer of an LOR10A at 2500 rpm, 60 s, 1000 rpm/s. Drying at 200 °C for 5 min.
4. Spinning of the second layer of the LOR10A at 2500 rpm, 60 s, 1000 rpm/s. Drying at 200 °C for 5 min.
5. Transfer of the sample to evaporation room (some exposure to UV radiation from daylight lamps was possible).
6. Evaporation of 150 nm Cr at the rate of 0.5 nm/s.
7. Spinning of an AZ1512HS at 4000 rpm, 60 s, 2000 rpm/s. Drying at 100 °C for 50 s.
8. UV mask-exposure for 25 s.
9. Development of the AZ1512HS with an AZ developer for 45 s. Washing with DI water, drying with compressed air.
10. Etching of Cr with a commercial chromium etchant ("Cr-etch") until of a color change (~2 min). Washing with DI water, drying with compressed air.
11. Stripping of the Z1512HS in acetone (~2 min).
12. Development of the LOR10A with an AZ MIF326. During this step, in ~1 min the entire Cr layer unexpectedly peeled off from the sample.

Observations with an optical microscope did not reveal any major defect after the Cr etching step (Fig. 5.17). After 1 min of the LOR development, the Cr layer peeled unexpectedly, revealing a dark region of unexposed LOR (Fig. 5.18). The possible reason for the Cr layer peeling is a high residual stress in the metal layer, common in this metal. A limited exposure of LOR to UV during the sample transfer to the evaporation room might have worsened the problem.

To sum up, a lower rate of Cr deposition should be tried to ensure less residual stresses. In addition, it may be worth to protect the LOR against UV radiation on its way into the evaporation system chamber.

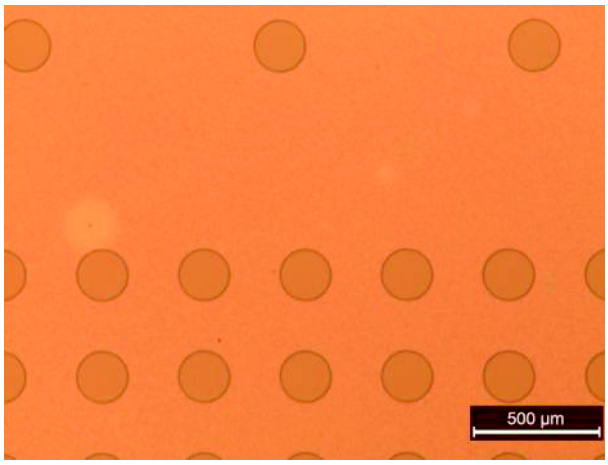

Fig. 5.17. Optical image after the step of the Cr etching of the procedure LO5. Brighter color corresponds to the Cr layer covered with the AZ1512HS. Darker color corresponds to the LOR (circles) observed through the openings.

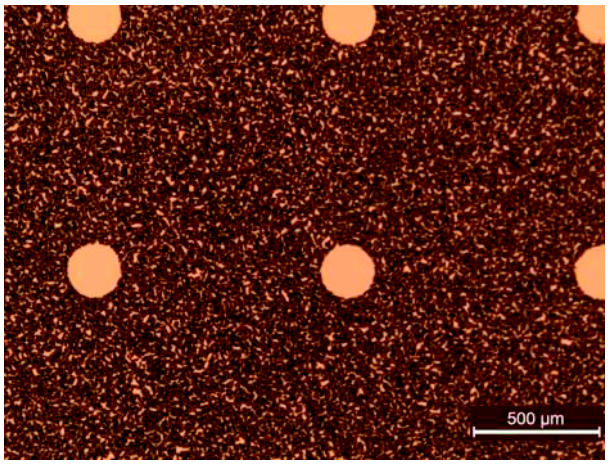

Fig. 5.18. Optical image after the stage of the LOR development of the procedure LO5. The Cr layer peeled off.

5.3.2.7 Procedure LO6: LOR10A/Cr(evaporated)

Compared to the procedure LO5, the following changes were made.

1. A single LOR layer was used instead of a bi-layer. The spin rate was decreased to have a thicker layer.
2. The light in the evaporation room was switched off during the sample transfer.
3. The Cr deposition rate was decreased down to 0.1 nm/s.
4. The photoresist layer on the Cr layer remained during the LOR development. This layer was stripped at the end of the lift-off structure fabrication firstly with acetone and then using O_2 plasma.
5. After the Cr etching stage, the wafer was cut into squares of 1.5 cm for studying the LOR development to find out an optimal development time.

The procedure LO6 consisted of the following steps.

1. Cleaning of a 100 mm Si wafer surface with acetone, ethanol, IPA.
2. Dehydration: drying for 5 min at 200 °C.
3. Spinning of the LOR10A at 1000 rpm, 60 s, 200 rpm/s. Drying at 200 °C for 10 min.
4. Transfer of the sample to the evaporation room with the light switched off.
5. Deposition of 150 nm Cr at 0.1 nm/s.
6. Spinning of AZ1512HS at 4000 rpm, 60 s, 2000 rpm/s. Drying at 100 °C for 50 s.
7. UV mask-exposure for 25 s.

8. Development of AZ1512HS with an AZ developer for 45 s. Washing with DI water, drying with compressed air.
9. Cr etching with a commercial chromium etchant ("Cr-etch") until the color change (~2 min). Washing with DI water, drying with compressed air.
10. Development of the LOR10A with an AZ MIF326. Three durations were tested: 1 min 30 s, 2 min, 2 min 30 s. Washing with DI water, drying with compressed air.
11. Stripping of Z1512HS in acetone (~2 min). Washing with DI water, drying with compressed air.
12. Stripping of Z1512HS residuals using O_2 plasma.
13. Sputter deposition of 500 nm Ti-Ni-Cu layer.
14. Lift-off using AR-300-70 remover at 50 °C during 50 min with an ultrasound agitation.
15. Washing with DI water, drying with compressed air.

The AZ1512HS development was found to be successful by optical imaging (**Ошибка! Источник ссылки не найден.**). A brighter colour is the Cr layer in the photoresist layer opening. A network of black lines on the image revealed a granular structure of the Cr layer. This structure was not expected a priori, but it was learned later that it is a usual Cr structure with the evaporation machine used for the deposition. It is likely due to a Cr oxidation during the deposition [**166**].

This time, the Cr layer did not peel off during the LOR development (which could be thanks to the preventing of LOR from UV exposure, or to less stressed Cr, or to both reasons). During the fabrication, it was observed that in 1 min 30 s the bottom of the LOR layer was still not reached, but 2 min were enough to reach the substrate (**Ошибка! Источник ссылки не найден.**). As it was revealed by SEM (**Ошибка! Источник ссылки не найден.**), 2 min were an optimal time, since in 2 min 30 s the size of the cap was already excessive (~2 μm).

It can be also observed from both optical and SEM images that the edges of the Cr layer openings were not regular, but had a jagged profile. This was probably due to a brittleness of Cr on the grain boundaries [**166**].

Optical images after the Ti-Ni-Cu deposition step (**Ошибка! Источник ссылки не найден.**) show that the metal top bilayer cap profile is less deformed compared to the processes using a photoresist instead of a Cr. On the other hand, a net of cracks was observed on the surface. SEM revealed that LOR layer was swelled up near the openings (**Ошибка! Источник ссылки не найден.**) and the cap profile was not observed anymore. The possible reason for this is a generation and a subsequent relaxation of thermal and mechanical stresses during the Ti-Ni-Cu deposition.

Optical images after the lift-off step showed that the removing process started both at the openings and the cracks (Fig. 5.24). In 50 min of exposure to AR-300-70 remover, lift-off was almost completed. However, some residues were still present on the surface. These residues were also

observed by SEM (Fig. 5.25). SEM also revealed that the jagged pattern Cr edges were transferred to our Ti-Ni-Cu deposits (~2 µm in amplitude).

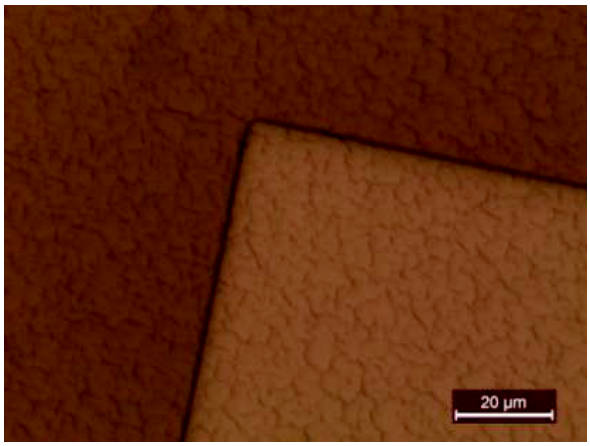

Fig. 5.19. Optical image after the AZ1512HS development step (above the Cr layer).

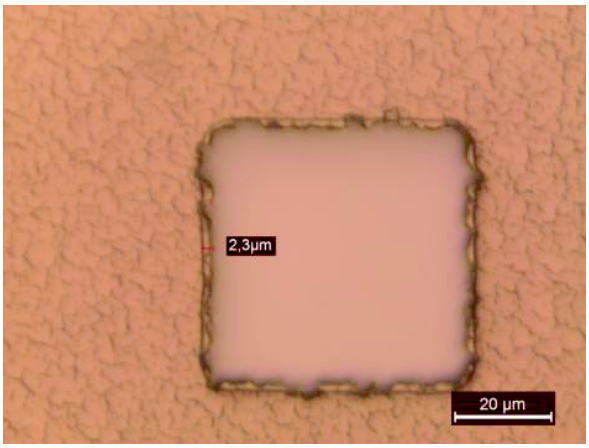

Fig. 5.20. Optical image after the step of the LOR development (AZ MIF 2 min).

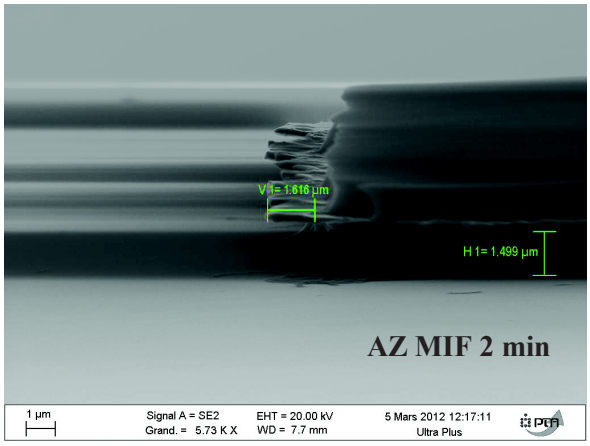

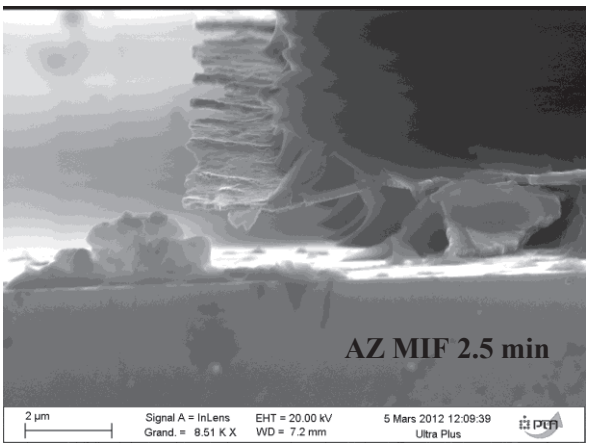

Fig. 5.21. SEM secondary electron images after the LOR development step of the procedure LO6.

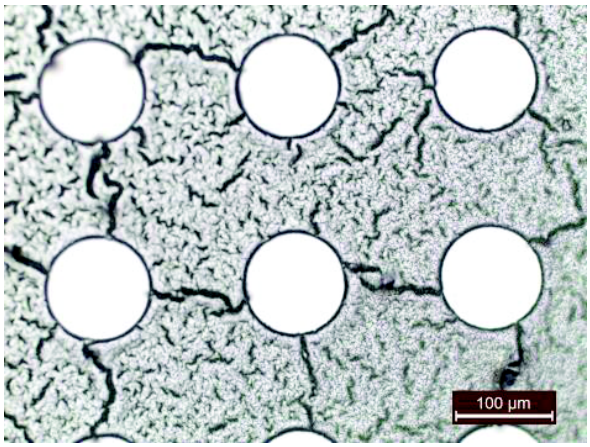

Fig. 5.22. Optical image after the Ti-Ni-Cu deposition step of the procedure LO6.

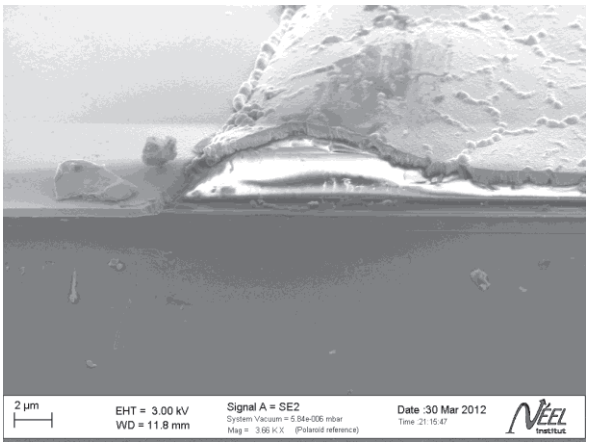

Fig. 5.23. SEM secondary electron image after the Ti-Ni-Cu deposition step of the procedure LO6.

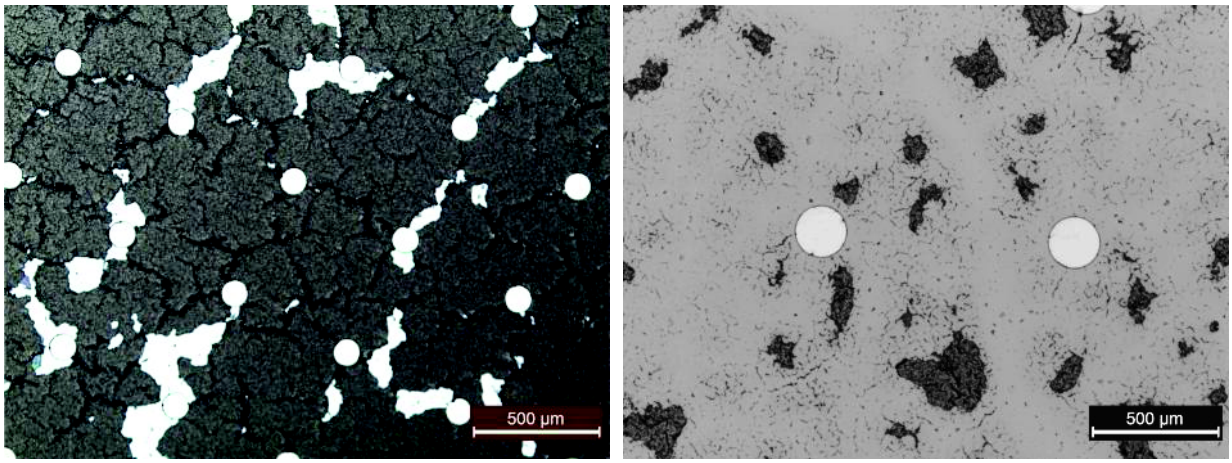

30 min in AR-300-70 50 min in AR-300-70

Fig. 5.24. Optical images after the lift-off step of the procedure LO6. Left: Image after 30 min of exposure to the remover. Right: Image after 50 min of exposure to the remover.

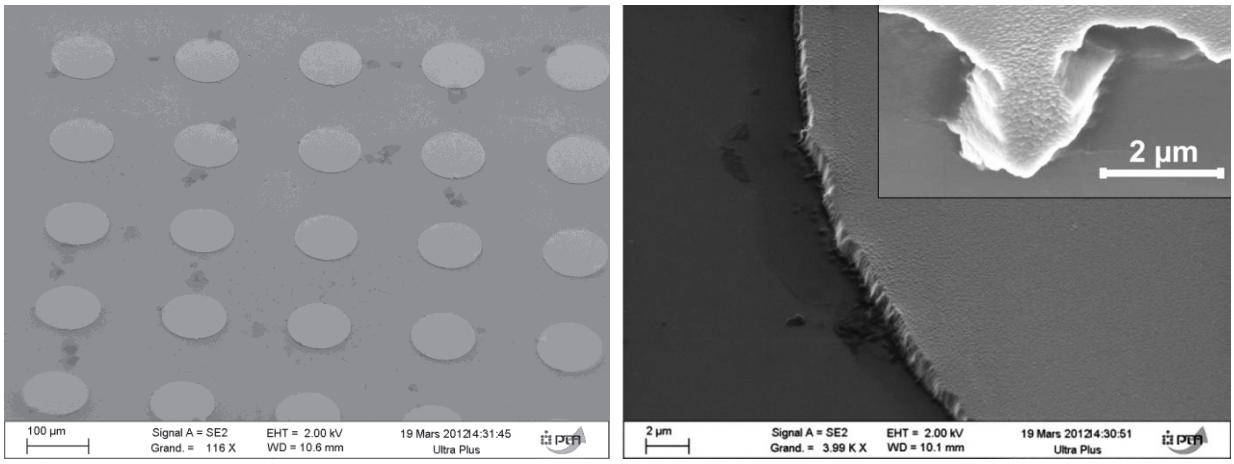

Fig. 5.25. SEM secondary electron images after the lift-off step of the procedure LO6.

It can be concluded for the procedure LO6 that the LOR10A/Cr bi-layer lift-off structure was successfully fabricated and thermal problems of the top layer were eliminated, but it still did not provide a satisfactory lift-off. The reasons for that were: (1) the LOR deformation during the Ti-Ni-Cu deposition due to the surface overheating and (2) jagged shape of the Cr layer openings due to its brittle granular structure. However, in spite of the disappearance of the cap profile, globally the deformation of the intended patterns was much less than for the previous procedures, the pattern edges were free of residues and the lift-off worked on the most of the sample. Another metal, which would be less brittle, should be tried as a top layer for the lift-off structure.

5.3.2.8 Procedure LO7: LOR10A/Ni(evaporated)

The next idea was to try Ni instead of Cr as a top layer for the lift-off structure. The procedure 7 consisted of the following steps.

1. Cleaning of a 100 mm Si wafer surface with acetone, ethanol, IPA.
2. Dehydration: drying for 5 min at 200 °C.
3. Spinning of an LOR10A at 1000 rpm, 60 s, 200 rpm/s. Drying at 200 °C for 10 min.
4. Transfer of the sample to the evaporation room with the light switched off.
5. Evaporation deposition of 150 nm Ni layer at 0.1 nm/s.
6. Spinning of an AZ1512HS at 4000 rpm, 60 s, 2000 rpm/s. Drying at 100 °C for 50 s.
7. UV mask-exposure for 25 s.
8. Development of the AZ1512HS with an AZ developer for 45 s. Washing with DI water, drying with compressed air.
9. Ni etching with 20 vol.% HNO_3 (65 vol.% HNO_3 diluted with DI water with a volume ratio of 1:2) until the color change (~45 s). Washing with DI water, drying with compressed air.
10. Development of the LOR10A with an AZ MIF326 for 2 min 10 s. Washing with DI water, drying with compressed air.
11. Stripping of the Z1512HS in acetone (~1 min). Washing with DI water, drying with compressed air.
12. Stripping of Z1512HS residuals using O_2 plasma.
13. Sputter deposition of 500 nm Ti-Ni-Cu layer.
14. Lift-off using an AR-300-70 remover at 50 °C for 50 min with an ultrasound agitation. The sample was put in a vessel upside down on a convex glass plate to prevent redeposition of the particles.
15. Washing with DI water, drying with compressed air.

As it can be observed from the optical and SEM images (Fig. 5.26 and Fig. 5.27), the Ti-Ni-Cu deposition resulted in a wave-like deformation similar to that obtained when using a photoresist for the top layer. We believe that the cracks in the Cr layer in the previous procedure provided a partial relaxation of the LOR layer stresses, thus limiting the overall deformation of the bilayer. A SEM observation revealed that the LOR layer had swelled up around the openings and the cap profile folded once more.

An SEM observation after the lift-off step revealed that though the lift-off worked on the entire surface of the sample, the pattern edges presented residues due to the folding of the cap profile (Fig. 5.28).

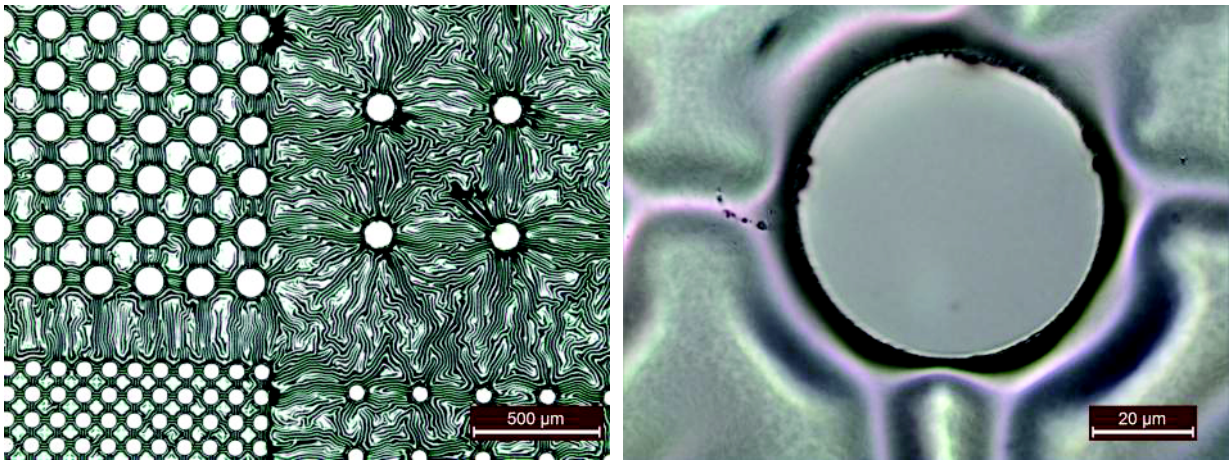

Fig. 5.26. Optical images after the Ti-Ni-Cu deposition step of the procedure LO7.

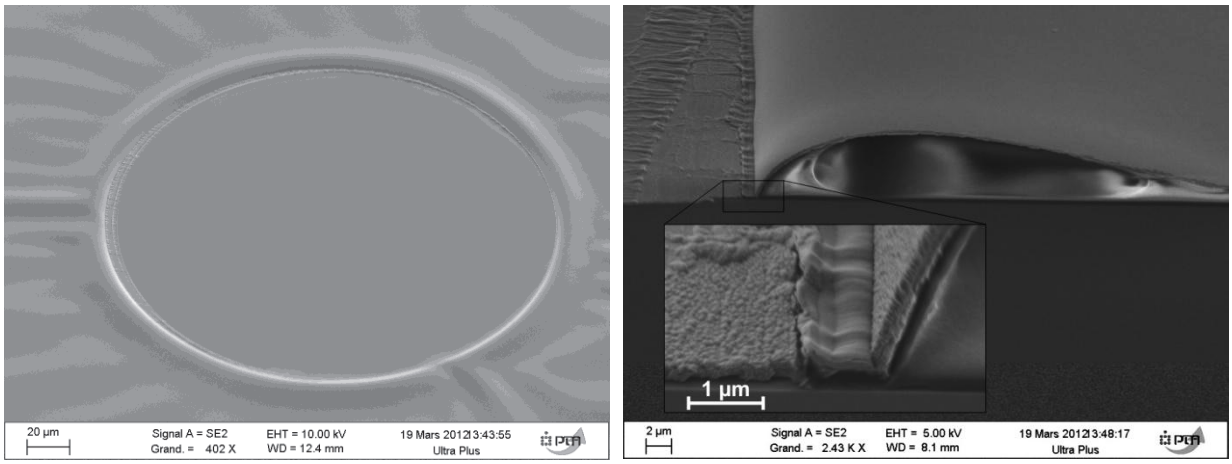

Fig. 5.27. SEM secondary electron images after the Ti-Ni-Cu deposition step of the procedure LO7.

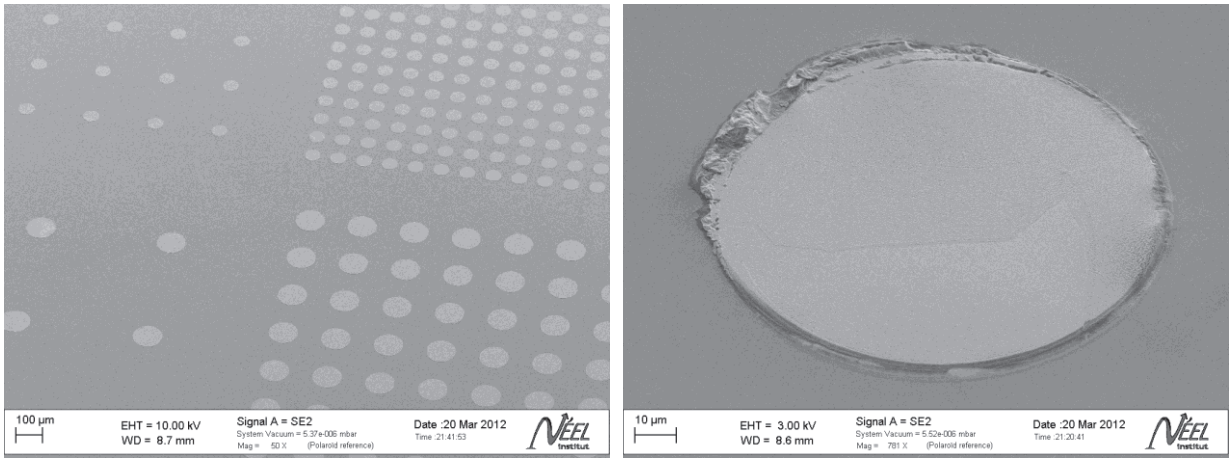

Fig. 5.28. SEM secondary electron images after the lift-off step of the procedure LO7.

It can be concluded here, that a Ni layer without any granules and cracks was successfully fabricated as a top layer of the bilayer lift-off structure. Probably the absence of cracks resulted in much more significant surface wrinkling after the Ti-Ni-Cu deposition compared to the case of a Cr layer. Though the lift-off was successful, the pattern edges were of unsatisfactory quality due to the disappearance of the cap profile during deposition. This means that heating at deposition was high enough to soften LOR which started to deform due to a simultaneous action of thermal and mechanical stresses. It can be finally concluded that with the triode machine settings of the time LOR10A was not compatible with the deposition technique used for the Ti-Ni-Cu deposition. With the temperatures reached by the substrate during deposition, it can be proposed to substitute the bottom layer with some more thermally stable material, e.g. a metal.

5.3.2.9 Procedure LO8: Al(evaporated)/Cr(evaporated)

The next idea was to substitute LOR10A, which didn't withstand the temperature reached in the triode sputtering, for Al. Several microns of Al can be easily deposited, since it is relatively inexpensive and both the sputtering and evaporation rates are high. For the lift-off, a base can be used to dissolve Al, since a Ti-Ni-Cu is not etched by bases. For example, a 30 w.% solution of KOH in water at 80 °C can etch an evaporated Al at 13 μm/min [**150**]. Some technological patterns can be imagined to reduce the lift-off time. For the top layer, Ni presented fewer problems than Cr. However, a standard Al etchant also attacks Ni fast enough to dissolve a thin Ni layer during the etching of the bottom Al layer [**150**]. So, in order to simplify the proof of concept test, Cr was preferred to Ni. The procedure LO8 consisted of the following steps.

1. Cleaning of a 100 mm Si wafer (thermally oxidized on both sides) surface with acetone, ethanol, IPA.
2. Dehydration: drying for 5 min at 200 °C.
3. Deposition of 1 μm Al layer at 1 nm/s.
4. Deposition of 150 nm Ni layer at 0.1 nm/s.
5. Spinning of an AZ1512HS at 4000 rpm, 60 s, 2000 rpm/s. Drying at 100 °C for 50 s.
6. UV mask-exposure for 20 s.
7. Development of the AZ1512HS with an AZ developer for 45 s. Washing with DI water, drying with compressed air.
8. Cr etching with a commercial solution "Cr Etch No 1" until the color change (~2 min). Washing with DI water, drying with compressed air.

9. Al etching with a commercial solution “Al Etch”: ~30 min until the color change (observation of SiO_2 on the bottom of the openings) and then ~6 min to ensure a cap profile. Washing with DI water, drying with compressed air.
10. Stripping of the Z1512HS in acetone (~17 min) with an ultrasound agitation. Washing with DI water, drying with compressed air.
11. Sputter deposition of 500 nm Ti-Ni-Cu layer.
12. Lift-off with 25 vol.% TMAH for 2 h. Tests were done at 40 °C and at room temperature.
13. Washing with DI water, drying with compressed air.

As one can observe from the optical images in Fig. 5.29, at some places of the pattern, the Al layer did not etch fully. This revealed an inhomogeneity of the Al layer thickness throughout the wafer. As seen on optical image in Fig. 5.30 and on SEM images in Fig. 5.31, the photoresist stripping with a simultaneous ultrasound action resulted in a damage of the Cr layer at the opening edges. Nevertheless, a cap profile of ~1 µm was successfully fabricated.

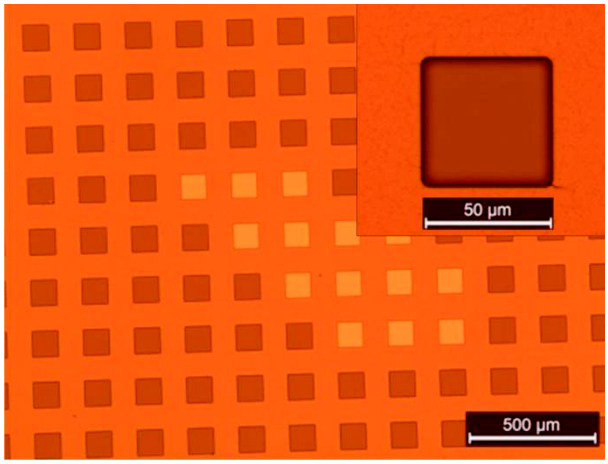

after 36 min in “Al Etch”

Fig. 5.29. Optical images after the Al etch step of the procedure LO8.

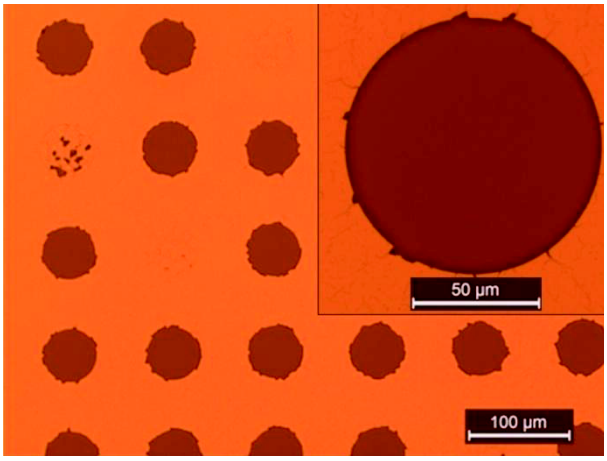

after 17 min in acetone with ultrasound

Fig. 5.30. Optical images after the photoresist stripping step of the procedure LO8.

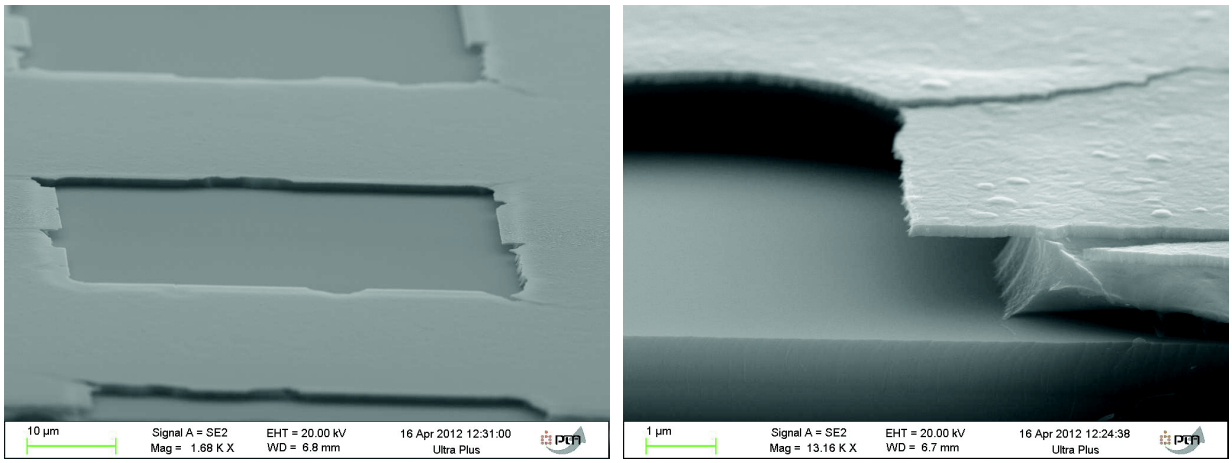

Fig. 5.31. SEM secondary electron images after the photoresist stripping step of the procedure LO8.

SEM images of the Ti-Ni-Cu layer after the deposition (Fig. 5.32) revealed a perfect conservation of the cap profile and sharp edges of the Ti-Ni-Cu pattern objects. Such a regular pattern edge was observed for the first time in this work. Thus, using two thermally stable metals for the cap profile exposed to high temperatures during Ti-Ni-Cu deposition allows a proper lift-off.

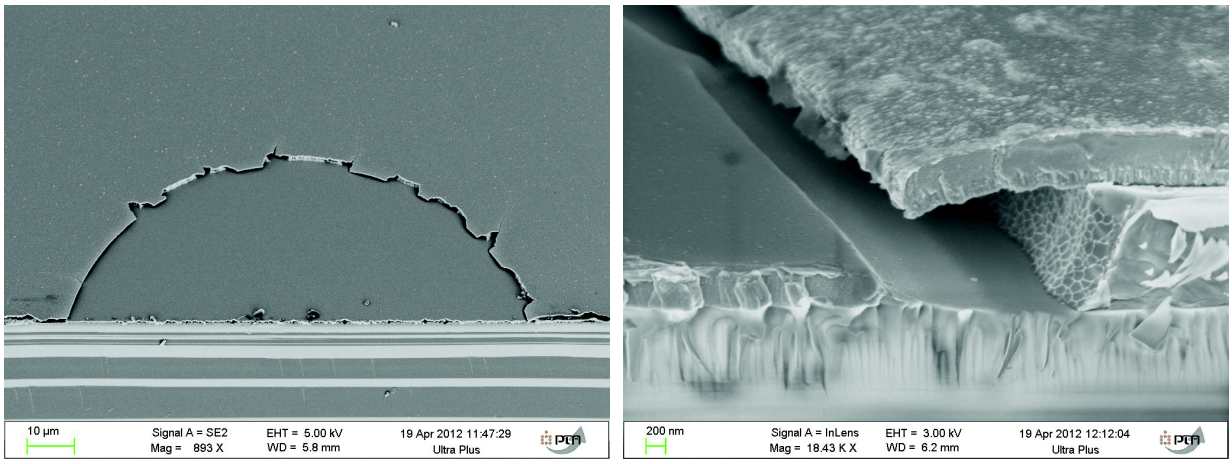

Fig. 5.32. SEM secondary electron images after the Ti-Ni-Cu deposition step of the procedure LO8.

After the Ti-Ni-Cu deposition step, the sample was cut into several pieces. A solution of 25 vol.% of tetramethylammonium hydroxide (TMAH), which is usually used for a Si anisotropic etching, was tested for the Al etching. In ~2 h the lift-off was finished for the sample with the smallest distance between the pattern objects (Fig. 5.33 and Fig. 5.34). For the samples with the larger distances, the amount of Al to etch increases, and for these cases the lift-off worked partially (Fig. 5.33). The pattern objects were fully liberated when the distance between them was less than 100 µm.

No difference in etching rate was found between the sample etched at 40 °C and the one etched at room temperature. ~100 µm of Al were etched in 2 h, giving an etch rate of ~830 nm/min.

It can be concluded for the procedure LO8 that the Al/Cr lift-off structure was successfully fabricated and found to be perfectly thermostable at the conditions used for the Ti-Ni-Cu deposition. However, the brittleness of the evaporated Cr caused a jagged edge of the pattern when using ultrasounds for cleaning. In order to obtain satisfactory lift-off results, this problem should be solved. It was shown that Al can be laterally removed using TMAH solution, but it takes longer that a common lift-off. If the use of KOH or NaOH at 80 °C was available in our facility, it would reduce the lift-off duration in ~10 times.

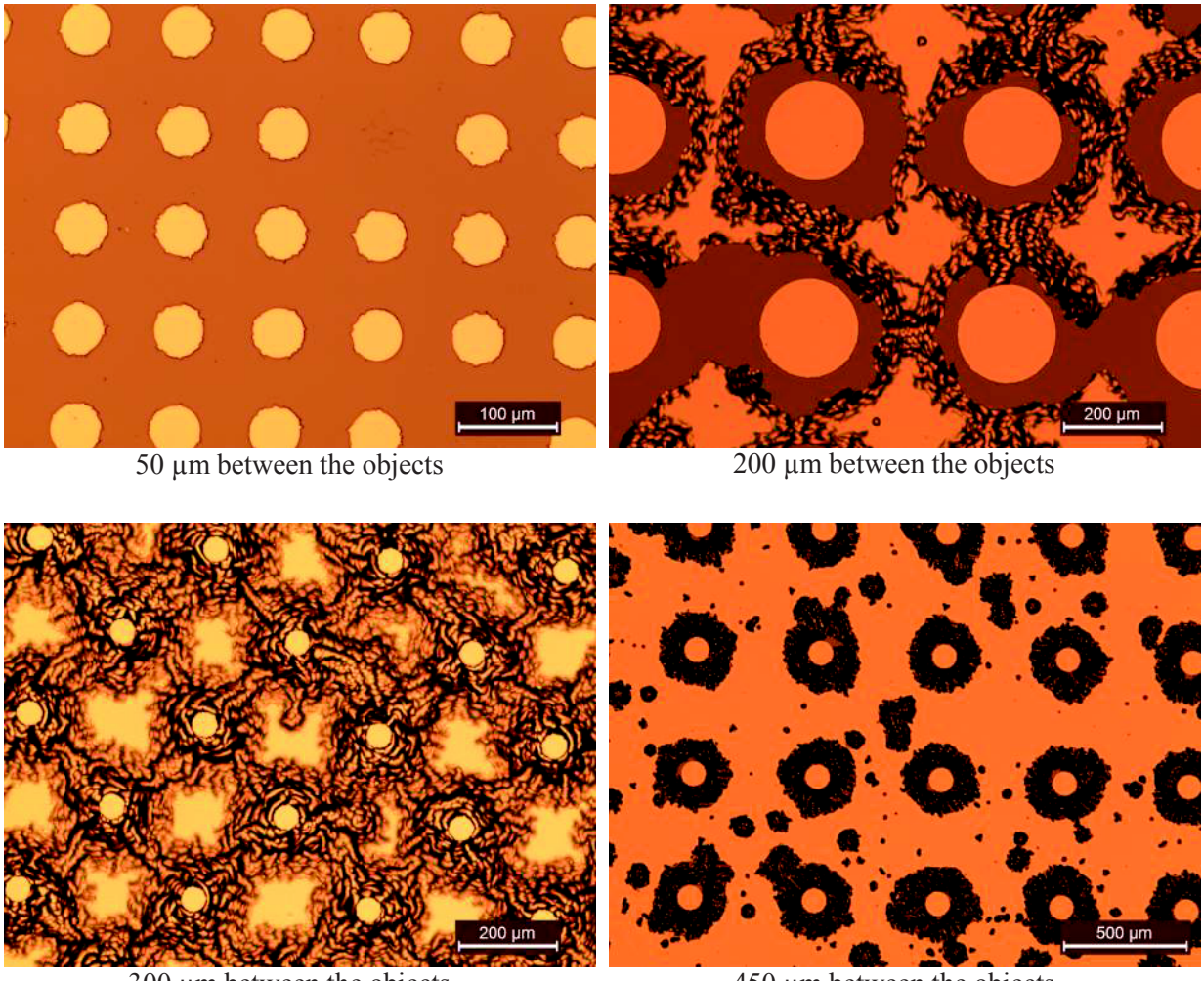

50 µm between the objects | 200 µm between the objects

300 µm between the objects | 450 µm between the objects

Fig. 5.33. Optical images after the lift-off step using 25 vol.% TMAH for 40 min.

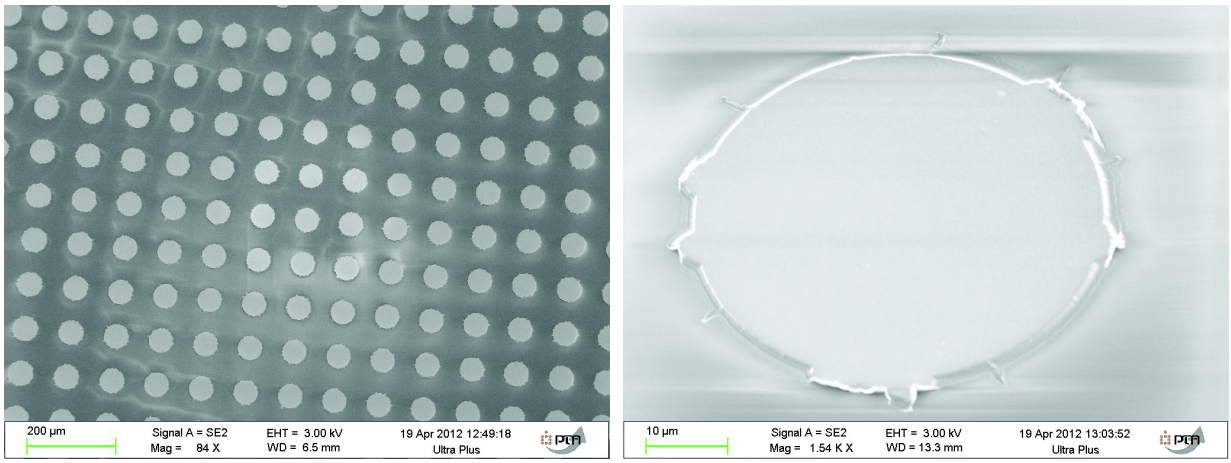

Fig. 5.34. SEM secondary electron images after the lift-off step of the procedure LO8.

5.3.2.10 Procedure LO9: Al(sputtered)/Cr(sputtered)

It is known from literature that sputtered Cr is less brittle that evaporated Cr [**166**]. Our next test was to deposit both Cr and Al using the same triode sputtering system as for the Ti-Ni-Cu deposition. The procedure LO9 consisted of the following steps.

14. Deposition of 1 µm Al layer at nominal rate of 1.5 nm/s.
15. Deposition of 150 nm Cr layer at nominal rate of 0.3 nm/s.
16. Cleaning of the surface with acetone, ethanol, IPA.
17. Dehydration: drying for 5 min at 200 °C.
18. Spinning of an AZ1512HS at 4000 rpm, 60 s, 2000 rpm/s. Drying at 100 °C for 50 s.
19. UV mask-exposure for 20 s.
20. Development of the AZ1512HS with an AZ developer for 45 s. Washing with DI water, drying with compressed air.
21. Cr etching with a commercial solution "Cr Etch No 1": ~3 min until the color stopped changing (the changing started in 1 min 30 s at the wafer's center). Washing with DI water, drying with compressed air.
22. Al etching with a commercial solution "Al Etch": ~26 min until the color stopped changing (the changing started in 12 min at the wafer's center). Washing with DI water, drying with compressed air.
23. Stripping of the Z1512HS in acetone (~45 min) without ultrasound agitation. Washing with DI water, drying with compressed air.

SEM images of the final Al/Cr lift-off structure are shown in Fig. 5.35. Both sputter-deposited Al and Cr layers were very rough. Probably due to this roughness, the Cr layer was broken at some places, spoiling the cap profile.

Furthermore, the thickness of both layers was significantly inhomogeneous throughout the wafer: they were ~2 times thicker in the wafer's center compared to its border.

To conclude, the sputter-deposited Cr layer had no evident cracks and was less brittle than the evaporated one. However, some destructions of the cap profile occurred, probably due to its high roughness.

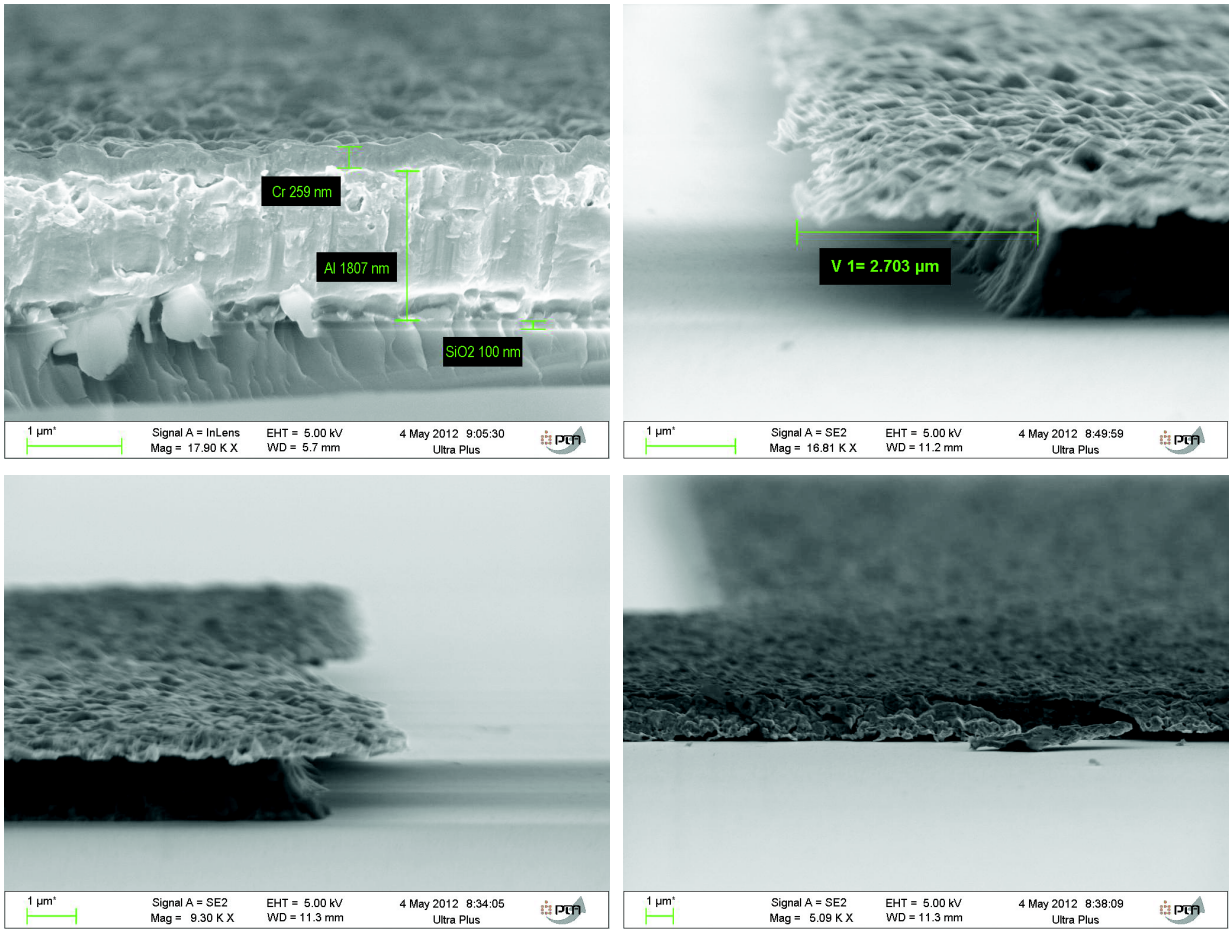

Fig. 5.35. SEM secondary electron images of the final Al/Cr lift-off structure of the procedure LO9.

5.3.2.11 Procedure LO10: Al(sputtered)/Ni(evaporated)

Since no way was found to obtain a satisfactory Cr layer, it was decided to develop a method for Al/Ni lift-off structure fabrication. As it was mentioned in subsection 5.1.8, "Al etch" is known to attack Ni. However, Ni has been reported to resist against bases [**150**]. Thus, the etchant used in this

procedure was a 1:1 25 vol.% TMAH solution diluted with water. The procedure LO10 consisted of the following steps.

1. Sputter-deposition of 1 μm Al layer at nominal rate of 3.1 nm/s.
2. Deposition of 250 nm Ni layer by evaporation at rate of 0.1 nm/s.
3. Cleaning of wafer with acetone, ethanol, IPA.
4. Dehydration: drying for 5 min at 200 °C.
5. Spinning of an AZ1512HS at 4000 rpm, 60 s, 2000 rpm/s. Drying at 100 °C for 50 s.
6. UV mask-exposure for 20 s.
7. Development of the AZ1512HS with an AZ developer for 45 s. Washing with DI water, drying with compressed air.
8. Ni etching of with 20 vol.% HNO_3 (1:2 65 vol.% HNO_3 diluted with DI water) until the color change (~2 min). Washing with DI water, drying with compressed air.
9. Al etching with a 12.5 vol.% TMAH: ~2 min 30 s until the color stopped changing (the changing started in 30 s at the wafer's center). A residual bluish layer was observed after etching. This layer was removed with commercial "Al etch". Washing with DI water, drying with compressed air.
10. Stripping of the Z1512HS in acetone (~45 min) without ultrasound agitation. Washing with DI water, drying with compressed air.

When etching the sputter-deposited Al layer, its thickness inhomogeneity throughout the wafer was confirmed once again. It resulted in over-etching of the patterns at the wafer's central part. An unexpected residual bluish layer was observed both visually and by SEM (Fig. 5.36) after the etching with TMAH. Since we know a Cu contamination was possible with our triode-sputtering system it was supposed and confirmed by EDX analysis that the residual layer contains Cu.It was successfully removed by commercial "Al etch" (Fig. 5.37) since "Al etch" attacks Cu. SEM observation of the final Al/Ni structure revealed a perfect cap profile with a moderate roughness of Ni layer (caused by a rough sputter-deposited Al layer).

To conclude, the Al/Ni lift-off structure with a cap profile withstanding the high temperatures of the triode sputtering machine at the time of our work was successfully fabricated. Further optimization of this process would involve the use of an appropriate technique for Al deposition ensuring thickness homogeneity and low surface roughness, such as evaporation or magnetron sputtering.

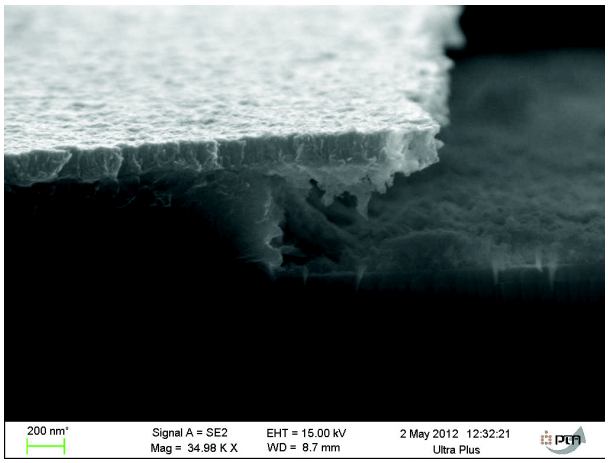

Fig. 5.36. SEM secondary electron image after the Al etching step with TMAH.

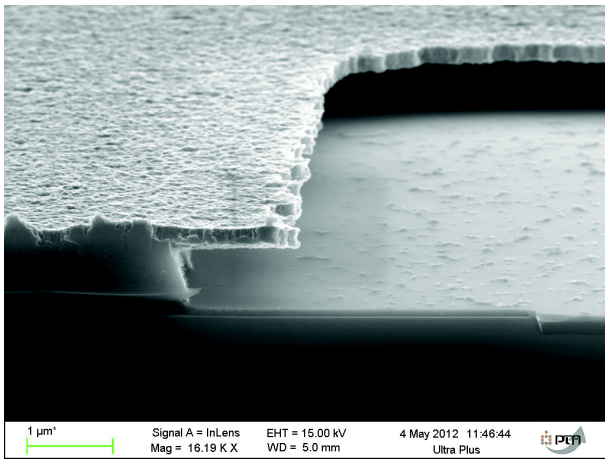

Fig. 5.37. SEM secondary electron image after the residual layer etching step with "Al etch".

5.3.2.12 Summary

The results of the lift-off procedure development for the Ti-Ni-Cu thin films are summarized in Table 5.2. Neither conventional photoresists nor LOR were found to be compatible with the triode sputtering system setup used for the Ti-Ni-Cu deposition available at the time. Finally, metals were used to provide a sufficient thermal stability for lift-off structure under these conditions. Al was found to be an optimal metal for the bottom layer since it is relatively simple to deposit, to pattern and to remove. Lift-off (Al lateral etching) was proved to be possible on both Al/Cr and Al/Ni structures using either commercial "Al etchant" or a TMAH solution. Ni was found to be an optimal metal for the top layer compared to Cr, since it is rigid enough and compatible with Al for selective patterning. However, the overall complexity of an all-metal lift-off cap profile fabrication and its removing is comparable to that of wet etching. Under rough temperature conditions for the deposition of a desired material, if wet etching is available and the undercut it causes in the patterns is acceptable, it would be a more time and cost effective for patterning Ti-Ni-Cu thin films.

Table 5.2. Summary of the lift-off development for Ti-Ni-Cu thin films.

N	Structure	Parameters for lift-off	Result
1	LOR10A/AZ1512HS	Remover AR-300-70, 1 h at 50 °C with ultrasound	Strong surface deformation after Ti-Ni-Cu deposition. Lift-off was not satisfactory.
2	2×LOR10A/AZ1512HS	Remover AR-300-70, 1 h at 50 °C with ultrasound	Strong surface deformation after Ti-Ni-Cu deposition. Lift-off was not satisfactory.
3	LOR10A/AZ4562 (polymerized)	Remover AR-300-70, 1 h at 50 °C with ultrasound	Strong surface deformation after Ti-Ni-Cu deposition. Lift-off was not satisfactory.
4	2×LOR10A/AZ4562 (polymerized)	Remover AR-300-70, 1 h at 50 °C with ultrasound	Strong surface deformation after Ti-Ni-Cu deposition. Lift-off was not satisfactory.
5	2×LOR10A/Cr	not done	Fabrication was unsuccessful due to the following possible reasons: (1) highly stressed Cr layer; (2) short LOR exposure to UV radiation.
6	LOR10A(UV protected)/Cr(evaporated)	Remover AR-300-70, 1 h at 50 °C with ultrasound	Strong deformation of LOR after Ti-Ni-Cu deposition. Lift-off was not satisfactory.
7	LOR10A (UV protected)/Ni(evaporated)	Remover AR-300-70, 1 h at 50 °C with ultrasound	Strong surface deformation after Ti-Ni-Cu deposition. Lift-off was not satisfactory.
8	Al (evaporated)/Cr (evaporated)	TMAH 25%, at least 2 h	The cap profile is perfectly thermostable. Low pattern edge quality due to Cr layer brittleness. Lift-off is possible using TMAH 25%, with a lateral rate of ~830 nm Al / 1 min.
9	Al(sputtered)/Cr(sputtered)	not tested	Some destructions of the cap profile occurred, probably due to the high roughness of the sputtered Cr.
10	Al(sputtered)/Ni(evaporated)	not tested	Perfect lift-off cap profile with high quality edges. Another deposition technique (e.g. evaporation) is needed for Al layer to provide a homogeneous thickness.

5.3.3 Wet-etching

5.3.3.1 Choice of procedure

Ti-Ni-based alloys are known to resist to all kind of etchants except of a mixture of HF and HNO_3. The only other option known from literature is an electropolishing process with an electrolyte composed of H_2SO_4 and CH_3OH [**153**], but this method is hardly applicable for a microsystem fabrication. Different ratios of HF, HNO_3 and H_2O were reported in literature (see Table 5.3), but unfortunately, the values were rarely clearly given and the procedures were not detailed. Thus, our own solution was developed: 60 ml HF (10 vol.%), 60 ml HNO_3 (65 vol.%), 60 ml H_2O. The corresponding volume ratio of the components is as follows: HF : HNO_3 : H_2O = 1 : 6.5 : 22.5. It was mixed in the following order: HF, HNO_3, H_2O. The etching rate was ~2 µm/min, being close to that reported for a similar etchant solution [**153**].

Table 5.3. Literature data on etching of Ti-Ni-based alloys with a mixture of HF, HNO_3 and H_2O.

Volume ratio HF : HNO_3 : H_2O	**Alloy**	**Mask material**	**Etching rate, µm/min**	**Reference**
not reported	NiTi	AZ4110	not reported	[**152**]
1 : 4 : 5	$Ni_{50}Ti_{50}$	no	30	[**153**]
1 : 5 : 20	$Ni_{50}Ti_{50}$	no	6	[**153**]
1 : 1 : 20	$Ni_{50}Ti_{50}$ amorphous	AZ4620, 5 µm	0.6	[**154**]
1 : 1 : 20	$Ni_{50}Ti_{50}$ crystallized	AZ4620, 5 µm	0.2	[**154**]
1 : 1 : 5	$Ni_{50}Ti_{50}$	Au/Cr and AZ4620	not reported	[**159**]
1 : 1 : 20	$Ni_{50}Ti_{50}$ crystallized	Au/Cr and AZ4620	0.25	[**159**]
not reported	$Ni_{48.5}Ti_{51.5}$	AZ3330	not reported	[**155**]
1 : 1 : 20	$Ni_{47}Ti_{53}$ crystallized	AZ4620	not reported	[**156**]
1 : 1 : 20	NiTi crystallized	AZ4562, 4.8 µm	not reported	[**157**]
1 : 1 : 20	$Ti_{50}Ni_{47}Cu_3$ crystallized	AZ4562, 4.8 µm	0.55	[**158**]

The choice of the etching mask material is highly critical for such an aggressive mixture. A compromise should be found between the chemical stability of the material, its selectivity compared to Ti-Ni-Cu and the convenience of its deposition and removing. Several mask materials were tried for this purpose in [**159**], including gold and various photoresists.

Our own study was carried out and various materials were tried as an etching mask: gold, AZ5214, AZ4562 and LOR10A. LOR10A was found to be an optimal choice. The detailed description of the procedures and the results of the tests are given below.

A graphical schematic of the pattern definition of a Ti-Ni-Cu film through wet etch process is given in Fig. 5.38. A Cr mask was used for photolithography pattern definition. Pattern features were circles and squares with the sizes ranging from 50 to 200 μm.

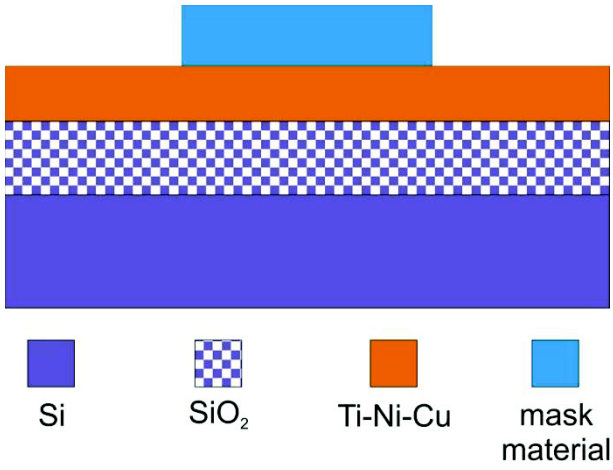

Fig. 5.38. Graphical schematic for wet etching of Ti-Ni-Cu layer.

5.3.3.2 Procedure WE1: gold mask

The procedure WE1 consisted of the following steps.

1. Deposition of 1 μm Ti-Ni-Cu layer onto Si/SiO_2 100 mm wafer.
2. Cleaning with acetone, ethanol, IPA.
3. Dehydration of wafer at 200 °C for 5 min.
4. Spinning of LOR10A at 4000 rpm, 60 s, 2000 rpm/s. Drying at 200 °C for 5 min.
5. Spinning of AZ1512HS at 4000 rpm, 60 s, 2000 rpm/s. Drying at 100 °C for 1 min 30 s.
6. UV exposition for 25 s.
7. Development of both photoresist and LOR with AZ MIF326 for 1 min 40 s.
8. 150 nm gold layer deposition by "Nordico" magnetron sputtering. To ensure good adhesion, plasma clean in argon was first carried out at 500 W for 1 min to further remove residual resists.
9. Lift-off of Au layer with 1112A remover at 50 °C.
10. Wet etching of Ti-Ni-Cu layer with a mixture of 60 ml HF (10 %), 60 ml HNO_3 (65 %), 60 ml H_2O for 3 min. Order of mixing: H_2O, HNO_3, HF.
11. Washing with DI water, drying with compressed air.

As it can be observed in Fig. 5.39, the undercut due to over-etching was 15 μm after 3 min of exposure to the mixture of acids. It gives an estimation of the etching rate at 5 μm/min. More tests are needed to confirm this value. The Au layer could be removed by any conventional Au etchant. It was not tested, since it is a standard proven procedure.

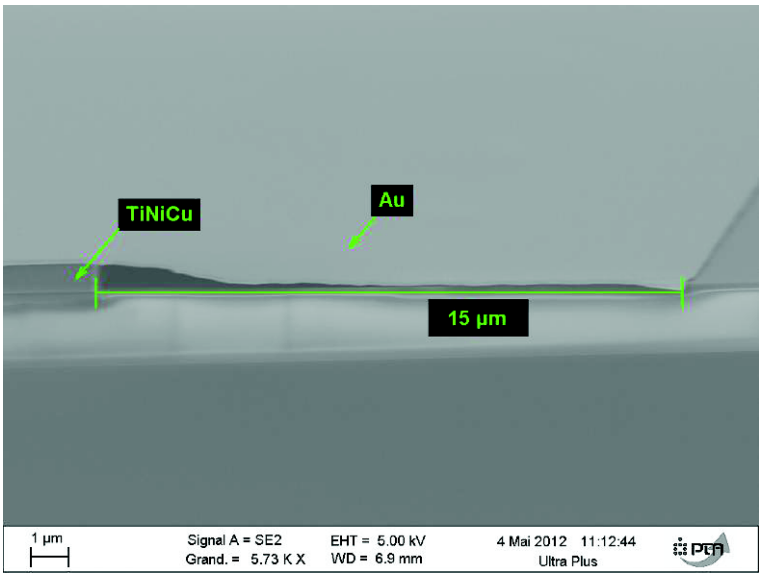

Fig. 5.39. SEM image after wet etching.

For the procedure WE1, it can be concluded that the mixture of hydrofluoric and nitric acids does etch Ti-Ni-Cu alloy, but the concentrations need to be adjusted to decrease the etching rate down to values convenient in terms of technological control. As expected, the Au mask was not attacked by the mixture, but materials which would be easier to remove should be tested.

5.3.3.3 Procedure WE2: AZ5214 mask

For this procedure, a mask of AZ5214 photoresist, 1.4µm thick at nominal spinning conditions, was used instead of gold. The procedure WE2 consisted of the following steps.

1. Deposition of 1 µm Ti-Ni-Cu layer onto Si/SiO_2 100 mm wafer.
2. Cleaning with acetone, ethanol, IPA.
3. Dehydration of wafer at 200 °C for 5 min.
4. Spinning of hexamethyldisilazane (HMDS), an adherence promoter for photoresist, using standard parameters.
5. Spinning and drying of AZ5214 using standard parameters.
6. UV exposition using standard parameters.
7. Development of the photoresist with AZ developer using standard parameters.
8. Wet etching of Ti-Ni-Cu with a mixture of 60 ml HF (10 %), 60 ml HNO_3 (65 %), 60 ml H_2O for 30 s. Order of mixing: H_2O, HNO_3, HF.
9. Stripping with 1112A remover and H_2O (1:1, volume ratio) for 4 min.
10. Washing with DI water, drying with compressed air.

The resulting patterns are shown in Fig. 5.40. As no lateral over-etching was observed, the etching rate can be estimated at 2 µm/s. This value significantly differs from that determined in the previous test. More tests should be done to confirm this.

The attacked zone of the Ti-Ni-Cu surface inside the patterns reaches ~8 µm under the photoresist and attack traces were observed even farther. This was due to a lateral delamination of the resist. It can be thus concluded that the AZ5214 has a poor resistance to the etchant. More resistant material should be found.

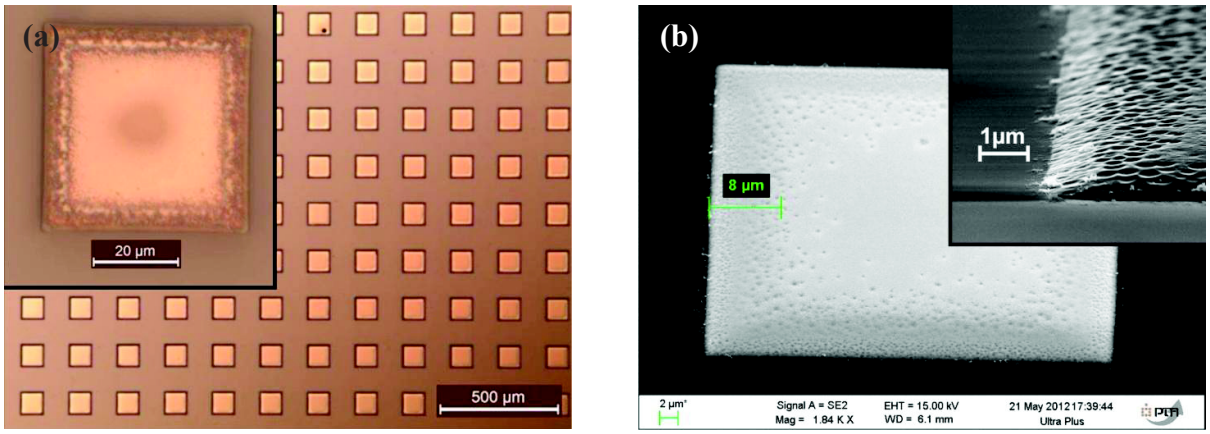

Fig. 5.40. Optical microscope (a) and SEM (b) images of the final pattern of the procedure WE2.

5.3.3.4 Procedure WE3: AZ4562 mask

The procedure WE3 was the same as the WE2, except the use of AZ4562 photoresist (with standard parameters of preparation) instead of AZ5214. The AZ4562 photoresist has a standard thickness of 6.2 µm, it is more viscous and more resistant than the AZ5214. The resulting patterns are shown in Fig. 5.41. As seen, ~3-4 µm of the Ti-Ni-Cu surface were attacked by the etchant into the pattern. Therefore, an AZ4562 photoresist resists better against the etchant than an AZ5214, but still not good enough.

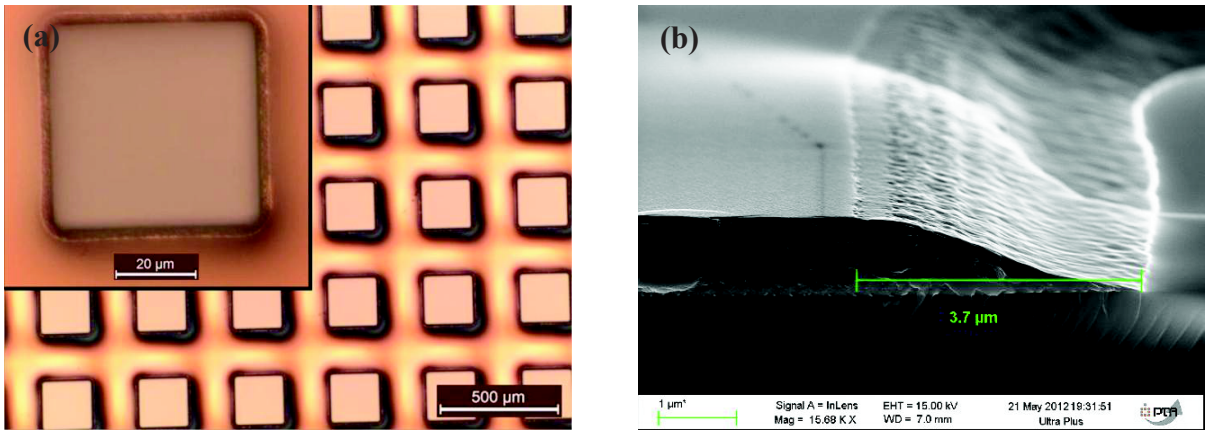

Fig. 5.41. Optical microscope (a) and SEM (b) image of the final pattern of the procedure WE3.

5.3.3.5 Procedure WE4: LOR10A mask

LOR10A resist is more chemically resistant than ordinary photoresists. It is ~1.0 µm thick when prepared using standard parameters (spin speed of 3000 rpm). Since it is a resist designed to be the bottom layer of a bilayer lift-off, it is not intended as a photoresist and its properties against UV radiation have not been reported. Thus, it was patterned through a mask of AZ5214 photoresist. The schematic of the resulting etching mask structure is shown in Fig. 5.42a. The LOR10A was spun with a speed of 4000 rpm (to make it denser) for 60 s with an acceleration of 2000 rpm/s The AZ5214 was spun and developed using standard parameters. Finally the LOR10A was developed with an AZ MIF326. After the Ti-Ni-Cu etching the whole was stripped with a mixture of 1112A remover and water (1:1, volume ratio) for 60 min. All the other steps of this procedure (concerning wafer preparation and Ti-Ni-Cu etching) were the same as for the procedures WE2 and WE3.

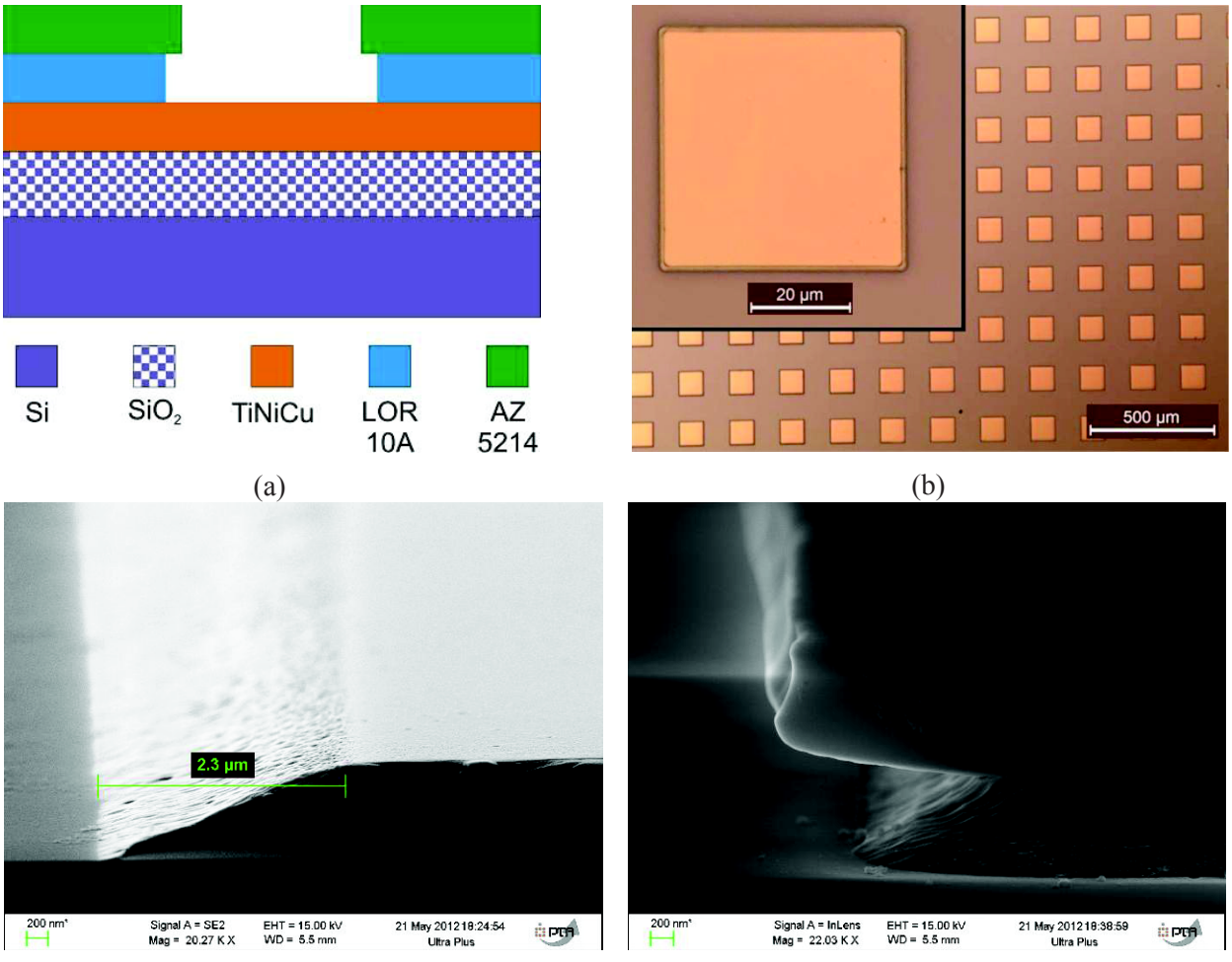

Fig. 5.42. Procedure WE4. (a) Schematic of the resulting etching mask structure. (b) Optical microscope image of the final pattern. (c) SEM of the final pattern: left image shows the pattern well released, right shows the pattern with the LOR still present after stripping.

The resulting patterns are shown in Fig. 5.42b and c. As seen, ~2 μm of the Ti-Ni-Cu surface were attacked by the etchant. This value is close to that of the film thickness (1 μm) and therefore is mainly due to the undercut formed when etching and not due to a resist delamination. It can be concluded that an LOR10A resists sufficiently against the etchant and is suitable as a mask material.

5.3.3.6 Summary

The results of the etching tests performed for different mask materials for Ti-Ni-Cu thin film etching with mixtures of HF and HNO_3 are summarized in Table 5.4.

To make a general conclusion, gold was found to have a perfect resistance to the etchant, but its deposition and removing are complicated compared to conventional photolithographic resists. On the other hand, the ordinary photoresists showed moderate resistance to the etchant and delaminated causing the attack of the Ti-Ni-Cu surface. LOR10A seems to be an optimal solution for our purpose, since its resistance to the etchant is sufficiently high while being relatively simple to deposit and to remove.

Table 5.4. Summary of the test of different mask materials for Ti-Ni-Cu thin film etching.

Mask material	**Size of attacked zone, μm**	**Conclusion**
Au	0	Perfect resistance to the etchant, but relatively complicated from technological point of view.
AZ5214	8	Poor resistance to the etchant.
AZ4562	3-4	Moderate resistance to the etchant.
LOR10A	2	Good resistance to the etchant, but it takes more time to prepare and to strip.

5.3.4 Patterning: summary and conclusions

1. Lift-off technology was developed for patterning 1 μm thick Ti-Ni-Cu films deposited at elevated temperatures (up to ~300 °C). A cap profile consisted of Al as a bottom layer and Ni as a top layer. Lift-off was proved to be possible with 25 % TMAH solution. This method is considerably less efficient in terms of costs and time than standard lift-off procedures, but exhibits an excellent thermal stability. Conventional polymer photoresists used did not withstand our deposition temperatures.
2. As an alternative to lift-off, wet-etching technology using a mixture HF-HNO_3 was developed for patterning 1 μm thick Ti-Ni-Cu films. LOR was an optimal etch mask material. This method is quite simple technologically, but requires the use of HF which is restricted at our facilities.

5.4 Fabrication procedure for Ti-Ni-Cu-based bridges/cantilevers

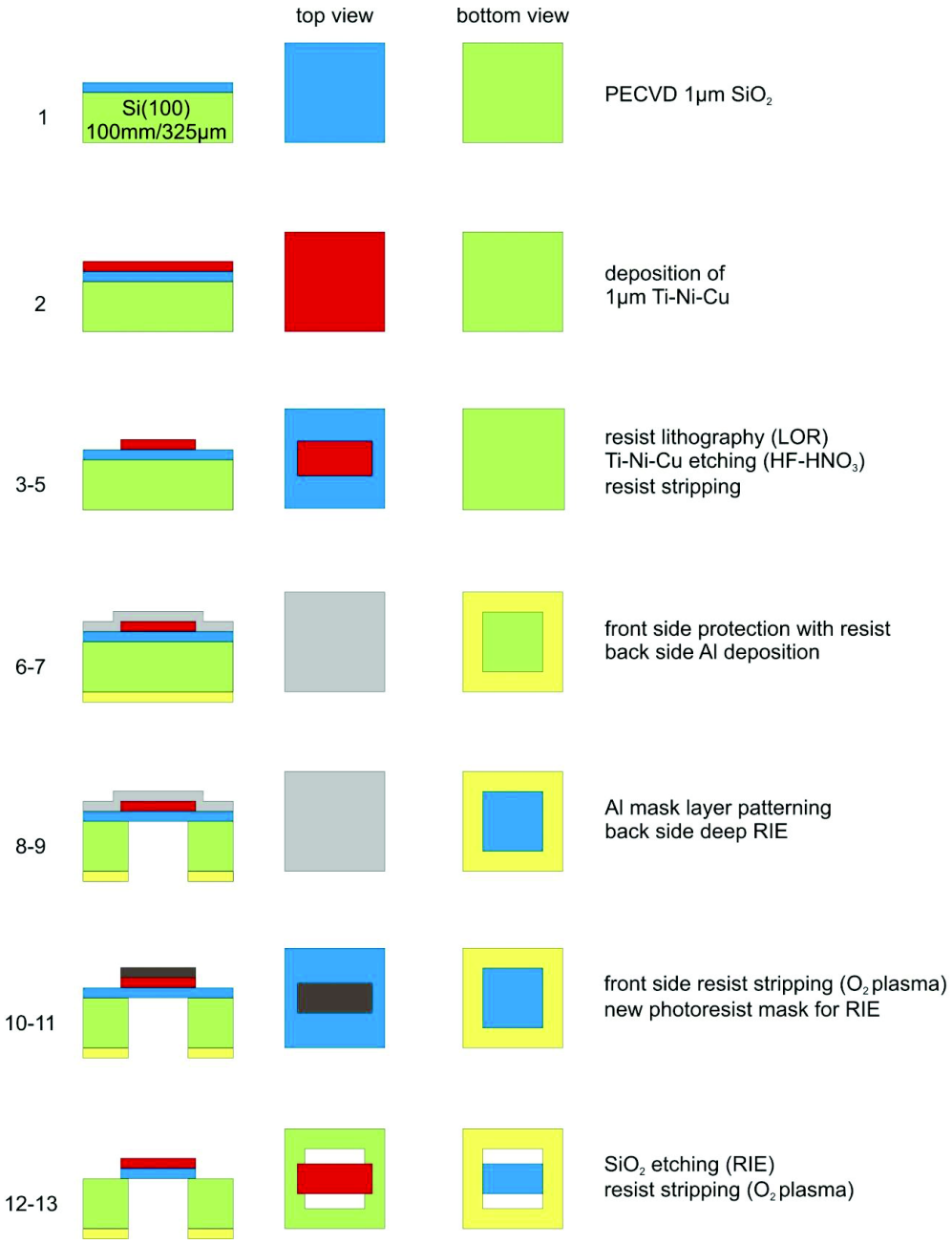

Fig. 5.43. Fabrication procedure scheme for bimorph microstructures Ti-Ni-Cu/SiO_2 of bridge/cantilever type (only the bridge case is shown).

Here we propose a procedure for future fabrication of Ti-Ni-Cu-based bridges/cantilevers from 325-μm-thick Si wafers (⌀ 100 mm). These thinner wafers (standard thickness is 500 μm) are chosen to facilitate the back side deep reactive ion etching (RIE) liberation step. The procedure comprises Ti-

Ni-Cu layer patterning, which we preliminary propose to realize by wet-etching with a mixture of HF and HNO_3 acids. The process is schematically shown in Fig. 5.43.

Firstly (step 1), 1 μm of SiO_2 is deposited by plasma-enhanced chemical vapor deposition (PECVD). This layer will be both an elastic part of the bimorph membrane and a stop layer for deep RIE. Then, 1 μm of Ti-Ni-Cu is deposited by triode sputtering (step 2). This will be the functional part of the bimorph membrane. Afterwards (steps 3-5), the Ti-Ni-Cu layer is patterned by wet etching using the mixture of HF, HNO_3 and H_2O through the LOR resist mask, which is stripped after the Ti-Ni-Cu patterning. Then, silicon is etched from the back side using DRIE through an Al mask down to the SiO_2 layer (steps 6-9). Then the structure is released from the front side by dry etching of SiO_2 using reactive ion etching (RIE, steps 10-13). Dry etching is chosen because wet etching on a liberated structure may cause damage due to stiction.

This procedure is planned to be tested in the future work.

5.5 Ti-Ni-Cu-based micro-structures: summary and conclusions

1. A simple fabrication method, comprising only Si patterning, was tested to obtain thin Ti-Ni-Cu/SiO_2 membranes (down to 2 μm of total thickness). The membranes were quite robust, with functional properties of Ti-N-Cu layer almost unchanged compared to an unpatterned layer. They should be suitable for first tests on thermally-controlled actuation, e.g. using interferometric methods.
2. Two patterning technologies were developed for 1 μm thick Ti-Ni-Cu films deposited at elevated temperatures: the first exploits lift-off method and the second uses wet-etching. Both were shown to be feasible, but delicate to implement. Considering that recent modification of the sputtering machine used for Ti-Ni-Cu film deposition has allowed enhancing of substrate cooling, it would be worth trying anew the lift-off patterning using conventional photoresists.
3. A procedure to fabricate Ti-Ni-Cu-based bridges and cantilevers on Si wafer was proposed. It should allow a future fabrication of a functional micro-scale thermal energy harvester.

Conclusions and outlook

The aims of this work were to experimentally evaluate the interest of coupling pyroelectric, piezoelectric and shape memory effects for thermal energy harvesting applications and to make first steps towards MEMS harvester fabrication on silicon.

Two original configurations of coupling shape memory and (pyro-)/piezoelectric materials were proposed and tested: a hybrid shape memory alloy (SMA)/piezoelectric machine and a hybrid laminated composite. All prototypes (even not optimized) showed relevant energy density for small temperature variations. The machine provided ~1.5 mJ/cm^3 at ΔT ~35°C and the composite ~0.5 mJ/cm^3 at ΔT ~50°C. It was shown that an SMA with a sharp phase transition is required for harvesting small temperature variations. The harvested energy could be increased by at least 1 order of magnitude, thanks to reasonable mechanical optimization (mostly gluing and assembling), and by decreasing the required amplitude of temporal temperature variation down to a few °C by fine tuning the SMA composition.

In contrast to the majority of piezoelectric-based energy harvesting studies, this work dealt with a quasi-static deformation of the piezoelectric (since quasi-static temperature variations are targeted). It was shown that the problem of piezoelectric charge leakage is critical in this case, and this aspect of piezoelectric materials has required a comprehensive investigation and lead to technical improvements through original contact-less measurement methods and electronics for the device.

The possibility of enhancement of any pyroelectric material by its coupling with an SMA was also proposed in this work, for the first time. Compared with the idea of coupling a pyroelectric just with an ordinary elastic material, our approach provides much higher thermally induced strain in a narrow temperature range. We achieved figure of merit of 6 V/°C which is 50 % of increase regarding conventional pyroelectric system.

Further, the use of soft (pyro-)piezoelectric polymers (PVDF and its co- and ter-polymers) would be advantageous for the proposed composite harvester. This approach is currently investigated in the frame of the PhD theses of Elena Gusarova (LETI) and Boris Gusarov (G2Elab).

Since the exploited effects do not deteriorate at scaling down, the study of how to integrate such materials into microscales with silicon technologies is now capital. It is even more decisive in terms of applications, since modern data transmission energy requirements are being reduced down to micro-Joules (and soon pico-Joules) per sent bit, which are values compatible with micro(nano)systems integration. In this work, first steps were taken towards a MEMS harvester while investigating the major building blocks:

- deposition of functional thin Ti-Ni-Cu films on silicon,
- film patterning with various techniques
- fabrication of Ti-Ni-Cu/SiO_2 bimorph membranes.

Establishing this know-how was crucial as 200 mm-Si integration in the LETI platform is now considered to go further towards industrial partnership.

Thereby, critical fabrication issues were assessed:

- Functional thin Ti-Ni-Cu films were successfully fabricated with a phase transformation close to room temperature. A combinatorial approach allowed obtaining alloys with various transition temperatures on one substrate (A_f ranging from 27 to 42 °C). However, the transformation should still be optimized in terms of temperature interval width. Now that the suitable compositions are known, the fabrication method should also be optimized in order to provide a more reproducible composition and homogeneous thickness. The most critical point was to avoid or reduce diffusion of silicon which is usually the unwelcome result of any process with high thermal balance (> 400°C). We enlighten the remarkable and atypical chemical interaction of the Ti-Ni-Cu film with SiO_2 which is commonly used as a diffusion barrier in microsystems. More specific studies are needed to ascertain the main source of oxidation/diffusion of species into Ti-Ni-Cu films.

- Ti-Ni-Cu/SiO_2 bimorph membranes were successfully fabricated using back side deep reactive ion etching of the Si substrate, and were found to be quite robust mechanically. The films functional properties remained almost unchanged after patterning. The optimization directions were given.

The fabrication of a complete MEMS harvester may likely require patterning and releasing membranes of the Ti-Ni-Cu layer depending on the chosen structures. Patterning of Ti-Ni-Cu films was studied for the first time within the CMOS technological community at MINATEC. It was shown that the use of lift-off method is difficult if, as in our case, the substrate cannot be cooled properly during film deposition. Therefore, wet etching is preferable, but it requires in turn specific chemistries which have been successfully investigated. The detailed lift-off and wet etching procedures were reported. Also, a procedure for the release of Ti-Ni-Cu/SiO_2 bimorph membrane and/or cantilever structures using wet etching was proposed but not yet tested.

To conclude, this study is one of the pioneer works, together with few others which appeared during last two years, exploring in details the coupling of shape memory, piezoelectric and pyroelectric effects. The results and prospects presented here are promising and establish some of the first stones towards industrial applications for an alternative technology for thermal harvesting. It is worth writing that the conservative CMOS industry is now opened to evaluate such concept. Besides the silicon industry, this concept already extends to plastic technologies. New markets such as active RF-ID tags are based on expected breakthrough flexible solutions for energy harvesting, and our concept is compatible. Two PhD works are already exploring these new territories.

Last but not least, the SMA-based functional structures that were targeted in this work can be coupled not only with (pyro-)piezoelectrics, but also with other functional materials. For example, thanks to their high controllable strain, they can be used as stress generators for magnetization rotation of magnetostrictive materials as developed by Gor Lebedev [**167**]. Based on this idea, new

(micro)composite materials with controllable magnetic properties can be proposed, opening even broader new horizons in successful integration and exploitation of multifunctional materials.

References

[1] T Huesgen, P Woias, and N Kockmann, "Design and fabrication of MEMS thermoelectric generators with high temperature efficiency ," *Sensors and Actuators A: Physical*, vol. 145-146, pp. 423-429, 2007.

[2] S Sebald, E Lefeuvre, and D Guyomar, "Pyroelectric energy conversion: optimisation principles," *IEEE Trans. Ultrason. Ferroelectr. Freq. Control*, vol. 55, pp. 538-551, 2008.

[3] L Carlioz, J Delamare, and S Basrour, "Proc. Solid-State Sensors, Actuators and Microsystems Conf., Transducers 2009," in *Temperature threshold tuning of thermal harvesting switch*, 21-25 June, Denver, USA, 2009, pp. 1385-1388.

[4] A Sozinov, A A Likhachev, N Lanska, and K Ullakko, "Giant magnetic-field-induced strian in NiMnGa seven-layered martensitic phase," *Appl. Phys. Lett.*, vol. 80, pp. 1746-1748, 2002.

[5] D C Lagoudas, *Shape memory alloys: modeling and engineering applications*. New York, USA: Springer, 2008.

[6] N Nersessian, G P Carman, and H B Radousky, "Energy harvesting using thermoelectric material," US patent application publication US 2005/0205125 A1, 2005.

[7] G A Lebedev et al., "Thermal energy harvesting using shape memory/piezoelectric composites," in *Proc. 16th Int. Conf. on Solid-State Sensors, Actuators and Microsystems, Transducers 2011*, Beijing, China, 2011, pp. 669-670.

[8] O C Namli and M Taya, "Design of Piezo-SMA Composite for Thermal Energy Harvester Under Fluctuating Temperature," *Journal of Applied Mechanics* , vol. 78, no. 3, p. 031001, 2011.

[9] R Zarnetta et al., "R-phase formation in Ti39Ni45Cu16 shape memory thin films and bulk alloys discovered by combinatorial methods," *Acta Materialia*, vol. 57, pp. 4169-4177, 2009.

[10] P Wollants, J R Roos, and L Delaey, "On the stress dependence of the latent heat of transformation as related to the efficiency of a work performing cycle of a memory engine," *Scr. Metall*, vol. 14, no. 11, pp. 1217-1223, 1980.

[11] T A Buldakova, Yu V Voitenko, V A Likhachev, and A I Razor, "Thermomechanical cycles in martensite energy converters," *Journal of Engineering Physics*, vol. 59, no. 2, pp. 1029-1035, 1990.

[12] Young Liu, "The work production of shape memory alloy," *Smart Mater. Struct.*, vol. 13, pp. 552-561, 2004.

[13] S Miyazaki, Y Fu, and W Huang, *Thin Film Shape Memory Alloys: Fundamentals and Device*

Applications. New York, USA: Cambridge University Press, 2009.

[14] C M Jackson, H G Wagner, and R G Wasilewski, "55-Nitinol – The alloy with a memory: its physical metallurgy, properties, and applications," National Aeronautics and Space Administration, Washington, D.C, Report NASA - SP 5110, 1972.

[15] (2012) www.piceramic.com.

[16] J Fang, H Frederich, and L Pilon, "Harvesting Nanoscale Thermal Radiation Using Pyroelectric Materials," *Journal of Heat Transfer*, vol. 132, p. 092701, 2010.

[17] D Zakharov et al., "An enhanced composite scheme of shape memory actuator for smart systems," *Physics Procedia*, vol. 10, pp. 58–64, 2010.

[18] C. He, M.E. Kiziroglou, D.C. Yates, and E.M. Yeatman, "A MEMS Self-Powered Sensor and RF Transmission Platform for WSN Nodes," *IEEE Sensors Journal*, vol. 11, no. 12, pp. 3437-3445, 2011.

[19] D. Steingart, "Power sources for wireless sensor networks," in *Energy harvesting technologies*, S. Priya and D.J. Inman, Eds. New York, USA: Springer, 2009, ch. 9, p. 273.

[20] P.-S. Song, "Molecular topography of solar energy harvesting pigments in marine algae," *Trends in Biochemical Sciences*, vol. 3, no. 1, pp. 25-27, 1978.

[21] F.R. Aussenegg, M.E. Lippitsch, and M. Riegler, "Picosecond spectroscopy of photoreceptor molecules," *Laser Chem.*, vol. 6, pp. 269-289, 1986.

[22] N. Vlachopoulos, P. Liska, J. Augustynski, and M. Gratzel, "J. Am. Chem. Soc," *Very efficient visible light energy harvesting and conversion by spectral sensitization of high surface area polycrystalline titanium dioxide films*, vol. 110, no. 4, pp. 1216-1220, 1988.

[23] T. Starner, "Human-powered wearable computing," *IBN Systems Journal*, vol. 35, no. 3&4, pp. 1-12, 1996.

[24] J. Kymissis, C. Kendall, J. Paradiso, and N. Gershenfeld, "Parasitic power harvesting in shoes," in *Digest of Papers. Second International Symposium onWearable Computers*, Pittsburgh, PA, USA, 1998, pp. 132-139.

[25] J.M. Rabaey, M.J. Ammer, J.L. da Silva, D. Patel, and S. Roundy, "PicoRadio supports ad hoc ultra-low power wireless networking," *Computer*, vol. 33, no. 7, pp. 42-48, 2000.

[26] S.R. Anton and H.A. Sodano, "A review of power harvesting using piezoelectric materials (2003–2006)," *Smart Mater. Struct.*, vol. 16, pp. R1-R21, 2007.

[27] S.P. Beeby, M.J. Tudor, and N.M White, "Energy harvesting vibration sources for microsystems applications," *Meas. Sci. Technol.*, vol. 17, pp. R175-R195, 2006.

[28] H.A. Sodano, D.J. Inman, and G. Park, "A review of power harvesting from vibration using piezoelectric materials," *LA-UR-03-5397, The Shock and Vibration Digest*, vol. 36, no. 3, pp.

197-205, 2004.

[29] (2014) Energy harvesting wireless solutions and networks from EnOcean. [Online]. http://www.enocean.com/

[30] (2014) ALGRA AG. [Online]. http://www.algra.ch/

[31] (2014) Micropelt Energy Saving. [Online]. http://www.micropelt.com/

[32] (2014) Pertuum. [Online]. http://www.perpetuum.com/

[33] G. Sebald, D. Guyomar, and A. Agbossou, "On thermoelectric and pyroelectrci energy harvesting," *Smart. Mater. Struct.*, vol. 18, p. 125006, 2009.

[34] S.K.T. Ravindran, M. Kroener, and P. Woias, "A bimetallic micro heat engine for pyroelectric energy conversion," in *Proc. Eurosensors XXVI*, Kraków, Poland, 2012, pp. 33-36.

[35] S.R. Hunter et al., "Development of MEMS based pyroelectric thermal energy harvesters," in *Proc. SPIE 8035, Energy Harvesting and Storage: Materials, Devices, and Applications II*, Orlando, Florida, USA, 2011.

[36] G.J. Snyder, "Small thermoelectric generators," *The Electrochemical Society Interface*, no. Fall 2008, pp. 54-56.

[37] G.J. Snyder and E.S. Toberer, "Complex thermoelectric materials," *Nature Materials*, vol. 7, pp. 105-114, 2008.

[38] G.J. Snyder, "Thermoelectric energy harvesting," in *Energy harvesting technologies*, S. Priya and D.J. Inman, Eds. New York, USA: Springer, 2009, ch. 11, pp. 325-336.

[39] H.B. Radousky and H. Liang, "Energy harvesting: an integrated view of materials, devices and applications," *Nanotechnology*, vol. 23, p. 502001, 2012.

[40] M. Stordeur and I. Stark, "Low power thermoelectric generator-self-sufficient energy supply for micro systems," in *Proceedings ICT '97. XVI International Conference onThermoelectrics*, Dresden, 1997, pp. 575-577.

[41] J.A. Paradiso and T. Starner, "Energy scavenging for mobile and wireless electronics," *IEEE Pervasive Computing*, vol. 4, no. 1, pp. 18-27, 2005.

[42] W.G. Cady, *Piezoelectricity*. New York/London: McGraw-Hill Book Company, 1946, ch. XXIX, p. 699.

[43] S.B. Lang, "Pyroelectricity: From Ancient Curiosity to Modern Imaging," *Physics Today*, vol. 58, pp. 31-36, 2005.

[44] S. Priya and D.J. Inman, Eds., *Energy harvesting technologies*. New York, USA: Springer, 2009.

[45] J. Paulo and P.D. Gaspar, "Review and future trend of energy harvesting methods for portable medical devices," in *Proceedings of the World Congress on Engineering 2010 Vol II*, London, UK, 2010.

[46] S. Chalasani and J.M. Conrad, "A survey of energy harvesting sources for embedded systems," in *IEEE Southeastcon*, Huntsville, AL, 2008, pp. 442-447.

[47] J. Xie, P.P. Mane, C.W. Green, K.M. Mossi, and K.K. Leang, "Energy harvesting by pyroelectric effect using PZT," in *Proceedings of ASME Conference on Smart Materials, Adaptive Structures and Intelligent Systems*, Ellicott City, Maryland, USA, 2008, pp. 1-5.

[48] P. Mane, J. Xie, K.K. Leang, and K. Mossi, "Cyclic energy harvesting from pyroelectric materials," *IEEE transactions on ultrasonics, ferroelectrics, and frequency control*, vol. 58, no. 1, pp. 10-17, 2011.

[49] A. Cuadras, M. Gasulla, and V. Ferrari, "Thermal energy harvesting through pyroelectricity," *Sensors and Actuators A: Physical*, vol. 158, pp. 132-139, 2010.

[50] C.R. Bowen, H.A. Kim, P.M. Weaver, and S. Dunn, "Piezoelectric and ferroelectric materials and structures for energy harvesting applications," *Energy Environ. Sci.*, vol. 7, no. 25, pp. 25-44, 2014.

[51] R.E. Newnham, D.P. Skinner, and L.E. Cross, "Connectivity and piezoelectric-pyroelectric composites," *Mat. Res. Bull.*, vol. 13, pp. 525-536, 1978.

[52] M.L. Dunn, "Micromechanics of coupled electroelastic composites: effective thermal expansion and pyroelectric coefficients," *J. Appl. Phys.*, vol. 73, no. 10, pp. 5131-5140, 1993.

[53] C.-W. Nan, "Product property between thermal expansion and piezoelectricity in piezoelectric composites: pyroelectricity," *Journal of materials science letters*, vol. 13, pp. 1392-1394, 1994.

[54] L. Pintilie, I. Pintilie, and I. Matei, "Equivalent pyroelectric coefficient of a pyroelectric bimorph structure," *Journal of applied physics*, vol. 88, no. 12, pp. 7264-7271, 2000.

[55] M. Alexe and L. Pintilie, "Thermal analysis of the pyroelectric bimorph as radiation detector," *Infrared Physics & Technology*, vol. 36, pp. 949-954, 1995.

[56] H.H. Chang and Z. Huang, "Substantial pyroelectric effect enhancement in laminated composites," *Appl. Phys. Lett.*, vol. 92, p. 52903, 2008.

[57] H.H.S. Chang, R.W. Whatmore, and Z. Huang, "Pyroelectric effect enhancement in laminate composites under short circuit condition," *J. Appl. Phys.*, vol. 106, p. 114110, 2009.

[58] H.H.S. Chang and Z. Huang, "Pyroelectric effect enhancement through product property under open circuit condition," *J. Appl. Phys.*, vol. 106, p. 014101, 2009.

[59] M.J. Hockley, H.H.S. Chang, and Z. Huang, "Pyroelectric coefficient difference under open and short circuit conditions and their enhancements in laminate composites," *Journal of Applied Physics*, vol. 109, p. 064102, 2011.

[60] H.H.S. Chang and Z. Huang, "Laminate composites with enhanced pyroelectric effects for energy harvesting," *Smart Mater. Struct.*, vol. 19, p. 065018, 2010.

[61] L. Carlioz, J. Delamare, and S. Basrour, "Energy scavenging using hybrid thermo-magnetic/PZT structure," in *Proc. of Joint European Magnetics Symposia (JEMS'08)*, Dublin, Ireland, 2008.

[62] L. Carlioz, J. Delamare, S. Basrour, and G. Poulin, "Hybridization of magnetism and piezoelectricity for an energy scavenger based on temporal variation of temperature," in *Proc. of Symposium on Design, Test, Integration and Packaging of MEMS/MOEMS*, Nice, France, 2008.

[63] C. Jean-Mistral et al., "Thermo-magnetic, piezo-electric and electroactive energy harvesting devices," *MRS Proceedings*, vol. 1218, pp. 1218-Z04-03, 2009.

[64] V. Srivastava, Y. Song, K. Bhatti, and R.D. James, "The Direct Conversion of Heat to Electricity Using Multiferroic Alloys," *Adv. Energy Mater.*, vol. 1, pp. 97-104, 2011.

[65] I. Soursa, J. Tellinen, K. Ullakko, and E. Pagounis, "Voltage generation induced by mechanical straining in magnetic shape memory materials," *Journal of Applied Physics*, vol. 95, no. 12, pp. 8054-8058, 2004.

[66] I. Karaman, B. Basaran, and H.E. Karaca, "Energy harvesting using martensite variant reorientation mechanism in a NiMnGa magnetic shape memory alloy," *Appl. Phys. Lett.*, vol. 90, p. 172505, 2007.

[67] J.L. Wardlaw, I. Karaman, and A.I. Karsilayan, "Low-power circuits and energy harvesting for structural health monitoring of bridges," *IEEE Sensors Journal*, vol. 13, no. 2, pp. 709-722, 2013.

[68] J. Chen., Q.C. Xu, M. Blaszkiewicz, R. Jr. Meyer, and R.E. Newnham, "Lead Zirconate Titanate Films on Nickel-Titanium Shape Memory Alloys: SMARTIES," *J. Am. Ceram. Soc.*, vol. 75, no. 10, pp. 2891-2892, 1992.

[69] D.C. Lagoudas and Z. Bo, "The cylindrical bending of composite plates with piezoelectric and SMA layers," *SmanMaler. Slruct.*, vol. 3, pp. 309-317, 1994.

[70] S.B. Choi, Y.K. Park, and T. Fukuda, "A proof of concept investigation on active vibration control of hybrid smart structures," *Mechatronics*, vol. 8, pp. 562-578, 1998.

[71] B. Jiang and R.C. Batra, "Micromechanical modeling of a composite containing piezoelectric and shape memory alloy inclusions," *Journal of Intelegent Material Systems and Structures*, vol. 12, pp. 165-182, 2001.

[72] H.A. Kim, D.N. Betts, A.I.T. Salo, and C.R. Bowen, "Shape Memory Alloy-Piezoelectric Active Structures for Reversible Actuation of Bistable Composites," *AIAA Journal*, vol. 48, no. 6, pp. 1265-1268, 2010.

[73] D.N. Betts, H.A. Kim, and C.R. Bowen, "Modeling and optimization of bistable composite laminates for piezoelectric actuation," *Journal of Intelligent Material Systems and Structures*, vol. 22, no. 18, pp. 2181-2191, 2011.

[74] M.R. Alam, A. Kumar, N. Shu, H.L. Chan, and Q. You, "Preparation of TiNi ferroelastic–ferroelectric thin film heterostructures," *Applied Surface Science*, vol. 109/110, 393-398 1997.

[75] A. Kumar, M.R. Alam, J.J. Weimer, and L. Sanderson, "Synthesis and characterization of laser ablated TiNi films ," *Appl. Phys. A* , vol. 69, pp. S917-S920, 1999.

[76] T.J. Zhu, X.B. Zhao, and L. Lu, "Pb(Zr0.52Ti0.48)O3/TiNi multilayered heterostructures on Si substrates for smart systems," *Thin Solid Films*, vol. 515, pp. 1445–1449, 2006.

[77] H. Sato, "Development of multifunctional wire that combines shape-memory alloy to piezo electric material," in *Proc. SPIE 6929, Behavior and Mechanics of Multifunctional and Composite Materials*, San Diego, USA, 2008, p. 69291I.

[78] M. Zheng, S.W. Or, and H.L.W. Chan, "Effect of phase transformation on the converse magnetoelectric properties of a heterostructure of Ni49.2Mn29.6Ga21.2 and 0.7PbMg1/3Nb2/3O3-0.3PbTiO3 crystals," *Appl. Phys. Lett.*, vol. 96, no. 18, p. 182503, 2010.

[79] M. Zhang, S.W. Or, and H.L.W. Chan, "Large magnetoelectric effect from mechanically mediated magnetic field-induced strain effect in Ni–Mn–Ga single crystal and piezoelectric effect in PVDF polymer," *Journal of Alloys and Compounds*, vol. 490, pp. L5–L8, 2010.

[80] M. Zheng, S.W. Or, and H.L.W. Chan, "Magnetic field-induced strain and magnetoelectric effects in sandwich composite of ferromagnetic shape memory Ni-Mn-Ga crystal and piezoelectric PVDF Polymer," *IEEE transactions on ultrasonis, ferroelectrics, and frequency control*, vol. 57, no. 10, pp. 2147-2153, 2010.

[81] O.C. Namli, J.-K. Lee, and M. Taya, "Modeling of piezo-SMA composites for thermal energy harvester," in *Proc. SPIE 6526, Behavior and Mechanics of Multifunctional and Composite Materials* , San Diego, California, 2007, p. 65261L.

[82] D. Zakharov et al., "Thermal energy conversion by coupled shape memory and piezoelectric effects," *J. Micromech. Microeng.*, vol. 22, p. 094005, 2012.

[83] D. Avirovik, A. Kumar, R.J. Bodnar, and S. Priya, "Remote light energy harvesting and actuation using shape memory alloy-piezoelectric hybrid transducer," *Smart Mater. Struct.*, vol. 22, p. 052001, 2013.

[84] J. Ye, R.K. Mishra, A.R. Pelton, and A.M. Minor, "Direct observation of the NiTi martensitic phase transformation in nanoscale volumes," *Acta Mater*, vol. 58, pp. 490–498, 2010.

[85] D.I. Zakharov et al., "A composite functional material with shape memory effect exhibiting a giant reversible straining," *Functional Materials*, vol. 15, no. 3, pp. 448-454, 2008.

[86] V.V. Khovaylo et al., "Imprinting Bias Stress in Functional Composites," *Japanese Journal of Applied Physics*, vol. 49, p. 100212, 2010.

[87] D.I. Zakharov et al., "Actuators based on composite material with shape-memory effect,"

Journal of Communications Technology and Electronics, vol. 55, no. 7, pp. 874-886, 2010.

[88] D. Zakharov et al., "Submicron-sized actuators based on enhanced shape memory composite material fabricated by FIB-CVD," *Smart Mater. Struct.*, vol. 21, p. 052001, 2012.

[89] A. Irzhak et al., "Development of laminated nanocomposites on the bases of magnetic and non-magnetic shape memory alloys: Towards new tools for nanotechnology," *Journal of Alloys and Compounds*, vol. 586, pp. S464–S468, 2014.

[90] A Lee et al., "A practical microgripper by fine alignment, eutectic bonding and SMA actuation," *Sensors and Actuators A*, vol. 54, pp. 755-759, 1996.

[91] K. Akatyeva et al., "Shape memory effect in microsized samples of rapidly quenched ferromagnetic alloy Ni-Mn-Ga," *Solid State Phenomena*, vol. 190, pp. 295-298, 2012.

[92] K. Otsuka and C.M. Wayman, Eds., *Shape memory materials*. Cambridge, UK: Cambridge Univercity Press, 1998.

[93] K. Otsuka and X. Ren, "Physical metallurgy of Ti-Ni-based shape memory alloys," *Progress in Materials Science*, vol. 50, pp. 511-678, 2005.

[94] R. Zarnetta, "Combinatorial developement and discovery of ternary and quaternary shape memory alloys," Ruhr-Universitat Bochum, Bochum, Dissertation 2010.

[95] M. Tomozawa, H.Y. Kim, and S. Miyazaki, "Shape memory behavior and internal structure of Ti–Ni–Cu shape memory alloy thin films and their application for microactuators," *Acta Materialia*, vol. 57, pp. 441-452, 2009.

[96] M. Tomozawa, H.Y. Kim, A. Yamamoto, S. Hiromoto, and S. Miyazaki, "Effect of heat treatment temperature on the microstructure and actuation behavior of a Ti-Ni-Cu thin film microactuator," *Acta Materialia*, vol. 58, pp. 6064-6071, 2010.

[97] M. Tomozawa, H.Y. Kim, and S. Miyazaki, "Microactuators using R-phase transformation of sputter-deposited Ti-47.3Ni shape memory alloy thin films," *Journal of Intelligent Material Systems and Structures*, vol. 17, no. 12, pp. 1049-1058, 2006.

[98] N J Conway, Z J Traina, and S-G Kim, "A strain amplifying piezoelectric MEMS actuator," *J. Micromech. Microeng.*, vol. 17, pp. 781–787, 2007.

[99] J-H Park et al., "Tensile test of lead zirconate titanate (PZT)/Platinum (Pt) thin film," *Mat.-wiss. u.Werkstofftech.*, vol. 42, no. 5, pp. 478-484, 2011.

[100] R Dittmer et al., "Microstructural analysis and mechanical properties of Pb(Zr,Ti)O3 fibers derived by different processing routes," *J. Am. Ceram. Soc.*, vol. 93, no. 8, pp. 2403–2410, 2010.

[101] T Tanimoto, K Yamamoto, and T Morii, "Nonlinear stress-strain behavior of piezoelectric ceramics under tensile loading," in *Proceedings of the Ninth IEEE International Symposium on Applications of Ferroelectrics*, University Park, PA, 1994, pp. 394-397.

[102] I P Lipscomb, P M Weaver, J Swinglera, and J W McBridea, "The effect of relative humidity, temperature and electrical field on leakage currents in piezo-ceramic actuators under dc bias," *Sensors and Actuators A: Physical*, vol. 151, pp. 179–186, 2009.

[103] (2010) Smart Material MFC technical data sheet. [Online]. http://www.smart-material.com

[104] H.A. Sodano, "Macro-fiber composites for sensing, actuation and power generation," Virginia Polytechnic Institute and State University, Blacksburg, Virginia, Thesis of Master of Science 2003.

[105] A V Shelyakov et al., "Melt-spun thin ribbons of shape memory TiNiCu alloy for micromechanical applications," *International Journal of Smart and Nano Materials*, vol. 2, no. 2, pp. 68-77, 2011.

[106] E. Gusarova et al., "An improved method for piezoelectric characterization of polymers for energy harvesting applications," *Journal of Physics: Conference Series*, vol. 476, p. 012061, 2013.

[107] R. Brett Williams, Daniel J. Inman, and W. Keats Wilkie, "Temperature-dependent thermoelastic properties for Macro Fiber Composite actuators," *Journal of Thermal Stresses*, vol. 27, no. 10, pp. 903-915, 2004.

[108] W Y Ng, Bernd Ploss, H L W Chan, F G Shin, and C L Choy, "The 2000 12th IEEE International Symposium On Applications Of Ferroelectrics," in *Pyroelectric Properties of PZT/P(VDF-TrFE) 0-3 Composites*, vol. 2, Honolulu, Hawaii, 2000, pp. 767-770.

[109] L Pintilie and I Pintilie, "Temperature dependence of the pyroelectric voltage in a 2–2 connectivity pyroelectric bimorph," *Ferrorlrctrics*, vol. 200, pp. 219-235, 1997.

[110] E E Crisman, J S Derov, A J Drehman, and O J Gregory, "Large pyroelectric response from reactively sputtered aluminum nitride thin films," *Electrochemical and Solid-State Letters*, vol. 8, no. 3, pp. H31-H32, 2005.

[111] J Xie, X P Mane, C W Green, K M Mossi, and K K Leang, "Performance of thin piezoelectric materials for pyroelectric energy harvesting," *Journal of Intelligent Material Systems and Structures*, vol. 21, no. 3, p. 243, 2010.

[112] (2013) Morgan Electro Ceramics. [Online]. http://www.morganelectroceramics.com/resources/piezo-ceramic-tutorials/typical-properties/

[113] Thomas Lafont et al., "Magnetostrictive–piezoelectric composite structures for energy harvesting," *J. Micromech. Microeng.*, vol. 22, p. 094009 (6pp), 2012.

[114] N BarChaim, M Brunstein, J Grunberg, and A Seidman, "Electric field dependence of the dielectric constant of PZT ferroelectric ceramics," *J. Appl. Phys.*, vol. 45, no. 6, pp. 2398-2405, 1974.

[115] Ch Ang and Zh Yu, "Dielectric behavior of PbZr0.52Ti0.48O3 thin films: Intrinsic and extrinsic dielectric responses," *Appl. Phys. Lett.*, vol. 85, no. 7, pp. 3821-3823, 2004.

[116] G D Boyd, R C Miller, K Nassau, W L Bond, and A Savage, "LiNbO3: an efficient phase matchable nonlinear optical material," *Appl. Phys. Lett.*, vol. 5, no. 11, p. 234, 1964.

[117] W R Cook, D A Berlincourt, and F J Scholz, "Thermal expansion and pyroelectricity in lead titanate zirconate and barium titanate," *J. Appl. Phys.*, vol. 34, no. 5, p. 1392, 1963.

[118] Yongqing Fu and Hejun Du, "RF magnetron sputtered TiNiCu shape memory alloy thin film," *Materials Science and Engineering A*, vol. 339, pp. 10-16, 2003.

[119] John J Friel, *X-ray and image analysis in electron microscopy*, 2nd ed. Princeton, USA: Princeton Gamma-Tech, 2003.

[120] M Tomozawa, H Y Kim, and S Miyazaki, "Shape Memory Behavior and Internal Structure of Ti-Ni-Cu Shape Memory Alloy Thin Films and Their Application for Microactuators," *Acta Materialia*, vol. 57, pp. 441-452, 2009.

[121] X.-D. Xiang et al., "A combinatorial approach to materials diiscovery," *Science*, vol. 268, no. 5218, pp. 1738-1740, 1995.

[122] Sputtering yield rates. [Online]. http://www.semicore.com/reference/sputtering-yields-reference

[123] M Nishida, C M Wayman, and T Honma, "Precipitation processes in near-equiatomic TiNi shape memory alloys," *Metallurgical Transactions A*, vol. 17A, pp. 1505-1515, 1986.

[124] Xiaopeng Liu, Mingzhou Cao, and Wei Jin, "Effect of annealing temprerature on transformation behaviors of Ti-50.2 at pct Ni thin film," *J. Mater. Sci. Technol.* , vol. 17, no. 1, pp. S40-S42, 2001.

[125] Takashi Fukuda, Tomoyuki Kakeshita, and Toshio Saburi, "Copper content dependence of the lattice parameters of Ti(NiCu)2," *Materials Transactions JIM*, vol. 41, no. 7, pp. 837-840, 2000.

[126] Cesare Borgia, Sven Olliges, Marianne Dietiker, Giancarlo Pigozzi, and Ralph Spolenak, "A combinatorial study on the influence of Cu addition, film thickness and heat treatment on phase composition, texture and mechanical properties of Ti–Ni shape memory alloy thin films," *Thin Solid Films*, vol. 518, pp. 1897–1913, 2010.

[127] A E Dwight, "Institute of Metals Division - CsC1-type equiatomic phases in binary alloys of transition elements," *Trans. Am. Inst. Mining Metal. Eng.*, vol. 215, p. 283, 1959.

[128] T Goryczka and H Morawiec, "Structure studies of the R-phase using X-ray diffraction methods," *Journal of Alloys and Compounds*, vol. 367, pp. 137-141, 2004.

[129] W Biihrer, R Gotthardt, A Kulik, O Mercier, and F Staub, "Powder neutron diffraction study of nickel-titanium martensite," *J. Phys. F: Met. Phys.*, vol. 13, pp. L77-L81, 1983.

[130] P L Potapov et al., "Crystal structure of orthorombic martensite in TiNi-Cu and TiNi-Pd

intermetallics," *J. Phys. IV*, vol. 112, p. 727, 2003.

[131] T Saburi, S Nenno, and T Fukuda, "Crystal structure and morphology of the metastable X phase in shape memory Ti-Ni alloys," *Journal of the Less-Common Metals*, vol. 125, pp. 157-166, 1986.

[132] W Mayo, H & M Analytical Services, Inc., Allentown, NJ, USA, ICDD Grant-in-Aid 1999.

[133] M H Mueller and H W Knott, "The Crystal Structures of Ti2Cu, Ti2Ni, Ti4Ni2O and Ti4Cu2O," *Trans. Met. Soc. AIME*, vol. 227, p. 674, 1963.

[134] Toru Hara, Takuya Ohba, Kazuhiro Otsuka, and Minoru Nishida, "Phase transformation and crystal structures of Ti2Ni3 precipitates in Ti-Ni alloys," *Materials Transactions JIM*, vol. 38, no. 4, pp. 277-284, 1997.

[135] Susanne Stemmer, Gerd Duscher, Christina Scheu, Arthur H. Heuer, and Manfred Ruhle, "The reaction between a TiNi shape memory thin film and silicon," *J. Mater. Res.*, vol. 12, no. 7, pp. 1734-1740, 1997.

[136] L.S. Hung and J.W. Mayer, "Interactions of four metallic compounds with Si substrates," *Journal of Applied Physics*, vol. 60, no. 3, pp. 1002-1008, 1986.

[137] I Sieber, H Lange, and K Schade, "Phase Transformations in the Ni-Ti-Si System," *phys. stat. sol. (a)*, vol. 126, pp. 171-179, 1991.

[138] Sarah Ackerbauer, Nataliya Krendelsberger, Franz Weitzer, Kurt Hiebl, and Julius C. Schuster, "The constitution of the ternary system Fe–Ni–Si," *Intermetallics*, vol. 17, pp. 414-420, 2009.

[139] Franz Weitzer, Julius C. Schuster, Masaaki Naka, Frank Stein, and Martin Palm, "On the reaction scheme and liquidus surface in the ternary system Fe-Si-Ti," *Intermetallics*, vol. 16, pp. 273-282, 2008.

[140] F Weitzer et al., "The Ternary System Nickel/Silicon/Titanium Revisited," *Z. Anorg. Allg. Chem.*, vol. 636, pp. 982-990, 2010.

[141] A Grytsiv et al., "Crystal chemistry of the G-phases in the

[142] F. Bosselet, J. Viala, C. Colin, B. Mentzen, and J. Bouix, "Solid-state solubility of aluminium in the delta-Ni2Si nickel silicide," *Mater. Sci. Eng.*, vol. 167, no. 1-2, pp. 147-154, 1993.

[143] B. Shoemaker and D.P. Shoemaker, "A ternary alloy with PbCl2-type structure: TiNiSi(E)," *Acta Crystallogr.*, vol. 18, p. 900, 1965.

[144] G.V. Samsonov, L.N. Okhrenchuk, N.F. Podgrushko, I.A. Podchernyaeva, and V.S. Fomenko, "Relations between the electron work function and certain physical properties in silicides of group-IV transition metals," *Inorg. Mater. (Engl. Transl.)*, vol. 12, p. 720, 1976.

[145] X.L. Yan et al., "On the ternary Laves phases (Sc,Ti)2M3Si (M = Cr, Mn, Fe, Co, Ni) with MgZn2-type," *J. Alloys Compds.*, vol. 429, no. 10, p. 18, 2007.

[146] E. Horache, T. Feist, and J. Stuart, "Neutron Rietveld refinement of the structure of the ternary silicide Ti4Ni4Si7," *Journal of Materials Research*, vol. 5, no. 9, pp. 1887-1893, 1990.

[147] O Thomas et al., "Residual Stresses in Metallic Multilayers," *Journal de Physique IV*, vol. 6, pp. C7-125, 1996.

[148] T. Waitz, V. Kazykhanov, and H.P. Karnthaler, "Martensitic phase transformations in nanocrystalline NiTi studied by TEM," *Acta Materialia*, vol. 52, pp. 137-147, 2004.

[149] J.O. Diaz, "A feature-to-wafer-scale model of etch-rate non-uniformity in deep reactive ion etching," Massachusetts Institute of Technology. Dept. of Electrical Engineering and Computer Science, Thesis (M. Eng.) 2010.

[150] K.R. Williams, K. Gupta, and M. Wasilik, "Etch rates for micromachining processing—Part II," *Journal of Microelectromechanical systems*, vol. 12, no. 6, pp. 761-778, 2003.

[151] S. Jensen, J.M. Jensen, U.J. Quaade, and O. Hansen, "Uniformity-improving dummy structures for deep reactive ion etching (DRIE) processes," in *Proc. SPIE 5715, Micromachining and Microfabrication Process Technology X*, San Jose, CA, 2005, pp. 39-46.

[152] J A Walke, K J Gabriel, and M Mehregany, "Thin film processing of TiNi shape memory alloy," *Sensors and Actuators*, vol. A21-A23, pp. 243-246, 1990.

[153] J Z Chen and S K Wu, "Chemical machined thin foils of TiNi shape memory alloy," *Materials Chemistry and Physics*, vol. 58, pp. 162-165, 1999.

[154] John J Gill, David T Chang, Leslie A Momoda, and Greg P Carman, "Manufacturing issued of thin film NiTi microwrapper," *Sensors and Actuators A*, vol. 93, pp. 148-156, 2001.

[155] Dong Xu et al., "Characteristics and fabrication of NiTi/Si diaphragm micropump," *Sensors and Actuators A*, vol. 93, pp. 87-92, 2001.

[156] Daniel D Shin, Dong-Gun Lee, Kotekar P Mohanchandra, and Gregory P Carman, "Thin film NiTi microthermostat array," *Sensors and Actuators A*, vol. 130-131, pp. 37-41, 2006.

[157] Y Q Fu et al., "A shape memory microcage of TiNi/DLC films for biological applications," *J. Micromech. Microeng.*, vol. 18, p. 035026, 2008.

[158] Y Q Fu et al., "Microactuators of free-standing TiNiCu films," *Smart Mater. Struct.*, vol. 16, pp. 2651-2657, 2007.

[159] John J Gill, Ken Ho, and Carman P. Greg, "Three-dimensional thin-film shape memory alloy microactuator with two-way effect," *J. Microelectromech. Syst.*, vol. 11, no. 1, pp. 68-77, 2002.

[160] Yousuke Nakamura, Shigeo Nakamura, Lionel Buchaillot, and Hiroyuki Fujita, "A three-dimensional shape memory alloy loop actuator," *Proc.IEEE: Micro Electro Mechanical Systems, MEMS 97*, pp. 262-266, 1997.

[161] I Roch, Ph Bidaud, D Collard, and L Buchaillot, "Fabrication and characterization of an SU-8

gripper actuated by a shape memory alloy thin film," *J. Micromech. Microeng.*, vol. 13, pp. 330-336, 2003.

[162] Myunghoon Seong, K P Mohanchandra, Yohan Lin, and Gregory P Carman, "Development of a 'bi-layer lift-off' method for high flow rate and high frequency Nitinol MEMS valve fabrication," *J. Micromech. Microeng.*, vol. 18, p. 075034, 2008.

[163] S T Davies et al., "Characterization of micromachining processes during KrF excimer laser ablation of TiNi shape memory alloy thin sheets and films," *Smart Mater. Struct.*, vol. 11, pp. 708-714, 2002.

[164] (2013) MicroChem: Innovative Chemical Solutions for MEMS and Microelectronics. [Online]. http://microchem.com/pdf/PMGI-Resists-data-sheetV-rhcedit-102206.pdf

[165] Jeremy Golden, Harris Miller, Dan Nawrocki, and Jack Ross. Optimization of Bi-layer Lift-Off Resist Process. [Online]. http://microchem.com/pdf/LOR-Extended-Abstract-Final.pdf

[166] John O Stoner Jr., "Stretched chromium foils," *Nuclear Instruments and Methods in Physics Research*, vol. A 480, pp. 44-49, 2002.

[167] G. Lebedev, "Composites multiferroïques pour dispositifs magnéto-électriques intégrés ," Universite de Grenoble, Grenoble, Dissertation 2012.

Scientific contributions and other records

PUBLICATIONS

- International peer-reviewed journals:

1. Thermal energy conversion by coupled shape memory and piezoelectric effects. D. Zakharov, G. Lebedev, O Cugat, J. Delamare, B. Viala, T. Lafont, L. Gimeno, and A. Shelyakov. 2012 *J. Micromech. Microeng.* **22** 094005
2. Converse magnetoelectric effect dependence with CoFeB composition in ferromagnetic/piezoelectric composites. G. Lebedev, B. Viala, T. Lafont, D. Zakharov, O. Cugat, and J. Delamare. 2012 *J. Appl. Phys.* **111** 07C725
3. Magnetostrictive-piezoelectric composite structures for energy harvesting. T. Lafont, L. Gimeno, J. Delamare, G. Lebedev, D. Zakharov**,** B. Viala, O. Cugat, N. Galopin, L. Garbuio, and O. Geoffroy. 2012 *J. Micromech. Microeng*. **22** 094009
4. Electric field controlled magnetization rotation in exchange biased antiferromagnetic/ferromagnetic/piezoelectric composites. G.A. Lebedev, B. Viala, T. Lafont, D.I. Zakharov, O. Cugat, J. Delamare. 2011 *Appl. Phys. Lett.* **99**, 232502

- Proceeding and reports:

1. Combined pyroelectric, piezoelectric and shape memory effects for thermal energy harvesting. D. Zakharov, B. Gusarov, E. Gusarova, B. Viala, O. Cugat, J. Delamare, and L. Gimeno. 2013 *J. Phys.: Conf. Ser.* **476** 012021
2. An improved method for piezoelectric characterization of polymers for energy harvesting applications. E. Gusarova, B. Gusarov, D. Zakharov, M. Bousquet, B. Viala, O. Cugat, J. Delamare, and L. Gimeno. 2013 *J. Phys.: Conf. Ser.* **476** 012061
3. Nanofunction-WP5 Annual and Final Report & Deliverable. Section 9.5 “Composites of thermal shape memory alloy and piezoelectric materials” B. Viala and D. Zakharov

- Patent:

1. Energy recovery system. B. Viala, G. Lebedev, J. Delamare, O. Cugat, D. Zakharov, L. Gimeno. Publication date: May 1, 2014. Publication number: WO2014063952 A1.

CONFERENCES

Presenting author is starred (*).

- Talks:

1. **The 11th International Workshop on Micro and Nanotechnology for Power generation and Energy Conversion Applications** PowerMEMS, Seoul, Korea, November 15-18, 2011 *Thermal energy conversion by coupled shape memory and piezoelectric effects* D. Zakharov*, G. Lebedev, O. Cugat, J. Delamare, B. Viala, T. Lafont, and A. Shelyakov
2. **2èmes Journées Nationales sur la Récupération et le Stockage d'Energie pour l'alimentation des microsystèmes autonomes** Grenoble, France, March 26, 2012 *Thermal energy conversion by coupled shape memory and piezoelectric effects* D.I. Zakharov*, G.A. Lebedev, J. Delamare, B. Viala, O. Cugat, T. Lafont, L. Gimeno
3. **The 13th International Workshop on Micro and Nanotechnology for Power generation and Energy Conversion Applications** PowerMEMS, London, UK, December 3-6, 2013 *Combined pyroelectric, piezoelectric and shape memory effects for thermal energy harvesting* D. Zakharov*, B. Gusarov, E. Gusarova, B. Viala, O. Cugat, J. Delamare, and L. Gimeno

- Posters:

1. **16th International Conference on Solid State Sensors, Actuators and Microsystems** Transducers'11, Beijing, China, June 5-9, 2011 *Thermal energy harvesting using shape memory/piezoelectric composites* G.A. Lebedev*, B.V, Gusarov, B. Viala, J. Delamare, O. Cugat, T. Lafont, and D.I. Zakharov
2. **Colloque National MECAMAT**, Aussois, France, January 22-28, 2012 *Thermal energy conversion by coupled shape memory and piezoelectric effects* D. Zakharov*, G. Lebedev, O. Cugat, J. Delamare, B. Viala, and T. Lafont

CONTESTS

The idea of commercialization of the scientific results obtained in the framework of this thesis was proposed by Gor Lebedev. Corresponding business plan prepared by Gor and myself together was selected and recognized by several high-level business competitions:

1. French national competition on innovation ideas "Innovons Ensemble", Paris, France, 2011: **2nd place**
2. European competition on business ideas "Intel Business Challenge Europe", Sopot, Poland, 2012: **Investors' Prize**
3. World competition on business ideas "Intel Global Challenge", Berkeley, USA, 2012: one of the **World's best 30** projects

Matériaux composites à base d'alliage à mémoire de forme et pyro-/piézoélectrique pour la récupération d'énergie thermique

RESUME

Cette thèse étudie expérimentalement la possibilité de récupérer l'énergie thermique en utilisant un alliage à mémoire de forme (AMF) couplé à un matériau pyro-/piézoélectrique. Cette méthode est prometteuse pour récupérer les variations lentes et petites de température. Les premiers prototypes de récupérateurs d'énergie ont été fabriqués et ont démontré pouvoir produire une énergie spécifique intéressante. Les technologies de dépôt de couches d'AMF Ti-Ni-Cu micro-structurées ont été développées. Ce travail servira de base pour la future fabrication de micro-récupérateurs d'énergie thermique exploitant des AMFs.

Composite materials on the basis of a shape memory alloy & a pyro/piezoelectric material for thermal energy harvestin

ABSTRACT

This thesis experimentally studies the possibility of thermal energy harvesting using coupled shape memory alloy (SMA) and pyro-/piezoelectric material. This method is promising for harvesting slow & small temperature variations. First prototypes of energy harvesters were fabricated and their ability to produce an increased amount of specific energy was shown. Technologies of Ti-Ni-Cu SMA thin layer deposition & patterning were developed. This work will serve as a base for future fabrication of chip-scale thermal energy harvesters exploiting SMAs.